Dissertation zur Erlangung des Doktorgrades
der Fakultät für Chemie und Pharmazie
der Ludwig–Maximilians–Universität München

Controlling the Optical Response of Low-Dimensional Materials through Exciton Dynamics

---

von
Lucas Christopher Lange
aus
Lengerich, Deutschland
2025

Erklärung

Diese Dissertation wurde im Sinne von § 7 der Promotionsordnung vom 28. November 2011 von Herrn Prof. Dr. Achim Hartschuh betreut.

Eidesstattliche Versicherung

Diese Dissertation wurde eigenständig und ohne unerlaubte Hilfe erarbeitet.

Lucas Lange

Lucas Christopher Lange
München, 26. August 2025

Dissertation eingereicht am: 26. August 2025

Mündliche Prüfung am: 9. Dezember 2025

1. Gutachter: Prof. Dr. Achim Hartschuh

2. Gutachter: Prof. Dr. Alexander Högele

Erscheinungsjahr: 2026

Abstract

Excitons are bound electron-hole pairs and responsible for the fascinating optoelectronic properties of low-dimensional materials. Their large oscillator strength results in strong optical absorption and enhanced nonlinear effects [1–3]. At elevated excitation densities, exciton-exciton interactions introduce many-body effects such as spectral broadening, reduced coherence and nonradiative recombination through annihilation [4, 5]. These interactions can also shift excitonic resonances, reduce binding energies and eventually lead to a Mott transition, where excitons dissociate into a free electron-hole plasma [4, 6–9]. This thesis presents two projects exploring how exciton dynamics can be utilized to control the optical response of low-dimensional systems.

The first project investigates how an optical antenna can control the photon statistics of 1D nanostructures and convert them into single-photon sources. The antenna focuses the light-matter interaction to a strongly confined area, resulting in locally enhanced exciton-exciton annihilation and radiative recombination rates. Experimentally, the degree of antibunching in the photoluminescence of single-walled carbon nanotubes in the presence of an antenna was analyzed at room temperature. Numeric simulations were performed to explore the relevant parameters and the potential of antenna-controlled antibunching. The results indicate that optical antennas can significantly alter the photon emission statistics of 1D nanosystems and convert them into single-photon sources.

The second project examines the impact of optical pulse shaping on nonlinear signal generation in transition metal dichalcogenide monolayers. By tailoring the phase of broadband 12 fs excitation pulses, overlapping the first excitonic resonance, the four-wave mixing (FWM) signal in WSe_2 and $MoSe_2$ was enhanced by a factor of $\sim$2, compared to the transform-limited case. However, at elevated excitation densities, the influence of the excitonic resonance diminished, as confirmed in fluence-dependent differential reflection experiments. Classical and quantum-mechanical models predicted the optimal phase profile at low excitation densities, although both underestimated the vanishing phase influence at strong excitation. Excitation-induced dephasing together with the Mott transition to a free electron-hole plasma were identified as the primary cause for the diminishing excitonic resonance, effectively hindering coherent population control at room temperature. In contrast, sum-frequency generation (SFG) showed no such enhancement and appeared unaffected by the first excitonic resonance. This is explained by higher-energy excitonic resonances dominating this process.

Overall, these studies advance both the fundamental understanding of many-body excitonic effects and the practical control of light-matter interactions at room temperature. They provide a pathway for engineering novel single-photon sources and ultrafast, tunable optoelectronic devices, contributing to the development of scalable quantum technologies.

Contents

1. Introduction

Semiconductors form the foundation of modern electronics, powering the technological advancements that have revolutionized daily life. Their unique ability to act as both conductors and insulators, depending on external conditions such as temperature, doping, applied electric fields or illumination with light, enables the creation of key components for all digital devices. From the silicon chips in smartphones to high-speed processors and solar panels, semiconductors are indispensable in modern technology.

The functionality of semiconductors hinges on their electronic band structure, in which a forbidden energy gap separates the valence and conduction bands. In the ground state, electrons occupy the valence band and cannot contribute to conduction, rendering the material insulating. However, upon excitation, either through thermal, electrical or optical energy, electrons can be promoted across the bandgap into the conduction band, leaving behind positively charged holes. These charge carriers enable current flow and interaction with electromagnetic radiation, giving rise to a variety of linear and nonlinear optical phenomena.

Excitons are bound electron-hole pairs, responsible for the fascinating optical phenomena observed in low-dimensional materials. These quasiparticles are stabilized by the Coulomb attraction between the negatively charged electron and the positively charged hole. In conventional bulk semiconductors this Coulomb interaction is screened by the surrounding electronic environment, resulting in relatively low exciton binding energies on the order of 10 meV [10, 11]. At room temperature, thermal fluctuations are sufficient to dissociate these weakly bound pairs and excitons are stable only at cryogenic temperatures. In contrast, low-dimensional materials exhibit strongly enhanced Coulomb interactions due to reduced dielectric screening and spatial confinement. This results in much higher exciton binding energies, often exceeding hundreds of meV, and excitons are stable even at room temperature [12–14]. In contrast to the broad, continuous absorption typical for bulk systems, low-dimensional semiconductors exhibit sharp optical features at excitonic resonances. The large oscillator strength of these excitons leads to pronounced optical absorption and a significant enhancement of nonlinear optical effects. Nonlinear processes such as sum-frequency generation (SFG) and four-wave mixing (FWM) are particularly amplified at energies close to excitonic transitions [1–3]. This enables efficient frequency conversion even at relatively low excitation intensities.

However, at moderate to high excitation densities, exciton-exciton interactions give rise to many-body effects that significantly alter excitonic properties. Collisional interactions between excitons result in homogeneous spectral broadening and a loss of optical coherence [15], thereby limiting the feasibility of coherent control over excitonic states. At moderate densities, excitons attract each other, similar to the case of atomic van der Waals attraction, leading to a red-shift of excitonic resonances. Additionally, screening of the Coulomb potential becomes noticeable, leading to a reduction in exciton binding energy and a bandgap renormalization [4]. At high densities, this can drive the system toward the Mott transition, where excitons dissociate into a dense free electron-hole plasma due to the breakdown of exciton binding [6–9]. In contrast, at high excitation densities, exciton wavefunctions begin to overlap and the Pauli exclusion principle introduces a repulsive component to the interaction and leads to a blue-shift of the excitonic resonance [4]. Moreover, exciton-exciton annihilation (EEA) introduces a nonlinear, density-dependent nonradiative recombination channel, where one exciton recombines and transfers its energy to another. This process reduces exciton lifetimes and the PL quantum yield but also plays a important role in enabling single-photon emission [16–18]. Understanding and controlling these many-body effects is essential for tailoring the optical response of low-dimensional materials.

The rich potential of low-dimensional semiconductors for advancing integrated photonic technologies make them an interesting subject of research. Their pronounced many-body interactions offer an promising platform for exploring condensed matter physics and quantum phenomena at the nanoscale. Their exceptional excitonic properties, including strong light-matter coupling, room-temperature stability and pronounced nonlinear responses, make them highly interesting for key applications such as ultracompact photonics [19], nanoscale optoelectronic devices [11], on-chip quantum light sources [20] and coherent optical control schemes [21]. In particular, the ability to generate single photons, modulate light with high precision and exploit many-body interactions for functionality provides a versatile platform for next-generation quantum communication and optoelectronics [22–24]. Exploring how excitonic behavior can be actively controlled and harnessed under realistic conditions is thus a crucial step toward translating these fundamental properties into practical device architectures.

In this thesis, two projects are presented that explore the potential of exploiting exciton dynamics in low-dimensional materials to control light-matter interactions and tailor the optical response, as required for emerging photonic applications.
The first project demonstrates effective control of photon emission statistics in 1D nanosystems by using an optical antenna. The antenna locally enhances excitation and recombination rates in single-walled carbon nanotubes, enabling single-photon emission at room temperature without altering their electronic state energies.
The second project explores how spectral phase shaping of ultrashort laser pulses can coherently control nonlinear optical responses in 2D semiconductors, revealing both the potential and limits of excitonic coherence under varying excitation densities.

Each project is presented in a dedicated chapter, preceded by a detailed introduction at the chapter's beginning.

2. Fundamentals

2.1. Linear and nonlinear optics

The interaction of light with matter is important for many modern optical technologies and fundamental research [25]. This chapter introduces the theoretical concepts of both linear and nonlinear optical phenomena relevant for the experiments presented in this work. The chapter begins with the concept of optical susceptibility, which characterizes the response of a material to an applied electromagnetic field. This is important for the distinction between linear and nonlinear optics. In the regime of linear optics, the material response scales proportionally with the applied field, giving rise to well-known effects such as absorption and photoluminescence [26]. However, at high field intensities, nonlinear effects emerge, where the response depends on higher powers of the electric field. These nonlinear interactions enable phenomena such as second-harmonic generation (SHG), sum-frequency generation (SFG) and four-wave mixing (FWM), all of which are essential to the experimental investigations in this work. The chapter concludes with a brief introduction to the density matrix formalism to provide a more fundamental understanding of the description of light-matter interaction at the microscopic level. This quantum-mechanical framework provides the description of coherence and population dynamics. Together, these theoretical contemplation form the basis of the interpretation of the optical experiments presented in the following chapters.

2.1.1. Optical susceptibility

In the classical description of linear excitation in a dielectric medium, the electrons are assumed to be bound by harmonic forces to the positively charged hole [26]. The transverse electric field of a light beam, assumed to be polarized in the x-direction, can be expressed in the complex notation as:

$$E(t) = E(\omega)e^{-i\omega t} + c.c. \tag{2.1}$$

where *c.c.* denotes the complex conjugate. The oscillating field induces a displacement x of the electrons from their equilibrium positions, resulting in a macroscopic electric polarization in the material. This polarization P, defined as the dipole moment per unit volume, arises from the collective microscopic displacement of the bound charges.

$$P = \frac{N}{V} \cdot ex = n_0 \cdot d \tag{2.2}$$

with the number of electrons N, the volume V, the elementary charge $e = -1.6 \cdot 10^{-19}$ C, the mean electron density $n_0 = \frac{N}{V}$ and the electric dipole moment $d = ex$. This classical oscillator model yields reasonable results, as long as the excitation does not overcome the free-particle band gap and the electron is still in a bound state. The motion of the electron under the influence of the electric field is described as a damped driven harmonic oscillator,

$$m\frac{d^2x}{dt^2} + 2\gamma m\frac{dx}{dt} + m\omega_0^2 x = eE(t) \tag{2.3}$$

with the mass of the electron m, the damping constant γ and the resonance frequency of the oscillator ω_0.
The ansatz

$$x(t) = x(\omega)e^{-i\omega t} \tag{2.4}$$

leads to

$$x(\omega) = \frac{-e}{m(\omega^2 - \omega_0^2 + 2i\gamma\omega)}E(\omega) \tag{2.5}$$

and with Equation 2.2 to the polarization

$$P(\omega) = -\frac{n_0e^2}{m(\omega^2 - \omega_0^2 + 2i\gamma\omega)}E(\omega) = \chi(\omega)E(\omega). \tag{2.6}$$

Here, the optical susceptibility $\chi(\omega))$ is the complex coefficient between the external electric field E(ω) and the induced polarization P(ω) and can be expressed as:

$$\begin{aligned}
\chi(\omega) &= -\frac{n_0e^2}{m} \cdot \frac{1}{(\omega^2 - \omega_0^2 + 2i\gamma\omega})\\
&= -\frac{n_0e^2}{m} \cdot \frac{1}{(\omega - \omega_0' + i\gamma)(\omega + \omega_0' + i\gamma)}\\
&= -\frac{n_0e^2}{m \cdot 2\omega_0'} \cdot \frac{(\omega + \omega_0' + i\gamma) - (\omega - \omega_0' + i\gamma)}{(\omega - \omega_0' + i\gamma)(\omega + \omega_0' + i\gamma)}\\
&= -\frac{n_0e^2}{2m\omega_0\prime}\left(\frac{1}{\omega - \omega_0\prime + i\gamma} - \frac{1}{\omega + \omega_0\prime + i\gamma}\right)
\end{aligned} \tag{2.7}$$

with the shifted resonance frequency $\omega_0\prime = \sqrt{\omega^2 - \gamma^2}$. In general, $\chi(\omega)$ is a tensor that relates the polarization vector $\mathbf{P}(\omega)$ to the electric field $\mathbf{E}(\omega)$. Its frequency dependence characterizes how the material responds to an external field.

It is important to note that this expression defines a susceptibility $\chi(\omega)$ that carries physical units and does not yet include the vacuum permittivity ε_0. In SI units, the macroscopic polarization is usually expressed as $P(\omega) = \varepsilon_0 \chi^{(1)}(\omega) E(\omega)$, where $\chi^{(1)}$ is the dimensionless linear susceptibility. This implies the relation

$$\chi^{(1)}(\omega) = \frac{1}{\varepsilon_0}\chi(\omega) = -\frac{n_0 e^2}{\varepsilon_0 m(\omega^2 - \omega_0^2 + 2i\gamma\omega)}. \tag{2.8}$$

Since the susceptibility derived here originates from a microscopic model the vacuum permittivity does not appear explicitly until the transition to macroscopic electrodynamics.

The susceptibility has poles at complex frequencies $\omega = \pm\omega_0' - i\gamma$, which lie in the lower half of the complex frequency plane, i.e. negative imaginary parts. As a result, $\chi(\omega)$ is analytic in the upper half-plane, including the entire real positive frequency axis, that is accessible in experiments. This analytic structure is a direct consequence of causality. The polarization response $P(t)$ can only depend on the electric field at earlier times $E(t - \tau)$, which means the response function $\chi(t)$ must vanish for $t < 0$. According to complex analysis, such a causal time-domain response leads to a frequency-domain function $\chi(\omega)$ that is analytic in the upper half-plane. The poles in the lower half-plane correspond to exponentially decaying oscillations in time, consistent with a retarded response. The real part ω_0' of the pole, defines the resonance frequency, while the imaginary part γ determines the linewidth or damping rate. This analytic structure ensures the validity of the Kramers-Kronig relations, which link the real and imaginary parts of the susceptibility, and guarantees that $\chi(\omega)$ can be safely evaluated on the real axis for $\omega > 0$ [25].

The imaginary part of the susceptibility, $\operatorname{Im}\chi(\omega)$, determines the absorptive response of the system and exhibits a Lorentzian lineshape for each resonance. For a single resonant pole at ω_0', the susceptibility takes the form of Equation 2.7 and its imaginary part becomes

$$\operatorname{Im}\chi(\omega) = A \cdot \frac{\gamma}{(\omega_0' - \omega)^2 + \gamma^2}, \tag{2.9}$$

a Lorentzian function centered at ω_0 with a full width at half maximum (FWHM) of 2γ [27]. The peak value is reached at $\omega = \omega_0'$ and is given by

$$\operatorname{Im}\chi(\omega_0') = \frac{A}{\gamma}. \tag{2.10}$$

This inverse dependence on γ implies that narrow, long-lived resonances appear as sharp peaks, while broad, short-lived resonances are less pronounced. This relationship ensures that the total spectral weight, represented by the area under the curve, remains proportional to the oscillator strength A. The height and width of these peaks thus reflect the strength and lifetime of the excitation, respectively. This structure explains the sharp resonance features commonly observed in optical absorption spectra.

The complex susceptibility $\chi(\omega) = \chi'(\omega) + i\chi''(\omega)$ characterizes the full linear response of a medium to an external electric field. While the imaginary part $\chi''(\omega)$ describes the absorptive response, the real part $\chi'(\omega)$ accounts for the dispersive behavior of the material. Together they fully determine the response of the system in termes of amplitude and phase.

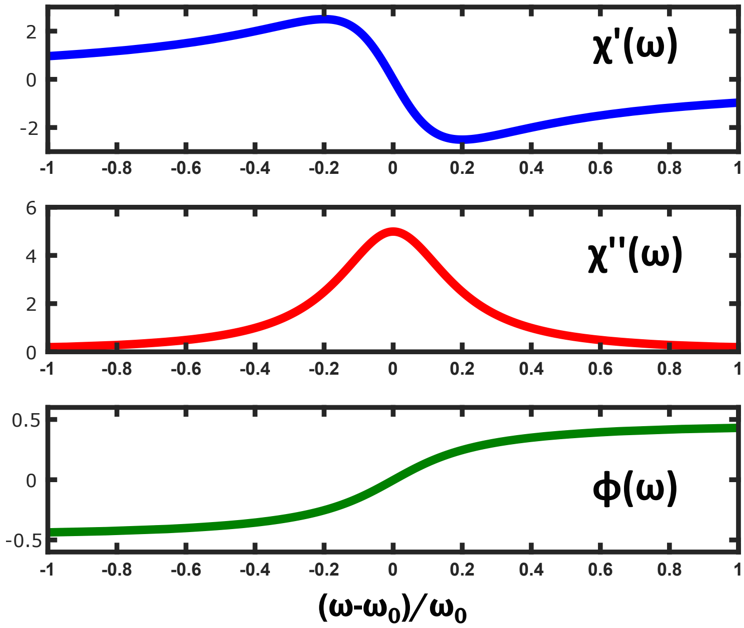

Figure 2.1.: Dispersion of real part, imaginary part and phase of the complex optical susceptibility around a resonance. The real part $\chi'(\omega)$ accounts for the dispersive behaviour of the system, while the imaginary part $\chi''(\omega)$ describes the absorptive response and exhibits a Lorentzian peak. The phase shift $\Phi(\omega)$ in radiant units of π between the driving field and the induced polarization crosses zero at the resonance and takes a step of π.

Figure 2.1 illustrates the dispersion of real part, imaginary part and phase of the complex susceptibility around a resonance. Near a resonance, the imaginary part $\chi''(\omega)$ exhibits a Lorentzian peak, representing strong absorption at the resonance frequency. Simultaneously, the real part $\chi'(\omega)$ displays its characteristic dispersive shape. It changes rapidly and passes through zero at the resonance. This structure corresponds to a π-step change in the phase response of the medium.

The phase shift between the driving electric field and the induced polarization is given by the argument of the complex susceptibility

$$\phi(\omega) = \tan^{-1}\left(\frac{\chi''(\omega)}{\chi'(\omega)}\right). \tag{2.11}$$

As the frequency crosses the resonance, the phase undergoes a transition by approximately π. This phase step is a universal feature of driven damped oscillators and reflects the causal and retarded nature of the response.

The expression for the complex susceptibility in Equation 2.7 contains resonant responses at both positive and negative frequencies. However, real physical fields are typically described using positive frequencies, as the negative-frequency components are redundant due to the real-valued nature of the physical field. Thus, the frequency-dependent susceptibility close to an optical resonance can be modeled as a complex Lorentzian function with a pole structure term of the form:

$$\chi(\omega) \propto \frac{1}{\omega_n - \omega - i\gamma_n} \tag{2.12}$$

where ω_n is the resonance frequency and γ_n describes the linewidth of the resonance due to finite lifetime or dephasing. Although the poles are not located directly on the real axis, their real parts correspond to the energies at which resonances are observed in optical spectra.

Miller's rule

The model presented so far for determining the linear optical susceptibility assumes a perfectly harmonic potential. However, in real materials, the potential in which electrons are bound is not exactly parabolic. Instead, it exhibits anharmonic components, which can be described by an additional nonlinear term ax^2 in the equation of motion for the electron (see Equation 2.3), with a being a measure of the strength of the nonlinearity. Instead, it exhibits anharmonic components, represented by an additional nonlinear term ax^2 in the equation of motion for the electron (see Equation 2.3), where a characterizes the strength of the anharmonicity. In this case, no exact analytic solution exists. Nevertheless, if the applied field is sufficiently weak, the nonlinear term remains much smaller than the linear term, and the solution can be approximated using a perturbation expansion. In Equation 2.13, the driving field $E(t)$ is scaled by a parameter λ, which ranges between zero and one and characterizes the strength of the perturbation.

$$m\frac{d^2x}{dt^2} + 2\gamma m\frac{dx}{dt} + m\omega_0^2 x + ax^2 = -\lambda eE(t) \tag{2.13}$$

As a result, the solution of Equation 2.13 can be approximated by a power series expansion in powers of λ and higher-order contributions to the susceptibility can be calculated. The detailed derivation can be found in [27].

For the general second-order case of SFG, the second-order nonlinear susceptibility depends on the two fundamental frequencies ω_1 and ω_2, as well as the generated sum-frequency $\omega_{\mathrm{SFG}} = \omega_1 + \omega_2$. It turns out that this second-order susceptibility can be approximated by a product of the linear susceptibilities at the corresponding frequencies:

$$\chi^{(2)}(\omega_{\mathrm{SFG}}; \omega_1, \omega_2) \sim \chi^{(1)}(\omega_{\mathrm{SFG}}) \cdot \chi^{(1)}(\omega_1) \cdot \chi^{(1)}(\omega_2) \tag{2.14}$$

This correlation was originally formulated as an empirical rule by Miller in 1964 [28]. He observed that the ratio of the second-order nonlinear susceptibility to the product of the relevant linear susceptibilities remains approximately constant in noncentrosymmetric materials [27].

$$\frac{\chi^{(2)}(\omega_{\mathrm{SFG}}; \omega_1, \omega_2)}{\chi^{(1)}(\omega_{\mathrm{SFG}}) \cdot \chi^{(1)}(\omega_1) \cdot \chi^{(1)}(\omega_2)} \approx \text{const.} \tag{2.15}$$

An analogous consideration can be made for FWM (see Section 2.1.3). The third-order nonlinear susceptibility, governing the process, can be approximated as:

$$\chi^{(3)}(\omega_{\mathrm{FWM}}; \omega_1, \omega_2, \omega_3) \sim \chi^{(1)}(\omega_{\mathrm{FWM}}) \cdot \chi^{(1)}(\omega_1) \cdot \chi^{(1)}(\omega_2) \cdot \chi^{(1)}(\omega_3) \tag{2.16}$$

This practical model, originally formulated for nondispersive and nonabsorbing media, has recently been shown to be applicable for describing FWM in plasmonic nanoantennas with single resonances within the excitation laser spectrum [29].

2.1.2. Linear optics

In the regime of linear optics the material polarization responds linearly to the applied electric field. Here, the first-order susceptibility $\chi^{(1)}$ fully characterizes the optical response of the medium. This regime describes many of the most familiar optical phenomena and the considerations presented here form the basis for the more complex nonlinear processes discussed later. When light interacts with matter, it induces a displacement of the electron cloud relative to the atomic nuclei in atoms or molecules. This displacement gives rise to a macroscopic polarization $P(\omega)$, which is directly proportional to the applied electric field $E(\omega)$ and mediated by the optical susceptibility $\chi(\omega)$:

$$P(\omega) = D(\omega) - \epsilon_0 E(\omega) = \epsilon_0(\epsilon(\omega) - 1) \cdot E(\omega) = \chi(\omega) E(\omega), \tag{2.17}$$

where $D(\omega)$ is the electric flux density, $\epsilon(\omega)$ is the dielectric function, describing how the material influences the expansion of the electric field. $\epsilon(\omega)$ also is a complex function and linked to the susceptibility trough:

$$\epsilon(\omega) = \frac{1}{\epsilon_0}\chi(\omega) + 1 = \epsilon_{\mathrm{r}} + i\epsilon_{\mathrm{i}}. \tag{2.18}$$

Closely related to the dielectric function is the complex refractive index $n(\omega)$, which governs how the light propagates through a material:

$$n(\omega) = \sqrt{\epsilon(\omega)} = n_{\mathrm{r}} + in_{\mathrm{i}}. \tag{2.19}$$

Because these quantities are interdependent, their imaginary parts are also directly connected.

$$\chi_{\mathrm{i}} \propto \epsilon_{\mathrm{i}} \propto n_{\mathrm{i}}. \tag{2.20}$$

Each of these imaginary components carries physical meaning, describing the absorption of light within the medium. To understand how absorption manifests during wave propagation, a plane wave $E(z,t))$ is considered, traveling in the z-direction through a medium with refractive index $n(\omega)$. Using the relation $k = \frac{2\pi}{\lambda} = \frac{n\omega}{c}$, the electric field in the medium can be expressed as:

$$\begin{aligned} E(z,t) &= E_0 \cdot e^{-i(\omega t - kz)} && (2.21)\\ &= E_0 \cdot e^{-i\omega t + i\frac{\omega n_{\mathrm{r}}}{c}z + \frac{\omega n_{\mathrm{i}}}{c}z} && (2.22)\\ &= E_0 \cdot e^{\frac{\omega n_{\mathrm{i}}}{c}z} \cdot e^{-i\left(\omega t - \frac{\omega n_{\mathrm{r}}}{c}z\right)}. && (2.23) \end{aligned}$$

Here, this electric field has a fast oscillating component, which is described by the real part of the complex refractive index n_{r}. However, the amplitude is governed by the imaginary part of the refractive index n_{i}, as the field propagates through the medium. Near resonance frequencies of the material, n_{i} is negative, resulting in an exponential decay of the field with increasing depth, describing optical absorption [26]. The corresponding intensity $I(z)$ of the light field follows

$$I(z) = I(0) \cdot e^{\frac{2\omega n_{\mathrm{i}} z}{c}} = I(0) \cdot e^{-\alpha z}, \tag{2.24}$$

where $\alpha = -\frac{2\omega n_{\mathrm{i}}}{c}$ is the extinction coefficient, proportional to the imaginary part of n and characterizing how strongly the medium absorbs light.

The energy of the decaying light field is typically absorbed by the electrons in the material and needs to be discussed quantum-mechanically. In isolate atoms, optical absorption leads to transitions between levels of discrete energies. However, in solids the formation of energy bands from delocalized states affect the absorption process. For an electron the transition from the valence band to the conduction band is possible if the gap energy E_g is met by the photon energy $\hbar\omega$.

$$E_\mathrm{g} = E_\mathrm{c} - E_\mathrm{v} = \hbar\omega \tag{2.25}$$

In Equation 2.25, E_c and E_v denote the energy levels of the conduction band and the valence band, respectively.

The reverse process, in which an electron from the conduction band relaxes spontaneously to the lower-energy valence band after its characteristic lifetime by emitting a photon, is referred to as interband luminescence. The rates of both absorption and emission are governed by Fermi's Golden Rule, which gives the transition probability per unit time as

$$W_{i\to f} = \frac{2\pi}{\hbar} \left|\langle f|H'|i\rangle\right|^2 \rho(E_f)\,, \tag{2.26}$$

where $\rho(E_f)$ is the density of final states. In the dipole approximation the perturbation Hamiltonian is

$$H' = -\hat{\vec{d}} \cdot \vec{E}(t), \tag{2.27}$$

with the electric dipole operator $\hat{\vec{d}} = -e\vec{r}$. The matrix element between the initial and final states defines the *transition dipole moment* $\vec{\mu}_{fi}$,

$$\vec{\mu}_{fi} = \langle f|\hat{\vec{d}}|i\rangle, \tag{2.28}$$

so that the transition probability can be written as

$$W_{i\to f} = \frac{2\pi}{\hbar} |\vec{\mu}_{fi} \cdot \vec{E}|^2 \, \rho(E_f). \tag{2.29}$$

If this radiative recombination was originally initiated by optical excitation, the resulting emission is called photoluminescence (PL). The analysis of PL serves as a key experimental technique for probing the electronic properties of semiconductors and low-dimensional materials. It provides a direct, non-invasive way to access the energy landscape and dynamics of electronic excitations.

Conservation of momentum dictates that during an interband transition the change in crystal momentum of the electron must match the momentum k of the absorbed or emitted photon:

$$k_c - k_v = k, \tag{2.30}$$

k_c and k_v denote the wave vectors of the conduction and valence band electron states, respectively. However, the magnitude of the photon wave vector at optical frequencies is on the order of $10^7\ \mathrm{m}^{-1}$, whereas typical electron wave vectors in solids span the Brillouin zone, which has a characteristic scale of $\frac{\pi}{a} \sim \frac{\pi}{10^{-10}\ \mathrm{m}} \sim 10^{10}\ \mathrm{m}^{-1}$, with a being the lattice constant. This means that the photon's momentum is several orders of magnitude smaller than that of the electrons involved.

As a result, in most optical transitions, the photon momentum can be neglected and the electronic transition must occur between states with approximately the same crystal momentum, $k_c \approx k_v$. Such transitions are referred to as direct optical transitions. In contrast, indirect transitions require a significant change in crystal momentum and must involve a phonon, carrying the additional momentum to satisfy momentum conservation. The radiative lifetime τ_{rad} of an electron is defined as the average time an excited electron remains in the conduction band before recombining under the emission of a photon. It is the inverse of the radiative rate, which depends on the radiative recombination coefficient B and the carrier density n.

$$\tau_{\mathrm{rad}} = \frac{1}{\Gamma_{\mathrm{rad}}} \propto \frac{1}{B \cdot n} \tag{2.31}$$

Due to the necessarity of phonons involved in indirect transition, typically direct transitions exhibit shorter lifetimes compared to indirect transitions. The total decay rate Γ_{tot} is the sum of all radiative Γ_{rad} and nonradiative rates Γ_{nonrad}.

$$\Gamma_{\mathrm{tot}} = \Gamma_{\mathrm{rad}} + \Gamma_{\mathrm{nonrad}} \tag{2.32}$$

The Quantum Yield (QY) is describes the ratio of radiative rate and the total decay rate.

$$QY = \frac{\Gamma_{\mathrm{rad}}}{\Gamma_{\mathrm{tot}}} \tag{2.33}$$

2.1.3. Nonlinear optics

Nonlinear optical effects arise when the response of a material to an applied optical field becomes nonlinear with respect to the strength of the driving field. For example, in second-order nonlinear processes, the intensity of the generated light scales with the square of the incident laser intensity, while in third-order processes, it scales with the cube.

Unlike in linear optics, where the material polarization $P(t)$ is directly proportional to the electric field $E(t)$, nonlinear optics occurs, when the material response becomes dependent on the excitation intensity. To account for nonlinear optics, the polarization can be extended as a power series in the electric field:

$$\begin{aligned} P(t) &= \epsilon_0 \left[\chi^{(1)} E(t) + \chi^{(2)} E^2(t) + \chi^{(3)} E^3(t) + \dots\right] \\ &= P^{(1)}(t) + P^{(2)}(t) + P^{(3)}(t) + \dots \end{aligned} \tag{2.34}$$

In Equation 2.34, the coefficients $\chi^{(2)}$ and $\chi^{(3)}$ are the second- and third-order nonlinear susceptibilities, respectively. $P^{(2)}(t)$ and $P^{(3)}(t)$ are higher-order polarization terms and describe how the material generates new frequency components of the electromagnetic field. The time-varying polarization acts as the source of new components of the electromagnetic field, reflecting the motion and acceleration of the charges in the medium [27].

Compared to the linear susceptibility $\chi^{(1)}$, which is of the order of unity, the nonlinear susceptibilities are significantly smaller, with $\chi^{(2)}$ on the order of $10^{-12}\ m/V$ and $\chi^{(3)}$ on the order of $10^{-24} m^2/V^2$. Consequently, nonlinear optical processes become relevant only at sufficiently high optical intensities, such as those provided by pulsed lasers [30].

Nonlinear optics plays a crucial role in various modern technologies, from telecommunications to laser development. Nonlinear optical imaging techniques, such as multi-photon microscopy, enable high-resolution, deep-tissue imaging with reduced photodamage, making them valuable in biological and medical research. Saturable absorption, where a material's absorption decreases with increasing light intensity, plays an important role in ultrafast pulses creation through mode-locking. Higher harmonic generation (HHG), difference frequency generation (DFG), sum-frequency generation (SFG), four-wave mixing (FWM) and self-phase modulation (SPM), allow access to new spectral regions and are widely used in spectroscopy and ultrafast laser development. Optical parametric amplification (OPA) and optical parametric oscillation (OPO) provide tunable coherent light sources across broad wavelength ranges. Self-focusing, arising from a self-induced change in the refractive index by the optical Kerr effect, is central to nonlinear phenomena like laser filamentation and supercontinuum generation. These effects are extensively discussed in [27].

In the following, SHG, SFG and FWM are described in more detail, based on [27], as these nonlinear optical processes form the basis of the experimental investigations presented in Section 4.4.

Second-Harmonic Generation

In second-harmonic generation (SHG) two photons are effectively combined to create a single photon with twice the frequency, or half the wavelength of the original light. This can be illustrated by considering a laser field with an electric field given by

$$E(t) = E_0 e^{-i\omega t} + c.c., \tag{2.35}$$

where ω is the angular frequency and E_0 is the complex amplitude of the field. According to Equation 2.34, the second-order nonlinear polarization induced in a material with nonzero $\chi^{(2)}$ is

$$P^{(2)}(t) = \epsilon_0 \chi^{(2)} E^2(t) = \epsilon_0 \chi^{(2)} \left(2E_0 E_0^* + E_0^2 e^{-i2\omega t} + c.c.\right) \tag{2.36}$$

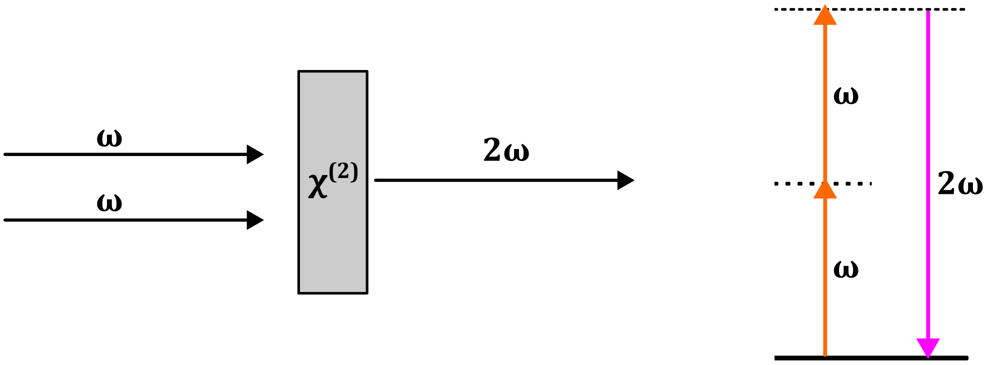

Figure 2.2.: Schematic illustration of the SHG process. *Left:* Two photons at frequency ω interact with a nonlinear crystal exhibiting a second-order susceptibility $\chi^{(2)}$. As a result, a single photon at the second-harmonic frequency 2ω is emitted. *Right:* Schematic energy level diagram of the SHG process. The solid line indicates the ground state, while the dashed lines represent virtual energy levels. Two ω photons are combined in a single quantum-mechanical process, leading to the emission of one 2ω photon.

The first term in Equation 2.36 is a static contribution for optical rectification and does not generate radiation as it lacks time variation. In contrast, the second term represents a oscillation at frequency 2ω, corresponding to the second harmonic of the input light. This oscillating polarization acts as a source of radiation at the second harmonic frequency. Figure 2.2 illustrates the SHG process, where two photons at frequency ω interact within a nonlinear medium, accessing a virtual energy level and generate a single photon at frequency 2ω in a single, coherent quantum-mechanical process.

Sum-Frequency Generation

In the case of a non-monochromatic laser beam or two laser beams, two distinct frequency components can interact within a nonlinear medium. The electric field can be expressed as:

$$E(t) = E_1 e^{-i\omega_1 t} + E_2 e^{-i\omega_2 t} + c.c. \tag{2.37}$$

where ω_1 and ω_2 are the angular frequencies of the two spectral components and E_1 and E_2 are their respective complex amplitudes. According to Equation 2.34, the resulting second-order nonlinear polarization in a medium with susceptibility $\chi^{(2)}$ is then given by:

$$\begin{aligned} P^{(2)}(t) =& \epsilon_0 \chi^{(2)} \Big[E_1^2 e^{-2i\omega_1 t} + E_2^2 e^{-2i\omega_2 t} + 2E_1E_2 e^{-i(\omega_1+\omega_2)t} \\ & + 2E_1E_2^* e^{-i(\omega_1-\omega_2)t} + c.c. \Big] + 2\epsilon_0\chi^{(2)} \left[E_1E_1^* + E_2E_2^*\right] \end{aligned} \tag{2.38}$$

The first and the second terms describe SHG of the individual input frequencies ω_1 and ω_2, respectively, on its own, as discussed in Section 2.1.3. The third term describes the sum-frequency $\omega_{\text{sum}} = \omega_1 + \omega_2$. The fourth term describes the difference-frequency process resulting in $\omega_{\text{diff}} = \omega_1 - \omega_2$. The last term without any frequency dependence again describes the constant nonradiative static electrical field. Although theoretically all these new frequency components can be present, typically they do not, because the efficient generation relies on a certain phase-matching condition, which cannot be satisfied for all nonlinear signals simultaneously. For this work, the sum-frequency process, illustrated in Figure 2.3, is of central importance.

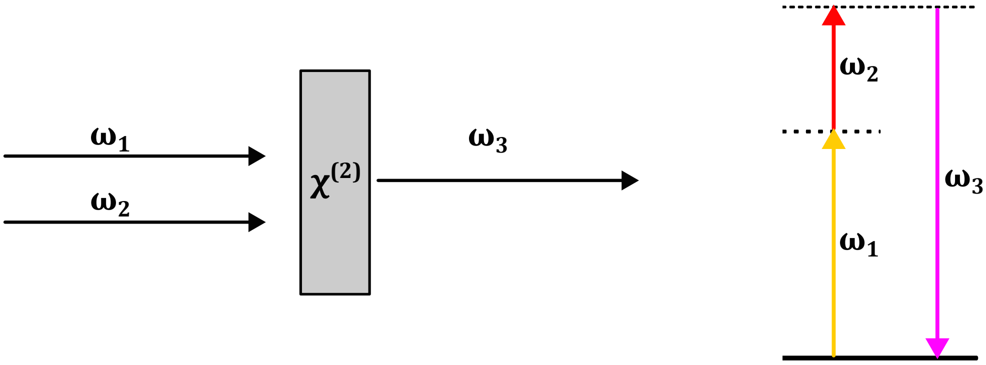

Figure 2.3.: Schematic illustration of the SFG process. *Left:* Two photons at frequencies ω_1 and ω_2 interact with a nonlinear crystal exhibiting a second-order susceptibility $\chi^{(2)}$. As a result, a single photon at the sum-frequency $\omega_{sum} = \omega_1 + \omega_2$ is emitted. *Right:* Schematic energy level diagram of the SFG process. The solid line indicates the ground state, while the dashed lines represent virtual energy levels. Two photons at ω_1 and ω_2 are combined in a single quantum-mechanical process, leading to the emission of one sum-frequency photon.

Due to the broad spectral bandwidth of ultrafast pulses, wave mixing processes can involve a wide range of frequency components. In such a scenario, quantum interference between multiple simultaneous coherent excitation pathways, leading to the same final quantum state, can significantly contribute to the resulting nonlinear signal [27, 30, 31]. In particular, the intensity at 2ω can be complemented by SFG pathways, where two different photons with frequencies ω_1 and ω_2 combine to produce the same output frequency, $\omega_3 = \omega_1 + \omega_2 = 2\omega$.

The total SFG intensity spectrum, including the SHG contribution, can be expressed as:

$$
\begin{aligned}
I_{\mathrm{SFG}}(\omega) = c\epsilon_0 \Bigg| \iint_{\omega_{\min}}^{\omega_{\max}} & \chi^{(2)}(\omega;\omega_1,\omega_2) \cdot E(\omega_1)E(\omega_2) \\
& \cdot\delta(\omega-\omega_1-\omega_2)\, d\omega_1\, d\omega_2 \Bigg|^2 ,
\end{aligned} \tag{2.39}
$$

$$
\begin{aligned}
= c\epsilon_0 \Bigg| \iint_{\omega_{\min}}^{\omega_{\max}} & \chi^{(2)}(\omega;\omega_1,\omega_2) \cdot A(\omega_1)A(\omega_2)\, e^{i[\varphi(\omega_1)+\varphi(\omega_2)]} \\
& \cdot\delta(\omega-\omega_1-\omega_2)\, d\omega_1\, d\omega_2 \Bigg|^2 ,
\end{aligned} \tag{2.40}
$$

where $E(\omega_{1,2}) = A(\omega_{1,2})e^{i\varphi(\omega_{1,2})}$ represent the complex electric field with amplitude $A(\omega_{1,2})$ at frequencies ω_1 and ω_2, respectively. $\delta(\omega-\omega_1-\omega_2)$ ensures energy conservation in the sum-frequency generation process. The interference of all these coherent frequency pairs contributes to the final shape and intensity of the SFG signal. Hence, the process is crucially sensitive to the spectral phase of the input pulses.

Symmetry considerations in the second-order nonlinear response

Existence and strength of nonlinear optical effects are directly tied to the symmetries of the medium in which they occur. In particular, the second-order nonlinear susceptibility tensor $\chi^{(2)}$ is subject to strong symmetry constraints. One of the most important results is that in a material with inversion symmetry or centrosymmetry, all components of $\chi^{(2)}$ must vanish.
According to Equation 2.34, the second-order contribution to the polarization is given by:

$$
P^{(2)}(t) = \varepsilon_0 \chi^{(2)} E^2(t). \tag{2.41}
$$

In a centrosymmetric material, the structure of the medium remains unchanged under spatial inversion ($\vec{r} \to -\vec{r}$). This symmetry imposes the constraint on the macroscopic response functions that the polarization must transform as:

$$
\vec{P}(-\vec{E}) = -\vec{P}(\vec{E}). \tag{2.42}
$$

This implies that reversing the direction of the applied electric field must also reverse the direction of the induced polarization. However, applying this to the second-order polarization term yields:

$$
-P^{(2)}(t) = \varepsilon_0 \chi^{(2)} [-E(t)]^2 = \varepsilon_0 \chi^{(2)} E^2(t) = P^{(2)}(t). \tag{2.43}
$$

Equation 2.43 shows that $P^{(2)}(t)$ must equal -$P^{(2)}(t)$, which can only be true for all times, despite the trivial case of $E(t) = 0$, if

$$\chi^{(2)} = 0 \quad \text{in centrosymmetric media.} \tag{2.44}$$

In other words, for a material with inversion symmetry, the polarization response must be an odd function of the electric field. As a result, all even-order nonlinearities, including $\chi^{(2)}$, must vanish. Consequently, second-order processes such as SHG and SFG can only occur in non-centrosymmetric materials. In contrast, third-order processes such as FWM remain allowed even in centrosymmetric media, since $\chi^{(3)}$ is unaffected by inversion symmetry.

Four-Wave Mixing

Since the second-order susceptibility $\chi^{(2)}$ vanishes in centrosymmetric media due to inversion symmetry, the lowest-order nonlinear optical response arises from the third-order susceptibility $\chi^{(3)}$. In third-order nonlinear processes, the intensity of the generated signal scales with the cube of the incident laser intensity:

$$P^{(3)}(t) = \epsilon_0 \chi^{(3)} E^3(t) \tag{2.45}$$

If the applied electric field consists of three distinct frequency components,

$$E(t) = E_1 e^{-i\omega_1 t} + E_2 e^{-i\omega_2 t} + E_3 e^{-i\omega_3 t} + \text{c.c.}, \tag{2.46}$$

then the resulting third-order polarization $P^{(3)}(t)$ contains a broad spectrum of frequency components. In the most general case, new frequencies are generated as three electromagnetic waves interact within a nonlinear medium to generate a fourth wave, according to the relation:

$$\omega = | \pm \omega_1 \pm \omega_2 \pm \omega_3|. \tag{2.47}$$

As a special case, similar to SHG, the individual fundamental frequencies can give rise to third-harmonic generation (THG). When all three frequencies add constructively, the process corresponds to third-order SFG. Aside from these special cases, the remaining frequency combinations are referred to as FWM.

$$\omega_{\text{FWM}} = \omega_1 \pm \omega_2 - \omega_3. \tag{2.48}$$

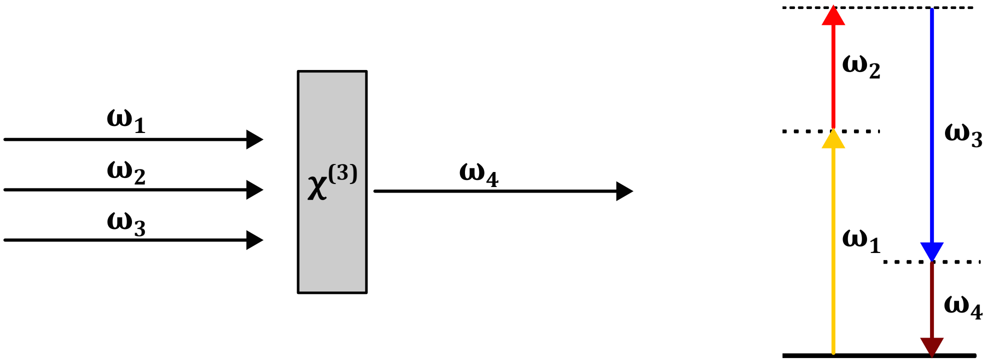

Figure 2.4.: Schematic illustration of the FWM process. *Left:* Three input photons at frequencies ω_1, ω_2 and ω_3 interact with a nonlinear crystal exhibiting a third-order susceptibility $\chi^{(3)}$. As a result, a new photon at the FWM frequency $\omega_4 = \omega_1 + \omega_2 - \omega_3$ is generated. *Right:* Schematic energy level diagram of the FWM process. The solid line indicates the ground state, while the dashed lines represent virtual energy levels.

Thus, in an overview the representative third-order nonlinear processes are:

- **Third-harmonic generation (THG)**: $3\omega_1$, $3\omega_2$, $3\omega_3$
- **Third-order sum-frequency generation (SFG)**: $\omega_1 + \omega_2 + \omega_3$
- **Four-wave mixing (FWM)**: $\omega_1 \pm \omega_2 - \omega_3$

All frequency combinations that conserve energy are, in principle, allowed, including degenerate cases such as $2\omega_1 \pm \omega_2$. Among these third-order processes, in this work the experimental investigations presented in Section 4.4.2 focus specifically on FWM. This process is governed by the third-order susceptibility $\chi^{(3)}(\omega_4; \omega_1, \omega_2, \omega_3)$, a fourth-rank tensor whose specific components depend on the symmetry properties of the medium and the particular combination of the involved frequencies ω_1, ω_2, ω_3, and ω_4. Figure 2.4 schematically illustrates the fundamental principle of the FWM process.

For efficient FWM, both energy and momentum must be conserved:

$$\omega_4 = \omega_1 + \omega_2 - \omega_3, \tag{2.49}$$

$$\vec{k}_4 = \vec{k}_1 + \vec{k}_2 - \vec{k}_3, \tag{2.50}$$

where $\vec{k}_i$ are the wavevectors of the interacting fields. Violations of phase matching result in destructive interference and reduced FWM efficiency. In low-dimensional materials phase-matching constraints are relaxed due to the limited spatial extent of the nonlinear interaction. As a result, momentum conservation applies only in the directions where the material extends significantly, while phase matching becomes irrelevant perpendicular to the material. Physical electric fields are real-valued, even though complex notation is often used for convenience.

$$E(t) = E_0 e^{-i\omega t} + E_0^* e^{+i\omega t} \tag{2.51}$$

For FWM the nonlinear polarization term is represented by:

$$P^{(3)}(t) \sim \chi^{(3)} E_1 E_2 E_3^* e^{-i(\omega_1+\omega_2-\omega_3)t} \tag{2.52}$$

The complex conjugate E_3^* in Equation 2.52 reflects the fact that here the field E_3 is associated with the negative frequency $-\omega_3$. The interaction depends on the coherent combination of all three fields with both positive and negative frequency components. The field E_3 is not depleted, but rather it is amplified in a stimulated emission process, redistributing energy from the pump fields (ω_1 and ω_2) into the signal field (ω_3) and the generated idler field (ω_4).

If all three input fields have distinct frequencies ω_1, ω_2 and ω_3, the process is called *non-degenerate* FWM. This typically requires three separate laser sources. In contrast, when two or more of the interacting waves share the same frequency, the process is referred to as *degenerate* FWM. In the fully degenerate case, all input fields have the same frequency ω, leading to a generated signal at $\omega_{\mathrm{FWM}} = \omega + \omega - \omega = \omega$. Despite the output having the same frequency, the new wave can differ in direction, phase or polarization, depending on the geometry of the crystal.

In the experimental investigations presented in this work, FWM signals are generated using a single broadband laser pulse. As the involved frequencies are spectrally close, mixing across the spectral bandwidth becomes significant, resulting in a continuous spectral broadening. This scenario is referred to as *near-degenerate* FWM (ND-FWM).

Accounting for frequency mixing, the FWM intensity I_{FWM} can be calculated according to Equation 2.52 by integration over all frequencies involved:

$$\begin{aligned} I_{\mathrm{FWM}}(\omega) = c\epsilon_0 \Bigg| \iiint_{\omega_{\min}}^{\omega_{\max}} & \chi^{(3)}(\omega;\omega_1,\omega_2,\omega_3) \cdot E(\omega_1)E(\omega_2)E^*(\omega_3) \\ & \cdot\delta(\omega-\omega_1-\omega_2+\omega_3)d\omega_1 d\omega_2 d\omega_3 \Bigg|^2 \\ = c\epsilon_0 \Bigg| \iiint_{\omega_{\min}}^{\omega_{\max}} & \chi^{(3)}(\omega;\omega_1,\omega_2,\omega_3) \cdot A(\omega_1)A(\omega_2)A^*(\omega_3) e^{i(\varphi(\omega_1)+\varphi(\omega_2)-\varphi(\omega_3))} \\ & \cdot\delta(\omega-\omega_1-\omega_2+\omega_3)d\omega_1 d\omega_2 d\omega_3 \Bigg|^2 \end{aligned} \tag{2.53}$$

In Equation 2.53, the complex electric fields $E(\omega_n)$ at the frequencies ω_1, ω_2 and ω_3 are expressed as a product of a real-valued spectral amplitude $A(\omega_n)$ and a complex phase term $e^{i\varphi(\omega_n)}$. The delta function $\delta(\omega - \omega_1 - \omega_2 + \omega_3)$ enforces energy conservation in the FWM process. The resulting FWM signal arises from the coherent superposition of all possible frequency triplets, making the process highly sensitive to the spectral phase of the input fields.

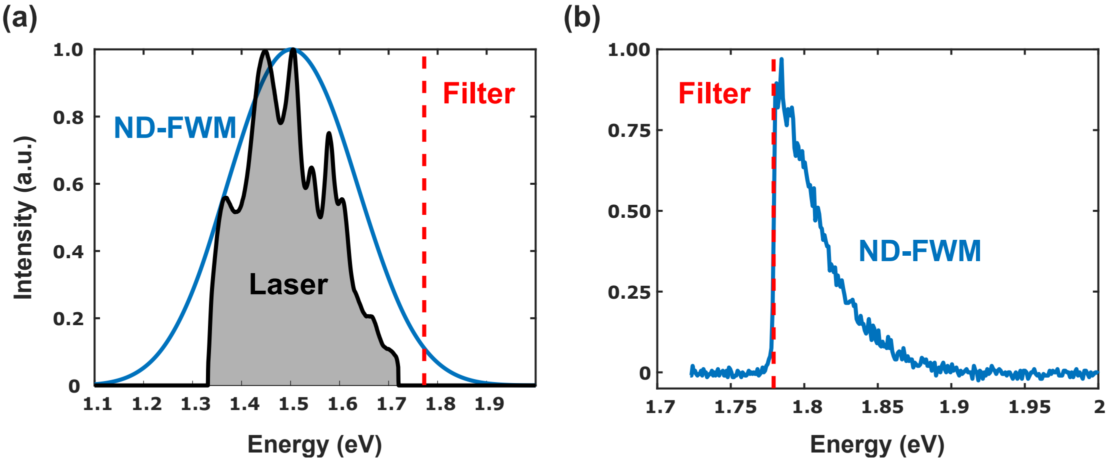

Figure 2.5.: Calculated ND-FWM spectrum generated from a broadband laser pulse. (a) Frequencies from the structured input spectrum (gray shaded) mix via the FWM process, according to Equation 2.53, resulting in a broad and smooth FWM output (blue). A flat spectral phase was assumed, corresponding to a transform-limited pulse. To isolate the anti-Stokes side of the FWM signal and suppress the fundamental laser light in the experiment, a short-pass filter with a cutoff at 1.77 eV (700 nm) was applied, indicated by the red dashed line. (b) The measured spectrum shows the experimentally accessible portion of the high-energy anti-Stokes edge of the FWM signal.

Figure 2.5 (a) illustrates the calculated spectrum of a ND-FWM signal generated from a single broadband laser pulse, following Equation 2.53. The structured input spectrum, in combination with a flat phase profile, leads to a broad and smooth FWM output due to coherent mixing of distinct frequency components. In the experiment, only the anti-Stokes edge of the FWM spectrum is detected, as a short-pass filter must suppress the fundamental laser spectrum. In panel (b), the measured high-energy edge of the spectrum is presented, showing the experimentally accessible part of the FWM signal.

As a versatile and widely applicable nonlinear process, FWM plays a central role in fields such as ultrafast spectroscopy, quantum optics and optical communication. Its dependence on both the amplitude and phase of the interacting fields also makes it a powerful tool for probing coherent optical phenomena.

2.1.4. Density matrix formalism

The generation of nonlinear signals is conventionally described by susceptibilities derived from a perturbative treatment of the equation of motion of the electron, as introduced in Section 2.1.1 [27]. However, when there is a considerable shift of population to the excited states, the susceptibility-based approach no longer holds and must be replaced by a time-dependent treatment of the density-matrix dynamics in the presence of the laser field [32].
The density matrix describes a statistical ensemble of quantum states and allows for the determination of probabilities for any measurement applied to the systems within the ensemble. Unlike pure state representations, which rely on wavefunctions, the density matrix provides a general framework that accounts for the coherent superposition of mixed quantum states. In this formalism, entangled or open quantum systems such as a system interacting with an external environment, can be properly described, including the loss of coherence and the emergence of mixed states [33].

A pure state, for which full information is available, can be written as the general state vector $|\Psi\rangle$ in orthonormal basis $|e_j\rangle$:

$$|\Psi\rangle = \sum_j c_j |e_j\rangle \tag{2.54}$$

For a pure state with a normalized state vector the density operator is defined as the outer product of the state:

$$\rho = |\Psi\rangle \langle\Psi| \tag{2.55}$$

The operator is uniquely associated to the physical state $|\Psi\rangle$. Applied to an arbitrary state vector $|\Phi\rangle$ the operator projects this state to the one-dimensional sub-space defined by $|\Psi\rangle$.

$$\rho |\Phi\rangle = |\Psi\rangle \langle\Psi|\Phi\rangle \tag{2.56}$$

For a coherent superposition state

$$|\Psi\rangle = a|1\rangle + b|2\rangle \tag{2.57}$$

the density operator reads:

$$\begin{aligned}\rho &= |\Psi\rangle \langle\Psi| \\ &= (a|1\rangle + b|2\rangle)(a^* \langle 1| + b^* \langle 2|) \\ &= |a|^2 |1\rangle \langle 1| + ab^* |1\rangle \langle 2| + a^* b |2\rangle \langle 1| + |b|^2 |2\rangle \langle 2|\end{aligned} \tag{2.58}$$

The density operator can be expressed as the density matrix, provided the $|1\rangle$ and $|2\rangle$ are orthogonal basis vectors.

$$\rho = \begin{pmatrix} |a|^2 & ab^* \\ a^*b & |b|^2 \end{pmatrix} \tag{2.59}$$

A mixed state, for which the information available is incomplete, represents an incoherent statistical ensemble of different quantum states, rather than a single pure state. It arises when a system is in one of several possible quantum states with certain probabilities. In a mixed state the pure states $|\Psi_i\rangle$ appears with the probability p_i, such that $0 \leq p_i < 1$ and $\sum_i p_i = 1$. In a general form for a mixed state the density operator can be expressed as:

$$\rho = \sum_i p_i \left|\Psi_i\right\rangle \left\langle\Psi_i\right| \tag{2.60}$$

In an orthonormal basis $|e_j\rangle$, every state $|\Psi_i\rangle$ can be expanded as:

$$\left|\Psi_i\right\rangle = \sum_j c_{ij} \left|e_j\right\rangle, \tag{2.61}$$

where c_{ij} are complex coefficients. The projector to the state $|\Psi_i\rangle$ reads:

$$\left|\Psi_i\right\rangle \left\langle\Psi_i\right| = \sum_{j,k} c_{ij} c_{ik}^* \left|e_j\right\rangle \left\langle e_k\right| \tag{2.62}$$

With the definition of the density operator in Equation 2.60 this gives:

$$\rho = \sum_i \sum_{j,k} p_i c_{ij} c_{ik}^* \left|e_j\right\rangle \left\langle e_k\right| \tag{2.63}$$

Finally, the density matrix is formed by the matrix elements ρ_{jk} in the chosen basis $|e_j\rangle$.

$$\rho_{jk} = \sum_i p_i c_{ij} c_{ik}^* \tag{2.64}$$

The general form of a $N \times N$ density matrix is:

$$\rho = \begin{pmatrix} \rho_{11} & \rho_{12} & \cdots & \rho_{1N} \\ \rho_{21} & \rho_{22} & \cdots & \rho_{2N} \\ \vdots & \vdots & \ddots & \vdots \\ \rho_{N1} & \rho_{N2} & \cdots & \rho_{NN} \end{pmatrix} \tag{2.65}$$

The diagonal elements of the density matrix, denoted as $\rho_{jj} = \sum_i p_i |c_{ij}|^2$, are real numbers that satisfy the conditions $0 \leq \rho_{jj} < 1$ and $\sum \rho_{jj} = 1$. These elements represent the occupation probabilities of the respective basis states. The off-diagonal elements, ρ_{jk} for $j \neq k$, are complex numbers that encode quantum interference effects in superposition states. They provide information about the quantum coherence and the phase relationship between different states.

In a fully decohered mixed state, all off-diagonal elements vanish, meaning no quantum coherence remains. In a partially mixed state, the off-diagonal elements may still be nonzero but are typically smaller than in a pure state, indicating partial coherence. The magnitude of the off-diagonal elements determines the degree of coherence in the system.

The time evolution of the density operator follows naturally from the time-dependent Schrödinger equation, with the Hamiltonian H of the system.

$$\begin{aligned}\frac{\partial}{\partial t}\rho(t) &= \frac{\partial}{\partial t}\Big(\left|\Psi\right\rangle \left\langle\Psi\right| \Big) \\ &= \left(\frac{\partial}{\partial t}\left|\Psi\right\rangle\right)\left\langle\Psi\right| + \left|\Psi\right\rangle\left(\frac{\partial}{\partial t}\left\langle\Psi\right|\right) \\ &= -\frac{i}{\hbar}H\left|\Psi\right\rangle\left\langle\Psi\right| + \frac{i}{\hbar}\left|\Psi\right\rangle\left\langle\Psi\right|H \\ &= -\frac{i}{\hbar}\Big[H(t),\rho(t)\Big]\end{aligned} \tag{2.66}$$

Equation 2.66 is the Von Neumann equation, which describes the reversible, unitary evolution of a quantum system with the hamiltonian H without accounting for interactions with an external environment.

To extend this framework to an open quantum system coupled to the environment, effects such as dissipation and decoherence must be incorporated. This is achieved in the Lindblad master equation, which modifies the Von Neumann equation by introducing a dissipator term $D(\rho)$ that captures environmental interactions.

The Lindblad equation describes the non-unitary evolution of the system, covering both the coherent dynamics specified by the internal Hamiltonian and irreversible processes such as relaxation and dephasing. It is given by:

$$\begin{aligned}\frac{d\rho}{dt} &= -\frac{i}{\hbar}[H,\rho] + D(\rho) \\ &= -\frac{i}{\hbar}[H,\rho] + \sum_j \left(L_j \rho L_j^\dagger - \frac{1}{2}\{L_j^\dagger L_j, \rho\}\right)\end{aligned} \tag{2.67}$$

L_j are the Lindblad jump operators that represent the system's coupling to environmental modes like spontaneous emission or the loss of coherence through dephasing. The commutator and anticommutator terms account for the coherent dynamics and dissipative components of the evolution, respectively. The jump operators for spontaneous emission and dephasing can be expressed as:

$$\textbf{Spontaneous emission:}\ L_{sp} = \sqrt{\gamma}\,|g\rangle\langle e| \tag{2.68}$$

$$\textbf{Dephasing:}\ L_{deph} = \sqrt{\Gamma}\,|e\rangle\langle e| \tag{2.69}$$

In Equation 2.68, L_{sp} describes population transfer due to spontaneous decay from the excited state $|e\rangle$ to the ground state $|g\rangle$. This results in a decrease of the excited state population ρ_{ee} and an increase of the ground state population ρ_{gg}. The decay rate γ sets the lifetime of the excited state. In addition, spontaneous emission causes a loss of phase coherence, which leads to damping of the off-diagonal elements ρ_{eg} and ρ_{ge}.

The jump operator L_{deph} in Equation 2.69 describes no population transfer, but a loss of phase coherence. The pure dephasing rate Γ controls how fast the coherence is lost. As a consequence, the diagonal elements of the density matrix ρ_{ee} and ρ_{gg} remain unchanged while the off-diagonal elements ρ_{eg} and ρ_{ge} decay purely due to the loss of coherence.

$$\frac{d\rho}{dt} = -\frac{i}{\hbar}[H,\rho] + \left(L_{\mathrm{sp}}\rho L_{\mathrm{sp}}^{\dagger} - \frac{1}{2}\{L_{\mathrm{sp}}^{\dagger}L_{\mathrm{sp}},\rho\}\right) + \left(L_{\mathrm{deph}}\rho L_{\mathrm{deph}}^{\dagger} - \frac{1}{2}\{L_{\mathrm{deph}}^{\dagger}L_{\mathrm{deph}},\rho\}\right) \tag{2.70}$$

The two terms in each Lindblad contribution serve distinct roles in modeling dissipation. The first term, $L_j\rho L_j^{\dagger}$, represents a quantum jump and transfers population between states, such as from $|e\rangle$ to $|g\rangle$ in the case of spontaneous emission. The second term, $-\frac{1}{2}\{L_j^{\dagger}L_j,\rho\}$, ensures that the total probability (i.e., the trace of ρ) is conserved. It effectively accounts for the loss of population and coherence due to the coupling to the environment. Together, these terms accurately describe the irreversible processes of decay and dephasing in the system.

2.2. Excitons

An exciton is a quasi-particle formed by a bound state of an electron and a hole, held together by their Coulomb interaction. The hole represents a missing electron in the valence band and behaves like a positively charged particle. The exciton represents the quantized excitation energy of an electron-hole pair, moving within a periodic crystal structure. While excitons transport energy, they do not carry charge, as they are electrically neutral. They play a crucial role in various optical phenomena, such as luminescence and photoconductivity [10].

The concept of ”excitation waves” was introduced by Frenkel in 1931 as a result of light absorption. He considered systems in which the interaction between electrons from neighboring atoms is weak compared to the forces binding the electron to its host atom. This is the case in most insulators with closed electron shells [34].

When an electron absorbs a quantum of light and gains enough energy to escape its closed shell, the minimum energy required for this excitation corresponds to the formation of a stable bound state between the electron and the vacancy it leaves behind.

The electron experiences the influence of the positive charge field created by its absence from the closed shell. The vacancy, in turn, behaves like an electron in all respects except for its positive charge and is typically referred to as a hole. The electron and hole forming the exciton remain bound by the Coulomb potential energy.

Unlike a localized atomic excitation, an exciton is not bound to a specific atom but can move through the crystal. Its transport can proceed via band transport, where the exciton is delocalized and moves coherently across the lattice or via hopping, where it jumps between localized sites. Band transport dominates in clean crystals at low temperatures, where scattering is minimal and coherence can be maintained. In contrast, at higher temperatures or in materials with significant impurities or disorder, excitons are more likely to become localized, and their motion occurs predominantly through phonon-assisted hopping.

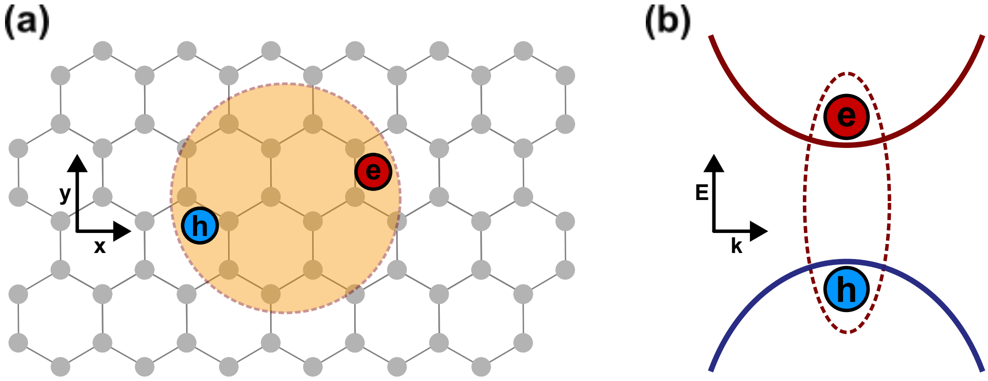

Figure 2.6.: Schematic illustration of an exciton. **(a)** illustrates the Coulomb-bound exciton on a crystal lattice. **(b)** shows the band diagram representation of a bound electron-hole pair.

However, in insulators, Frenkel excitons exhibit an electron-hole separation on the order of the atomic dimensions, meaning that dielectric screening plays a minor role. As a result, the Coulomb potential remains relatively strong, leading to tightly bound excitons. In contrast, in solids, where valence electrons are no longer associated with a specific atom, such as many semiconductors, the interaction between neighboring atoms is significantly stronger. The wavefunction of valence electrons, which are responsible for bonding, typically extends over multiple atoms. Despite this delocalization, valence electrons do not move freely through the crystal or contribute to electrical conductivity. Instead, they occupy states within the valence band, while the next available energy states lie in the conduction band, separated by an energy gap known as the band gap. This band gap of a semiconductor can be overcome by photon absorption, exciting an electron from the valence band into the conduction band and leaving behind a hole. In such a system, the strong dielectric screening weakens the Coulomb attraction between the electron and the hole, resulting in Wannier-Mott excitons with radii extending over tens to hundreds of atomic sites. Consequently, the screening effect can be effectively described by a single dielectric constant, as shown in Equation 2.71,

$$V(r) = -\frac{e^2}{4\pi\epsilon \cdot r} \tag{2.71}$$

where r is the electron-hole separation and $\epsilon = \epsilon_0 \epsilon_r$ is the dielectric constant of the material. The dielectric constant accounts for the screening effects from the surrounding atomic structure and free charges in the crystal, which reduce the effective Coulomb interaction. This bound electron-hole pair exhibits a series of discrete energy states, analogous to the hydrogen atom. The upper limit of this series represents the binding energy, required to completely free the electron from the Coulomb attraction of the hole.

The free-particle band gap, illustrated in band-structure diagrams, typically describes single-particle excitation and represents the sum of energies required to bring an electron and a hole into the system, separately. In contrast, optical excitation, through the absorption of a photon, creates an electron in the conduction band and a hole in the valence band, simultaneously [11].

$$E_{\mathrm{ex}} = E_{\mathrm{gap}} - E_{\mathrm{b}} \tag{2.72}$$

The energy required to create an exciton, is reduced by their attractive Coulomb interaction compared to the free-particle band gap, as described by Equation 2.72. Not the free-particle band gap E_{gap} but this reduced exciton energy E_{ex}, measured from the top of the valence band, needs to be matched by the photon energy E_γ. As a result, well defined absorption peaks occur already at energies below the band gap due to the formation of excitons. The difference between the free-particle and the optical band gap is referred to as the exciton binding energy E_{b}, which represents the energy required to dissociate the exciton.

The relative motion of the electron-hole pair interacting through the attractive Coulomb potential $V(r)$ can be described by the two-particle Schrödinger equation, also known as the Wannier equation. This is analogous to the hydrogen atom but modified by the material's dielectric properties and under the assumption that the Coulomb potential varies little within one unit cell. With the Coulomb potential from Equation 2.71 the Wannier equation is given by:

$$\left[-\frac{\hbar^2}{2\mu}\nabla^2 - \frac{e^2}{4\pi\epsilon r}\right]\psi(\mathbf{r}) = (E_{gap} - E_b)\psi(\mathbf{r}) \tag{2.73}$$

where $\mu = \frac{m_e^* m_h^*}{m_e^* + m_h^*}$ is the reduced mass of the electron-hole system with the effective masses of the electron and hole m_e^* and m_h^*, respectively. This equation is equivalent to the hydrogen atom, but with an effective Coulomb interaction screened by the dielectric constant. Although the effective mass of the valence band, obtained from the band curvature

$$m^* = \hbar^2 \left(\frac{\partial^2 E}{\partial k^2}\right)^{-1} \tag{2.74}$$

is negative due to the downward curvature near the valence band maximum, it is customary to describe the resulting hole, i.e., the absence of the electron, as a positively charged quasiparticle with a positive effective mass. This is achieved by defining the hole mass as the absolute value of the valence band effective mass: $m_h^* = |m_v^*|$. This convention simplifies the modeling of hole dynamics, particularly in exciton formation and charge transport.

When an electron is excited from the valence band to the conduction band, it leaves behind an unoccupied state at crystal momentum k. This missing electron removes both energy and momentum k from the system. To describe the remaining system in terms of a hole, a crystal momentum $-k$ is assigned to the hole, accounting for the lost momentum.

For excitons in three dimensional crystal structures the solution of Equation 2.73 follows the hydrogen-like model. The detailed calculation can be retraced in [25, 35]. The discrete bound-state energies and orbital radii are:

$$E_n = E_{gap} - \frac{\mu e^4}{8\epsilon^2 h^2}\frac{1}{n^2} = E_{gap} - \frac{R_X}{n^2} \tag{2.75}$$

$$a_n = n^2 \cdot \frac{4\pi\epsilon\hbar^2}{\mu e^2} = n^2 a_e \tag{2.76}$$

with the effective exciton Rydberg energy $R_X = \frac{\mu}{\epsilon_r^2 m_e} R_y$, the hydrogen Rydberg energy $R_y = \frac{m_e e^4}{8\epsilon_0^2 h^2}$, the free electron mass m_0, the elementary charge e, the Planck constant h, the principal quantum number $n = 1, 2, 3, ...$, the effective exciton Bohr radius $a_e = \frac{m_e \epsilon_r}{\mu} a_H$

and the hydrogen model Bohr radius $a_H = \frac{4\pi\epsilon_0\hbar^2}{e^2 m_e} \approx 5.29 \cdot 10^{-11}$ m.

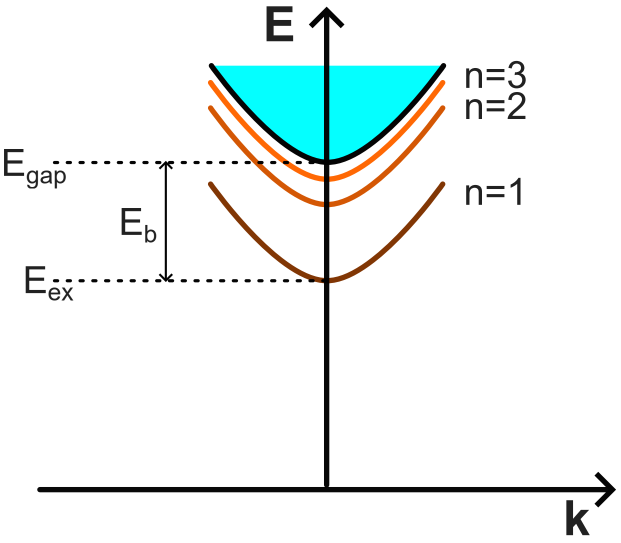

Figure 2.7.: Schematic band structure model of exciton energy levels. The band gap energy E_{gap} denotes the minimum energy required to promote an electron from the valence band to the conduction band, reaching the unbound continuum of free carriers (blue-shaded area). Exciton states, labeled by the principal quantum number $n = 1, 2, 3, \ldots$, lie below the band edge due to the Coulomb attraction between the electron and hole. The corresponding exciton energy E_{ex} is reduced by the exciton binding energy E_{b}.

As illustrated in Figure 2.7, the energy levels of a Wannier-Mott exciton are quantized and follow a Rydberg-like series, analogous to the energy levels of the hydrogen atom. These levels are labeled by a principal quantum number n and the associated binding energies decrease with increasing n. However, unlike the hydrogen atom, the exciton binding energy, often referred to as the effective Rydberg energy, is modified by both the reduced effective mass μ of the electron-hole pair and the dielectric constant ϵ_r of the host material. These parameters significantly alter the interaction between the electron and the hole, leading to a binding energy that is typically much smaller than in atomic hydrogen. Specifically, in a typical covalent semiconductor with a dielectric constant $\epsilon_r \approx 10$ and reduced mass $\mu \approx 0.2m_e$, the exciton binding energy is approximately 500 times smaller than the hydrogenic Rydberg energy of 13.6 eV. Correspondingly, the effective Bohr radius of the exciton is about 50 times larger, reflecting the influence of dielectric screening and the reduced effective mass. These material-dependent corrections result in an exciton with a relatively large spatial extent and low binding energy, on the order of tens of meV. At room temperature ($T = 295$ K), the thermal energy associated with lattice vibrations is given by $k_B T \approx \frac{1}{40}$ eV $= 25$ meV, which is comparable to the exciton binding energy $E_b = R_X = \frac{1}{500} R_y = \frac{13.6\ eV}{500} = 27.2$ meV. Under these conditions, thermal fluctuations are sufficient to ionize the exciton, dissociating the bound electron-hole pair into free carriers.

As a result, the corresponding excitonic absorption feature is significantly broadened at room temperature. Consequently, the observation and study of Wannier-Mott excitons typically require cryogenic conditions, where thermal energies are sufficiently low to preserve excitonic states [10, 11].

As further discussed later in Section 2.3, the binding energy of excitons also strongly depends on dimensionality and increases significantly as dimensionality is reduced. While the ideal Wannier-Mott model predicts that the exciton binding energy in two-dimensional systems is four times larger than in three dimensions [11], experimental observations in atomically thin materials report much higher binding energies, often an order of magnitude greater than in their bulk counterparts [4, 12]. This discrepancy arises from two main factors not accounted for in the ideal model. First, in two dimensions, the electron-hole interaction is more accurately described by the Rytova-Keldysh potential rather than the $\frac{1}{r}$ Coulomb potential. This model accounts for nonlocal dielectric screening and results in a stronger attractive interaction at short distances. Second, dielectric screening is significantly reduced in the 2D limit due to the dielectric contrast between the atomically thin layer and its surrounding environment, further enhancing the binding energy [11, 25]. As a consequence, excitons in low-dimensional materials often exhibit substantial binding energies, sufficiently large to remain stable at room temperature.

In one-dimensional systems, the motion of electrons and holes is restricted to a single spatial direction. This leads to a further enhancement of the Coulomb interaction as a result of the strong spatial confinement. Additionally, the dielectric screening by surrounding charges is further reduced in these 1D systems [36]. Finally, the spatial dependence of the Coulomb potential differs with dimensionality. While in three-dimensional systems the potential scales as $1/r$, in 1D systems the interaction exhibits a more singular character due to confinement effects, approximated by a modified $1/r$ potential [37]. This further enhances the exciton binding energy in 1D.

Excitons at high densities

At low excitation densities, the density of excitons is small and their separation is large. Hence, the interaction of excitons is negligible under these conditions and PL dynamics exhibit single-exponential decay. However, with increasing density, exciton wave functions begin to overlap and exciton-exciton interaction becomes significant.

Exciton-exciton annihilation (EEA) is a many-body effect in which two excitons interact upon encounter, resulting in the non-radiative recombination of one exciton while its energy is transferred to the other, which is excited to a higher energy state.

$$E + E \rightarrow (EE) \rightarrow E^* \tag{2.77}$$

In Equation 2.77, E denotes an isolated exciton, (EE) represents a transient exciton pair and E^* is an exciton in an excited state. The excited exciton typically relaxes by either dissociating into free carriers or dissipating its excess energy through phonon emission.
EEA serves as a fast non-radiative decay channel in photoexcited materials and is essentially the excitonic analog of Auger recombination, a non-radiative process in semiconductors for densely packed free charge carriers, in which excess energy from one carrier is transferred to another carrier.
The decay dynamics of excitons are governed in the rate equation [16, 17]:

$$\frac{dn_X(t)}{dt} = -\frac{1}{\tau}n_X(t) - \frac{1}{2}\gamma n_X(t)^2 \tag{2.78}$$

The first term corresponds to single-exciton recombination with the characteristic lifetime τ, while the second term accounts for the bimolecular process of EEA. Here, $n_X(t)$ is the exciton density and γ is the EEA rate constant. The factor of $\frac{1}{2}$ in the annihilation term ensures that each exciton pair is counted only once.
EEA and Auger recombination are considered particularly important in systems with reduced dimensionality. In bulk materials, exciton-exciton interactions are generally less frequent, mainly due to the greater spatial separation between excitons. However, in two-dimensional systems the planar confinement leads to higher exciton densities, which makes EEA more likely to occur [11]. In one-dimensional structures exciton diffusion is restricted along a single axis, which further increases the chance of interaction and results in especially efficient EEA [18]. Experimentally, EEA is identified through nonlinear PL responses under increasing excitation fluence, reduced emission lifetimes at high carrier densities and saturation effects in time-resolved PL or transient absorption measurements.

The **Mott transition** occurs if the average exciton-exciton distance becomes comparable to the exciton diameter as introduced in Equation 2.76. At this point, the exciton density reaches the Mott threshold, which can be estimated as the inverse of the volume occupied by a single exciton.

$$n_{\mathrm{Mott}} \approx \frac{1}{\frac{4}{3}\pi a_n^3} \tag{2.79}$$

In this case, the Coulomb interaction between charge carriers gets strongly screened, eventually leading to an ionization of the excitons and causing the exciton gas to dissociate into an electron-hole plasma. As a result, absorption spectra become broader with a reduction of the absorption strength. Effectively, the absorption coefficient becomes dependent on the intensity of the light [4, 6–9].

2.3. Low-dimensional materials

The concept of low-dimensional materials dates back to the 1930s when scientists first began developing theories about the properties of two-dimensional (2D) systems. In 1947, Philip R. Wallace proposed the electronic structure of graphene - long before it was experimentally realized. During the 1950s and 1960s, the first studies on thin films and surface effects began to emerge.

A major milestone was reached in 1985 with the discovery of fullerenes (C_{60}) by Kroto, Smalley and Curl [38], an achievement that was later honored with the 1996 Nobel Prize. The spherical structure of carbon atoms exhibits unique electronic and mechanical properties. While working with fullerenes in 1991, Sumio Iijima discovered carbon nanotubes, a cylindrical structure formed by a single rolled-up sheet of carbon atoms [39]. Once again, this new form of carbon demonstrated extraordinary mechanical, thermal and electronic properties. This marked the beginning of the nanotechnology era. In 2004, Geim and Novoselov successfully isolated a single layer of carbon atoms, leading to the discovery of graphene [40]. They accomplished this using the ”Scotch tape” method, a technique in which bulk graphite is progressively thinned down to monolayer thickness. For this discovery, they were awarded the Nobel Prize in 2010.

Since then, several other 2D materials have been discovered. Phosphorene (black phosphorus) features a high hole mobility and a tunable bandgap, making it highly interesting for electronics and photonics [41]. Hexagonal boron nitride (h-BN), often referred to as ”white graphene”, due to its structural similarity, is an electrical insulator with interesting dielectric properties and excellent thermal and chemical stability [42]. Transition metal dichalcogenides (TMDs) are semiconductors with fascinating electro-optical properties, making them valuable for applications in transistors and optoelectronics [43].

Despite early studies by Frindt (1966) and Morrison (1986), it wasn’t until 2010 that the direct bandgap in monolayer MoS_2 was described and photoluminescence was observed [43, 44], and intense research into their exciting optical and electronic properties began. TMDs have also emerged as excellent candidates for exploring condensed matter physics of two-dimensional systems and quantum phenomena at the nanoscale [1, 2].

This chapter explores the fundamental properties of single-walled carbon nanotubes (SWCNTs) as a representative one-dimensional (1D) system and monolayer TMDs as representatives of two-dimensional (2D) systems.

2.3.1. Transition Metal Dichalcogenides

Transition metal dichalcogenides (TMDs) are a class of group VI semiconducting materials with the general formula MX_2, where M represents a transition metal (e.g. Mo, W) and X denotes a chalcogen (e.g. S, Se, Te). A single TMD layer consists of three atomic planes, a hexagonally packed plane of metal atoms sandwiched between two planes of chalcogen atoms. Due to this structure, it is often referred to as a tri-layer (TL) of atomic thickness. Within each layer, strong covalent bonding holds the atoms together. The transition metal atoms typically contribute four valence electrons to the bonding states. Formally, the transition metal and chalcogen atoms carry oxidation states of +4 and -2, respectively, giving rise to the 1 : 2 stoichiometry of the compound [11]. The metal atoms are six-fold coordinated within a TL, adopting either trigonal prismatic or octahedral coordination geometries, as illustrated in Figure 2.8. Each X atom bridges two M atoms in this shared coordination of the crystal structure. Since the transition metal provides only four valence electrons, some M-X bonds can be described as coordinate covalent, where both electrons in the bond originate from the chalcogen atom. As a result, TMD surfaces are highly stable and chemically inert due to the absence of dangling bonds [12].

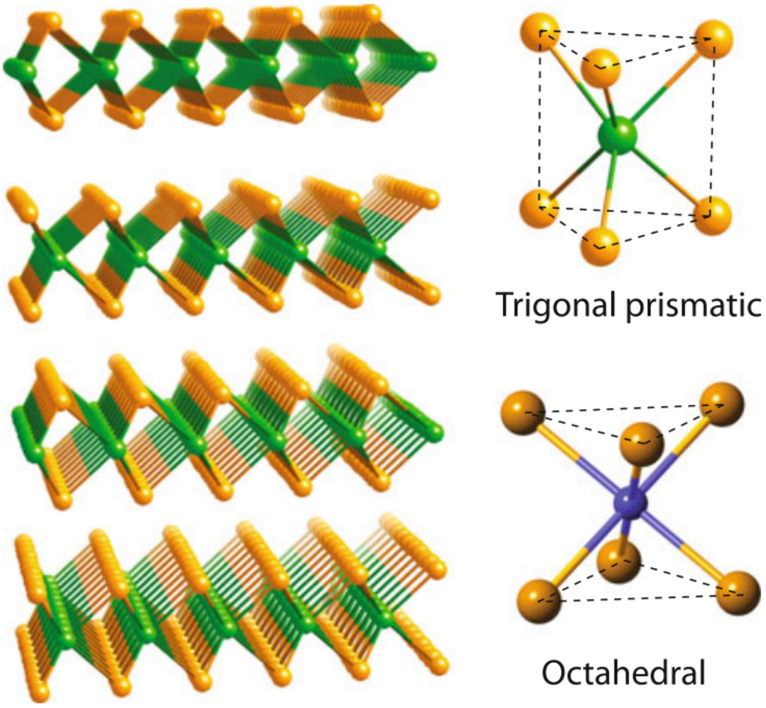

Figure 2.8.: Schematic structure and configuration of TMD triple layers. *Left:* Illustration of bulk TMDs in the 2H crystal structure, where green spheres represent metal atoms and yellow spheres represent chalcogen atoms for the trigonal prismatic configuration. *Right:* Possible bonding geometries within a single TL, showing the trigonal prismatic configuration (top) and the octahedral configuration (bottom). Adapted with permission from [11]. Copyright © 2016, Springer International Publishing Switzerland.

In their bulk form, the layers in TMD crystals are held together by weak van der Waals (vdW) forces, making them easily cleavable, similar to graphite. In the octahedral coordination, the layers stack directly on top of each other, forming the so-called 1T phase. In contrast, the trigonal prismatic coordination leads to an A-B-A-B stacking arrangement, known as the 2H phase. These labels refer to the stacking order, where the number denotes the number of layers per unit cell and the letter corresponds to the crystal symmetry, trigonal (T) or hexagonal (H). A comprehensive description of TMD structures and properties can be found in [11]. In the following, only the 2H configuration is considered, as it is the most common and the focus of this work.

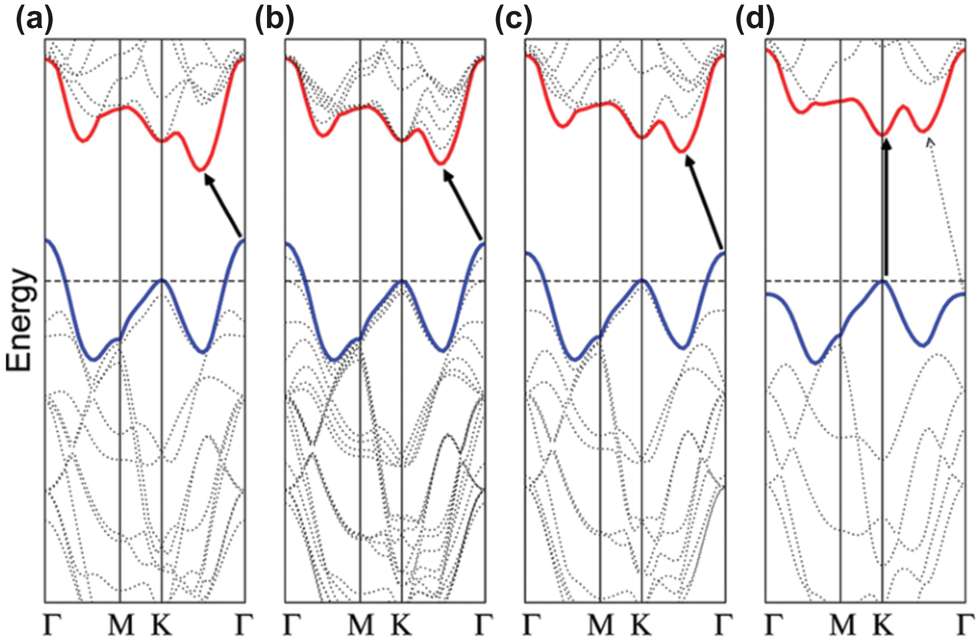

Figure 2.9.: Calculated band structure of MoS_2 for (a) bulk material, (b) four TL (c) bilayer (2 TLs) and (d) monolayer (1 TL) thickness. The valance band is indicated in blue while the conduction band is indicated in red. The allow denotes the lowest-energy transition. In bulk MoS_2 the bandgap is indirect with valence band maximum at Γ and the conduction band minimum halfway between the Γ and K points. As the layer number decreases, the energy levels especially at the Γ point rearrange and the indirect bandgap increases. In the monolayer limit, MoS_2 becomes a direct bandgap semiconductor, with the lowest-energy transition occurring at the K point. Reprinted with permission from [44]. Copyright 2010, American Chemical Society.

Bulk TMDs exhibit an indirect bandgap, with the valence band maximum (VBM) at the Γ point and the conduction band minimum (CBM) located between the Γ and K points. Since photons carry negligible momentum, only vertical transitions are optically allowed in momentum-space. As the layer number decreases, the indirect bandgap increases due to modifications in the interlayer coupling. In the monolayer (single TL) limit, the indirect bandgap surpasses the direct transition at the K point, causing the material to transition into a direct bandgap semiconductor. This behavior is illustrated in Figure 2.9, which presents calculated band structure diagrams of MoS_2 for different material thicknesses. As a result strong PL occurs from these materials as the probability of a direct transition from the excited state to the ground state without additional phonon assistance is strongly enhanced by multiple orders of magnitude [43, 44].

Today, several techniques for producing few-layer and monolayer TMDs exist. Micromechanical exfoliation, often referred to as the ”Scotch tape” method, involves removing thin crystal layers by exploiting the weak interlayer bonds, effectively thinning the material down to monolayer thickness. This technique typically yields flakes with lateral dimensions on the order of tens of micrometers [45]. Large-area TMD monolayers can be grown through chemical vapor deposition (CVD) [46] or by molecular beam epitaxy (MBE) under ultra-high vacuum conditions over the entire wafer [47].

Excitons in TMDs

In bulk TMDs, the high relative permittivity ϵ_r, defined as the ratio of the material's dielectric response to that of vacuum, results in an effective dielectic screening of Coulomb interactions between charge carriers by the surrounding charges inside the material, as introduced in Section 2.2. As a result, exciton binding energies are typically on the order of 10 meV, making them unstable at room temperature, where thermal energy is sufficient to dissociate the electron-hole pair. Hence, stable excitons in bulk material can only be observed at cryogenic temperatures [13]. However, when the material is thinned down, approaching the monolayer limit, this dielectric screening is highly reduced due to the missing surrounding material. The majority of electrical field lines between the separated charge carriers are outside of the material, where the relative permittivity is typically lower. This is illustrated in Figure 2.10.

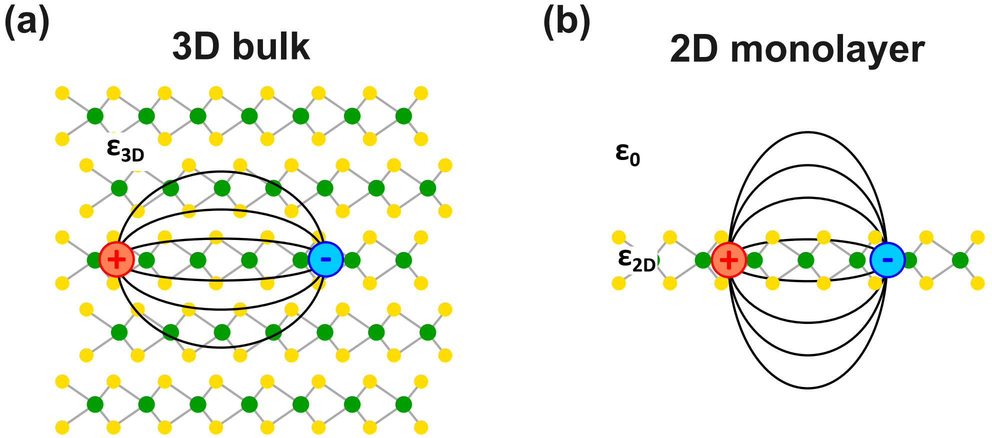

Figure 2.10.: Electric field lines. (a) In a 3D bulk material the electrical field lines between the separated charge carriers extend inside of the material and are screened by surrounding charges. (b) In the case of a 2D material the dielectric screening is highly reduced due to the missing surrounding material.

In monolayer TMDs, excitons are tightly bound with binding energies of hundreds of meV [4, 12]. As a result, excitons in monolayer TMDs are stable at room temperature, leading to strong light absorption and dominate the optical properties [43, 44, 48, 49].

In TMDs, strong spin-orbit coupling (SOC) arises from the interaction between the electron's spin and its orbital motion in the presence of an atomic electric field. When the electron's spin aligns parallel to its orbital angular momentum, the energy of the state is higher compared to when the spin is anti-parallel to the orbital angular momentum. This effect is particularly pronounced in TMDs due to the presence of heavy transition metal atoms, such as Mo and W, which have high atomic numbers and thus large spin-orbit coupling constants (SOC $\propto Z^4$).

The broken inversion symmetry in monolayer TMDs means that for each electronic state at momentum k, there is no longer an equivalent state at momentum -k with the same energy and opposite spin. In other words, electrons traveling in opposite directions experience distinct energetic environments. The valence band states at the K and K$'$ valleys in momentum space are primarily derived from the $d_{x^2-y^2}$ and d_{xy} orbitals of the transition metal atom, while the conduction band edge is dominated by the d_{z^2} orbital [50]. The term valley is generally used to designate energy states close to the band extremum in momentum space [12]. As a result, spin-orbit coupling lifts the spin degeneracy at the K and K' points, introducing a spin splitting of several hundred meV in the valence band and of a few to tens of meV in the conduction band. The spin projection perpendicular to the monolayer plane becomes well-defined and the two split bands exhibit opposite spin characters $E_\uparrow$ and $E_\downarrow$. From this spin splitting of the valence band, the first two lowest-lying transitions are referred to as the A and B exciton and emerge at the K and K' points with bright PL emission reported [44].

Incident photons with a given energy and optical helicity can only excite electrons with a specific spin orientation and consequently, from a particular sub-band. As a result, the valley in momentum space becomes inherently coupled to the electron's spin in monolayer TMDs. This spin-valley locking allows for the excitation of individual valleys to be selectively addressed by circularly polarized light with the corresponding energy and helicity, enabling the valley-selective optical control of the material. This unique coupling is a key feature in the development of valleytronic applications [50–53].

Figure 2.11 illustrates the band splitting at the K and K' point, the origin of A and B excitons and the corresponding spin orientation. The minor splitting of the conduction band is not shown here for simplicity. Note that the conduction band spin splitting in molybdenum-based TMDs (MoS_2, $MoSe_2$) is negative, meaning that at the K point, the spin-up conduction band lies lower in energy than the spin-down band. Due to time-reversal symmetry, this ordering is reversed at the K' point. In contrast, tungsten-based TMDs (WS_2, WSe_2) exhibit positive conduction band splitting. The excitation with linearly polarized light, as used in the experiments presented in this work, corresponds to a superposition of left- and right-handed circularly polarized components and therefore leads to simultaneous generation of excitons at both the K and K' valleys.

Additional prominent excitonic features, appearing at higher photon energies, see Figure 4.16 and 4.36, are referred to as C and D or A$'$ and B$'$ excitons, depending on the literature reference. These excitons are associated with higher-energy electronic transitions at the band-nesting region close to the Γ point or other regions of the Brillouin zone, depending on the material. Because the conduction band states at these locations are more delocalized,

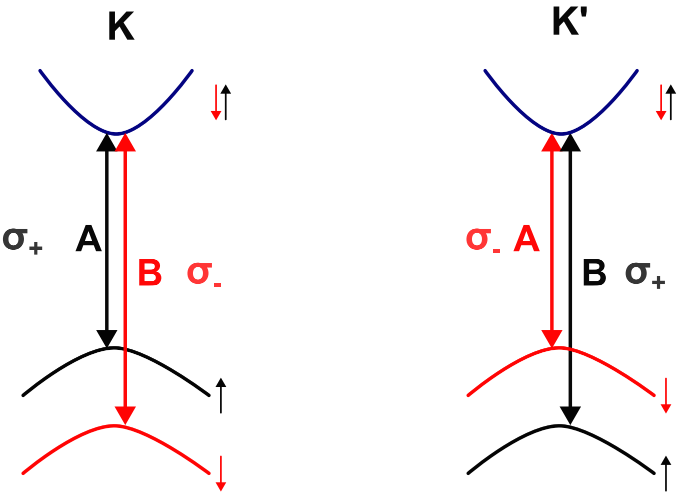

Figure 2.11.: Schematic illustration of valence band splitting at the K and K' point resulting in A and B excitons. Due to pronounced spin-orbit coupling in combination with broken inversion symmetry in TMD monolayers the valence band is strongly spin-split and each sub-band can be selectively addressed by circular polarized light of the corresponding helicity and energy. The two optical transitions are attributed to the A and B exciton species, respectively. For clarity, the minor splitting of the conduction band is not shown here.

the exciton binding energy for C and D excitons is lower than that of A and B excitons [54–57].

Bright excitons couple directly to light and form, when the electron and hole have aligned spin and momentum states allowing for efficient optical transitions, at one location in the Brillouin zone. In contrast, *dark excitons* do not couple efficiently to light due to spin or momentum mismatch. This leads to long-lived excitonic states that are of interest for exciton transport and quantum technologies [12]. In tungsten-based TMDs (WS_2, WeS_2) exciton states with electron and hole in different valley exist as energetically lower momentum-dark excitons. The to fullfil momentum conservation, simultaneous interaction with a phonon is required, making PL emission less efficient but detectable. As at low temperatures the majority of the population is in the energetically lowest dark exciton state, this compensates for the reduced probability of this process. As a result at low temperatures strong PL from dark excitons in tungsten-based TMDs can be observed. In molybdenum-based TMDs no such PL is observed as the momentum-dark exciton states are higher in energy [58].

Another class of excitons, known as *interlayer excitons*, arises in van der Waals heterostructures where an electron in one TMD layer binds to a hole in an adjacent layer. Due to the spatial separation of the charge carriers across different atomic layers, interlayer excitons exhibit significantly reduced wavefunction overlap, leading to long radiative lifetimes that can range from a few to hundreds of nanoseconds in high quality samples and in some cases extend to the microsecond regime at cryogenic temperatures. These extended lifetimes make interlayer excitons particularly promising for devices, where controlled transport and storage of excitonic states are desirable. Moreover, in moiré superlattices formed by twisting or lattice mismatch between layers, interlayer excitons can experience periodic potentials that localize them into arrays of quantum dots, enabling the exploration of strongly correlated quantum phenomena and the realization of excitonic lattices [59].

At intermediate exciton densities, neutral excitons can bind to an additional free charge carrier to form a three-particle bound state, referred to as a negatively or positively charged *trion*. In monolayer TMDs, trions appear as PL peaks that are red shifted relative to neutral excitons, reflecting their lower optical transition energy. The trion binding energy $E_b^{(T)}$ refers to the energy required to dissociate the trion into a neutral exciton and a free charge. This binding energy typically lies in the range of 20 - 40 meV, which is small compared to the binding energy of a neutral exciton $E_b^{(X)}$ [60].

$$E_X^{(T)} = E_{\text{gap}} - E_b^{(X)} - E_b^{(T)} \tag{2.80}$$

Nevertheless, the total energy $E_X^{(T)}$, emitted as a photon in the case of radiative recombination, is lower than that of a neutral exciton, reflecting its more tightly bound and stable configuration [12, 60]. The total binding energy of a trion, defined as the energy to fully dissociate a trion into three free particles, is given by the sum of the exciton and trion binding energies and thus is higher than that of a neutral exciton alone. The trion exhibits the oscillator strength of excitons combined with a positive or negative charge, making them luminescent charge carriers [61]. At room temperature, thermal broadening smears out the distinct trion peak, causing it to merge with the neutral exciton peak. This results in an asymmetric spectral line shape in PL spectra, see Figure 4.15 (a), a characteristic feature of trion-exciton coexistence at elevated temperatures [3].

Similarly, at intermediate excitation densities, two neutral excitons can bind through reciprocal Coulomb attraction to form a four-particle state, referred to as a *biexciton*. Analogous to the hydrogen molecule, the biexciton is stabilized by inter-exciton interactions and appears as an additional peak in the PL spectrum, redshifted relative to the neutral exciton by its binding energy. The biexciton binding energy, again defined as the energy required to dissociate it into two individual excitons, is typically in the range of 15 - 60 meV in monolayer TMDs. At room temperature, biexciton signatures are generally weak or absent due to thermal ionization, limited biexciton population and spectral broadening. Their observation usually requires cryogenic conditions and high excitation densities [12, 62].

Furthermore, excitonic properties in TMDs are highly tunable via external factors such as dielectric engineering, applied electric fields or mechanical strain, making them promising candidates for optoelectronic and photonic applications [12].

Nonlinear optical properties of TMDs

TMDs exhibit strong nonlinear optical responses due to the large oscillator strength of their excitonic resonances. Near excitonic transitions, the second- and third-order nonlinear susceptibilities, $\chi^{(2)}$ and $\chi^{(3)}$, are significantly enhanced due to strong interband transitions and large transition dipole moments [1–3, 63–65]. This unlocks efficient nonlinear processes such as SHG and THG, even under moderate excitation conditions. Notably, the spectral features of the nonlinear response often qualitatively reflect the underlying excitonic structure, offering a spectroscopic possibility into exciton dynamics. The exceptional nonlinear optical properties of TMDs include broadband spectral response, strong $\chi^{(2)}$ and $\chi^{(3)}$ nonlinearities and high conversion efficiencies for harmonic generation. These effects are further amplified by the inherently strong light-matter interaction in two-dimensional systems, making TMDs promising candidates for ultrathin nonlinear optical components and on-chip photonic integration [1, 2].

In particular, the broken inversion symmetry in monolayer TMDs allows for efficient second-order nonlinear optical processes such as SHG, see Section 2.1.3. As a result, SHG is highly efficient in odd-layered TMDs (monolayers, trilayers, ...) and vanishes in even-layered sheets due to restored inversion symmetry [63]. The SHG intensity is strongly dependent on the crystal orientation and polarization-resolved SHG measurements provide a powerful and non-destructive tool for characterizing the crystallographic axes and symmetry of TMD flakes [66–69].

Third-order nonlinear processes, including THG and FWM are also significant in TMDs and are not symmetry-forbidden in either centrosymmetric or non-centrosymmetric structures. THG has been observed in both monolayer and multilayer TMDs [70].

FWM has been originally demonstrated in MoS_2 monolayers, where strong signals were observed near the excitonic resonances due to an enhanced third-order susceptibility [3, 71, 72]. Subsequent studies have extended this to other TMD materials, confirming the generality of the effect and highlighting their potential for coherent nonlinear spectroscopy, ultrafast signal modulation and quantum optical applications [3, 68]. In general, TMDs exhibit strong FWM signal generation, increasing with the number of layers [68, 70, 73]. The polarizations of both, THG and FWM, aligns with the polarization of the incident fields, if the polarization of all incident beams are parallel [74].

2.3.2. Single-Walled Carbon Nanotubes

Since their discovery in 1993 by Iijima and Ichihashi [75], single-walled carbon nanotubes (SWCNTs) have emerged as one of the most intriguing nanomaterials in modern science. Structurally, they can be visualized as seamless hollow cylinders formed by rolling a single layer of graphene, an atomically thin sheet of sp^2-hybridized carbon atoms, arranged in a highly symmetric two-dimensional honeycomb lattice.

The simple act of rolling up graphene introduces remarkable structural and electronic complexity. The specific manner in which the graphene sheet is rolled is described by

its chirality. Chirality not only defines the symmetry and geometry of the nanotube but also its electronic band structure. SWCNTs can exhibit either metallic or semiconducting behavior, depending on their chirality, with a structure-dependent bandgap that allows for precise electronic and optoelectronic tunability. In particular, semiconducting SWCNTs display PL in the near-infrared (NIR) spectral range, a property that has drawn significant attention for applications in biomedical imaging, telecommunications and quantum technologies [76].
From a physical point of view, SWCNTs are considered quasi-one-dimensional systems [77]. They typically have diameters in the range of 1–2 nm while their lengths can reach from a few tens of nanometers up to several centimeters [76]. This extraordinary aspect ratio makes them an ideal platform for investigating one-dimensional physics.

Structure of Graphene and SWCNTs

The basis for describing the structural properties of SWCNTs, forming a seamless and hollow cylinder, lays in the origin as a rolled up flake of graphene. Graphene is formed as a two-dimensional monolayer of carbon atoms arranged in a hexagonal honeycomb lattice. The graphene lattice can be described as consisting of two equivalent sublattices, commonly labeled A and B, with each carbon atom belonging to one of them. These sublattices are offset from each other by a distance equal to the carbon-carbon bond length, denoted by a_{cc}. The unit cell of graphene contains two atoms, one from each sublattice, and is defined by two primitive lattice vectors, $\vec{a}_1$ and $\vec{a}_2$, which point towards the second-nearest neighbor in the lattice. The lattice can be described using the two lattice vectors:

$$\vec{a}_1 = \frac{a_{cc}}{2}(3, \sqrt{3}), \qquad \vec{a}_2 = \frac{a_{cc}}{2}(3, -\sqrt{3}), \tag{2.81}$$

with the carbon-carbon bond length in the lattice of approximately $a_{cc} = 142\ pm$ [78]. The first-order Brillouin zone in the reciprocal momentum space is spanned by the two reciprocal lattice vectors:

$$\vec{b}_1 = 2\pi \frac{\vec{z} \times \vec{a_2}}{\vec{a_1} \cdot (\vec{z} \times \vec{a_2})} = \frac{2\pi}{3a_{cc}}(1, \sqrt{3}) \tag{2.82}$$

$$\vec{b}_2 = 2\pi \frac{\vec{a_1} \times \vec{z}}{\vec{a_2} \cdot (\vec{a_1} \times \vec{z})} = \frac{2\pi}{3a_{cc}}(1, -\sqrt{3}), \tag{2.83}$$

Figure 2.12 illustrates the lattice structure of graphene together with the Brillouin zone and the corresponding high symmetry points.

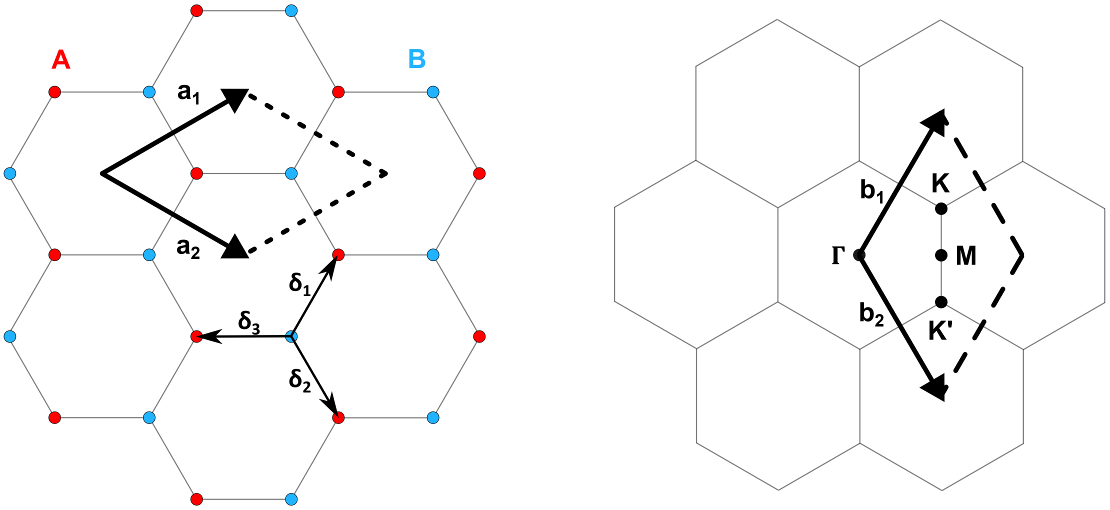

Figure 2.12.: Schematic illustration of the honeycomb lattice of graphene and its Brillouin zone. *Left:* Honneycomb lattice structure of graphene formed by two interpenetrating sublattices (A: red and B: blue). a_1 and a_2 illustrate the lattice unit vectors while δ_1, δ_2 and δ_3 denote the nearest-neighbor vectors. *Right:* First Brillouin zone in reciprocal space together with high symmetry points Γ, M, K and K'.

All carbon atoms in graphene are sp^2-hybridized, giving rise to a two-dimensional honeycomb lattice. Each carbon atom forms three equivalent σ-bonds with its nearest neighbors, resulting in a fully occupied energy band that is the reason for the exceptional mechanical, chemical and thermal stability of the graphene structure. The fourth valence electron in the unhybridized 2p$_z$ orbital is oriented perpendicular to the graphene plane. These orbitals overlap across the lattice to form a delocalized π-bonding system, which plays a central role in the remarkable electronic properties, including its high electrical conductivity and the emergence of massless Dirac fermions [79]. In undoped graphene, the Fermi energy lies at the energy of the Dirac points, the K and K' corners of the Brillouin zone in momentum-space, where the conduction and valence bands touch. The valence band is completely filled up to the Fermi energy and the conduction band is empty above it. At this point, the energy dispersion is linear and the electronic band structure forms a cone-like shape [14, 80].

A SWCNT can be conceptualized as a graphene sheet that is rolled up along a vector known as the *chiral vector* $\vec{C}_h$.

$$\vec{C}_h = n\vec{a}_1 + m\vec{a}_2 \tag{2.84}$$

It is defined by a pair of integers (n, m), denoted as the chiral index, while standard notation writes the larger number first. These are commonly used for naming the different nanotube types. All CNTs are being categorized into three groups, named *armchair* $(n = m)$, *zigzag* (n or $m = 0$) and the more general *chiral* forms ($n \neq m$ and neither is zero). Figure 2.13 illustrates the roll-up process along the chiral vector and shows how the different types are distinguished by their characteristic bond patterns.

The magnitude of the chiral vector $\vec{C}_h$ determines the circumference of the nanotube and is given by

$$C_h = \sqrt{3} \cdot a_{CC} \cdot \sqrt{n^2 + m^2 + nm}. \tag{2.85}$$

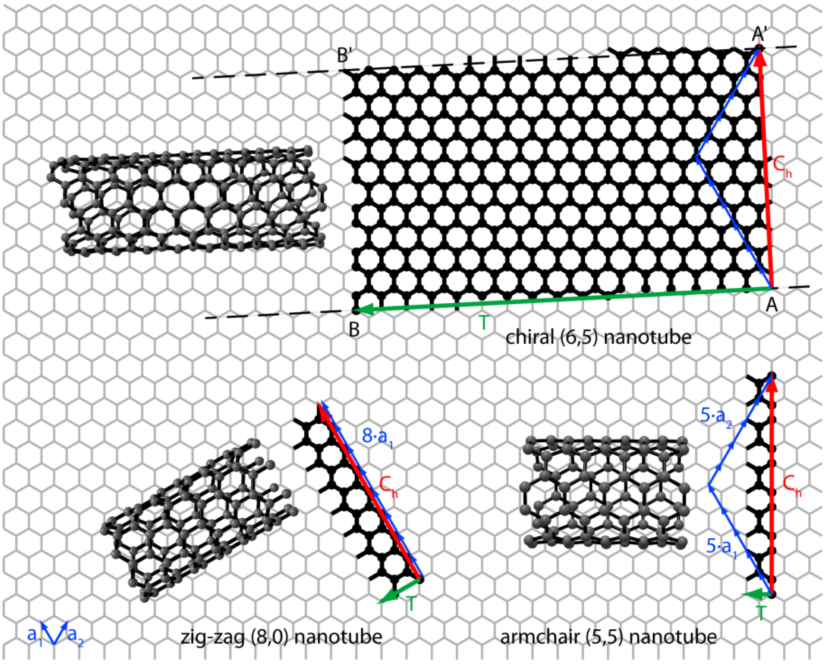

Figure 2.13.: Formation of SWCNTs. Rolling up a rectangular sheet of graphene results in a seamless hollow cylindric structure of a CNT. Here the rectangle formed by ABB'A' results in a (6,5)-SWCNT. The chiral indices define the orientation of the chiral vector $\vec{C}_h$. Additionally, the formation of (5,5) and (8,0) SWCNTs is indicated. Reproduced with permission from [81].

The chirality of a carbon nanotube plays an important role in determining the electronic and optical properties. In general, nanotubes whose chiral indices fulfill the condition $n - m = 3k$, where k is an integer ($k = 0, 1, 2, \ldots$), exhibit metallic behavior. All other configurations are semiconducting nanotubes [82]. In the following, this chapter will only refer to semiconducting SWCNTs, as only nanotubes with the chiral index (6,5) were studied in this work. An detailed discussion of the structure of CNTs can be found in [14, 80, 83].

Optical properties of semiconducting SWCNTs

In contrast to graphene, the optical properties of SWCNTs are fundamentally altered due to the effective 2D confinement of electrons, resulting in a quasi-1D electronic structure. The wave vector component $k_\parallel$ along the nanotube axis remains continuous, allowing electrons to move freely along the length of the tube. In contrast, the transverse component $k_\perp$, which wraps around the circumference of the nanotube, is quantized due to the periodic boundary condition:

$$|\vec{C}_h| = \mu \cdot \lambda = \mu \cdot \frac{2\pi}{|\vec{k}_\perp|}, \tag{2.86}$$

where $\mu \in \mathbb{Z}$ is an integer. This condition ensures that any allowed electron wavefunction must have a wave vector whose wavelength is an integer multiple of 2π of the nanotube's circumference. Only in this case the wavefunction will exhibit constructive interference and is suppressed by destructive interference otherwise. These wave vectors represent equidistant lines in the Brillouin zone, parallel to the axial lattice vector $k_\parallel$ with a spacing of $\frac{2\pi}{|\vec{C}_h|}$. In Figure 2.14 the fist Brillouin of armchair and zigzag SWCNTs are illustrated, together with the circular 2D band structure of graphene in the background.

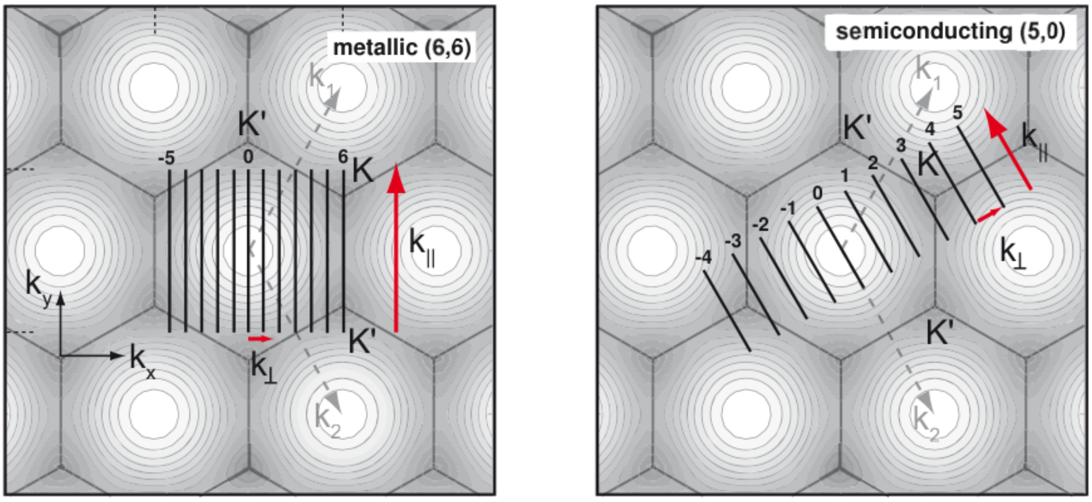

Figure 2.14.: Brillouin zone of a metallic and a semiconducting SWCNT. Equidistant black lines represent the allowed wavevectors with quantized $k_\perp$ components in the Brillouin zone (a) a metallic armchair (6,6) SWCNT and (b) a semiconducting zigzag (5,0) SWCNT. In the background the energy dispersion relation of graphene is indicated as a contour plot. The indexing represents values of μ. Reproduced with permission from [84].

To obtain the 1D energy dispersion relation for SWCNTs, the energy dispersion of graphene must be sampled along these "cutting lines". While $k_\perp$ is fixed for each allowed mode, the wave vector component along the tube axis, $k_{\parallel}$, remains continuous. Therefore, the energy bands of a SWCNT can be derived by intersecting the 2D band structure of graphene with these quantized lines and plotting the resulting dispersion as a function of $k_{\parallel}$:

$$E_{\lambda}(k_{\parallel}) = E_{\text{graphene}}(k_{\parallel}, k_{\perp}^{(\lambda)}), \tag{2.87}$$

where λ is the index of the quantized transverse modes. A detailed discussion of the dispersion relations across the Brillouin zone of graphene can be found in [14, 80]. This process sampling 2D graphene bands along discrete lines is referred to as *zone folding*, because it essentially folds the 2D Brillouin zone of graphene into a set of 1D subbands suitable for a quasi-1D system like a nanotube [14, 83, 84].

Whether a carbon nanotube behaves as a metal or a semiconductor depends on the position and number of the cutting lines of allowed wave vectors. If one of these quantized $k_{\perp}$ lines crosses a Dirac point, the conduction band of the SWCNT is connected to the valence band and the nanotube behaves like a metal. If none of the lines intersect a Dirac point, an energy gap appears and the nanotube exhibits semiconducting properties. This relationship between the geometry of the nanotube and its electronic behavior allows for precise tuning of its properties. By choosing the chirality, a nanotube can be tailored to fit a wide range of applications.

The density of states (DOS) describes how many electronic states are available in each energy interval for electrons to occupy. Since the allowed wave vectors $\vec{k}$ are typically evenly spaced, the DOS becomes high when many k-states have similar energies. This happens when the energy band is flat, i.e. when the band dispersion is slow and the curvature of the band $\left(\frac{dE}{dk}\right)$ is small. In such regions the DOS can exhibit pronounced features.
Unlike in graphene, where the DOS near the Dirac point increases linearly with energy, carbon nanotubes show a very different behavior because they are effectively one-dimensional. For a 1D system the DOS can be expressed as:

$$n(E) = \frac{\partial N(E)}{\partial E} = \frac{2}{l}\sum_{i}\int dk \quad \delta(k - k_i)\left|\frac{\partial \epsilon(k_i)}{\partial k}\right|^{-1} \tag{2.88}$$

with the length of the Brillouin zone $l = \int dk = \frac{2\pi}{a}$, a single, degenerate 1D energy band $\epsilon(k)$, the solutions k_i of the equation $E - \epsilon(k_i) = 0$ and the number of electron states $N(E)$ per unit cell and up to the energy E [85]. Equation 2.88 sums contributions from all wavevectors k where the energy matches $\epsilon(k) = E$, weighted by the inverse slope of the energy band $\frac{\partial \epsilon(k_i)}{\partial k}$. This relationship captures how the shape of the energy bands directly influences the density of available electronic states. The DOS spikes where the bands are flat and it exhibits singularities at local extrema $\frac{\partial \epsilon}{\partial k} = 0$. These points of diverging DOS in 1D systems are referred to as *van-Hove-singularities* (vHs). The optical properties of of CNTs are strongly determined by vHs. The positions of these peaks are determined by the tube's chirality (n, m) and diameter, which define the energy separation between subbands. In semiconducting CNTs, the first vHs appear symmetrically around a finite band gap, whereas in metallic CNTs, a singularity can occur at the Fermi level, giving rise to metallic conductivity.

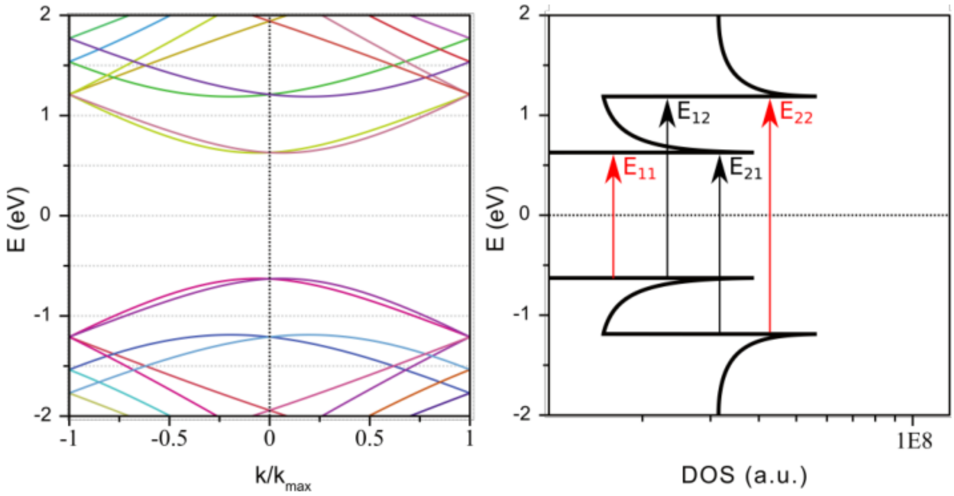

Figure 2.15.: Simulated band structure and DOS of a (6,4) SWCNT *Left:* The band structure diagram in the Brillouin zone shows multiple allowed energy bands, retrieved from the zone folding approach. *Right:* The corresponding DOS exhibits vHs at energies where the bands are flat. Dipole-allowed transitions are indicated for parallel polarized light as red arrows between same μ valence and conduction subbands $(E_{ii}, \Delta\mu = 0)$ and for perpendicular polarized light between neighboring μ subbands $(E_{ij}, \Delta\mu = \pm1)$ as black arrows. Reproduced with permission from [86].

Figure 2.15 presents a numerical simulation of the band structure of a (6,4) SWCNT together with the corresponding DOS. The band structure clearly exhibits an energy gap, corresponding to the semiconducting properties of the CNT. Within this gap, the DOS vanishes, reflecting the absence of available electronic states. At the pronounced extrema of the valence and conduction bands, sharp vHs peaks appear in the DOS.

As discussed in Section 2.3.1, only vertical transitions in the k-space are optically allowed due to conservation of momentum and the negligible photon momentum. In CNTs, transitions from the valence band i to the conduction band j are labeled E_{ij}. Allowed transitions depend on the polarization of the excitation light, due to conservation of the angular momentum. When light is polarized *parallel to the axis* of the nanotube, the electric field vector points in the axial direction only. Since it has no component around the circumference, it cannot change the angular momentum of the electronic states. In other words, the optical transition must conserve angular momentum. As a result, only transitions between subbands of equal angular momentum $\Delta\mu = 0$ are allowed. These correspond to the E_{ii} transitions at the same cutting line in the reciprocal space, indicated as red arrows in the right side of Figure 2.15. Contrary, light polarized *perpendicular to the axis* of the nanotube can induce transitions with $\Delta\mu = \pm 1$, as its electric field has a component around the tube. These transitions correspond to neighboring cutting lines in the reciprocal space and are indicated by the black arrows in the right side of Figure 2.15 [80, 87].

PL emission in CNTs predominantly occurs from the lowest-energy transition E_{11} and is polarized along the axis of the nanotube. When higher-energy states such as E_{22} are excited, they typically undergo rapid non-radiative relaxation down to the E_{11} state, from which photon emission takes place [88–90].

Excitons in SWCNTs

In the early phases of research on SWCNTs, their optical transitions were commonly interpreted as inter-subband transitions of free charge carriers, as depicted in Figure 2.15. However, this view was fundamentally revised following two-photon experiments [89, 91], which provided clear evidence for the formation of strongly bound Wannier-Mott exciton states, due to different symmetries of the excited states. These excitons are stable at room temperature and accompanied by a Rydberg series of higher excited states, highlighting that the optical response of SWCNTs is dominated by many-body effects rather than single-particle transitions. The argumentation is similar to the case of excitons in 2D TMDs, discussed earlier in Section 2.3.1. The quasi-one-dimensional confinement of charge carriers, together with a significantly reduced dielectric screening from the surrounding environment, enhances the Coulomb interaction between electrons and holes. As a result, exciton binding energies in CNTs are notably high and depend sensitively on the nanotube's chirality, its diameter and the dielectric properties of the surrounding medium. Despite the dominance of excitonic effects, the underlying single-particle band structure and the corresponding DOS still provide a framework for understanding and modeling optical transitions in CNTs.

As a result of the binding energy, exciton creation sets in hundreds of meV below the single particle band gap, i.e. the continuum state [91, 92]. Excitons in SWCNTs have an exciton Bohr radius on the order of some nanometers. While first experiments indicated exciton size of 2 ± 0.7 nm [89], recent results yielded in 13 ± 3 nm [93]. Compared to the lattice constant of 0.14 nm, the treatment in the Wannier-Mott picture seems valid. Hence, excitons are delocalized along the circumference of the tube and are mobile along the axis with diffusion lengths of about 100 nm [94]. The diffusion coefficient of excitons in SWCNTs is relatively low, with values around $D \approx 0.1$ cm^2/s. Despite strong absorption, the PL quantum yield is remarkably low, typically on the order of 10^{-4} to 10^{-3}, suggesting that non-radiative decay channels dominate exciton recombination. The radiative lifetime is on the scale of $\tau_{\mathrm{rad}} \approx 100$ ns, while non-radiative lifetimes are much shorter, in the range of $\tau_{\mathrm{nonrad}} \approx 10$-100 ps [92]. Ultrafast spectroscopy studies reveal a complex decay dynamics composed of multiple components. A fast decay process is attributed to exciton-exciton annihilation, which becomes particularly efficient under high excitation densities.

An intermediate decay component is associated with the population and dynamics of dark, optically inactive, exciton states. The slowest decay channel arises from weak radiative recombination, dominanted by phonon assisted relaxation processes. Moreover, many-body excitonic complexes, including trions and biexcitons, have been experimentally confirmed in SWCNTs [92, 95, 96].

Synthesis of CNTs

The first nanotubes were produced in 1990 by Iijima [39] using the *arc discharge evaporation method*. This technique is one of the earliest and most established and involves striking a high-temperature plasma arc, reaching up to 4000 °C, between two graphite electrodes in an inert gas atmosphere like helium or argon. The heat vaporizes carbon from the anode and in the presence of metal catalysts such as iron, cobalt or nickel this carbon vapor condenses to form nanotubes on the cathode and nearby surfaces. The arc discharge method is known for producing high-quality nanotubes with relatively few defects, although the result is often a mix of single-walled and multi-walled CNTs [76, 80, 97].
A few years later, in 1996, researchers developed the *laser ablation method*, offering another route to high-purity CNTs [98]. In this approach, a high-powered laser is used to vaporize a graphite target that has been doped with metal catalysts (usually nickel or cobalt) inside a furnace, heated to around 1200 °C. The process takes place in an inert gas flow, typically helium or argon. When the laser pulses hit the target, carbon atoms and catalyst particles are ejected into the gas phase where they cool down and self-assemble into nanotubes. The resulting CNTs are collected downstream on a cooler surface. While this method produces very high-quality SWCNTs with a narrow diameter distribution, it is expensive and not well-suited for mass production [80, 97, 98].
Today, the most widely used and scalable technique is *chemical vapor deposition (CVD)*. In this method, a carbon-containing gas such as methane or acetylene is introduced into a furnace at high temperatures, typically around 1000 °C. A substrate inside the furnace is coated with metal nanoparticles, commonly iron, nickel or cobalt, which act as a catalysts. These particles help break down the carbon source and guide the growth of nanotubes directly on the substrate. CVD offers fine control over the nanotube's alignment, length and diameter and can be tuned to produce either single- or multi-walled CNTs. Its scalability and versatility make it a well suited method for industrial and research applications [76, 80, 97].

3. Antenna Controlled Antibunching

"The following chapter is based on the publication: Controlling photon antibunching from 1D emitters using optical antennas" by Lange et al., published in Nanoscale (2019) [99]. Parts of the text and figures are reproduced, with permission from the Royal Society of Chemistry.

The current technological progress in quantum photonics opens this field to practical implementations in a wide range of applications, such as quantum-secure communication, quantum radiometry and efficient quantum computing. These new technologies make use of quantum mechanical principles like superposition and entanglement. Hence, the ability to generate single photons on demand is of crucial interest for many emerging quantum technologies. All emitted photons are supposed to be identical in all relevant degrees of freedom, like polarization, spectral shape, temporal and spatial mode. While classical light emits photons in bunches or at unpredictable times, single-photon sources (SPS) produce one photon at a time in a controlled fashion. This is particularly important in quantum systems, where a single extra photon can lead to errors or compromise security [100].

In quantum communication, single photons carry information in protocols like quantum key distribution, which offer theoretically unbreakable encryption through quantum-mechanical principles. Here, the guarantee that only one photon is emitted reflects that any attempt to intercept the information can be detected. Similarly, in quantum computing and photonic quantum networks, individual photons are used as quantum bits (qubits). To make these systems work reliably, the photons need to be not only single but also highly pure, ensuring precise control and reducing the chance of computational errors.

To meet the requirements of quantum technologies, a variety of quantum systems for reliable single-photon emission (SPE) have been explored. SPS are quantified by their brightness, single-photon purity and the indistinguishably. The single-photon purity is related to the degree of antibunching, the non-classical signature of quantum light. Up to now, zero-dimensional emitters such as isolated atoms, ions or quantum dots are the most common SPS due to their energy level configuration, naturally restricting photon emission to one photon at a time. While these systems can emit high-purity single photons, they suffer from practical limitations. For example, single atoms must be isolated by precise trapping techniques and cooled down to reduce Doppler broadening. Quantum dots typically require cooling to low temperatures to suppress phonon interactions and fabrication imperfections can lead to spectral inhomogeneity [100]. Additionally, coupling 0D emitters efficiently to optical circuits remains technically challenging due to their spatial and spectral variability [20].

Nonlinear optical processes like FWM or spontaneous parametric down conversion (SPDC) can be utilized as probabilistic sources of single photons. Here, photon pairs are created and the emission of one single photon is heralded to the detection of the other. Their technically simple operation does not require cryogenic temperatures, is spectrally tunable and compatible with photonic integrated circuits. On the downside, the probabilistic character of these sources makes it impossible to predict when a heralding signal will occur [100–102].

Increasing attention has turned to engineered low-dimensional materials, such as one-dimensional nanowires or CNTs and two-dimensional semiconductors, as promising platforms for scalable and robust single-photon emission. Their reduced dimensionality leads to enhanced quantum confinement, giving rise to stable excitonic resonances, responsible for strong light-matter interactions [20]. For these spatially extended materials, the number of excitons must be limited or reduced in order to achieve pure SPE. Excitons can be localized at distinct trap-states, minima in the energetic landscape, where EEA can be highly efficient. In layered semiconductors, such as tungsten diselenide, shallow trap-states occur from defect-states [20], crystal imperfections at special edge states [103] or can be induced by strain-engineering to direct energy into 'artificial atoms' [104], sufficient for exciton localization at liquid helium temperatures.
At room temperature, single photons can be emitted from defect-states in materials like hexagonal boron nitride (h-BN) [105, 106]. Another effective way is by embedding quantum dots within inorganic semiconducting nanowires, which helps to trap excitons efficiently and enhances SPE [107].
The same principle can be transferred to 1D CNTs, where shallow quantum-dot like states are generated by strain or environmental fluctuations [20, 108–110]. Single-photon properties in SWCNTs were shown to depend strongly on the length of the nanotube and on excitation density [111, 112]. However, room-temperature SPE from SWCNTs has been realized by the creation of deep, solitary impurity states through oxygen doping with excellent single-photon purity but suffering from inherent emission instability [113]. Covalent aryl functionalization acts as an alternative with significantly reduced perturbation of the electrostatic environment [114, 115]. Non-covalent functionalization of SWCNT with pentacene molecules was proven to enhance exciton localization by creating a modified energy landscape without altering their intrinsic structure. The pentacene molecules induce local dielectric screening, which effectively traps excitons and leads to photon antibunching behavior at room temperature, while preserving the fundamental properties of the nanotube [116].

Even without chemical doping, pronounced antibunching has been observed in pristine SWCNTs resulting form exciton diffusion, EEA and natural localization effects [5, 111, 117]. As a crucial factor, influencing the degree of antibunching in SWCNTs, the ratio between the optical excitation spot size and the exciton diffusion length was identified. When the excitation is strongly confined relative to the diffusion range the likelihood for multi-photon emission decreases and antibunching is enhanced [5, 111].
If an optical antenna, converting propagating radiation into local fields and vice versa, is placed in the vicinity of an absorber, the rates for optical absorption and emission are

locally strongly enhanced. Additionally, the antenna's directivity forces radiation to a specific direction [118]. For atom-like SPS, plasmonic nanostructure have been used as optical antennas to enhance the rate of usable photons significantly [119–121].

This chapter describes the use of an optical antenna as a near-field probe to control the photon statistics of SWCNTs. This concept was originally proposed in [111] and has been published in [99].
In Sections 3.1 and 3.2 the fundamentals of photon statistics and optical antennas are introduced, respectively. Subsequently, in Section 3.3 the experimental details such as sample preparation, technical devices and the setup are described. Section 3.4 discusses the experimental procedure and the results. Finally, in Section 3.5 a numerical investigation of the relevant parameters and the potential of antenna-control on the degree of antibunching in 1D emitters is given. This Monte-Carlo simulation of a random walk of excitons in 1D has been designed and performed by Dr. Richard Ciesielski from the research group of Prof. Achim Hartschuh at the LMU Munich.

3.1. Photon statistics and the quantum nature of light

The classical theory of light, based on Maxwell's equations, has been remarkably successful in describing a wide range of optical phenomena such as reflection, refraction, diffraction and interference. Within this framework, light is modeled as a continuous electromagnetic wave and its interaction with matter is explained using the well-established laws of classical electrodynamics.

But with the rise of quantum mechanics in the early 20th century the understanding of light began to change fundamentally. A key event was Einstein's interpretation of the photoelectric effect [122], which couldn't be explained by classical wave theory alone. Instead, Einstein proposed that light comes in discrete packets of energy. These photons behave like individual "bullets" or "darts" of energy [123], each with a specific amount of energy $E = \hbar\omega$ and momentum $p = E/c$ and capable of exciting an electron without any noticeable time delay. This implies a point-like localization of energy transfer, in contrast to the extended nature of classical waves.

Later experiments at extremely low light intensities revealed that, when single photons were sent through a double-slit setup, interference patterns still emerged over time. This showed that each photon somehow takes multiple paths and interferes with itself. This is a demonstration of the wave-particle duality, a key issue of modern quantum optics.

In interferometry, the correlation of the electromagnetic field is measured between various space-time points. Prominent examples are the *Young double slit interference experiment* and the *Michelson interferometer.* The fields at the detector position is a superposition of the incident fields described as:

$$E(x,t) = E_1(x_1,t) + E_1(x_2,t) = E_0 \left[e^{i(kx_1-\omega t)} + e^{i(kx_2-\omega t)} \right], \tag{3.1}$$

where x_1 and x_2 are the field's optical paths, k is the wavenumber, ω is the angular frequency and t is the time, while the same polarization and amplitude E_0 for both fields is assumed. The intensity at the fixed detector position depends on the path difference of the two fields, which can be expressed as a time delay $\tau = \frac{x_2-x_1}{c}$ of one field with respect to the other.

$$I(\tau) = \langle |E_1(t) + E_2(t+\tau)|^2 \rangle \tag{3.2}$$

In Equation 3.2, $\langle .. \rangle$ denotes to the time average. Expanding this reveals the cross term, which contains the information about the correlation between the fields.

$$I(\tau) = \langle |E_1(t)|^2 \rangle + \langle |E_2(t+\tau)|^2 \rangle + 2\Re \left[\langle E_1^*(t) E_2(t+\tau) \rangle \right] \tag{3.3}$$

Assuming the two fields are emitted from the same, stationary light source, E_1 and E_2 are not fundamentally different but rather the same field sampled at different times,

$$E_1(t) = E(t) \tag{3.4}$$

$$E_2(t+\tau) = E(t+\tau), \tag{3.5}$$

and Equation 3.3 becomes:

$$I(\tau) = \langle |E(t)|^2 \rangle + \langle |E(t+\tau)|^2 \rangle + 2\Re \left[\langle E^*(t) E(t+\tau) \rangle \right] \tag{3.6}$$

The interference term $\langle E^*(t)E(t+\tau)\rangle$ quantifies how well the fields remain correlated after the delay τ. This is summarized in the normalized first-order correlation function $g^{(1)}$, which measures the degree of coherence between the fields at different times or positions, normalized to the average intensity.

$$g^{(1)}(\tau) = \frac{\langle E^*(t) E(t+\tau) \rangle}{\langle |E(t)|^2 \rangle} \tag{3.7}$$

The spatial dependence is implicit in the fixed detector position. $|g^{(1)}(\tau)| = 1$ describes a perfectly coherent field. For an incoherent field $|g^{(1)}(\tau)| < 1$ and decays rapidly with increasing time delay, reflecting the loss of correlation between the fields. The contrast of the interference pattern is directly proportional to $|g^{(1)}(\tau)|$ [124].
While $g^{(1)}(\tau)$ is sensitive to the temporal phase coherence of the optical field it does not account for correlations in the photon arrival times. These fluctuations in intensity over time and the correlated photon statistics can be captured by the *second-order correlation function* $g^{(2)}(\tau)$.

$$g^{(2)}(\tau) = \frac{\langle I(t) I(t+\tau) \rangle}{\langle I(t) \rangle^2} \tag{3.8}$$

This correlation function quantifies the probability to detect intensity coincidences at two times separated by a time delay τ. Experimentally, $g^{(2)}(\tau)$ is accessible by photon counting techniques with avalanche photodiodes (APDs) (see Section 3.3.2) or photo-multiplier tubes (PMT).

In their pioneer work, in 1956 Hanbury Brown and Twiss developed a method to use the measurement of intensity correlations for the determination of the angular diameter of visual stars. Previously, such measurements relied on the determination of the spatial coherence length l_{coh} of the incident starlight using a Michelson interferometer. Importantly, phase fluctuations inside the coherence volume are related to the electric field strength and therefore to the amplitude. As a result, at two detectors within l_{coh} the intensity fluctuations are correlated and $g^{(2)}(0) > 1$. As the distance between the two detectors d is increased beyond the coherence length, $d > l_{\text{coh}}$, the correlation diminishes. This can be exploited to determine the angular diameter of the star [125].

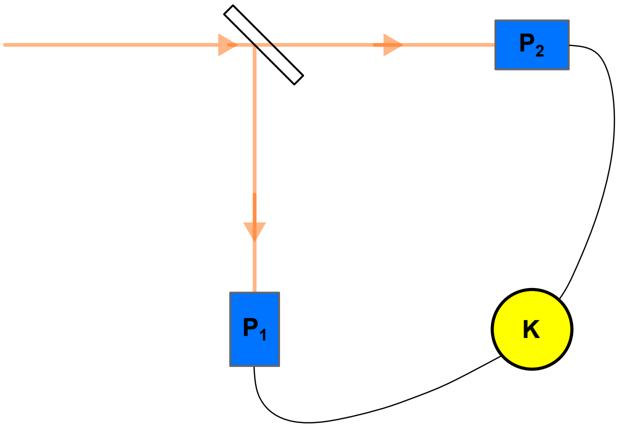

Figure 3.1.: Schematic principle of the Hanbury Brown Twiss intensity correlator setup. The incident light is devided at a 50:50 beamsplitter and send to two detectors at positions P_1 and P_2. The electric signals of the two detectors are correlated at the correlator K.

This method is equivalent to measuring coincident photon detection events, i.e. the simultaneous registration of photons at two detectors. The probability for the arrival of a photon at position P_1 is enhanced if a second photon arrives at position P_2. Figure 3.1 illustrates the schematic principle of such an intensity correlation setup. This surprising result originates in the superposition of the radiation of all atoms on the star's surface. In thermal light, the mean temporal width of a positive or negative intensity peak is on the order of the coherence time τ_{coh}. So within $\tau < \tau_{\text{coh}}$ the number of coincident events is enhanced compared to random coincidences for $\tau \gg \tau_{\text{coh}}$. Since τ_{coh} is inversely proportional to the spectral linewidth Δf, the temporal intensity correlations are directly connected to the spectral properties of the light source [126]. This enhanced probability for two photons at the same position within a small time interval is referred to as *photon bunching*. It describes the tendency of photons to bundle. In fact, this bunching directly mirrors the strong intensity fluctuations of thermal light sources.

In contrast, laser light is characterized by a fundamentally different photon statistics. This difference arises from the laser principle, which is based on stimulated emission, whereas thermal light is based on spontaneous emission. Inside a laser cavity, the electromagnetic field oscillates coherently and in phase with the macroscopic polarization of the laser medium. Each photon generated by stimulated emission is identical in terms of frequency, direction and polarization. This results in a highly ordered and phase-stable light field. However, the laser's remarkable amplitude stability leads to the characteristic photon statistics and is a direct consequence of a gain saturation mechanism. The probability of stimulated emission increases with the light intensity but the laser is pumped at a constant rate. So, a random intensity peak depletes the population inversion more quickly than average, effectively reducing the following gain. This automatic feedback mechanism smooths out intensity fluctuations, effectively damping them before they can grow [126, 127].

Since intensity fluctuations in laser light are strongly reduced, there is no excess of coincident photon detections compared to the average. As a result, the intensity correlation function $g^{(2)}$ becomes independent of the time delay τ and remains flat at $g^{(2)}(\tau) = 1$. This does not mean that photons arrive with a perfectly even photon distribution over time, but rather it means that the probability of detecting a photon at any given time is constant and independent of other events.
Such perfectly random and independent events are described by the *Poisson-distribution*. The Poisson distribution also models other independent random processes, such as radioactive decay or, as a famous historic example, the number of soldier deaths by horse kicks [128]. Following the Poisson distribution the probability of observing exactly n events in a given time interval with the expectation of λ is given by:

$$p_n = \frac{\lambda^n}{n!} e^{-\lambda} \tag{3.9}$$

A key feature of the Poisson distribution is that its mean $\langle n \rangle$ is equal to its variance σ^2:

$$\langle n \rangle = \sigma^2 = \lambda \qquad \textit{Poissonian} \tag{3.10}$$

λ is the expectation value. This means that the distribution becomes broader for an increase in the average number of events. In contrast, thermal light shows super-Poissonian statistics, as its variance exceeds the mean, reflecting the larger intensity fluctuations.

$$\sigma^2 > \langle n \rangle \qquad \textit{super-Poissonian} \tag{3.11}$$

As discussed above, for the super-Poissonian chaotic light of a thermal emitter, photons tend to arrive in groups, a phenomenon referred to as *photon bunching*. This leads to a intensity correlation peak at zero time delay, $g^{(2)}(0) > 1$, with $g^{(2)}(0) = 2$ being the theoretical maximum for an ideal thermal light source, see Figure 3.2 (b). This super-Poissonian behavior reflects the enhanced probability of detecting two photons in short succession.

Complementary to the Poissonian and the super-Poissonian light, the case of sub-Poissonian light is characterized by a photon number variance that is smaller than the mean:

$$\sigma^2 < \langle n \rangle \qquad \textit{sub-Poissonian} \tag{3.12}$$

While Poissonian photon statistics is exhibited by ideal coherent laser light, sub-Poissonian statistics indicate an even greater stability in the photon number. In fact, the observation of sub-Poissonian light is a clear signature of the quantum nature of light as such behavior cannot be explained classically. Quantum emitters such as single atoms or quantum dots emit photons one at a time. In these systems, the emission mechanism inherently prevents the simultaneous detection of two photons, leading to *photon antibunching*. Here, $g^{(2)}(0) < 1$, with $g^{(2)}(0) \to 0$ indicating perfect SPE. This sub-Poissonian statistic is a hallmark of verifying true SPS.

In practical experiments, a measured value of $g^{(2)}(0) < 0.5$ is often used as a benchmark to identify SPE. This condition means that the probability of detecting two photons at the same time is less than half of what would be expected from a classical light source with Poissonian photon statistics, such as a laser. In this regime, multiphoton emission events are strongly suppressed and the photon stream shows clear signs of antibunching.
To understand this more fundamentally, the Fock photon number state representation can be invoked. In this formalism, a light field that contains exactly n photons is described by the state $|n\rangle$. For such a state, the second-order correlation function at zero delay is given by:

$$g^{(2)}(0) = \frac{n(n-1)}{n^2}. \tag{3.13}$$

This expression shows that for a true single-photon state with $n = 1$, the ideal non-classical result is $g^{(2)}(0) = 0$, which means that two photons are never detected at the same time. For $n = 2$, the result is $g^{(2)}(0) = 0.5$, illustrating why this is commonly used as the threshold for SPE. Any measured value below this threshold indicates, that the source emits light with less than two photons per event on average, confirming its suitability as a single-photon emitter.

As decreasing values of $g^{(2)}(0)$ describe the emitters rising ability of sending out single photons, the degree of antibunching, $1 - g^{(2)}(0)$ can be used as a measure for SPE that is maximized in the case of ideal SPE.
Figure 3.2 summarizes this section and compares photon bunching, antibunching and coherent light in terms of the photon number streams (a) and the second-order correlation function (b), as solid lines. If the integration time τ_{int} exceeds the coherence time τ_{coh}, $g^{(2)}(\tau)$ cannot no longer be correctly resolved. This is indicated by the dotted lines in Figure 3.2 (b).

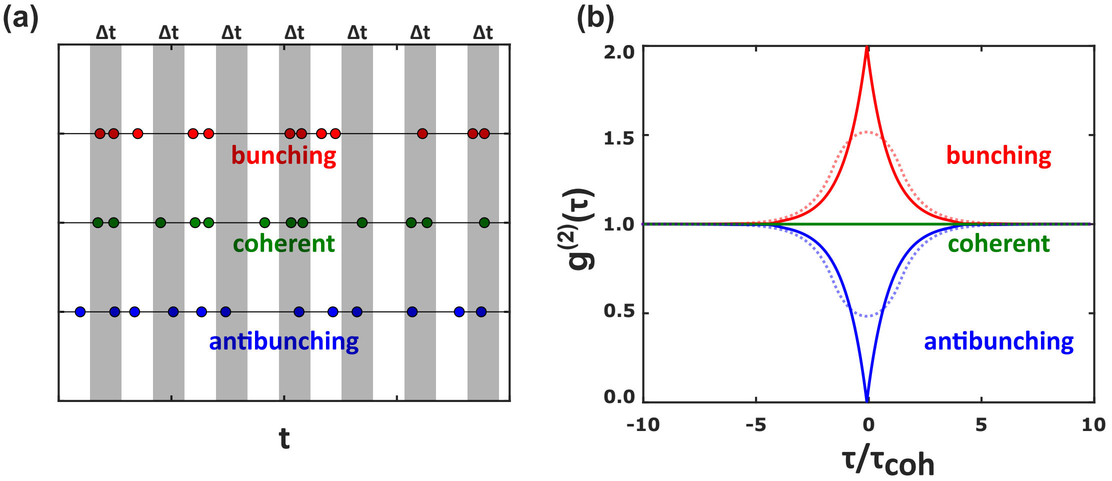

Figure 3.2.: Comparison of bunched, coherent and antibunched light. (a) Schematic illustration of photon streams divided into short time intervals Δt. For bunched light, intervals containing multiple photons occur more frequently than those with exactly one photon. For coherent light, the numbers are equal, whereas for antibunched light no interval contains more than one photon. (b) Corresponding second-order correlation function $g^{(2)}(\tau)$ as a function of the delay time τ, normalized to the coherence time τ_{coh}. Solid lines correspond to short integration times $\tau_{\text{int}} \ll \tau_{\text{coh}}$, while dotted lines represent longer integration times $\tau_{\text{int}} > \tau_{\text{coh}}$, where the correlation cannot be properly resolved.

Summarizing these findings, the concept of *photon statistics* allows to characterize light not just by its average intensity or frequency content but by the distribution and correlations of individual photon events. As such, photon statistics provide a framework to differentiate classical from non-classical light fields and to probe the quantum nature of light-matter interactions.

3.2. Optical antennas and the near-field

This short discussion of near field optics and optical antennas in this section is based on [129–133] and can be reviewed there in more detail.

The propagation of light in free space is described by the photon dispersion relation:

$$\hbar\omega = \frac{\hbar c}{2\pi\lambda} = c\hbar k \tag{3.14}$$

with $\hbar = \frac{h}{2\pi}$ the reduced Planck's constant, ω the angular frequency of the photon, λ the wavelength of the photon, c the speed of light and $k = \sqrt{k_x^2 + k_y^2 + k_z^2}$ the corresponding wavevector. Heisenberg's uncertainty principle, applied to the photon, entangles the uncertainty in the spatial position Δx with the uncertainty in the corresponding component of its momentum Δp_x.

$$\Delta p_x \cdot \Delta x = \hbar \Delta k_x \cdot \Delta x \geq \frac{\hbar}{2} \tag{3.15}$$

As a result, a wide range of wavevector components leads to a small uncertainty in the corresponding spatial direction. In other words, to achieve a high spatial resolution, the collected spread of spatial frequencies must be maximized. The maximum spread of spatial frequencies is the full wavevector in free-space $k = \frac{2\pi}{\lambda}$, so substituting Δk_x by k in Equation 3.15, leads to an expression similar to the Rayleigh diffraction limit [130]:

$$\Delta x \geq \frac{\lambda}{4\pi} \tag{3.16}$$

However, in a microscope, not all propagating components manage to arrive at the detector position, due to a limited collection angle of the microscope objective. The *numerical aperture (NA)* determines the fraction of the surrounding light cone that the system can capture.

$$\mathrm{NA} = n \cdot \sin(\theta) \tag{3.17}$$

where n is the refractive index of the medium between the lens and the sample and θ is the maximum half-angle of the cone of light that can enter or exit the objective.

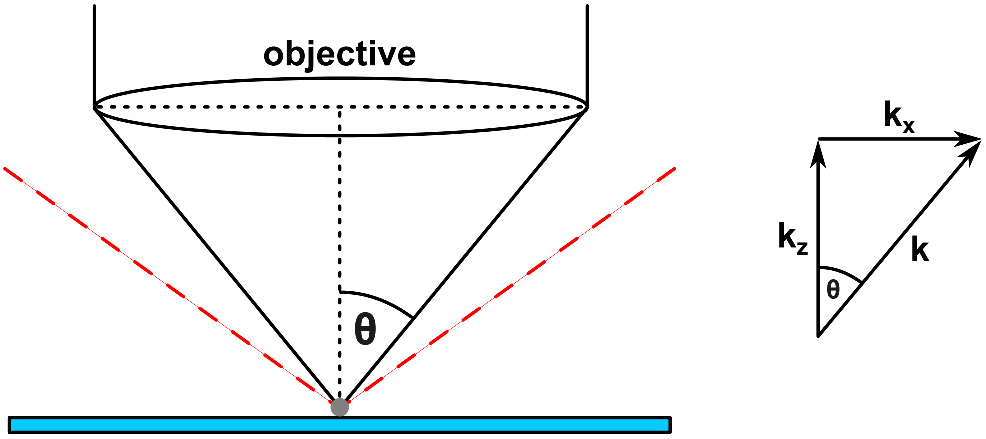

Figure 3.3.: The collection angle of a microscope objective is given by the numerical aperture. Waves with wavevector components inside the cone of the angle θ are collected by the objective, while larger angle components are not collected.

A higher NA indicates that a larger fraction of the light cone is collected. Thus, systems with larger NA provide higher spatial resolution. The maximum range of spatial frequencies that can be captured by the microscope objective is restricted by the NA:

$$k_{\mathrm{NA}} = \frac{2\pi}{\lambda} \cdot \mathrm{NA} \tag{3.18}$$

Hence, the resolution limit for experimental microscopy turns to:

$$\Delta x \geq \frac{\lambda}{4\pi \cdot \mathrm{NA}} \tag{3.19}$$

In the *angular spectrum representation*, a spatial spectrum of an optical field E at a certain position z is determined by the spectrum of spatial frequencies in a known starting point $z = 0$ and an optical transfer function $e^{\pm i k_z z}$.

$$E(k_x, k_y; z) = E(k_x, k_y; 0) \cdot e^{\pm i k_z z} \tag{3.20}$$

Here, the ± sign indicates the propagation in positive or negative z direction and $k_z = \sqrt{k^2 - (k_x + k_y)^2}$. If $(k_x + k_y)^2 < k^2$ the z component of the wavevector is real and $e^{\pm i k_z z}$ is an oscillating function, corresponding to the propagation of the field. However, if $(k_x + k_y)^2 > k^2$ the z component of the wavevector is fully imaginary and $e^{\pm i k_z z}$ becomes an exponentially decreasing function. In this case, the field contributions are non-propagating, evanescent waves. Upon propagation these parts of the field decay and the information from high-frequency spatial components is lost. Propagation acts as a low pass filter for spatial frequencies.

In a nutshell, optical microscopy suffers from the loss of spatial frequencies due to the diffraction of light in two distinct regimes. In the near field of an emitter, at distances much smaller than the optical wavelength ($r \ll \lambda$), high spatial frequencies correspond to non-propagating, evanescent waves that decay rapidly and are lost upon propagation. In the far field, at distances much larger than the wavelength ($r \gg \lambda$), additional spatial information is lost due to Fraunhofer diffraction at apertures of optical components.

One way to improve optical resolution is to capture the spatial information encoded in evanescent waves, thereby increasing the bandwidth of collected spatial frequencies. In fact, nanoscale objects brought into the near field of an emitter can couple efficiently to these evanescent components. They act as converters of localized electromagnetic energy into freely propagating light, essentially forming a bridge between the emitter's near field and the far-field radiation. Because of their functional analogy to radio-frequency antennas, these nanoscale structures are referred to as *optical antennas*. The reverse process is possible as well. They can focus incoming far-field radiation into a sub-diffraction volume via their own evanescent near-field components.

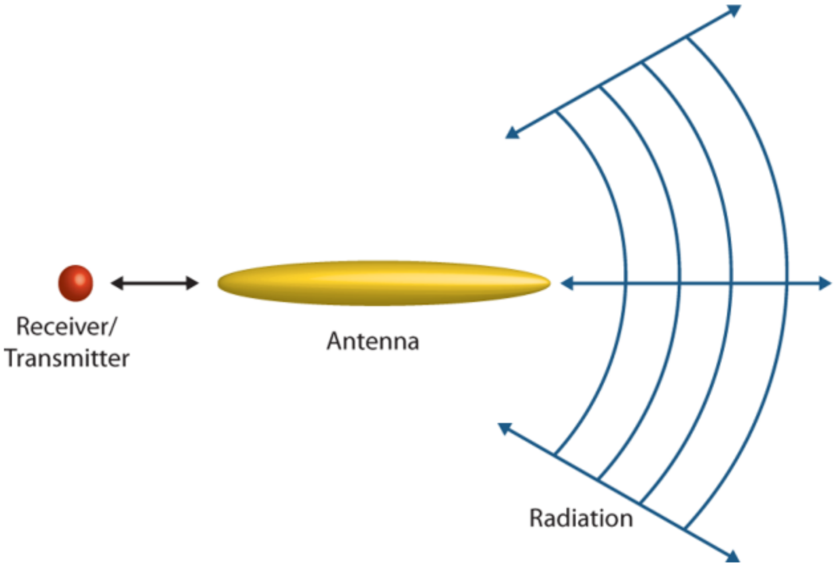

Figure 3.4.: Schematic principle of optical antennas. The optical antenna serves as a transducer between far-field radiation and localized near-field energy. It converts freely propagating electromagnetic waves from the far-field into strongly confined evanescent fields in the near-field and vice versa. Reproduced with permission from [134]. © 2017, American Chemical Society.

In the optical regime, many antennas are based on plasmonic nanostructures made from noble metals like gold or silver. When light interacts with such a nanostructure, it can excite a collective oscillation of the metal's free electrons, known as a *localized surface plasmon resonance* (LSPR). These oscillating charges create strongly localized and enhanced electromagnetic fields near the surface, particularly at sharp features like tips or edges. As a result, the local electric field can be amplified by several orders of magnitude compared to the incident field, enabling intense light-matter interactions on the nanoscale. The antenna's geometry governs its interaction with light, affecting the directionality, spectral response and scattering properties.

The dimensions of optical antennas are typically comparable to the wavelength of the interacting radiation, while the spatial resolution depends on how tightly the optical energy is confined at the apex of the antenna. Recent advances in nanoscience and nanotechnology have significantly improved fabrication capabilities. Techniques range from top-down approaches such as electrochemical etching, focused ion beam milling and electron-beam lithography, to bottom-up self-assembly methods [132].

The central idea of optical antenna technology is using antennas as both local illuminators and collectors. This dual role enhances the accessible spatial frequency bandwidth by retaining evanescent components of the optical field [130]. Due to the elevated field energy in the hot-spot of the antenna, absorption and emission rates of the sample are locally enhanced. Spatial resolution and detection sensitivity can benefit from that.

The influence of the antenna on the absorption of electromagnetic radiation can be quantified by comparing the *absorption cross section* with and without the antenna, denoted as σ_A and σ_0, respectively. This ratio indicates how effectively the antenna enhances the excitation of a nearby receiver. It reflects how efficiently the antenna concentrates incoming radiation of intensity I with a given polarization direction $\vec{n}_p$ and from a certain direction (Θ, Φ), into the receiver. It is also referred to as the *antenna aperture* A.

$$A(\Theta, \Phi, \vec{n}_p) = \frac{\sigma_A(\Theta, \Phi, \vec{n}_p)}{\sigma_0(\Theta, \Phi, \vec{n}_p)} = \frac{P_{exc}}{I(\Theta, \Phi)} = \frac{|\vec{n}_p \cdot \vec{E}|^2}{|\vec{n}_p \cdot \vec{E}_0|^2} \tag{3.21}$$

If the receiver behaves like a dipole, aligned along the vector $\vec{n}_p$, the excitation power P_{exc} is proportional to $|\vec{n_p} \cdot \mathbf{E}|^2$, where $\mathbf{E}$ is the local electric field at the position of the receiver in the presence of the antenna. Similarly, the incoming intensity I can be expressed by the given polarization direction and the local field without antenna E_0. This means that the provided absorption enhancement crucially depends on the direction and polarization of the incoming field. The more strongly the antenna modifies and enhances the field component along the dipole direction, the more efficiently it drives absorption. By assuming an identical direction of the enhanced field relative to the non-enhanced field, the *local field enhancement factor* f can be used to express the absorption enhancement.

$$f = \frac{E}{E_0} \tag{3.22}$$

In this case, the absorption cross section simplifies to:

$$\sigma = f^2\sigma_0. \tag{3.23}$$

Furthermore, the antenna radiation efficiency ϵ_{rad} quantifies the total radiated power $P_{\mathrm{rad}} = \int_0^{\pi}\int_0^{2\pi} p(\Theta,\Phi)d\Theta d\Phi$, with the angular power density $p(\Theta,\Phi)$, relative to the total dissipated power P.

$$\epsilon_{\mathrm{rad}} = \frac{P_{\mathrm{rad}}}{P} = \frac{P_{\mathrm{rad}}}{P_{\mathrm{rad}} + P_{\mathrm{loss}}} \tag{3.24}$$

In Equation 3.24, P_{loss} is the power dissipated into heat and other loss channels. The *antenna directivity* measures the ratio of the radiation that is pointed by the antenna to a certain direction.

$$D(\Theta,\Phi) = \frac{4\pi}{P_{\mathrm{rad}}} p(\Theta,\Phi) \tag{3.25}$$

Together with ϵ_{rad} it forms the *antenna gain* G and describes the directivity normalized to the total dissipated power.

$$G(\Theta,\Phi) = \epsilon_{\mathrm{rad}} D(\Theta,\Phi) = \frac{P_{\mathrm{rad}}}{P_{\mathrm{rad}} + P_{\mathrm{loss}}} \frac{4\pi}{P_{\mathrm{rad}}} p(\Theta,\Phi) \tag{3.26}$$

According to the reciprocity theorem, i.e. the principle that in a linear, time-invariant and reciprocal medium the response at a point A due to a source at point B is equal to the response at point B due to the same source placed at point A, the excitation rate k_{exc} of the emitter can be connected to it's radiation rate k_{rad} [133].

$$\frac{k_{\mathrm{exc},\Theta}}{k^0_{\mathrm{exc},\Theta}} = \frac{k_{\mathrm{rad},\Theta}}{k^0_{\mathrm{rad},\Theta}} \frac{D_\Theta(\Theta,\Phi)}{D^0_\Theta(\Theta,\Phi)} \tag{3.27}$$

In Equation 3.27, the superscript 0 indicates quantities in the absence of the antenna and the subscript Θ the polarization direction. An analogous expression can be formulated for the orthogonal polarization direction Φ. Hence, the antenna induced enhancement of the excitation rate is proportional to the enhancement of the radiative rate but the proportionality depend on the direction.

Assuming a parallel directivity for enhanced and non-enhanced fields, the radiative rate enhancement becomes proportional to the square of the field enhancement factor.

$$\frac{k_{\mathrm{rad}}}{k^0_{\mathrm{rad}}} = \frac{k_{\mathrm{exc}}}{k^0_{\mathrm{exc}}} \propto \left|\frac{E}{E_0}\right|^2 = f^2 \tag{3.28}$$

3.3. Experimental description

3.3.1. Preparation of (6,5) SWCNTs

The sample preparation methods described below, aiming to produce high-quality samples of individual (6,5) SWCNTs on microscope cover slips, were carried out by Frank Schäfer from the research group of Prof. Achim Hartschuh at the LMU Munich. Care was taken to follow well-established protocols and to compare all methods carefully with relevant literature throughout the preparation process.

For these experiments, SWCNTs were purchased from Sigma-Aldrich (CoMoCat (Cobalt-Molybdenum Catalysis) SG65, Product No. 704148), a commercial source known for its relatively high proportion of semiconducting nanotubes, especially those with (6,5) chirality. Since the raw SWCNT powder is highly hydrophobic and tends to form bundles in aqueous solutions, an initial dispersion step was necessary. A 1 mg/mL suspension was prepared in 1% sodium deoxycholate (DOC, BioXtra, Sigma-Aldrich), a bile salt surfactant commonly used to stabilize carbon nanotubes in aqueous solutions. The mixture was sonicated using a tip sonicator (Bandelin Sonoplus HD2200/UW 2200) for 8 minutes at 17–18% power, while keeping the sample under ice cooling to prevent overheating.

To isolate and enrich the (6,5) nanotubes from the mixed starting material, a two-step aqueous two-phase separation (ATPS) process was used, following a protocol adapted from [135]. This technique takes advantage of subtle differences in how different SWCNT chiralities interact with surfactants to separate them into two immiscible aqueous phases. The separation was carried out using polyethylene glycol (PEG-6000, Alfa Aesar) and Dextran-70 (Tokyo Chemical Industry) as the phase-forming polymers. A mixture of sodium cholate (SC), sodium dodecyl sulfate (SDS) and sodium chloride was added to fine-tune the separation conditions. Afterward, the enriched fractions were concentrated and cleaned using ultracentrifugation (Eppendorf 5430) with 100 kDa Amicon filter units (Millipore), which helped remove excess surfactants and unbound polymers.

In addition to these surfactant-dispersed samples a second type of (6,5)-enriched SWCNT sample was prepared using DNA-assisted dispersion. In this method, single-stranded DNA wraps around the nanotubes via non-covalent interactions, helping to both stabilize them in solution and selectively target certain chiralities. DNA wrapping improves solubility and dispersion of SWCNTs in water, while preserving the SWCNT's intrinsic electrical and optical properties. Following the approach described in [136], purified oligonucleotides with the sequence `CCG CCG CC` (Metabion International AG) were used. This particular sequence has been reported to achieve up to 11% selectivity for the (6,5) chirality. Notably, these DNA-wrapped samples were prepared without the use of surfactants like SDS or DOC, minimizing concerns about residual detergents interfering with downstream applications.

The SWCNT dispersion was deposited onto a 80 μm-thick borosilicate microscope cover slip (VWR Cover Slips, Thickness 0) via spin-coating. The substrate was subsequently dried for one minute under ambient conditions and rinsed with Milli-Q water to reduce the density and remove residual surfactants.

3.3.2. Time-resolved detection with APDs and TCSPC

For time-resolved measurements on timescales of $\sim 10\ ps$ up to μs, avalanche photodiodes (APDs) can be used in combination with Time-correlated single photon counting (TCSPC) electronics.

APDs are highly sensitive detectors capable of registering single photons by applying a high voltage to the photoelectric material. When a photon enters the device, it excites a single free charge carrier in the semiconducting material, which is accelerated by the high voltage and creates an avalanche of additional charge carriers upon collisions, resulting in a fast and detectable electrical pulse. However, random noise from thermally generated electrons (dark counts) has to be accepted, as well a specific dead time after each detection event during which no additional photons can be registered. Beyond a saturation threshold of detectable events per time, a nonlinear response occurs at high count rates. In the experimental usage of this work the photon detection rate of APDs is kept below 1 MHz, to avoid this saturation effect.

In TCSPC, each detected photon event is time-stamped relative to a reference signal, typically derived from the laser's repetition rate. The electronics operate by initiating a voltage ramp upon photon detection at the APD and stopping it at the arrival of the next laser pulse. The resulting voltage, proportional to the time difference, is then digitized and accumulated into a histogram.

The accuracy of such measurements depends on the instrument response function (IRF), which describes the minimal temporal resolution, i.e. the temporal broadening of an δ-peak signal, introduced by the detector and electronics. The IRF can vary slightly with intensity and wavelength, as the photon absorption can take place at varying depths of the material and charge carriers from outside the avalanche region result in uncorrelated events. For the time-correlated experiments in Section 3.4 the IRF was determined to $\sim 30\ ps$ (FWHM) by using TCSPC to measure the temporal width of the excitation laser pulse.

3.3.3. Tip-enhanced near-field optical microscope setup

For the tip-enhanced time-correlated PL experiments in this section an inverted confocal microscope was combined with a sharp gold nano-tip in close distance to the sample. The feedback mechanism for the z-position control of the antenna was based on the detection of the resonance frequency of the lateral oscillation of a tuning fork, on which the antenna was glued to, highly sensitive to the shear-force applied by short-ranged interactions with the sample. A detailed description of the feedback mechanism can be found in [130, 131, 137]. For excitation, a tunable pulsed fiber laser, operating at a repetition rate of 40 MHz was employed to achieve resonant excitation of the E_{22} transition of semiconducting (6,5) SWCNTs with 570 nm laser pulses. The laser is based on spectral broadening of a infrared

1560 nm fs pulse in a photonic-crystal-fiber and subsequent frequency doubling of selected spectral components. To avoid multiple sequential excitations in the SWCNT within the same pulse, the laser pulse duration of 1 ps was substantially shorter than the corresponding exciton lifetime of 10-50 ps [138]. The SWCNTs sample, deposited on top of thin borosilicate glass coverslip (80 μm), was placed in the focus of a high NA microscope objective (Nikon CFI apochromat TIRF NA=1.49 60x). The setup is illustrated in Figure 3.5.

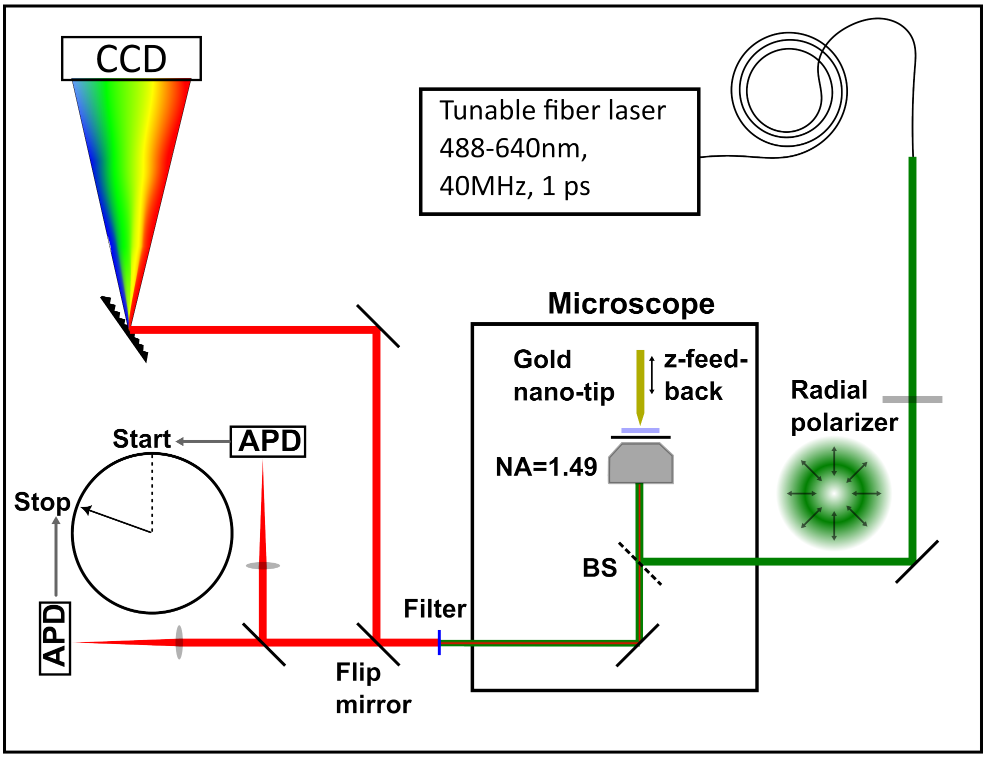

Figure 3.5.: Schematic overview of the tip-enhanced PL setup with HBT configuration. The (6,5) SWCNT sample is excited by a tunable ps fiber laser, operating at a wavelength of 570 nm and converted into a radially polarized donut mode. A gold nano-tip is brought into close distance to the sample controlled by a shear-force based tuning fork feedback. After spectral filtering the tip-enhanced PL from the E_{11} transition of the SWCNTs at 980 nm is sent to a HBT-setup of two time-correlated single photon detectors.

The linear polarized TEM$_{00}$ mode of the fiber laser doesn't have any vertical polarization components in the focus. In order to efficiently drive LSPRs in the gold tip, vertical out-of-plane field components in the focus were generated by conversion of the transversal laser mode into a radially polarized donut mode. For this purpose, a Liquid Crystal (LC) polarization converter (ARCoptix) was employed, operating at wavelengths between 400 nm and 1700 nm. The key component is a radial polarization converter based on a twisted nematic LC cell, as described in [139]. The alignment of the LC molecules is defined by surface rubbing with a linearly rubbed entrance plate in a fixed direction and a circularly rubbed exit plate. This creates a spatially varying twist in the LC orientation, such that the total twist angle depends on the angular position with respect to the axis of the cell. The wavelength of the light must be small compared to the twist and thickness of the LC cell so that the polarization can track the twist gradually.

$$d \cdot \Delta n \gg \lambda \tag{3.29}$$

In Equation 3.29, d is the thickness of the cell, Δn is the difference between extraordinary and ordinary refractive indices and λ is the wavelength of the particular light. When a linearly polarized light beam enters the cell under polarization-guiding conditions, its polarization follows the local twist of the LC molecules. As a result, the output polarization is not uniform but varies across the beam profile, enabling the generation of spatially structured polarization states such as radial or azimuthal polarization.

Figure 3.6 illustrates the polarization rotation procedure. If the incident light is polarized parallel to the cell axis, azimuthally polarized light is achieved. Radially polarized light is achieved for an incident polarization perpendicular to the cell axis. Subsequently, a spatial filter after the polarization converter is used to clean up residual inhomogenities in the intensity profile.

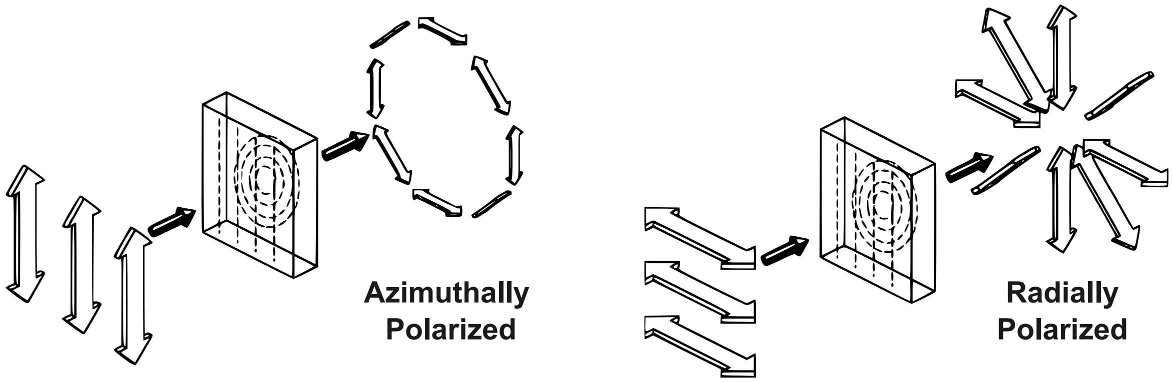

Figure 3.6.: Schematic illustration of the operating principle of a radial polarization converter. Linear polarized light enters a twisted nematic liquid crystal cell, whose entrance and exit plates are treated with linear and circular rubbing, respectively. The local polarization follows the twisted LC molecules, resulting in *Left:* azimuthally polarized light for parallel incident polarization and *Right:* radially polarized light for perpendicular incident polarization. Adapted with permission from [139]. © 1996, Optical Society of America.

The generated radiation was collected by the same high NA objective in epi-detection configuration, transmitted through the beamsplitter and reflected out of the microscope body. PL radiation at 980 nm from the first excitonic resonance (E_{11}) was detected after spectral filtering of the fundamental laser radiation, using an optical longpass filter (LP633nm), by two APD single photon detectors in a Hanbury-Brown-Twiss (HBT) configuration.
In a HBT setup, the second order intensity correlation function $g^{(2)}(\tau)$ is measured by detecting coincident events between two single-photon detectors placed at the outputs of a 50:50 beam splitter, using TCSPC electronics, as illustrated in Figure 3.1. This allows to assess the statistical properties of the light, depending on the time delay. In the experiment, a photon detection event at APD 1 serves as the start signal for time measurement, while a subsequent detection at APD 2 provides the stop signal. To ensure that the TCSPC electronics correctly registers the time interval, which requires the start signal to arrive before the stop, a delay to the stop channel is inserted via unmatched cable length. This introduces a well-defined time offset, guaranteeing the correct order of signal arrival regardless of the actual detection sequence. The distribution of measured time intervals is then used to construct the $g^{(2)}(\tau)$ histogram, presented in Figure 3.8 of Section 3.4.

3.4. Experimental antenna-controlled antibunching in SWCNTs

In this section the tip-enhanced near-field optical microscopy (TENOM) setup, introduced in Section 3.3.3, was employed to investigate the influence of an optical antenna on the photon statistics of the PL from a single (6,5) SWCNT, emitted from the lowest exciton state E_{11}. Nanotubes were deposited on a borosilicate microscope cover slip, as described in Section 3.3.1, and placed in the focus of the NA 1.49 objective. The sample was excited by a tunable ps fiber laser, tuned to an excitation wavelength of 570 nm, resonant with the E_{22} exciton transition of the (6,5) nanotubes. Single (6,5) SWCNT were identified by spectral analysis, retrieving the characteristic E_{11} PL emission peak at $\sim 980\ nm$, and confocal microscopy as well as tip-enhanced near-field microscopy, as illustrated by the example in Figure 3.7.

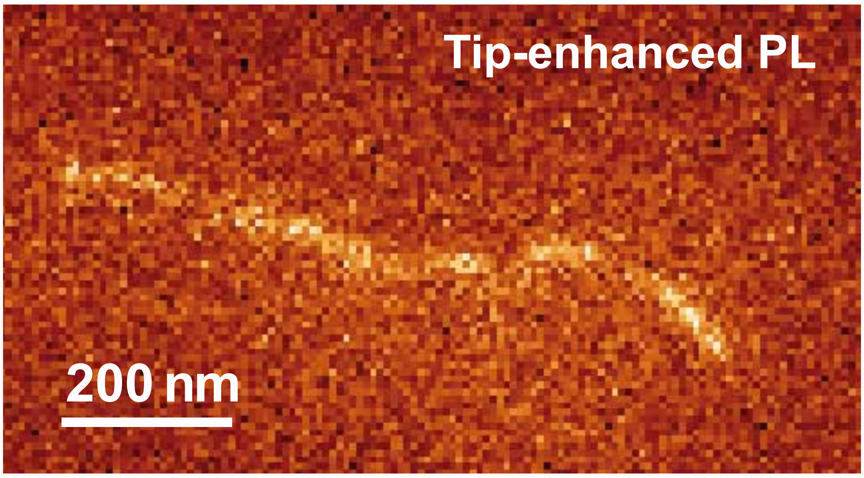

Figure 3.7.: Experimental antenna-enhanced PL microscope image of a (6,5) SWCNT. The PL intensity, measured at low excitation power for photon-correlation experiments, is enhanced in the near-field of the metal tip. The width of the enhanced PL signal indicates an optical near-field confinement of approximately $d \approx 20$ nm. Adapted from [99] with permission from the Royal Society of Chemistry..

Subsequently, the second-order correlation function $g^{(2)}(\tau)$ of the nanotube's PL emission signal was determined using two APDs in a Hanbury-Brown Twiss configuration, as introduced in Section 3.3.3. The sharp metal tip nano-antenna was constantly placed in the focus of the laser beam, closly above the nanotube. Thermal drift of the tip position was compensated manually by restoring the tip-enhanced PL count rate. Upon photo-excitation of the SWCNT by 1 ps pulses with a repetition rate of 40 MHz (25 ns), the number of correlated photon-detection events of the emitted PL was recorded with respect to the delay time between the events. The 1 ps pulse length ensures that no multiple sequential excitations, with lifetimes of 10-50 ps, occurred within the same laser pulse [138].

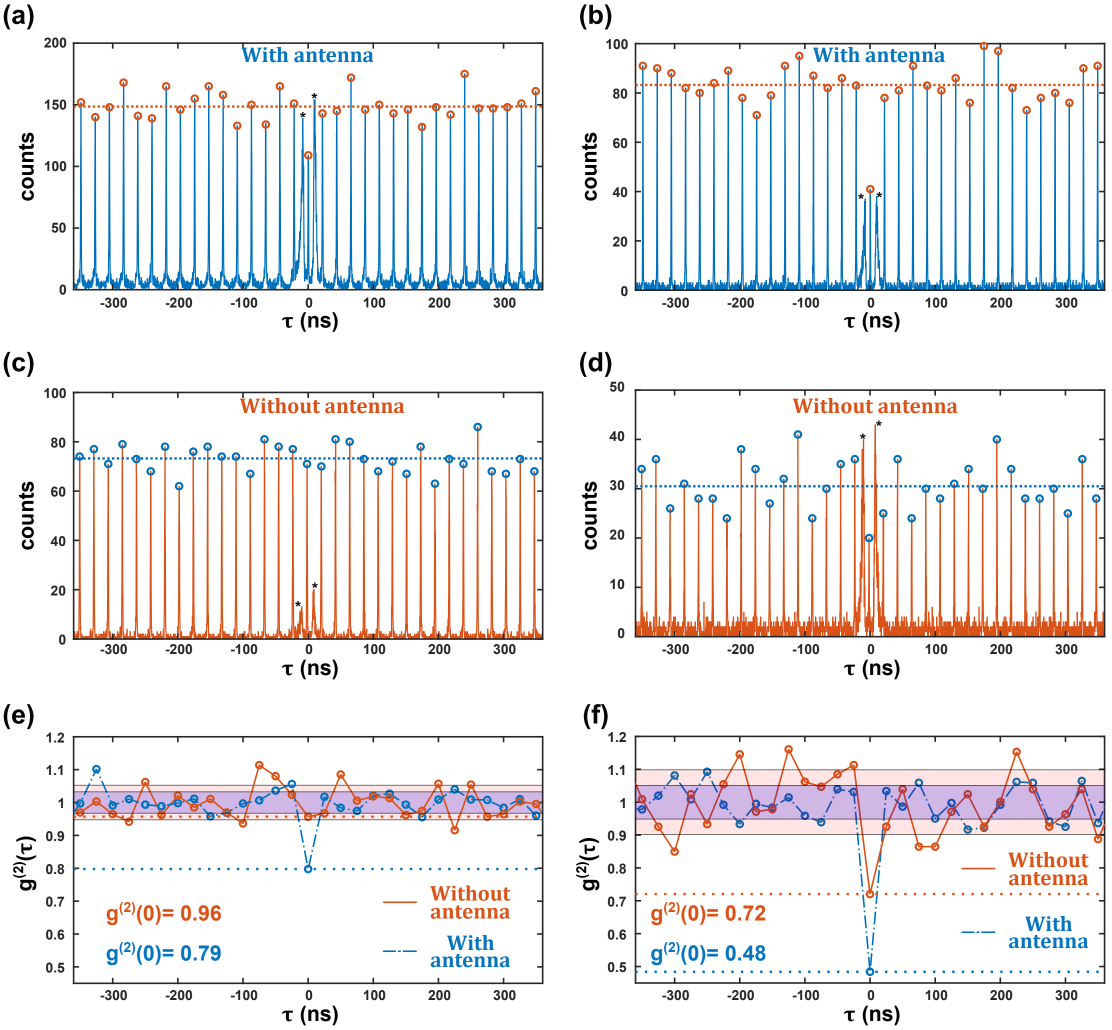

Figure 3.8.: Time-correlated photon counts and $g^{(2)}(\tau)$ data for two different SWCNTs. The data shows antenna-controlled antibunching at room temperature in the PL of two individual (6,5) SWCNTs. (a) and (b) present recorded correlated photon detection events in the HBT-setup as a histogram with respect to the delay time τ in the presence of an optical antenna. The peaks marked by the $*$ are artifacts arising from the combination of two APD photo-detectors. (c) and (d) presents the same without the optical antenna. (e) and (f) shows the corresponding normalized second-order correlation function derived from the data above. $g^{(2)}(0)$ is clearly reduced through the effect of the antenna. Adapted from [99] with permission from the Royal Society of Chemistry.

In Figure 3.8, the recorded data for two exemplary SWCNTs is presented. The panels (a) and (b) show the recorded data with the optical antenna, while panels (b) and (d) show the results for a confocal measurement without the optical antenna at the same nanotube position. Separated count number peaks with an equidistant spacing of 25 ns, corresponding to the laser's repetition rate, can be observed. In both cases the peak height at zero time delay is clearly reduced by the optical antenna ((a) and (b)) compared to the measurement without the antenna ((c) and (d)). The dotted horizontal line represents the average number of registered correlated events at all other times.

The peak at zero time delay is flanked by two broader peaks, not matching the regular time spacing of 25 ns. These are measurement artifacts attributed to afterpulsing of the APDs, caused by trapping of charges during the avalance process. The following photon emission by relaxation of these charges can be detected by the second APD resulting in mistaken correlated photon emission events [140].

To extract the second-order correlation function $g^{(2)}(\tau)$ from this data, the total number of correlated events per delay-time interval was determined by integrating over a time window of $\pm 1.5\ ns$ around each individual peak. The normalized $g^{(2)}(\tau)$ function was then obtained by dividing these integrated counts by the average of all peaks, excluding the one at zero time delay.

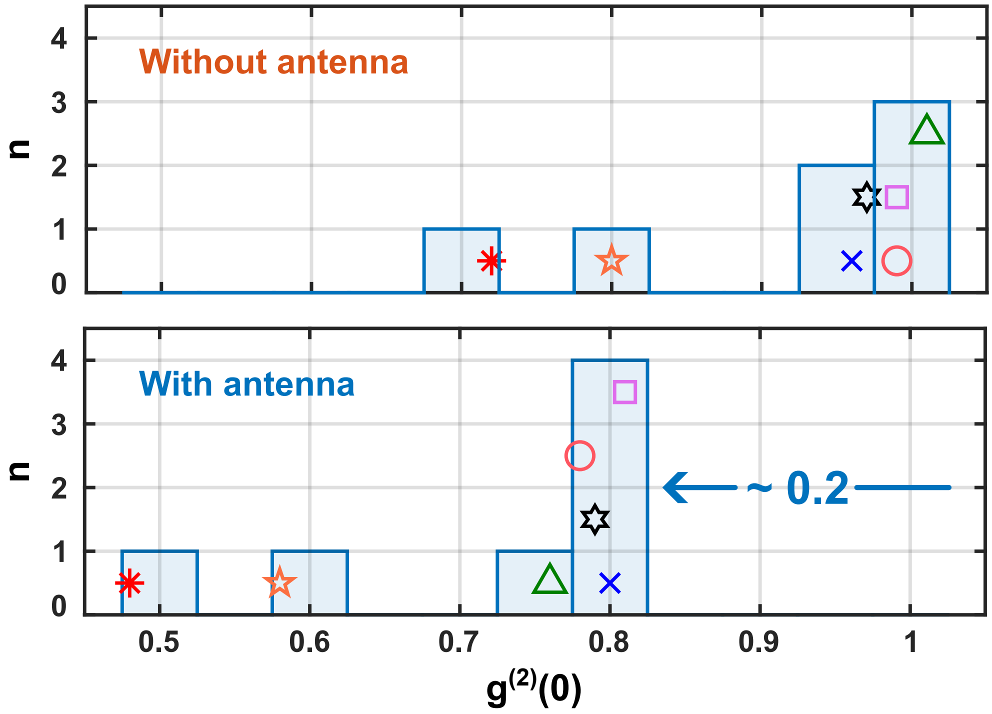

Figure 3.9.: Histogram of $g^{(2)}(0)$ values with and without an optical antenna for 7 individual (6,5) SWCNTs. Different symbols mark the $g^{(2)}(0)$ values for the same nanotube with and without the antenna in the lower and the upper part, respectively. The effect of the antenna is a reduction of $g^{(2)}(0)$ by approximately 0.2. Adapted from [99] with permission from the Royal Society of Chemistry.

The results for both exemplary nanotubes are presented in Figure 3.8 (e) and (f), respectively. Antenna-controlled antibunching is clearly observed as a tip-induced reduction of $g^{(2)}(0)$ by 0.17 from 0.96 to 0.79 in (e) and by 0.24 from 0.72 to 0.48 in (f). The red and blue shaded areas represent the standard deviation of $g^{(2)}(\tau)$ values, excluding $g^{(2)}(0)$. Comparable antenna-induced reductions in $g^{(2)}(0)$ of approximately 0.2 were consistently observed for additional (6,5) SWCNTs, as presented in the histogram in Figure 3.9. However, even in the absence of a near-field probe, SWCNTs were observed to exhibit varying degrees of antibunching due to an interplay of exciton diffusion, EEA and natural localization effects [5, 111, 117]. This is consistent with the confocal measurements presented in the upper part of Figure 3.9, where $g^{(2)}(0)$ values scatter between 0.7 and 1. The optical antenna further enhances the degree of antibunching by about 0.2.

3.5. Numerical approach - exciton diffusion and decay in 1D

To further explore the potential of controlling the degree of antibunching in 1D emitters through the near-field interaction with an antenna, Monte-Carlo simulations of exciton generation and decay together with a random walk in 1D were designed and performed by Dr. Richard Ciesielski from the research group of Prof. Achim Hartschuh at the LMU Munich.

A one-dimensional nanostructure, representing a single (6,5) SWCNT, is discretized into 256 spatial steps of 1.1 nm, corresponding approximately to the exciton Bohr radius in these systems, resulting in a total structure length of 281.6 nm [141].
An initial exciton population is created randomly along the nanotube, with the spatial probability weighted according to the local excitation intensity profile, which is a superposition of the confocal spot and the localized near-field contribution, as illustrated in Figure 3.10 (a). The local near-field enhancement is modeled as a scalar field enhancement factor $f = E/E_0$, neglecting the vectorial character of the fields for simplicity [132]. The average number of excitons $N_x = \langle n_x \rangle$ created per time step represents the excitation power, whereas the actual number of excitons n_x follows the Poisson distribution,

$$p(n_x)_{N_x} = \frac{(N_x)^{n_x}}{n_x!} e^{-N_x}. \tag{3.30}$$

A schematic illustration of this exciton creation process is shown in Figure 3.10 (a).

At each time step, excitons perform a random walk along the 1D lattice, modeling exciton diffusion, with the probability for a step to the right and to the left, P_{right} and P_{left}, respectively.

$$P_{\text{right}} = 0.5 = 1 - P_{\text{left}}. \tag{3.31}$$

A time step Δt is determined such that the exciton moves by one spatial unit ($1.1\ nm$) per time step, based on the lifetime τ and diffusion length L_D. The lifetime τ is the inverse of the sum of all decay rates k.

$$\tau = \frac{1}{k_{\text{rad}} + k_{\text{non-rad}}} \tag{3.32}$$

The diffusion of excitons after pulsed excitation for a single Monte-Carlo computation is shown in Figure 3.10 (b) as an example. For every time step, each exciton has a probability to decay either radiatively or non-radiatively, with the rates k_{rad} and $k_{\text{non-rad}}$, respectively.

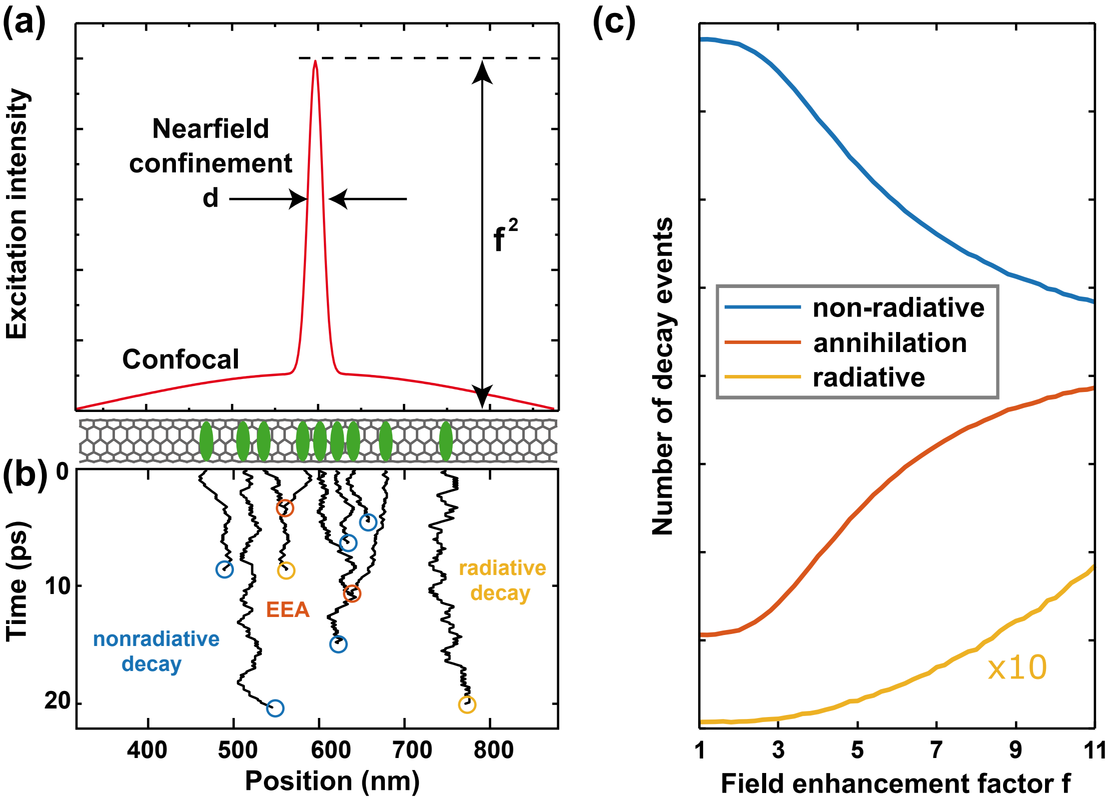

Figure 3.10.: Schematic illustration of the 1D Monte Carlo simulation. (a) shows the excitation intensity profile, composed of the diffraction-limited confocal spot and the additional locally enhanced near-field contribution from the antenna, represented by the field enhancement factor $f = E/E_0$. The SWCNT is indicated at the bottom. Excitons (green ellipses) are generated randomly along the nanotube's axis, with their positioning weighted according to the combined intensity profile. In (b) diffusion in 1D is illustrated, as excitons perform a one-dimensional random walk with one spatial step per time step. If two excitons encounter, EEA occurs with only one exciton remaining. Otherwise, excitons decay radiatively or non-radiatively, governed by their respective decay rates. (c) shows the development of the relative number of decay events with respect to the field enhancement. At low field enhancement factors, the non-radiative decay dominates the relaxation dynamics. With increasing field enhancement, both radiative decay and, in particular, EEA become more prominent, at the expense of the non-radiative process. Adapted from [99] with permission from the Royal Society of Chemistry.

At the end of the nanotube, excitons get quenched. Upon the encounter of two excitons at the same spatial position, they undergo exciton-exciton annihilation (EEA), leaving only one remaining exciton behind [16]. The ratio of the radiative decay rate relative to the total decay rate is determined by the PL quantum yield (QY) in the absence of the antenna.

$$QY = \frac{k_{\mathrm{rad}}}{k_{\mathrm{rad}} + k_{\mathrm{non-rad}}} \tag{3.33}$$

In the presence of the antenna's near-field the radiative decay rate is locally enhanced, scaling with the field enhancement factor f, according to:

$$k_{\mathrm{rad}}(x) = \frac{QY}{\tau} \cdot \left[1 + (f^2 - 1) \cdot \exp\left(-4 \cdot \log(2) \cdot \frac{x^2}{d^2}\right)\right], \tag{3.34}$$

where d denotes the spatial near-field confinement of the antenna.

Each Monte Carlo run simulates the full decay process of the initial population and records the number of radiative and non-radiative emission events, together with the number of EEA events, per excitation cycle. For the next run, a new initial exciton population is generated and the process repeats. For each parameter set, the simulation was carried out approximately 10^{12} times in parallel. From the statistics, the second-order intensity correlation function $g^{(2)}(0)$ was calculated as [111]:

$$g^{(2)}(0) = \frac{\langle n(n-1)\rangle}{\langle n\rangle^2} = \frac{\langle n^2\rangle - \langle n\rangle}{\langle n\rangle^2}, \tag{3.35}$$

where n is the number of radiative emission events per pulse or per simulation cycle and $\langle .. \rangle$ denotes the average.

The relative contributions of the exciton decay channels are strongly affected by the local field enhancement. As shown in Figure 3.10(c), at low field enhancement factors, the non-radiative decay dominates the relaxation dynamics. With increasing field enhancement, both radiative decay and, in particular, EEA become more prominent, at the expense of the non-radiative process.

In the following, the simulation is used to investigate how certain parameters influence $g^{(2)}(0)$. The analysis considers the effects of the field enhancement factor f, the average number of excitons per pulse N, the quantum yield QY, the near-field confinement d, the exciton lifetime τ and the diffusion length L_D.
Figure 3.11 (a) presents the simulation results for $g^{(2)}(0)$ as a function of the field enhancement factor f and for selected excitation intensities, expressed by the average number of created excitons. The remaining parameters are kept constant, with values of $QY = 0.001$, $\tau = 50\ ps$, $L_D = 300nm$ and $d = 10\ nm$, which are realistic for (6,5) SWCNTs and electrochemically etched gold tips [132, 142]. $g^{(2)}(0)$ decreases significantly with increasing

field enhancement and drops below 0.5 at values of $f > 6$ for all simulated average exciton numbers. In general, the trend is consistent for all simulated N, with lower values of $g^{(2)}(0)$ achieved at lower excitation intensities. Antibunching is enhanced by the antenna's field enhancement due to the locally increased likelihood of both, EEA and radiative recombination, as seen in Figure 3.10(c). More specifically, the antenna increases the local exciton generation probability within the near-field confinement region, where both EEA and the probability for PL emission are raised. At high f, the reduction of $g^{(2)}(0)$ saturates around 0.4, for the given parameter set. This can be attributed to the remaining non-zero probability that excitons leave the near-field interaction region, effectively escaping the influence of the antenna without undergoing annihilation or radiative recombination.
Following, the effect of the near-field confinement is investigated and presented in Figure 3.11 (b) for selected enhancement factors. In general, lowest values of $g^{(2)}(0)$ are achieved for a tight field localization and high enhancement factors. A potential reduction by the antenna down to values below 0.3 is predicted. Interestingly, at moderate field enhancement, a counterintuitive increase of $g^{(2)}(0)$ is predicted for decreasing d. This can be explained by considering the effect of smaller d on the excitation intensity profile, presented in Figure 3.10 (a). As f is kept constant, a decrease in d results in a unphysical reduction of the contribution of the near-field to the excitation profile. Effectively, the reduction of the nearfield confinement leads to an relative increase of the excition generation probability in the diffraction limited region. Alltough the trend suggests potentially even lower values of $g^{(2)}(0)$, the simulation is limited to $d \geq 5$. Achieving such tight confinement would require tip-sample distances in the same range, where quenching effects at the metal antenna become significant [143].

The influence of the diffusion length on $g^{(2)}(0)$ is presented in Figure 3.11 (c) for selected enhancement factors. The results indicate that high exciton mobility is beneficial for efficient antenna-controlled antibunching. This is because EEA becomes more probable for mobile or long-living excitons.

The extreme case of a tube length of 10 μm, strong field enhancement ($f = 20$), long exciton lifetimes ($\tau = 350\ ps$) and diffusion length up to $10^5\ nm$ is simulated and shown in Figure 3.11 (d). At these parameters, $g^{(2)}(0)$ can be reduced by the antenna down to 0.1, which highlights the potential for the efficient control of SPE in 1D emitters. However, at this parameter set, $g^{(2)}(0)$ is already strongly reduces even in the confocal case without the antenna.

It must be noted that the field enhancement factor can differ for excitation and detection, as it typically depends on the optical wavelength. When the energy difference between excitation and emission is large, it is possible that only one of the two processes is resonantly enhanced by the optical antenna. In that scenario, the antenna enhances either the exciton creation through light absorption or the rate of radiative emission. Figure 3.12 compares these two scenarios. The blue curve represents the double-resonant case, where both excitation and detection are enhanced by the antenna. The red curve represents the case

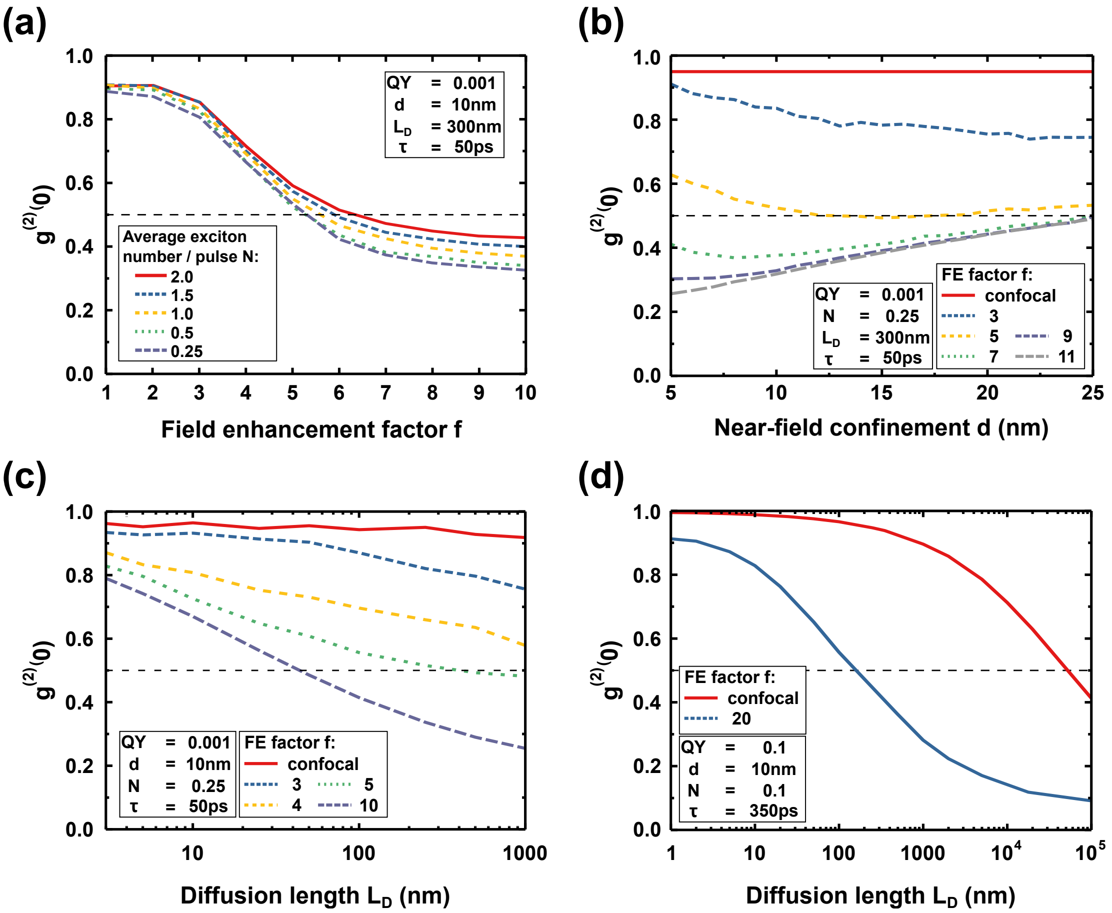

Figure 3.11.: Monte-Carlo simulation results for antenna control of $g^{(2)}(0)$. (a) Simulated dependence of photon antibunching on the field enhancement factor f for selected average numbers of created excitons. (b) Impact of the near-field confinement d for selected values of f, showing optimal antibunching at tight spatial confinement and high f. (c) Role of the exciton diffusion length L_D. Increased exciton mobility enhances antenna-controlled antibunching. (d) Under conditions of strong field enhancement, long exciton lifetimes and extended diffusion length, the antenna reduces $g^{(2)}(0)$ to vales as low as 0.1, highlighting its potential for efficient control of SPE in 1D emitters. Adapted from [99] with permission from the Royal Society of Chemistry.

where only the excitation wavelength is resonant, while the radiative rate enhancement is neglected and $f = 1$ is set in Equation 3.34. While in the later case the general trends with respect to field enhancement, near-field confinement and exciton diffusion length remain consistent with the discussion above regarding Figure 3.11, the absolute decrease of $g^{(2)}(0)$ is substantially weaker. Specifically, the radiative rate enhancement in the double resonance case leads to an additional decrease in $g^{(2)}(0)$ by approximately 0.2 - 0.3 on average, compared to the case with only excitation enhancement.

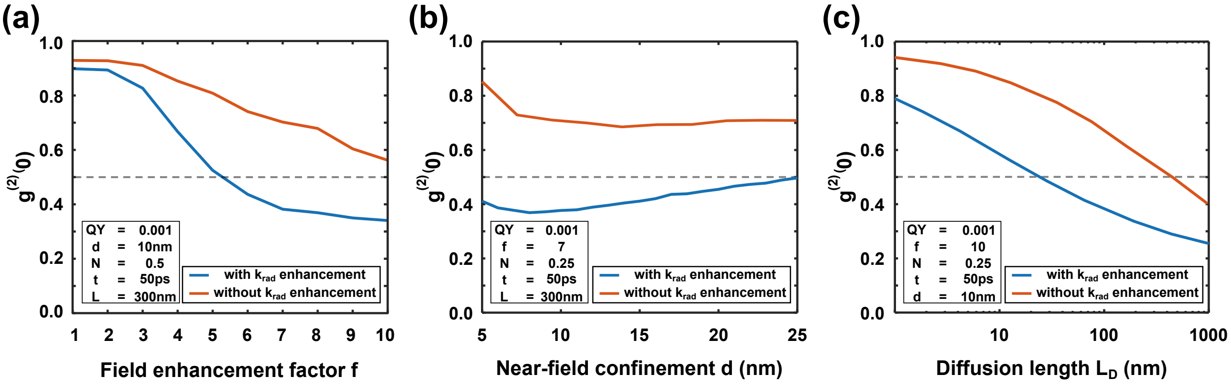

Figure 3.12.: Monte-Carlo simulation results for the influence of radiative rate enhancement on the antenna control of $g^{(2)}(0)$. The double-resonant case (blue) is compared to the case where only the excitation is enhanced by the antenna (red), for (a) varying field enhancement factor f, (b) varying field confinement d and (c) varying diffusion length L_D. Adding the enhancement of the radiative rate significantly reduces $g^{(2)}(0)$ by 0.2 - 0.3 on average. Adapted from [99] with permission from the Royal Society of Chemistry.

The numeric Monte-Carlo model confirms that the antenna can reduce $g^{(2)}(0)$ in one-dimensional emitters and turn the emission statistic towards that of a SPS. As key mechanisms, control over the number of excitons through enhanced EEA and the radiative recombination rate were identified. The experimentally observed reduction in $g^{(2)}(0)$ by the antenna of about 0.2 can be attributed to a field enhancement factor of 3 - 4 which is realistic for the electrochemically etched gold tips, used in the experiments. These results show that optical antennas can actively steer emission statistics toward ideal single-photon behavior through the control of spatial distribution and the radiative decay dynamics.

3.6. Conclusion and Outlook

In conclusion, effective control over the photon emission statistic of one-dimensional emitters has been demonstrated using an optical antenna as a near-field probe. Experimentally, the second-order correlation function at zero time delay, $g^{(2)}(0)$, in the PL of seven (6,5) SWCNTs was reduced by approximately 0.2 through the antenna interaction. This serves as a proof of concept experiment for antenna-controlled antibunching in quasi one-dimensional emitter.

Numerical simulations were used to investigate the influence of various parameters on the degree of antibunching. The results reveal that, under realistic conditions, a strong and spatially confined optical field can significantly enhance antibunching behavior in 1D, potentially reducing $g^{(2)}(0)$ from around 0.9 to below 0.3. High field enhancement, tight near-field confinement and long exciton diffusion lengths were identified as key factors favoring the emission of single photons. In extreme cases, with high field enhancement and optimized material parameters, values as low as $g^{(2)}(0) = 0.1$ are theoretically achievable. This antenna-control mechanism crucially relies on the locally enhanced radiative recombination rate, which increases PL emission from the small interaction region where excitons are favorably created and EEA of multiple excitons becomes highly probable. The experimentally observed reduction of $g^{(2)}(0)$ by approximately 0.2 aligns well with theoretical predictions, if a realistic field enhancement factor of 3 - 4 is assumed. Although this reduction by ~ 0.2 is insufficient for applications demanding high purity SPE, the simulation results indicates potential to further reduce $g^{(2)}(0)$.

While the focus of this work was on SWCNTs, the concept is expected to be transferable to other 1D systems with efficient EEA, such as inorganic semiconductor nanowires [144–146]. However, its applicability to 2D materials is expected to be more limited, as excitons in these systems can more easily diffuse out of the near-field interaction region due to the larger phase space, resulting in reduced EEA efficiency. For these higher-dimensional systems, additional perturbations of the energetic landscape, like strain or chemical modifications, might be necessary to localize excitons and achieve comparable antibunching effects.

The use of optical antennas to enhance antibunching offers several advantages. In contrast to inducing trap-states through chemical doping or mechanical strain, the antenna-control method is non-invasive and reversible, as it does not alter the electronic state energies of the emitter. Furthermore, the position of the antenna, and thus the location of the SPS, can be precisely controlled with nanometer accuracy, enabling spatial tuning of the emission behavior. The same concept can also be implemented with static nanoantenna designs, such as bow-tie structures, offering the potential of new nanophotonic single-photon devices [147].

4. Phase Control of the Nonlinear Responses in Monolayer TMDs

"The following chapter is based on the publication: Ultrafast Phase-Control of the Nonlinear Optical Response of 2D Semiconductors" by Lange et al., published in ACS Photonics (2024) [73]. Parts of the text and figures are reproduced.

The strong many-body interactions in TMDs make them an ideal platform for exploring fundamental condensed matter phenomena and quantum effects at the nanoscale. Additionally, the large oscillator strength associated with these excitonic resonances leads to enhanced nonlinear optical effects, making TMDs particularly promising for applications in ultrafast optics and photonics. Nonlinear optical processes such as SHG, SFG and FWM are greatly enhanced when the generated nonlinear optical field is resonant with excitonic transitions [1–3, 64, 65]. Furthermore, the possibility of controlling the excitonic response and population via coherent control techniques opens up exciting opportunities for manipulating the nonlinear optical response and for studying condensed matter physics in 2D systems. Under resonance conditions, light-matter interaction in monolayer WSe_2 was shown to become strong enough to drive Rabi flopping in the SHG spectra at cryogenic temperatures [32]. At similar conditions, the influence of excitonic resonances on the temporal dynamics of SHG and FWM intensities was demonstrated, revealing the potential for controlling the excited state population through pulse amplitude and pulse-to-pulse time delay [148]. Modern possibilities in pulse shaping, i.e. tailoring broadband optical pulses by manipulating their spectral amplitude and phase, enable the optimization of quantum pathway interference in multiphoton excitation processes, as well as the control of quantum state interference through the formation of coherent superpositions, thereby enhancing specific nonlinear optical phenomena.

Coherent control of quantum systems through their interaction with light is a fundamental concept in modern quantum physics, quantum information and quantum chemistry. The ability to manipulate quantum states has the potential to transform areas such as chemical synthesis, enabling the precise steering of chemical reactions, targeted bond dissociation and the control of population dynamics within quantum systems [31, 149]. A quantum system can be driven towards a desired state by exploiting quantum interference between competing transition pathways. This interference can be carefully managed to either enhance or suppress transition probabilities, depending on the intended outcome. For instance, Meshulach and Silberberg demonstrated the generation of "dark pulses" in cesium atoms, effectively controlling a two-photon transition [150]. In multi-photon processes, the interaction between virtual and resonant pathways can induce phase shifts, leading to partial destructive interference. This interference can be attenuated by blocking specific spectral components or compensating for the phase shift through precise control of the spectral phase [150–152]. Recently, the FWM signal intensity of monolayer WSe_2 was enhanced by a factor of 2.6 at ambient conditions by Meron et al. using a π-step spectral phase [153].

This chapter investigates the impact of shaping optical pulses on the generated nonlinear signal intensity at room temperature, utilizing a broadband laser spectrum that overlaps with the first excitonic resonance of two monolayer TMDs - WSe_2 and $MoSe_2$. A key factor in these experiments is that the coherence time of the excitonic excitation is significantly longer than the temporal duration of the laser pulses to allow for coherent light-matter interaction. This ensures that the excitonic system retains phase memory throughout the optical excitation, enabling the coherent control over quantum states. If temporal pulse length of the laser pulse would be too long, the system cannot respond coherently, suppressing interference effects and reducing the efficiency of coherent control and signal generation. This is guaranteed by the 12 fs laser pulses, with a spectral width of more than 300 meV, compared to the width of the A-exciton resonance of $\sim$ 20 meV, as presented in Figure 4.21.

Section 4.1 discusses the principles of optical pulse shaping, focusing on how the spectral phase influences the temporal shape of laser pulses for a given spectrum. It also covers the experimental implementation of pulse shaping and concepts for pulse compression to achieve a transform-limited pulse as a well-defined starting condition for further phase control experiments. Section 4.2 provides a detailed description of the sample preparation procedure and the two microscope setups employed for the experiments in this chapter. Section 4.3 outlines the pulse compression process and presents detailed pulse characterization measurements. Section 4.4 introduces the sample characterization measurements (4.4.1), the ultrafast phase-control experiments (4.4.2) for FWM, complemented by fluence-dependent absorption measurements (4.4.3). To provide deeper insight into the underlying physical mechanisms, Section 4.4.4 presents a classical model for calculating the nonlinear optical response of TMDs. The model assumes a Lorentzian lineshape for the A-exciton resonance and investigates the influence of the spectral phase. To complement this approach, in Section 4.4.5 a second, quantum-mechanical model, based on time-dependent density-matrix calculations for either a single or an ensemble of two-level systems, was adapted from [32]. Adaptation and execution of this model, which captures the population dynamics of the excitonic states, was performed by Dr. Sebastian Bange from the research group of Prof. John M. Lupton at the Department of Physics, University of Regensburg. Based on the shape of the resonance, used in the classical model, Section 4.4.6 describes the application of a certain spectral phase profile. Specifically, the model indicates that a π-step arctan phase function is theoretically optimal for addressing the excitonic resonance. In Section 4.4.7, the experiments and numerical models are applied on the SFG response of the two TMDs. Finally, Section 4.5 provides a concluding summary of the results obtained from the experiments and numerical models employed, along with the key procedures and effects investigated in this section.

4.1. Principles of optical pulse shaping

The first reliable generation of femtosecond laser pulses was achieved in 1981 with the invention of a modelocked ring dye laser [154]. Modelocking synchronizes multiple longitudinal modes of the laser cavity to oscillate in phase, thereby creating a pulse train with high peak intensities. This was accomplished by applying a periodic modulation to the laser's gain or cavity, which maintains a stable phase relation between the multitude of modes. For a given laser spectrum, the spectral phase profile of a laser pulse has great impact on the resulting temporal pulse shape, as will be discussed in 4.1.1. Through the remarkable progress in ultrafast optics during the past decades, the manipulation of this phase profile became possible, allowing for a wide range of applications by forming ultrashort optical pulses with widely tunable temporal shape [155, 156].
Key techniques in pulse shaping are methods to modify the amplitude and phase of the pulse in both the time and frequency domain. These techniques include the use of spatial light modulators (SLMs), acousto-optic devices and michro-mirror arrays [157]. Accurate shaping of femtosecond pulses allows for precise control over their interactions with matter, opening up experimental access to the unique coherent properties of quantum systems. Today pulse shaping is used in a variety of fields such as ultrafast spectroscopy, high-resolution imaging and nonlinear optics [73, 158, 159].

4.1.1. Spectral phase

The electric field E of a laser pulse can be described either in the time (t) or in the frequency (ω) domain. Both domains are connected via the complex Fourier transform ($\mathfrak{F}$):

$$\begin{aligned} E(\omega) &= \mathfrak{F}\big(E(t)\big) = \int_{-\infty}^{\infty} E(t)e^{-i\omega t}dt = A(\omega)e^{i\varphi(\omega)} \\ E(t) &= \mathfrak{F}^{-1}\big(E(\omega)\big) = \frac{1}{2\pi}\int_{-\infty}^{\infty} E(\omega)e^{i\omega t}d\omega \end{aligned} \tag{4.1}$$

In equation 4.1, $A(\omega) = |E(\omega)|$ represents the spectral amplitude, while $\varphi(\omega)$ denotes the spectral phase. From these relations the temporal pulse length $\Delta\tau$ and the spectral width $\Delta\omega$ can be determinded. These quantities are interconnected through the time-bandwidth product (TBD) and cannot vary independently of each other [160]. In the TBP,

$$\Delta t \cdot \Delta\omega \geq 2\pi \cdot c_{\mathrm{TBP}} = const. \tag{4.2}$$

c_{TBP} is a numerical constant typically on the order of unity [30]. The minimum achievable time-bandwidth product depends on the specific pulse shape and is attained for transform-limited pulses. These pulses are characterized by a perfectly flat spectral phase profile, which can be mathematically expressed as a constant first derivative of the phase with respect to angular frequency:

$$\frac{d\varphi(\omega)}{d\omega} = const. \tag{4.3}$$

Expanding the spectral phase as a Taylor series around the central frequency ω_0 where the pulse spectrum is centered, provides valuable insight into how the various phase contribution terms influence the shape of the laser pulse.

$$\begin{aligned}\varphi(\omega) = \quad & \varphi(\omega_0) \\ & + \left.\frac{d\varphi(\omega)}{d\omega}\right|_{\omega_0} (\omega - \omega_0) \\ & + \frac{1}{2!}\left.\frac{d^2\varphi(\omega)}{d\omega^2}\right|_{\omega_0} (\omega - \omega_0)^2 \\ & + \frac{1}{3!}\left.\frac{d^3\varphi(\omega)}{d\omega^3}\right|_{\omega_0} (\omega - \omega_0)^3 \\ & + \mathcal{O}((\omega - \omega_0)^4)\end{aligned} \tag{4.4}$$

In equation 4.4 the first term $\varphi(\omega_0)$ describes a constant phase offset which shifts the carrier wave relative to the envelope wave. The second term is a linear phase function, which is associated with a temporal shift of the pulse and is commonly refered to as *group delay* (τ_g). Notably, these first two phase terms do not alter the temporal pulse shape, as they leave the intensity envelope of the pulse in the time domain unaffected and Equation 4.3 is still valid.

Figure 4.1 shows the spectral phase profile for a given laser spectrum in the left column, alongside the corresponding calculated temporal pulse shape in the right column. In the top row, the phase is zero, resulting in a pulse shape that is transform-limited. In the middle row the phase is set to a constant value of $\varphi\left(\frac{\hbar}{e} \cdot \omega\right) = \pi$. This constant phase affects only the carrier wave while the envelope remains unaffected. Consequently, the pulse shape remains transform-limited. For this reason, a constant phase term is referred to as the carrier-envelope phase (CEP). In the bottom row a linear phase function $\varphi\left(\frac{\hbar}{e} \cdot \omega\right) = c \cdot (\omega - \omega_0)$ is applied, with $c = 20$ fs. As a result, the pulse shape remains unchanged but the pulse is shifted in time by exactly 20 fs, consistent with the input parameter of the linear phase function.

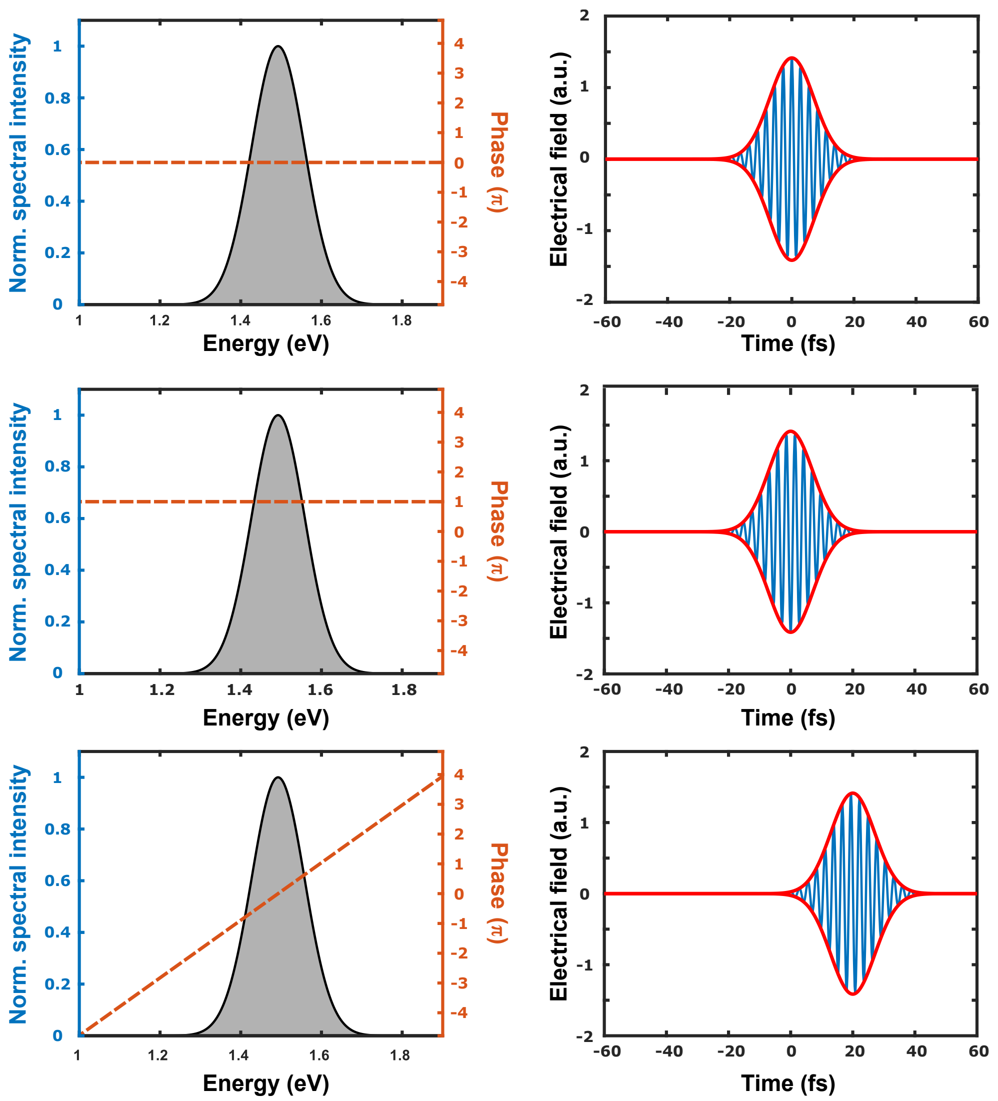

Figure 4.1.: Phase and pulse shape for constant and linear phase profiles. In general, for a given spectrum the phase profile determines the temporal shape of the laser pulse. Here in the left column the laser spectrum (grey shaded area) and the spectral phase (orange dashed line) are shown together with the corresponding temporal pulse shape in the right column, with the red envelope and the blue carrier wave. The top, middle and bottom rows show the cases of zero spectral phase, constant spectral phase and linear spectral phase, respectively.

The third term in equation 4.4 corresponds to a quadratic frequency dependence of the phase, which can also be interpreted as a linear frequency dependence of the group delay. This term is referred to as *group delay dispersion* (GDD) because it describes how different frequency components of a pulse experience varying delays. This variation in the instantaneous frequency within the laser pulse is referred to as chirp because the effect is similar to the chirping sound of a bird. Specifically, a positive chirp occurs when the instantaneous frequency increases with time, placing the lower frequencies on the leading edge of the pulse. For consistency with the other terms, this phase term will be referred to as *second-order dispersion* (SOD) in this work.

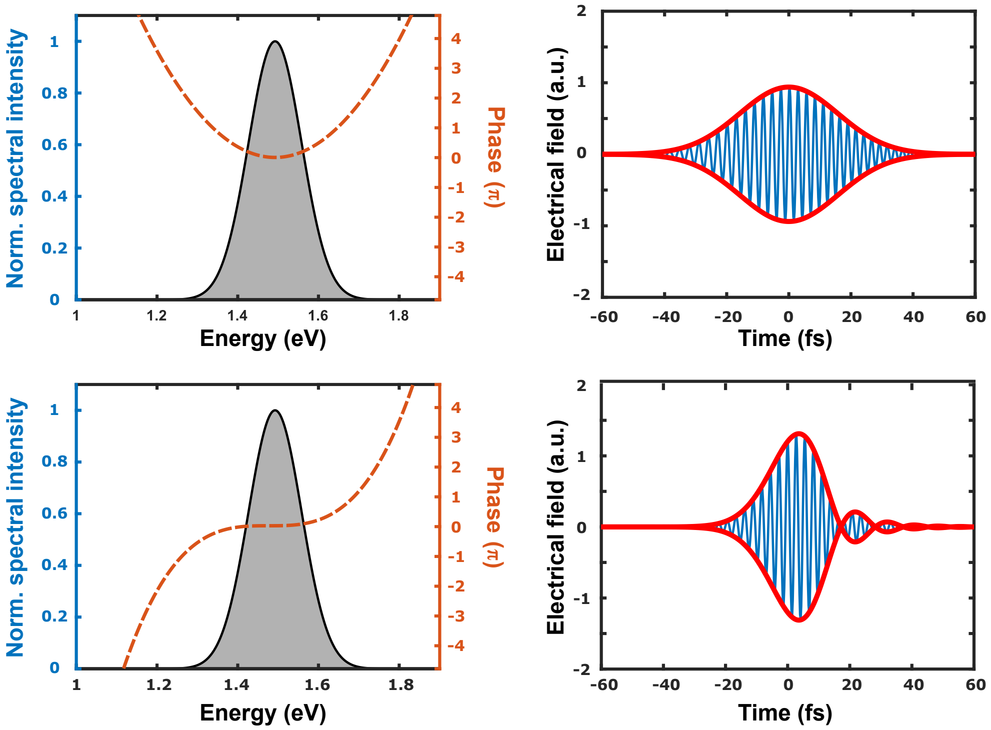

Figure 4.2.: Phase and pulse shape for second and third order dispersion phase profiles. The phase profile determines the temporal shape of a laser pulse for a given spectrum. In the left column, the laser spectrum (gray shaded area) and the spectral phase (orange dashed line) are shown, while the corresponding temporal pulse shape is displayed in the right column, with the red envelope and the blue carrier wave. The top row illustrates the effect of a quadratic spectral phase function, which symmetrically stretches the temporal pulse shape. The bottom row visualizes the impact of a third-order spectral phase function, introducing asymmetrical changes to the pulse shape.

The fourth term describes a cubic frequency-dependent phase contribution, which leads to more complex and asymmetric distortions of the pulse. This is referred to as *third-order dispersion* (TOD).

Equation 4.4 can now be written as:

$$\varphi(\omega) = \quad \mathrm{CEP} + \tau_g \cdot (\omega - \omega_0) + \frac{1}{2} \cdot \mathrm{SOD} \cdot (\omega - \omega_0)^2 + \frac{1}{6} \cdot \mathrm{TOD} \cdot (\omega - \omega_0)^3 + ... \tag{4.5}$$

In Figure 4.2 the impact of second- and third order phase phase terms on the pulse shape is illustrated. The left column displays the spectral phase profiles for a given laser spectrum, while the right column shows the corresponding calculated temporal pulse shapes. In the top row, the phase profile is a quadratic function $\varphi\left(\frac{\hbar}{e} \cdot \omega\right) = \frac{1}{2} \cdot \mathrm{SOD} \cdot (\omega - \omega_0)^2$ with SOD = 100 fs^2, while the bottom row shows the results for a cubic phase function $\varphi\left(\frac{\hbar}{e} \cdot \omega\right) = \frac{1}{6} \cdot \mathrm{TOD} \cdot (\omega - \omega_0)^3$ with TOD = 500 fs^3.

In the following experiments, the optimal spectral phase or pulse shape for nonlinear signal generation is investigated. To achieve this, the SOD and TOD parameters of the phase function are scanned while recording he resulting nonlinear signal intensity. These SOD or SOD/TOD scans are performed for laser pulse characterization in 4.3 and for the investigation of the nonlinear signal generation in 2D TMDs in 4.4.

4.1.2. Concept of pulse shaping

In this work, pulse shaping was realized by the use of a spatial light modulator (SLM) which allows for Fourier waveform synthesis by spatial masking of the spatially dispersed optical frequency spectrum [157, 160].
Figure 4.3 shows the basic setup for pulse shaping with the SLM as the central component. The incident femtosecond pulse is decomposed into its spectral components by a reflective grating and then focused into the modulator array. The SLM is positioned in the Fourier plane, where all spectral components are adequately separated. It consists of liquid crystal cells arranged in an array, which are controlled by a voltage applied to change the alignment of the individual crystals. These liquid crystal cells act as phase modulators, changing the refractive index for light passing through them, thereby modifying the phase of the transmitted light at specific locations. A double-cell array, as utilized in this work (see Section 4.2), enables additional attenuation of the spectral amplitude by partially rotating the polarization of selected spectral components. A following polarization analyzer ensures the corresponding attenuation of these components.

Behind the Fourier plane, the spectral components of the pulse are recombined by an identical configuration of a focusing element[1] and an optical grating. The setup needs to be carefully aligned in order to ensure optimal recombination and avoid frequency variations across the spatial dimensions of the beam, an aberration which is known as spatial chirp.

---

[1] In the experiments of this work (described in Chapter 4.2 and 4.4) instead of a lens a reflective spherical mirror is used as focusing element.

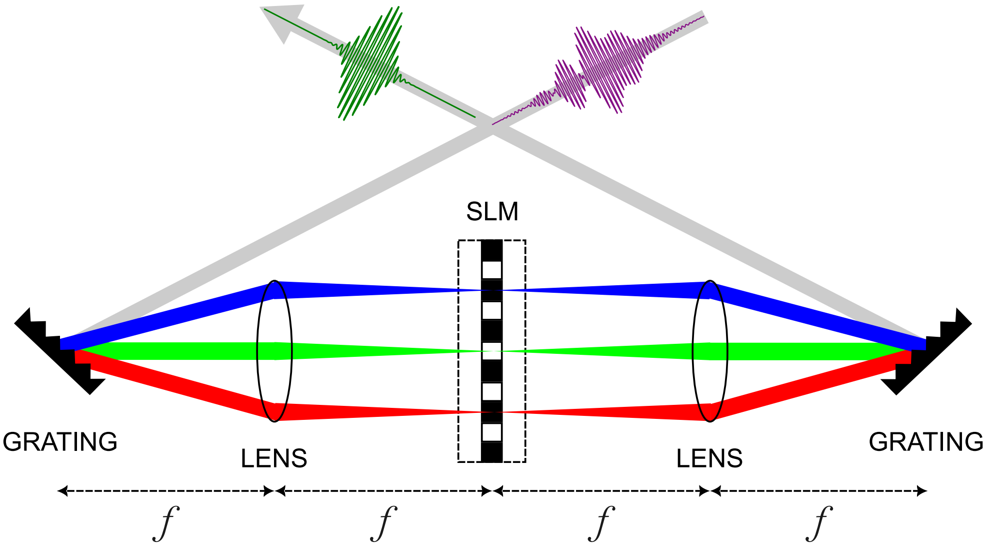

Figure 4.3.: Schematic setup of a Spatial Light Modulator in 4f configuration The incoming laser pulse of arbitrary shape is decomposed into it's frequency components by a diffraction grating and focused into the liquid crystal array. The manipulated spectral components are transmitted and recombined by an identical configuration of focusing lens and grating.

4.1.3. Pulse compression

The application of ultrafast laser pulses often critically relies on precise control over their temporal and spectral characteristics. The ability to generate arbitrarily shaped laser pulses, essential for femtochemistry, coherent control of chemical reactions and quantum communication, requires an accurate knowledge of the spectral phase profile. Transform-limited pulses are typically desired as they feature a flat spectral phase and provide an ideal starting point for further pulse manipulation. Achieving this generally involves two key steps: pulse characterization and pulse compression.

The temporal intensity profile of an optical signal can be accurately determined through cross-correlation (CC) with a shorter reference pulse of known shape. This process involves temporally scanning the signal with the reference pulse, using a time delay and recording the nonlinear signal generated by their temporal overlap [160].
As such a reference pulse, much shorter than the optical pulse being analyzed, is not available in most practical cases, the signal itself can be used as reference in an autocorrelation (AC). However, since in an AC the pulse is scanned with itself, it is inherently symmetrical, which limits the amount of information it can provide about the pulse shape [30]. These intensity correlation techniques share a common limitation: they do not provide any information about the phase of the laser pulse.

Frequency-Resolved Optical Gating (FROG) is a widely used method to reconstruct the

full electric field of the laser pulse, combining temporal and spectral information. Like in an AC the pulse is being scanned by itself in a nonlinear crystal while the generated nonlinear optical (usually SHG) spectra are recorded. From the nonlinear intensity as a function of the frequency and the delay time the complex electric field can be reconstructed [161].
Spectral Phase Interferometry for Direct Electric-field Reconstruction (SPIDER) is another technique used to fully characterize ultrashort laser pulses by directly retrieving their spectral phase and amplitude. The method relies on a self-referencing interferometric measurement between the pulse and a time-delayed, spectrally sheared replica, which are mixed in a nonlinear medium. To achieve the spectral shearing, the pulse pair is overlapped with a third, highly chirped, stretched copy of the pulse, ensuring each replica interacts with a different spectral component of the streched pulse. The resulting frequency-converted pulse pair generates a spectral interferogram, which is recorded and analyzed via Fourier analysis. This maps the spectral phase difference to a measurable quantity. Any dispersion in the original pulse manifests as slight deviations in the interferogram's nominal fringe spacing, enabling the retrieval of the spectral phase [162].

The characterized spectral phase can be compensated using suitable dispersive elements which can be classified into bulk dispersion (homogeneous materials like glass), geometrical dispersion (prism and grating arrangements), microstructured dispersion (fiber Bragg gratings, chirped mirrors, quasi-phase-matched crystals) and dispersion from interferometric effects [163–165]. A limitation of these elements is that they impose their fixed dispersion profile on the spectral phase of the laser pulse, which is always a predetermined combination of second-, third- and higher-order phase contributions.

The following sections describe two alternative methods used for pulse compression in the experimental part of this work. These techniques use the SLM to combine the phase characterization with the corresponding correction.

Multiphoton Intrapulse Interference Phase Scan

Multiphoton Intrapulse Interference Phase Scan (MIIPS) was introduced by Lozovoy et al. in 2004 [166] as a technique that combines the characterization of the spectral phase distortion with the necessary phase compensation for efficient pulse compression. It is based on the application of a well-defined spectral reference phase $f(\omega)$, which reduces phase distortions in some regions of the spectrum. The subsequent analysis of the resulting series of SHG spectra enables the determination of the unknown spetral phase $\phi(\omega)$ of the laser pulse.

$$\varphi(\omega) = \phi(\omega) + f(\omega) \tag{4.6}$$

In general, the SHG intensity spectrum at the frequency 2ω can be calculated as the convolution of the input field spectrum $E(\omega)$ with itself. This reflects the fact that, in SHG, multiple frequency pairs combine to generate the 2ω signal and connects the spectral phase of the laser pulse to its SHG spectrum.

$$\begin{aligned} I_{\mathrm{SHG}}(2\omega) &\propto \left| \int_0^\infty \chi^{(2)}(\omega) \cdot E(\omega+\Delta) \cdot E(\omega-\Delta)\, d\Delta \right|^2 \\ &= \left| \int_0^\infty \chi^{(2)}(\omega) \cdot \Big|E(\omega+\Delta)\Big| \cdot \Big|E(\omega-\Delta)\Big| \right. \\ &\qquad \left. \cdot \exp\Big(i \cdot \Big[\varphi(\omega+\Delta) + \varphi(\omega-\Delta)\Big]\Big)\, d\Delta \right|^2 \end{aligned} \tag{4.7}$$

Here the complex electric field of the laser pulse $E(\omega)$ is decomposed in the real amplitude term $|E(\omega)|$ and the complex phase term $\exp(i\varphi(\omega))$. In equation 4.7, $\chi^{(2)}(\omega)$ is the second-order nonlinear susceptibility of the material. For a flat-phase reference material without resonances in the range of the laser spectrum, $\chi^{(2)}(\omega)$ can be estimated as constant and it can be taken out of the integral.
According to equation 4.7, the SHG intensity maximizes if $\varphi(\omega+\Delta) + \varphi(\omega-\Delta) = 0$. This phase function can be expanded in a Taylor series around ω, with terms expressed in powers of Δ.

$$\varphi(\omega+\Delta) = \varphi(\omega) + \varphi'(\omega)\Delta + \frac{1}{2}\varphi''(\omega)\Delta^2 + \frac{1}{6}\varphi'''(\omega)\Delta^3 + \frac{1}{24}\varphi^{(4)}(\omega)\Delta^4 + \ldots \tag{4.8}$$

Since the constant term and the first-order term in Equation 4.8 do not affect the pulse shape, and therefore the SHG signal, they can generally be ignored in the context of non-linear signal generation. Additionally, the odd-order terms in the expansion are irrelevant because they cancel out in the interference term $\varphi(\omega+\Delta) + \varphi(\omega-\Delta)$. So the condition for maximum SHG intensity, neglecting higher even orders, reduces to:

$$\varphi(\omega)'' = \phi(\omega)'' + f(\omega)'' = 0 \tag{4.9}$$

This condition is met when the local second derivative (GDD) of the phase $\phi(\omega)$ is compensated by the reference phase $f(\omega)$. During a MIIPS scan the phase $\phi(\omega)$ of the laser pulse is modified by the well-defined cosine reference phase $f(\omega) = a \cdot \cos(\ b \cdot (\omega - \omega_0) + c\ )$, with a and b being parameters to determine range and resolution of the procedure. Experimentally, the SHG spectrum of a flat-phase reference material is collected while scanning the parameter c over a range of at least 2π, which effectively moves the cosine phase over the laser spectrum. Since the second derivative of the reference function is known, $\phi(\omega)''$ can be determined from the condition for maximized nonlinear signal generation (equation 4.9), the phase parameters (a, b) and the experimentally obtained offset c_{max} of the cosine phase that results in maximal SHG intensity at the specific frequency.

$$\phi(\omega)'' = -f(\omega)'' = a \cdot b^2 \cos(b \cdot (\omega - \omega_0) + c_{\mathrm{max}}(2\omega)) \tag{4.10}$$

Figure 4.4(a) illustrates the process of scanning the cosine phase across the laser spectrum, while (b) displays the simulated two-dimensional MIIPS trace for the case of a flat spectral phase. From this trace, $c_{max}(2\omega)$ can be determined. The pattern exhibits parallel maximum intensity lines with a periodicity of π, as $c_{max}(2\omega) = b \cdot (\omega - \omega_0) \pm \frac{\pi}{2}$, according to equation 4.10, corresponding to the zero-crossings of the cosine function. Figure 4.4 represents the ideal scenario where the spectral phase of the laser pulses is perfectly flat, which is the goal of pulse compression. If the initial phase is distorted, the pattern differ from the one shown in Figure 4.4(b). A linear chirp (second order phase distortion) would cause the parallel lines to be spaced no longer by π but asymmetrically, while a quadratic chirp (cubic phase distortion) would change the slope of the maximum intensity lines. This will be seen below in the experimental pulse compression section 4.3.

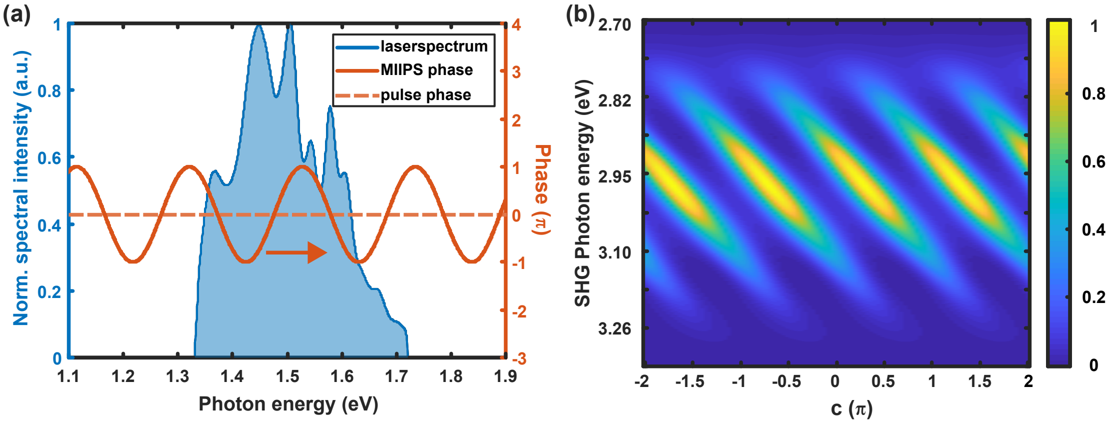

Figure 4.4.: Principle of MIIPS and simulation for a flat spectral phase profile. In MIIPS a cosine reference phase is applied by the SLM to modify the unknown spectral phase of the laser pulses. By scanning the position offset parameter c the reference phase is moved over the spectrum. (a) illustrates the reference spectral phase (red cosine curve) relative to the laser spectrum (blue shaded area) and the flat phase profile of the (here transform-limited) laser pulses (orange dashed line). (b) presents the simulated spectrally resolved intensity of the resulting SHG signal for a flat phase pulse, plotted as a function of the position offset c of the cosine reference phase.

Finally, the unknown spectral phase $\phi(\omega)$ can be directly retrieved by performing a double integration of $\phi(\omega)''$ over the frequency ω. The integration constants, corresponding to the constant and linear terms of the phase, are usually set to zero. The spectral phase

$\phi(\omega)$ can then be compensated by applying a corresponding correction phase profile $-\phi(\omega)$ via the SLM, effectively compressing the pulse. This process must be repeated iteratively, gradually reducing the parameters a and b step by step to narrow the GDD range and improve accuracy.

However, the standard MIIPS accuracy is limited when higher-order phase terms are present, as it assumes a locally quadratic spectral phase. Additionally, low modulation frequencies require high modulation amplitudes, which can introduce spectral artifacts such as phase wrapping due to pulse shaper limitations. Moreover, MIIPS assumes a slowly varying spectral intensity profile, which reduces its effectiveness for pulses with structured or rapidly varying spectra.

To address these limitations, Gated-MIIPS (G-MIIPS) is an improved MIIPS technique that introduces a spectral amplitude gate to restricts the analysis to narrow spectral regions. This improves the validity of the second-order approximation, reduces the influence of higher-order phase terms, minimizes phase-wrapping effects and allows accurate correction even for structured spectral amplitudes. G-MIIPS therefore can achieve more accurate phase retrieval and faster convergence than standard MIIPS [167].

Furthermore, a modified MIIPS algorithm has been developed to improve phase retrieval by explicitly accounting for the spectral amplitude of the pulse. Unlike the phase-only MIIPS approach, which can confuse amplitude variations with phase distortions, this technique simulates MIIPS maps, according to Equation 4.7, using both the spectral amplitude and phase. As a result, it can distinguish between pulses with identical MIIPS traces but differing spectral structures and retrieve the correct SOD in fewer iterations. This approach offers faster and more reliable characterization from a single MIIPS scan [168].

The genetic algorithm

A Genetic Algorithm (GA) is a versatile and robust optimization technique inspired by the principles of natural selection and evolution that can be used for complex problems, like linear as well as nonlinear optimization problems. Initially proposed by Alan Turing in 1950 as a ”learning machiene”, GAs were progressively developed by several researchers [169, 170] and became well-known through the work of John Holland [171]. In essence, the concept is to create a population of individuals, each defined as a set of specific properties or genomes. These individuals serve as candidate solutions for the problem defined as a mathematical function and are evaluated based on their ”fitness”. The fitness score reflects the deviation of the received output compared to the optimal result, with low fitness indicating high deviation. The least fit individuals are discarded, while the more fit members of the population survive to contribute to the next generation. A new generation is created by randomly selecting parents from the population using a scheme which favours higher fitness scores. Strong individuals might be selected multiple times while weaker induviduals may not be selected at all. The offspring individuals are created from the parents through crossover, which combines genomes from both parents, and mutation, which introduces random variations of individual genomes. This iterative process of evaluation, selection and reproduction continues until a satisfactory solution is reached or a predefined stopping condition is met. The process is illustrated in Figure 4.5.

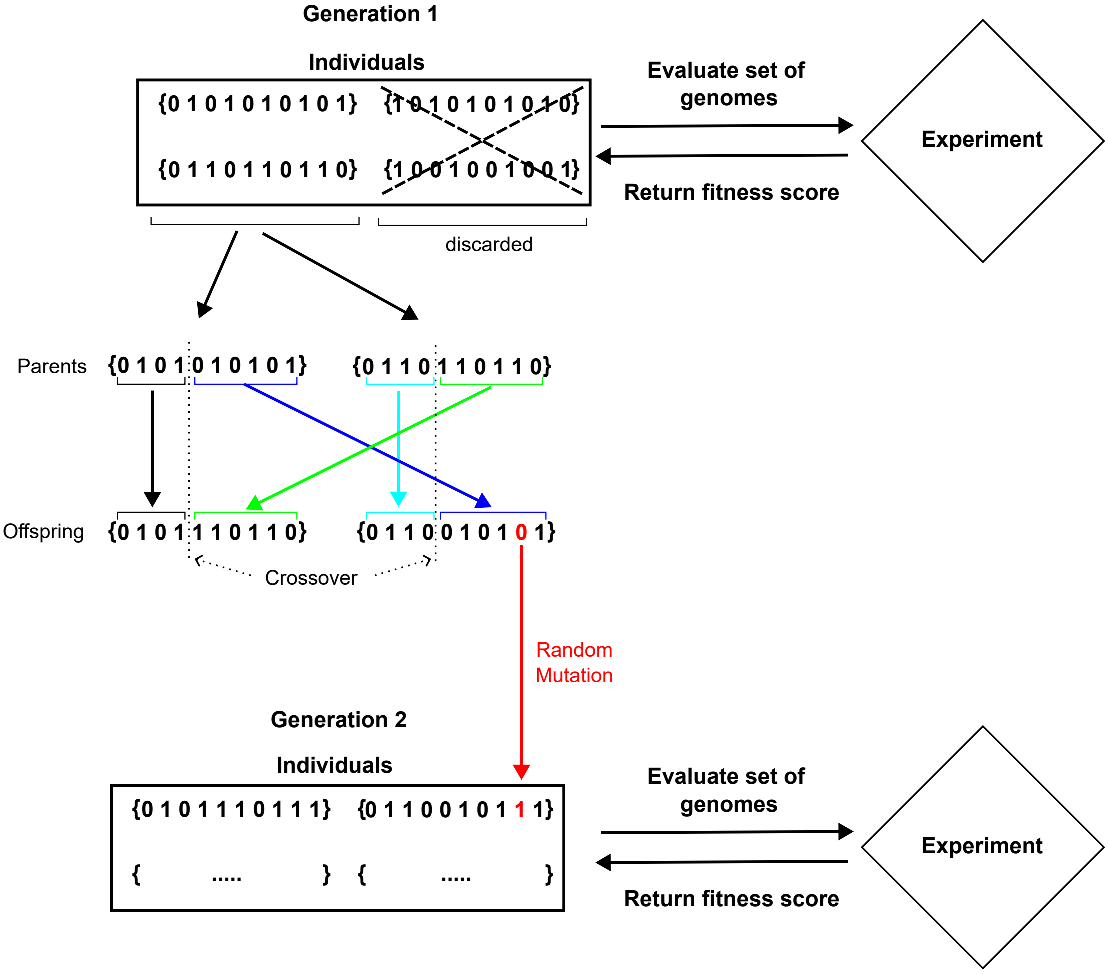

Figure 4.5.: Schematic overview of the Genetic Algorithm principle. The composition of the first generation is generated randomly. Each individual is evaluated and marked by a fitness score. Here the evaluation process is the optical experiment and the feedback signal is the nonlinear response of a reference material. The weakest individuals are being discarded, while the strongest are selected to contribute to the next generation. New offspring individuals are created through crossover of parent genomes and random mutation of individual genomes. The process iteratively continues until predefined conditions are met.

For pulse shaping and phase retrieval, GAs have been used since almost thirty years [172]. The LCM used in this work, described in Section 4.1, has 640 pixel that can be varied and act as free parameters for the optimization problem. To reduce computational and experimental demands, a number of nodal points are evenly distributed across the spectral range targeted for optimization. Between these nodal points, the phase values are interpolated using cubic interpolation to ensure smooth transitions and continuous phase adjustments. The nodal points act as genomes, with a set of nodal points collectively defining a single individual in the optimization process. The generated nonlinear optical intensity of a reference material (here SLG for FWM) is employed as the feedback signal. Details on the GA process used in this work can be found in [173, 174]. This GA procedure for pulse compression is applied experimentally in Section 4.3.

4.2. Experimental description

In this section, the experimental procedures and details are discussed, beginning with the sample preparation methods of monolayer TMD samples and relevant reference materials in Section 4.2.1. Subsequently, the experimental setups employed in this chapter are described in detail. All phase-control measurements (Sections 4.4.2 and 4.4.7) as well as the fluence-dependent absorption measurements (Section 4.4.3) were performed on the pulse shaping setup described in Section 4.2.2. The SHG intensity measurements, discussed in Section 4.4.7, were performed on the setup described in Section 4.2.3.

4.2.1. Sample preparation

As a reference material for SFG, iron iodate ($Fe(IO_3)_3$) nanocrystals were used These nanocrystals, acting as local probes, exhibit high photostability and generate a phase-free sum-frequency signal due to their lack of absorption in the near-infrared and visible spectral regions [175]. For sample preparation, the $Fe(IO_3)_3$ nanocrystals were emulsified in Milli-Q water and sonicated for 1 minute to ensure proper dispersion. Finally, the suspension was spin-coated onto a 130 μm thick borosilicate microscope cover slide. This process ensures a high concentration of single, diffraction-limited nanocrystals.

As a reference material for FWM, commercially available single layer graphene (SLG) on 90 nm SiO2/Si was purchased from ”Graphenea”. The SLG was CVD-grown and transferred onto the substrate by a semi-dry transfer process, ensuring complete coverage.
SLG was shown to be an excellent reference material for FWM measurements due to its inherently strong third-order nonlinear susceptibility, enabling efficient FWM signal generation [176]. Additionally, its broadband optical response and gapless linear electronic dispersion allow for phase-free nonlinear interactions across a wide spectral range [174].

The TMD monolayer samples were fabricated and provided by Dr. Bárbara Rosa from the research group of Prof. Stephan Reitzenstein at the Technische Universität Berlin. WSe_2, $MoSe_2$ and h-BN flakes were obtained by mechanically exfoliating [177] commercial bulk crystals onto polydimethylsiloxane (PDMS) stamps. PDMS provides a suitable adhesion to TMD flakes, enabling efficient mechanical exfoliation with minimal damage. It is flexible and elastic, ensuring good contact with bulk TMD crystals, improving exfoliation efficiency and facilitating the transfer process. PDMS assisted exfoliation allows for the dry transfer of monolayers onto different substrates without the need for additional solvents and, unlike adhesive tapes, leaves minimal residue on the TMD monolayer [45]. Subsequently, TMD monolayers were identified by optical contrast and photoluminescence spectroscopy, see Section 4.4.1, and transferred to borosilicate microscope cover slides by the dry-transfer method at 70°C [45].

Bare TMD monolayer samples directly deposited on borosilicate microscope cover slides were used for absorption measurements and low fluence phase scans, while for fluence-dependent and high intensity measurements, encapsulated monolayers were employed. For encapsulated samples, the monolayer was deposited between two thin h-BN layers of less than 15 nm as h-BN/TMD/h-BN.

Before the material deposition, the borosilicate microscope cover slides were carefully cleaned by sonication (Hellmanex III, Sigma Aldrich) in isopropanol and ethanol for 5 min each. Afterwards, the residual ethanol was removed by nitrogen blow-drying.

4.2.2. Pulse shaping setup

For the phase-control experiments, presented in this chapter, a pulse-shaping setup in combination with a confocal microscope was employed. For signal analysis an APD as single photon detector and a CCD camera for spectrally resolved measurements were included. A schematic overview is shown in Figure 4.6.

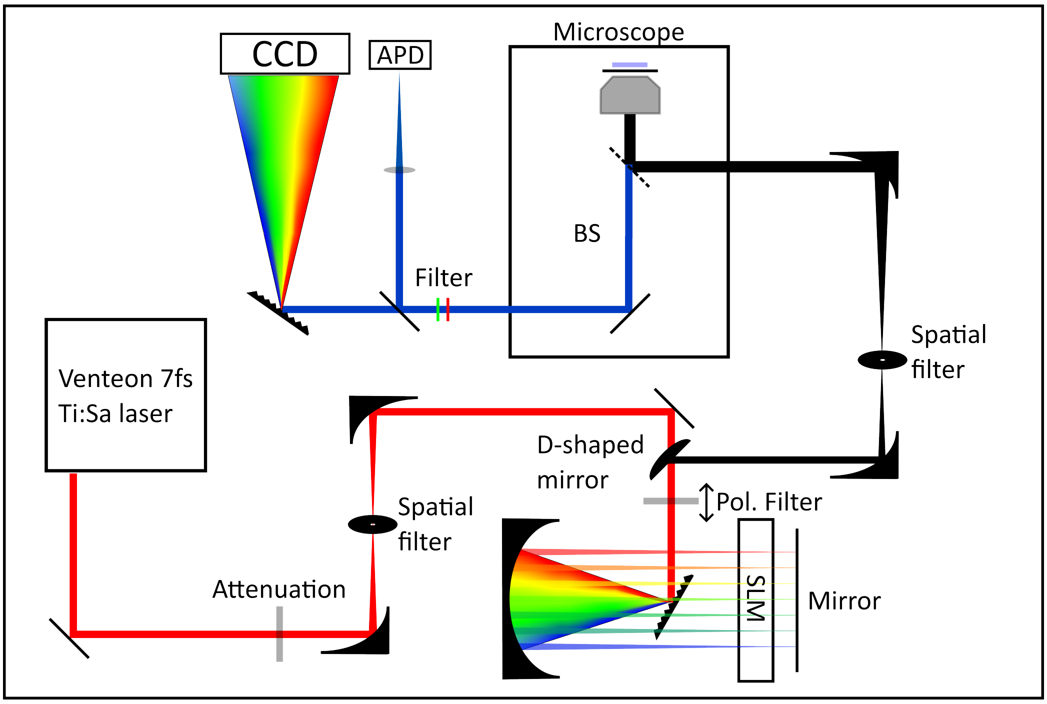

Figure 4.6.: Schematic overview of the pulse-shaping setup. Broadband mode-locked laser radiation (300 nm, 7 fs) is provided by a Venteon Ti:Sa laser. Pulse shaping is realized by a programmable liquid crystal spatial light modulator in reflective 4f configuration

Broadband 7 fs laser pulses are provided by a modelocked 80 MHz Ti:Sa laser source (Novanta Photonics Venteon). The spectral width of the laser radiation ranges from 650 nm to 950 nm. For minimal heat deposition, reflective attenuation filters are used to adjust the laser intensity. Cleaning the spatial laser mode was achieved by a spatial filter, focusing the laser radiation through a 50 μm pinhole and re-collimating it. This filters out higher spatial modes and resulting in a clean Gaussian laser mode. Gold-coated off-axis parabolic mirrors (Thorlabs MPD149-M01) are used instead of lenses to avoid additional dispersion by transmittive through the optical components. A linear polarization filter works as an analyzer for the input radiation and as a beam attenuator for the outgoing radiation. This way a change in polarization induced by the SLM translates in a change in intensity of the specific spectral component. The working principle of the SLM pulse shaper is described in Section 4.1.2. Subsequently, the spectral components of the radiation are seperated by an reflective optical grating (600 lines/mm, blazed at 750 nm) using the first diffraction order. Next, a gold-coated concave spherical mirror (f = 300 mm) is used to parallelize the spectral components and focus them on the SLM. The SLM used here is a commercially available 640 pixel double mask liquid crystal light modulator (Jenoptik SLM-S640d) allowing for simultaneous phase and amplitude shaping. The beams were reflected at the back of the SLM and pass through the two liquid crystal masks a second time. The applied voltage needs to accound for that double transmission. The spectral components were re-collimated at the spherical mirror and recombined at the grating. This process was adjusted carefully while controlling the focus position various spectral components in the microscope objective. Through a minimal tilt of the mirrors at the back of the SLM after passing the polarization filter on the way back the beam is reflected by the D-shaped mirror and send to a second spatial filter to clean the mode again after the spectral recombination. The second spatial filter also acts as a beam expander due to different focal length of the off-axis parabolic mirrors. The beam enters the microscope body and is reflected by the beamsplitter (Chroma 21017 Sputter-coated, non-polarizing 20/80) to the high numerical aperture immersion oil microscope objective (Nikon CFI S-Fluor 100x NA=1.3) with refracting index matching immersion oil (n = 1.51). The aperture of the objectie is completely filled by the beam diameter to ensure the high NA. The sample is placed on top of thin borosilicate glass coverslip (130 μm) and adjusted to the focus of the microscope objective.

The generated radiation is collected by the same high NA objective in epi-detection configuration, transmitted through the beamsplitter and reflected out of the microscope body. Subsequently, the spectral detection window is restricted by suitable optical shortpass filters, 2.76 – 3.54 eV (450 – 350 nm) for SFG or to 1.77 – 2.02 eV (700 – 615 nm) for anti-stokes FWM, respectively. For integrated intensity detection a silicon single-photon APD (Laser Components Count 100C) was employed while the spectral analysis was performed with a single-grating spectrometer (Aceton SpectraPro 2500i) combined with a CCD camera (Andor iDus 401 BR-DD).

The spectral detection sensitivity of the experimental setup was calibrated using a reference thermal light source (Thorlabs SLS201L), which provided a known and stable spectral output. By comparing the recorded spectra of the light source to its calibrated emission profile, the wavelength-dependent response of the detection setup has been determined. All spectra taken during the experiments were corrected using this calibration curve.

4.2.3. SHG intensity setup

For the SHG intensity experiments of WSe_2 and $MoSe_2$, presented in Section 4.4.7 two tunable fs laser sources of narrow bandwidth NIR pulses with partially overlapping tuning range are employed.

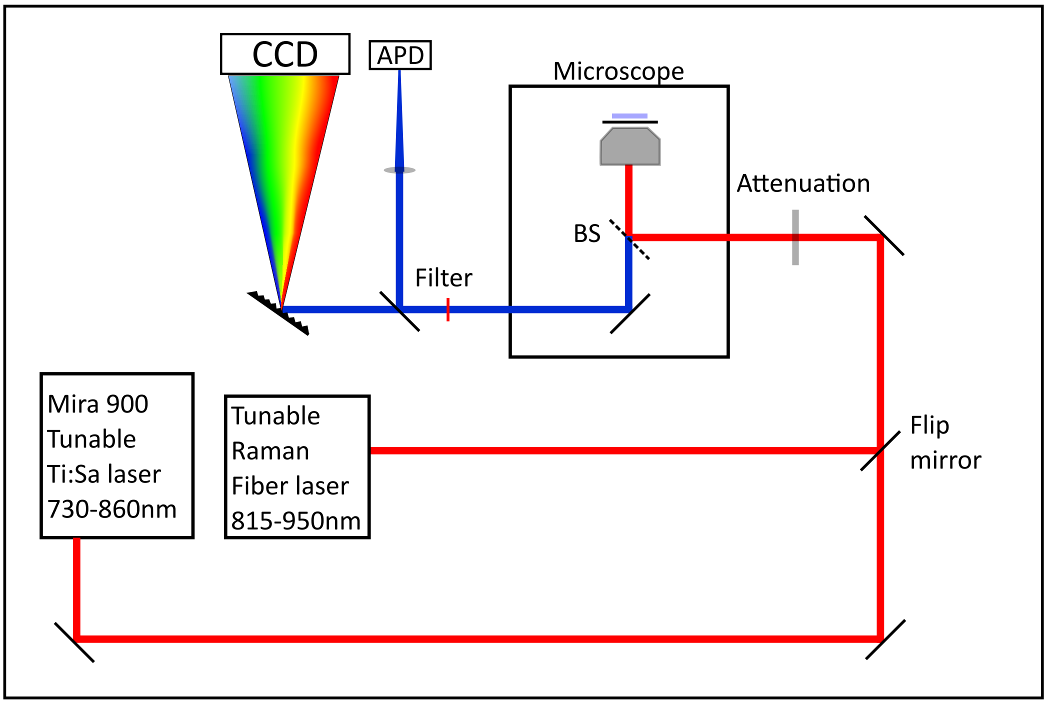

Figure 4.7.: Schematic overview of the SHG intensity setup. The intensity of the SHG response of monolayer TMDs relative to a quartz reference is analyzed in dependence of the excitation wavelength. Two laser sources (a Mira900, 730-860nm and a tunable Raman fiber laser, 815-950nm) provide tunable NIR pulses with overlapping spectral tuning range.

The laser radiation is focused onto the sample material in a concofal microscope. A schematic overview is shown in Figure 4.7. The first laser source is a Ti:Sa oscillator (Coherent Mira900), emitting pulses with a tunable center wavelength between 700 nm and 900 nm at a repitition rate of 76 MHz. For the experiments in Section 4.4.7 the center wavelength was tuned between 730 nm (1.70 eV) and 860 nm (1.44 eV) with a spectral width of ∼5 nm corresponding to a pulse length of ∼400 fs. The second laser source is a customized pump-probe fiber laser prototype system (TOPTICA Photonics AG) with two output ports. The pump output emits a ∼300 fs pulse centered at 780 nm, while the probe output provides ∼100 fs pulses with a spectral center wavelength tunable from 810 nm to 960 nm. The fiber laser prototype system is extensively described in [86]. For the experiments in Section 4.4.7 only the probe output was utilized and the tuning range was used from 815 nm (1.52 eV) to 950 nm (1.31 eV) to achieve a sufficient spectral overlap of the tuning ranges of the Mira 900 and the fiber laser system. Both laser beams were spatially overlapped, attenuated and guided into the confocal microscope. A flip mirror was used to switch between the laser sources. As described in Section 4.2.2, a highly transmittive beamsplitter (Chroma 21017 Sputter-coated, non-polarizing 20/80) and a high NA objective (Nikon CFI S-Fluor 100x NA=1.3) in combination with refractive index matching immersion oil (n=1.51) were used to focus the laser radiation through the substrate into the sample material, placed on top of a thin borosilicate glass coverslip (130 μm). The generated SHG response of the material was collected by the same high NA objective in epi-detection configuration, transmitted through the beamsplitter and reflected out of the microscope body. The fundamental laser radiation was blocked in the detection pathway by a suitable optical shortpass filter (Edmund Optics, 650 nm, Shortpass Filter). Subsequently, the spectral intensity of the generated SHG signal was analyzed with a single-grating spectrometer (Acton SpectraPro 2500i) equipped with a CCD camera (Andor Newton).

4.3. Pulse-compression and pulse-characterization

For pulse shaping experiments, it is essential to begin with a transform-limited pulse as it serves as the ideal reference point for further pulse-form manipulation. A transform-limited pulse is the shortest possible pulse that can be created within a given spectral bandwidth following the time-frequency uncertainty principle and is the result of a flat spectral phase profile. This provides a clean baseline from which further pulse manipulation effects can be accurately measured and analyzed. To achieve transform-limited intrafocus laser pulses, the SLM was used to eliminate the pre-existing distortions of the spectral phase, introduced by all transmittive optical elements (mainly the polarization filter and the high NA objective, see Section 4.2.2). In Figure 4.8 the laser spectrum which propagates through the SLM and ultimately reaches the focal point of the microscope objective is shown. The edges of the spectrum are truncated by the aperture of the SLM, which is placed in the Fourier plane of the spherical mirror (see Section 4.2.2). This cropping effect influences the spectral profile that is transmitted, limiting it to a spectral width of ∼200 nm. Additionally, two phase profiles are shown in Figure 4.8, as blue dotted and dashed lines. The dark blue dashed line illustrates the actual spectral phase of the laser pulse in the focus of the microscope objective before any pulse compression correction was applied[2] and must be pre-compensated by the SLM. The light blue dotted lines illustrates the case of a flat phase, associated with a transform-limited pulse. This is the goal for the following pulse compression procedure.

Starting with a completely unknown phase relation, MIIPS was used to increase the SFG response of diffraction limited iron iodate $Fe(IO_3)_3$ nanoparticles, as described in Section 4.1.3, and to progress towards a flat phase profile. $Fe(IO_3)_3$ nanoparticles are widely recognized as a standard reference material for SHG studies due to their strong nonlinear optical response and their flat spectral phase in the relevant NIR spectral range [173, 175]. Figure 4.9 shows the result of a single MIIPS scan in panel (a) and a following second MIIPS scan, with the resulting phase correction from the first scan applied, in panel (b). While in panel (a) the intensity pattern shows a asymmetric and not equidistant course, the pattern in panel (b) are already much more symmetrical, parallel and close to the ideal course of a transform-limited pulse (white dashed lines). The process was repeated iteratively until no further significant improvement was achieved. During each iteration, the required correction phase term was calculated using Equation 4.10 and subsequently added to the spectral phase profile applied by the SLM. This iterative approach allowed for a progressive approximation of the optimal spectral phase correction.

As the intensity of the laser spectrum drops significantly at the edges, see Figure 4.8, the corresponding SHG signal intensity in Figure 4.9 above 440 nm and below 380 nm diminishes into the dark noise floor. Therefore, compressing the edges using MIIPS becomes

---

[2] This phase profile naturally is unknown at this point before the pulse compression procedure. It is shown here for clarity with the retrospective knowledge of the following procedure.

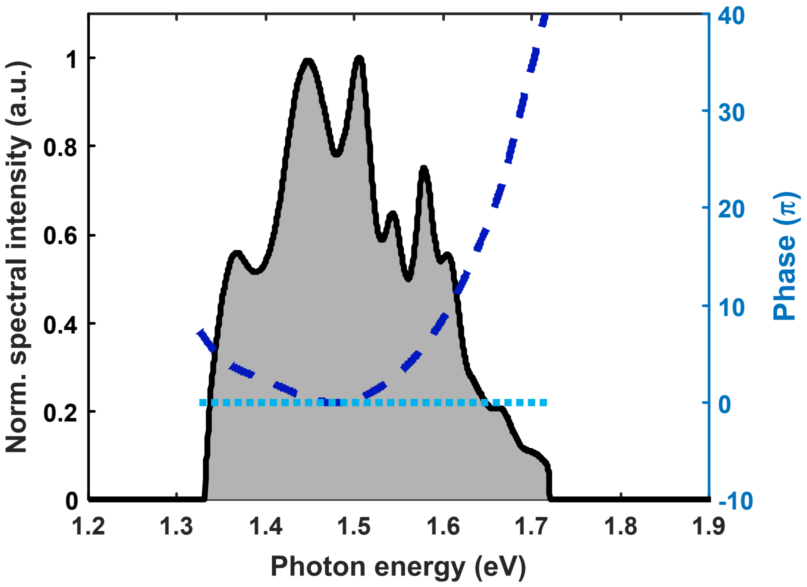

Figure 4.8.: Spectral intensity of the laser pulses in grey as passing through the pulse shaper and measured in the focus of the microscope objective. The dashed dark blue line represents the spectral phase of the laser pulses before any correction is applied by the SLM. The dotted light blue line represents the desired flat spectral phase of a transform-limited pulse.

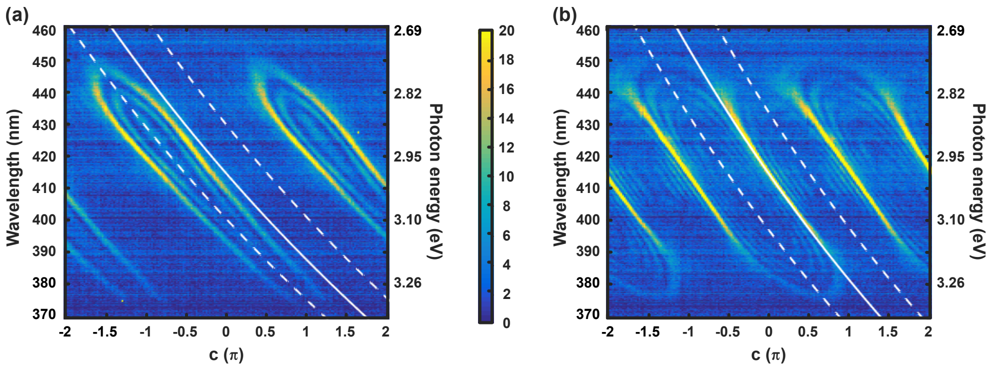

Figure 4.9.: Example of SHG intensity MIIPS scans on diffraction limited $Fe(IO_3)_3$ nanoparticles in the focus of a NA 1.3 microscope objective. While in **(a)** the maximum intensity lines are asymmetric and not equidistant to each other, after the first MIIPS correction the pattern in *(b)* are much more symmetrical and parallel. Compressing the edges of the laser spectrum using MIIPS turned out to be impractical, as the SFG intensity drops significantly above 440 nm and below 380 nm.

extremely challenging and impractical. To ensure optimal pulse compression by achieving precise fine-tuning of the spectral phase, particularly at the edges of the spectrum, the intensity of the FWM signal generated by SLG was further optimized. The third-order nonlinear susceptibility $\chi^{(3)}$ of SLG has been demonstrated to exhibit a flat response across a wide spectral range [173, 174, 176], especially in the NIR which is is interest in this work. This is reasonable, given that the physical origins of $\chi^{(3)}$ are interband and intraband electronic transitions and these transitions in graphene are not sharply resonant but distributed over a broad spectrum due to the unique electronic band structure (Dirac cone). As there is no direct analytical method to deduce the required spectral phase adjustments solely from FWM intensity measurements, a GA as an iterative approach is employed. As described in chapter 4.1.3, a GA is a robust optimization technique that can be used for linear as well as nonlinear optimization problems.

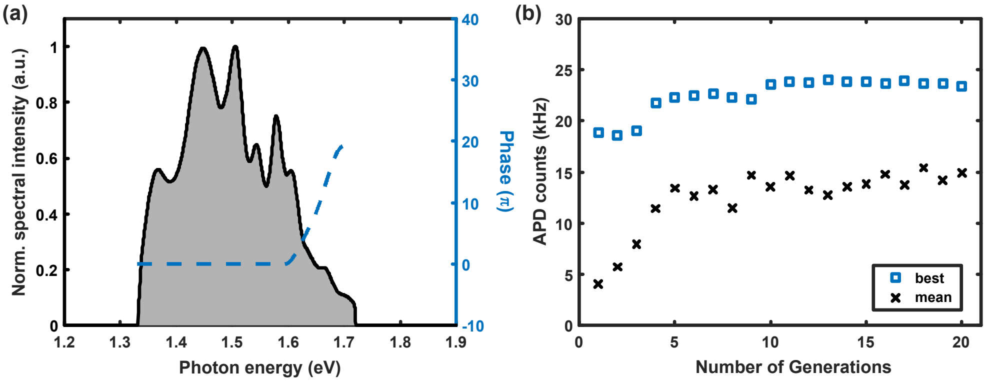

Figure 4.10.: Example of the Genetic Algorithm Procedure Optimizing the High-Energy Edge of the Laser Spectrum. The GA modifies the spectral phase at the high-energy edge of the laser spectrum, as illustrated in panel (a). The feedback signal used for optimization is the FWM intensity generated in the SLG. Panel (b) shows the best and mean FWM intensities for the individuals in each generation. The increasing trend in intensity plateaus after approximately 10 generations. The optimal phase profile, shown in panel (a), determined as the best individual across all generations, is combined with the initial phase profile to create the new phase correction.

Here the FWM intensity of SLG is employed as a feedback signal which is to be optimized. The additional phase profile is adjusted at 12 nodal points evenly distributed across the spectral target optimization range. Between these nodal points, the phase values are filled using cubic interpolation to ensure smooth transitions and continuous phase adjustments. Figure 4.10 provides an example of phase optimization for the high-energy edge of the spectrum. Panel (a) shows the laser spectrum along with the additional phase profile obtained after 20 generations of the genetic algorithm (GA). Panel (b) displays the FWM intensity, recorded as counts from the APD, throughout the GA process. The black crosses indicate the mean FWM intensity of all individuals in each generation, while the blue squares represent the FWM intensity achieved by the best individual in a given generation. The rising trend in intensity saturates after approximately 10 generations, so the procedure was terminated after the 20. generation. The optimized phase profile is determined by adding the best correction phase from the entirety of individuals of all 20 generations to the initial phase profile, which served as the starting point for the optimization process. This can be repeated iteratively and for both edges of the spectrum to further optimize the pulse compression.

The pulse quality was evaluated by performing specific characterization measurements and comparing the results with corresponding theoretical predictions. For these experiments, the SFG signal of small $Fe(IO_3)_3$ nanoparticles was employed as it is expected to be optimized by a transform-limited pulse. The simulation was performed using Equation 2.40 for a transform-limited pulse with a flat phase profile, based exclusively on the measured laser spectrum. To model a flat dispersion relation of the reference material, the second-order nonlinear susceptibility $\chi^{(2)}(\omega)$ was set constant.

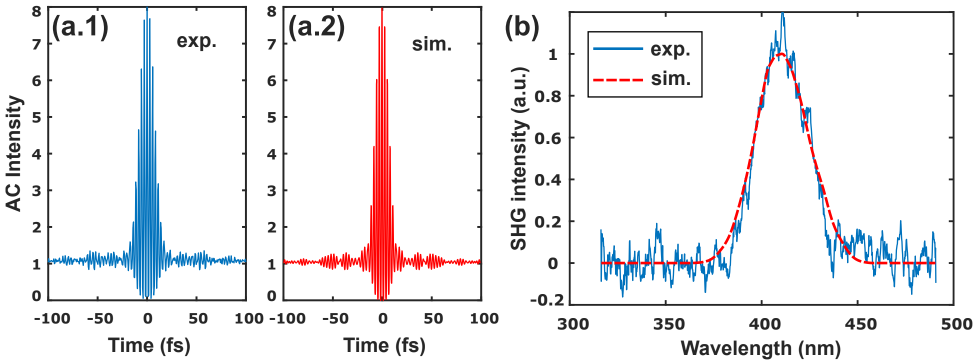

Figure 4.11.: Autocorrelation and SFG spectrum for pulse characterization. For the evaluation of successful pulse compression in panel (a.1) the interferometric autocorrelation scan of the laser pulse was compared to the simulated theoretical AC result in panel (a.2). Additionally, in panel (b) the experimental SFG spectrum of the laser pulse was compared to simulated SFG spectrum. For the simulation, using Equation 4.7, second-order nonlinear susceptibility was set constant to model a flat dispersion relation. Adapted with permission from [73]. Copyright 2024, American Chemical Society.

Figure 4.11 (a.1) displays the result of an interferometric autocorrelation (AC) scan, which aligns closely with the numerical simulation shown in (a.2). The interferometric AC scan was performed using the SLM. A cosine amplitude mask, $A(\omega) = \cos(\frac{\tau}{2} \cdot \omega)$, was applied to split the laser pulse into two identical copies without any phase difference, temporally separated by a delay time τ. Scanning τ causes the two pulse copies to partially overlap, as required for an AC measurement. Figure 4.11 (b) exhibits the experimental SFG spectrum (blue) of the same $Fe(IO_3)_3$ nanoparticle compared to the simulated SFG spectrum (red dashed line), obtained from the fundamental laser spectrum. The results of both measurements match the theoretical expectations for a transform-limited pulse well but they provide limited accuracy in the order of <100 fs^2 remaining GDD[173].

Additionally, the SFG spectra of a $Fe(IO_3)_3$ nanoparticle were recorded relative to the SOD parameter of the applied spectral phase of the laser pulse in a spectrally resolved SOD scan (see Equation 4.5). Figure 4.12 presents the experimental result of this scan in panel (a), alongside the theoretical prediction from the numerical simulation, assuming a transform-limited pulse, in panel (b). The close agreement between the experimental data and the simulation provides further evidence of successful pulse compression.

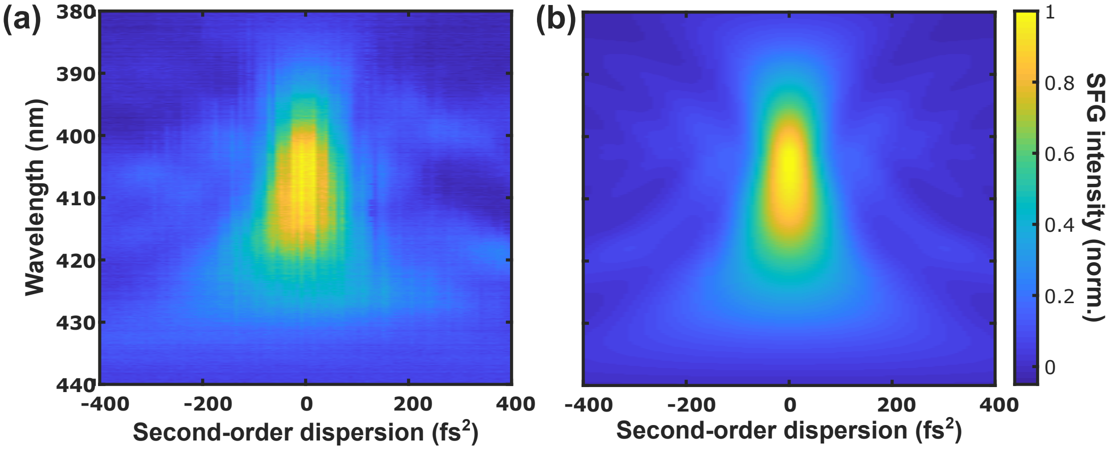

Figure 4.12.: Spectrally resolved SOD scan for pulse characterization. For the evaluation of successful pulse compression the experimental spectrally resolved SOD scan in panel (a) was compared to the simulated spectrally resolved SOD scan in panel (b) for a transform-limited pulse. Adapted with permission from [73]. Copyright 2024 American Chemical Society.

Finally, SOD/TOD phase scans according to equation 4.5 were conducted. As reference materials, $Fe(IO_3)_3$ was employed for SFG measurements, while SLG served as reference material for FWM measurements. The experimental results are compared to theoretical predictions and presented in Figure 4.13. The resulting experimental intensity patterns align closely with the numerical simulations, both in terms of the overall shape of the patterns as well as the positioning of their centers at (SOD/TOD)=(0/0). These characterization measurements are particularly meaningful, as they establish a precise reference for the experiments, performed on the 2D TMD materials later in section 4.4.

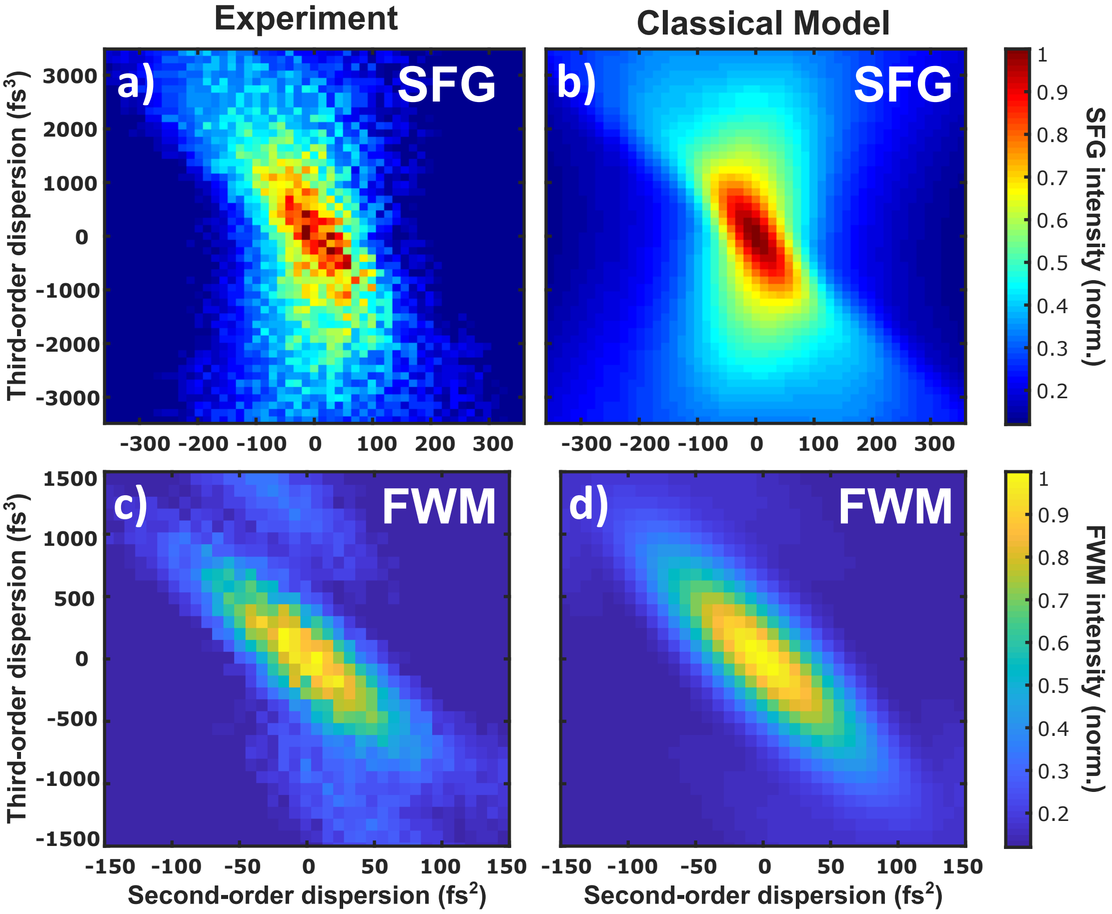

Figure 4.13.: Reference SOD/TOD scan for pulse characterization. In **(a)** the experimental results for SFG, measured on $Fe(IO_3)_3$, are presented, compared to the numerical simulation in **(b)**. In **(c)** the experimental results for FWM, measured on SLG, are presented, compared to the corresponding numerical simulation in **(d)**. Reproduced with permission from [73]. Copyright 2024 American Chemical Society.

4.4. Phase shaping of the nonlinear signal intensity in WSe_2 and $MoSe_2$

After introducing the fundamental concepts of optical phase shaping and successfully compressing the pulses to the transform-limited case, this section presents phase-control experiments on the two TMD monolayer materials, WSe_2 and $MoSe_2$, with their first excitonic resonance overlapping with the laser spectrum.

A key factor in the experiments is that the coherence time of the excitonic resonance is significantly longer than the temporal duration of the laser pulses to allow for coherent light-matter interaction. This ensures that the excitonic system retains phase memory throughout the optical excitation, enabling the coherent control over quantum states. If temporal pulse length of the laser pulse would be too long, the system cannot respond coherently, suppressing interference effects and reducing the efficiency of coherent control and signal generation. This is guaranteed by the 12 fs laser pulses with a spectral width of more than 300 meV compared to the width of the A-exciton resonance of ~ 20 meV, as presented in Figure 4.21.

First, comprehensive characterization measurements of the monolayer samples are performed. This is followed by phase-control experiments, focusing on the intensity of the FWM response in the two monolayer TMDs, and complemented by fluence-dependent measurements. Based on these findings, two numerical models are introduced to describe the experimental observations and provide deeper insight into the underlying excitonic effects. Subsequently, phase-control experiments with a specific phase shape are conducted and compared to the general phase-control measurements. Finally, the phase dependence of the SFG signal intensity is examined, following similar experimental and numerical approaches as those developed for FWM.

4.4.1. Monolayer characterization

TMD monolayers were initially localized by optical contrast and PL microscopy, followed by further characterization via SFG and FWM intensity imaging. Figure 4.14 shows raster scan intensity maps of a WSe_2 monolayer obtained using the microscope setup described in Section 4.2.2. For the PL imaging, the sample was excited by a cw laser source emitting radiation at 473 nm (2.62 eV). The radiation was attenuated to approximately 1 μW/cm^2 in the focal plane of the high-NA objective. To isolate the PL signal, a 615 nm (2.02 eV) longpass filter (Chroma hq615lp) was used to block the excitation light in the detection beam path.

The nonlinear signal images were taken using the broadband pulses of the modelocked Ti:Sa fs laser source, described in Section 4.2.2 and specific optical filters to restrict the spectral detection window and block the excitation light. For SFG a 650 nm (1.91 eV) together with a 450 nm (2.76 eV) shortpass filter (Edmund Optics Techspec Shortpass Filters) were used, while for FWM a 700 nm (1.77 eV) shortpass filter (Thorlabs FESH0700) together with a

615 nm (2.02 eV) longpass filter (Chroma hq615lp) were employed. Figure 4.14 (a) shows a clear PL signal from the monolayer, while surrounding flakes exhibit negligible emission. As discussed in Section 2.3.1, in contrast to bulk crystals, TMD monolayers possess a direct optical bandgap, making the PL intensity a clear indication of monolayer thickness. In Figure 4.14 (b), the monolayer shows a pronounced SFG signal intensity, whereas weaker signals are observed in some areas of the surrounding flakes. Since second-order nonlinear processes require a non-centrosymmetric crystal structure, SFG is only present in flakes with an odd number of layers, while those with even layer numbers exhibit negligible SFG intensity.

Figure 4.14(c) presents FWM intensity imaging, revealing a spatially uniform response from the monolayer, indicating a clean and homogeneous sample. In contrast, flakes with additional layers generate a stronger FWM signal.

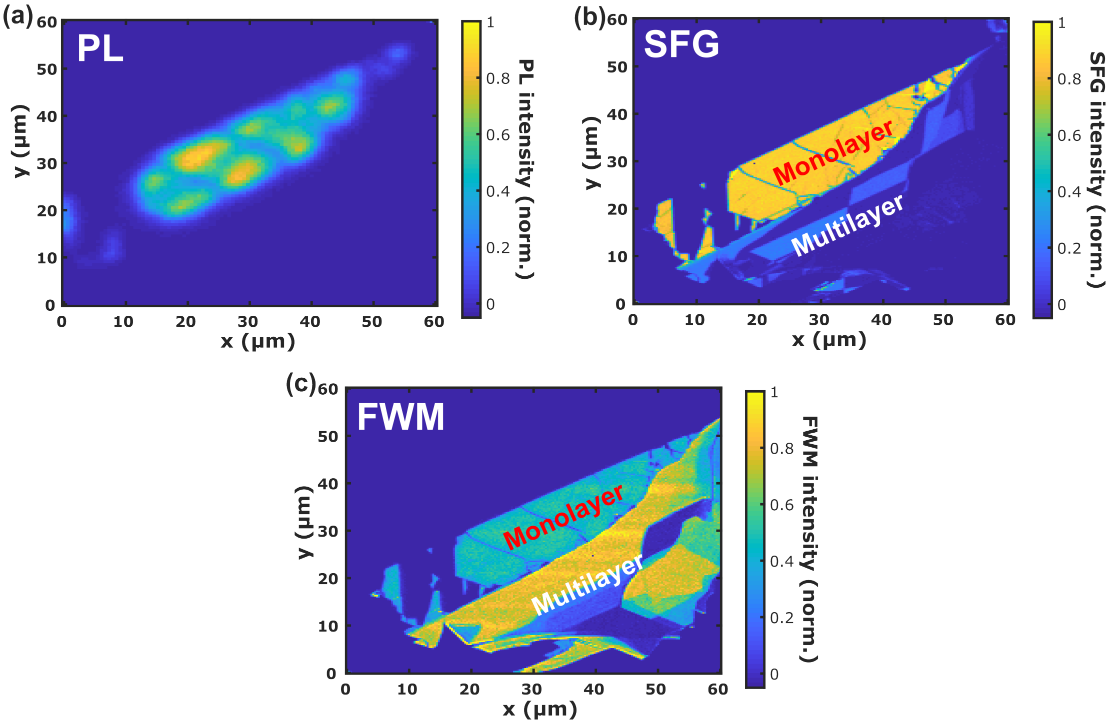

Figure 4.14.: Experimental raster scan images of a WSe$_2$ monolayer and surrounding. **(a)** PL intensity map: Due to the transition from an indirect to direct optical bandgap in the monolayer limit, a strong PL signal is emitted from the monolayer. **(b)** SFG intensity map: As SFG requires inversion symmetry breaking, the signal is observed only from flakes with an odd number of layers, with the monolayer exhibiting the strongest response. **(c)** Anti-Stokes ND-FWM intensity map: In contrast, the FWM signal is stronger in multilayer flakes compared to the uniform signal from the monolayer. Adapted with permission from [73]. Copyright 2024 American Chemical Society.

The experimental optical spectra, shown in Figure 4.15, provide additional confirmation of monolayer identification. Figure 4.15(a) displays a strong PL spectrum with a Gaussian-like shape, which is a strong indicator for monolayer thickness [43, 44]. The broad asymmetric spectral profile of the PL peak results from the presence of trions, which form at slightly lower energies than excitons [3, 60]. Figure 4.15(b) presents the high energy edge of the ND-FWM spectrum, which is located close to the excitation laser spectrum, along with the SFG spectrum at twice the laser photon energy. The red line indicates the cutoff position of the 700 nm (1.77 eV) shortpass filter used in the detection beam path. The experimental FWM spectrum was corrected for the hot linear PL contribution in the spectral range from 1.8-2.0 eV , which originates from the pulsed laser excitation [6].

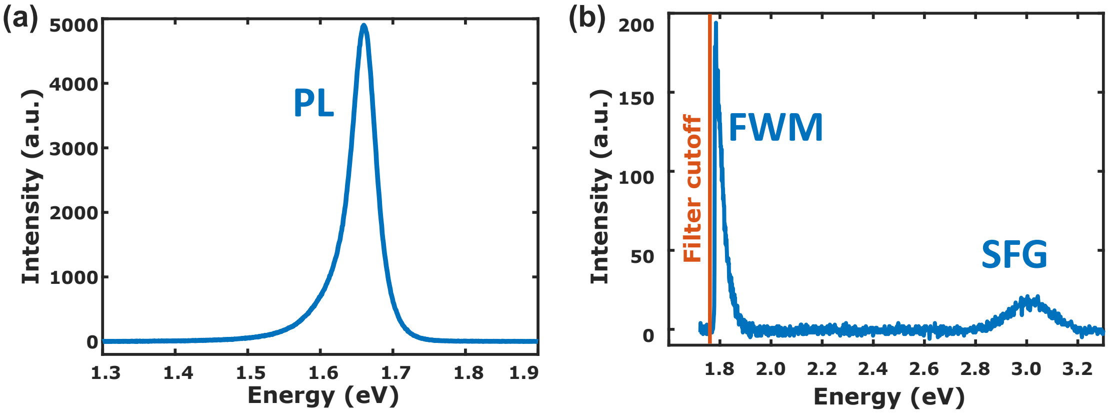

Figure 4.15.: Experimental optical spectra of the monolayer shown in Figure 4.14. **(a)** PL spectrum of the monolayer, excited at 2.62 eV. **(b)** SFG and anti-Stokes ND-FWM spectra of the monolayer, excited by the fs Ti:Sa laser source, introduced in Section 4.2.2 with a flat phase profile. Adapted with permission from [73]. Copyright 2024 American Chemical Society.

Additionally, absorption spectra for both WSe$_2$ and MoSe$_2$ monolayers were recorded by measuring the inverse relative transmission of the monolayer compared to the bare substrate. Since the reflectivity of TMD monolayers is an order of magnitude weaker than their absorption near excitonic resonances [54], this method provides a direct representation of their absorption characteristics [178]. A calibrated white light source (Thorlabs SLS201L) was used for illumination.

Figure 4.16 presents the resulting absorption spectra across the visible and near-infrared spectral range (1.3 - 3.1 eV / 400 - 950 nm). Distinct absorption peaks corresponding to excitonic resonances with common notations (A, B, C, D) are indicated in the figure. The signal-to-noise ratio decreases at higher photon energies due to the decreasing output intensity of the white light source.

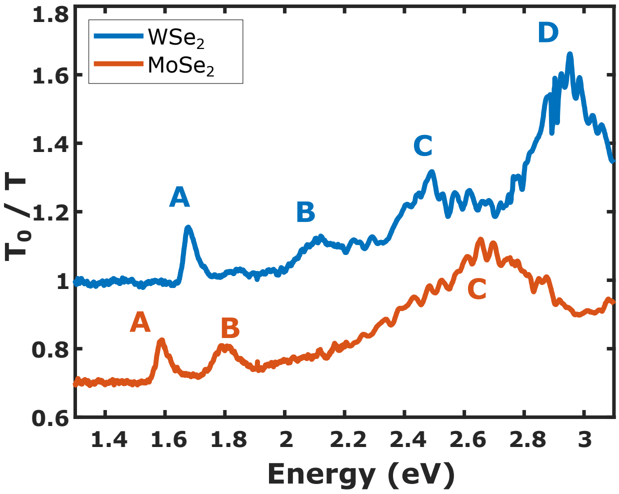

Figure 4.16.: Absorption spectra of WSe$_2$ and MoSe$_2$ monolayers. The transmission spectra of the monolayer samples were measured relative to the bare substrate, yielding the corresponding absorption spectra. Distinct excitonic resonances are clearly visible. For clarity, the MoSe$_2$ spectrum is vertically offset by 0.3. Reproduced with permission from [73]. Copyright 2024 American Chemical Society.

4.4.2. Experimental FWM phase scans

In the following, the experimental setup introduced in Section 4.2.2 was employed to perform SOD/TOD scans of the FWM signal intensity in WSe$_2$ and MoSe$_2$ monolayers. For this the FWM intensity was measured as a function of the second- and third-order dispersion parameters, as introduced in Section 4.1.1. The excitation laser intensity is given as the laser fluence F_{Laser}, defined as energy per laser pulse and focal spot area.

To isolate the spectral broadening at the anti-Stokes side caused by ND-FWM and to block the fundamental laser spectrum, the spectral detection window was restricted to 1.77 – 2.02 eV (700 – 615 nm), using appropriate optical shortpass filters. To confirm that the detected third-order nonlinear signal originates from FWM, additional double-bandpass measurements were conducted. The procedure and corresponding results are presented in Section A.2.

Figure 4.17 shows the SOD/TOD intensity pattern at a constant excitation density of 0.7 mJ/cm^2 for WSe$_2$ and MoSe$_2$ in panel (a) and (b), respectively. These patterns provide key insights into how dispersion influences FWM signal generation in these materials, if the laser spectrum is resonant with the excitonic transition. The tilted form of the scan pattern is a result of the asymmetric laser spectrum (see Section A.3). Apparently, maximum FWM intensity is not observed for the shortest excitation pulse but for distinctly phase-shaped pulses. The white cross marks the case of a transform-limited pulse, corresponding to zero second- and third-order dispersion. In the case of WSe$_2$, the FWM intensity patterns are clearly shifted to negative third-order (+8 fs^2 / -326 fs^3) and, in the case of MoSe$_2$, to negative second- and positive third-order (-52 fs^2 / +148 fs^3).

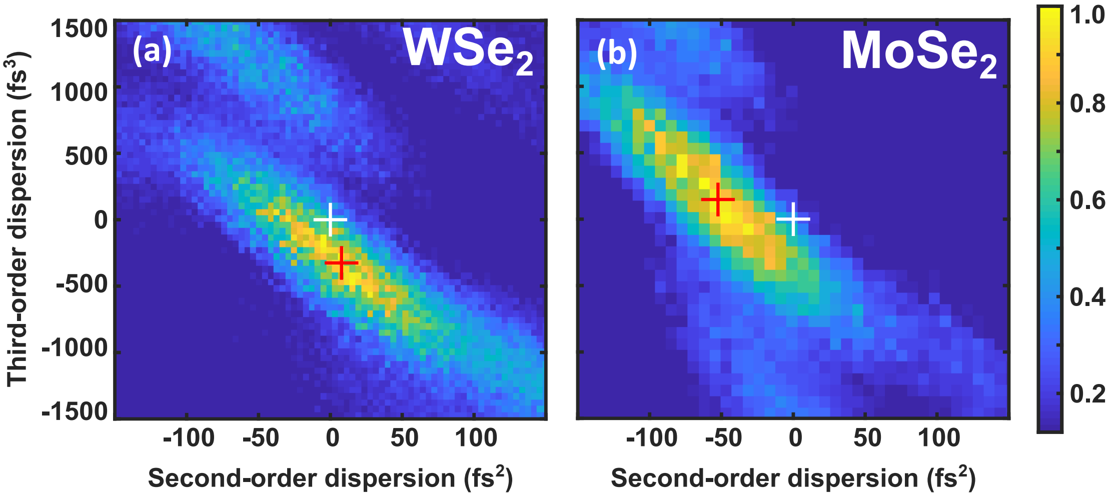

Figure 4.17.: Experimental SOD/TOD scans of the FWM signal intensity of **(a)** WSe$_2$ and **(b)** MoSe$_2$ monolayers at a fluence of 0.7 mJ/cm^2. The intensity was normalized to the maximum of each image. The strongest FWM intensity (marked by the red "+") is not observed for the transform-limited shortest pulse (marked by the white "+") but at (+8 fs^2 / -326 fs^3) for WSe$_2$ and at (-52 fs^2 / +148 fs^3) for MoSe$_2$. Adapted with permission from [73]. Copyright 2024 American Chemical Society.

This indicates that the spectral phase shift introduced by the excitonic resonance needs to be pre-compensated by the SLM in order to maximize the nonlinear signal intensity, causing the laser pulse to deviate from the transform-limited shape. This allows for coherent control over the fields involved in the multiphoton process in 2D TMDs by controlling the spectral phase. A signal enhancement factor of 1.9 is achieved for WSe$_2$ and of 1.5 for MoSe$_2$, respectively, which is defined as the ratio of maximum FWM intensity to the intensity generated by a transform-limited pulse. This effect can be interpreted as a local pulse compression, driven by the dispersion associated with the excitonic resonance of the material. This represents a solid-state, excitonic analogue to the phase-control of destructive interference of quantum pathways in broadband excitation of two-photon absorption, resonant with atomic states in rubidium gas [179], and of FWM generation in plasmonic gold nanostructures resonant with the fundamental light field [29].

While these SOD/TOD scans were conducted at a fixed excitation density of 0.7 mJ/cm^2 they provide valuable insights into the optimal phase conditions for maximizing the nonlinear signal intensity. However, aiming for a coherent control of the quantum system and eventually entering the strong-coupling regime, higher excitation intensities are required. To investigate how the nonlinear response of the system evolves with varying excitation densities, fluence-dependent measurements were conducted, providing a more comprehensive understanding of the system's behavior under different excitation conditions.

Figure 4.18 presents the result of SOD/TOD scans for low excitation density at 0.4 mJ/cm^2 in panel (a) and for high excitation density at 14.9 mJ/cm^2 in panel (b). The low excitation threshold was selected with respect to the limited detection sensitivity, so that the 2D scan

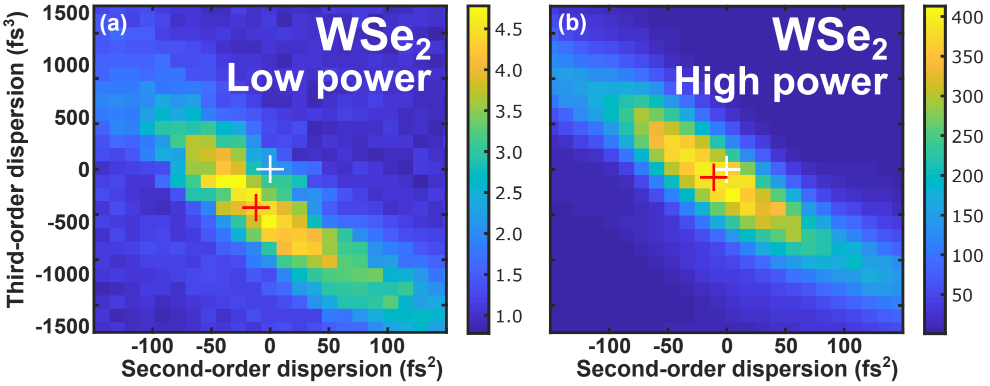

Figure 4.18.: Fluence-dependent experimental SOD/TOD scans of the FWM signal intensity of WSe$_2$ in kHz for **(a)** low fluence (0.4 mJ/cm^2) and **(b)** high fluence (14.9 mJ/cm^2). For low fluence maximum FWM intensity (marked by the red "+") is observed at (-12 fs^2 / -425 fs^3), while for high fluence maximum FWM intensity is observed at (-11 fs^2 / -87 fs^3). The FWM intensity generated by a transform-limited pulse is marked by the white "+". Adapted with permission from [73]. Copyright 2024 American Chemical Society.

pattern was still clearly detectable above the noise floor. The high fluence threshold was selected close to the damage threshold of the monolayer at ambient conditions, avoiding irreversible material modifications. The results reveal that the shift in the optimal SOD and TOD parameters of the spectral phase for maximizing FWM generation diminishes with increasing excitation fluence. At the low fluence, the maximum FWM intensity is achieved at (-12fs ^{2} / -425fs ^{3}), while at the high fluence, the maximum occurs at (-11 fs^2 / -87 fs^3). The full dataset of SOD/TOD scans for both WSe$_2$ and SLG is provided in the appendix A.1.

The same fluence-dependent series was not achieved for MoSe$_2$ because of early photodamage. The reasons for this are significantly lower generated FWM intensities [3, 180] and higher linear absorption due to more overlap of the laser spectrum with the A-exciton resonance. These factors resulted in an unreasonably small excitation density window for meaningful investigation.

The fluence dependence of the optimal phase for FWM generation in WSe$_2$ is further analyzed in Figure 4.19. Panel (a) illustrates the evolution of the optimal SOD and TOD parameter pairs as a function of pump fluence. For comparison, the corresponding phase parameter pairs for SLG, which remain close to zero across all intensities, are included as a reference, intrinsically indicating sufficient pulse compression.

The results reveal that, in WSe$_2$, deviations of the spectral phase from the transform-limited flat phase are dominated by the third-order dispersion, while the deviation in second-order dispersion remains negligible at all intensities. The third-order phase shift is most pronounced at low excitation densities and gradually diminishes as the excitation intensity increases.

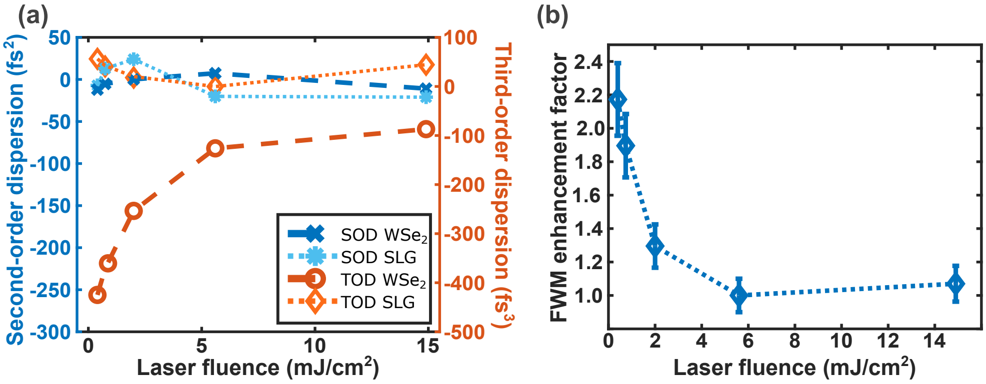

Figure 4.19.: **(a)** Fluence-dependent progression of the SOD and TOD values maximizing the FWM intensity of a WSe_2 monolayer, compared to the SLG reference measurement. For the SLG reference, at all fluences both optimal SOD and TOD values are close to zero, representing a transform-limited pulse. Similarly, the optimal SOD values for WSe_2 are close to zero. The optimal TOD values, however, exhibit a significant offset, which decreases with increasing excitation density. These values were extracted as center-of-mass determinations from the experimental SOD/TOD scans shown in Figure 4.18. **(b)** Corresponding fluence-dependent progression of the potential enhancement factor for the maximized FWM intensity of a WSe_2 monolayer, relative to the intensity generated by a transform-limited pulse. While for low excitation densities a signal enhancement factor of up to 2.2 can be achieved, for increasing pump fluence the effect diminishes and controllability is lost. Dotted and dashed lines are linear interpolations and serve as guides to the eye. Adapted with permission from [73]. Copyright 2024 American Chemical Society.

This means that the impact of selectively distorted laser pulses on optimal FWM generation is strongest at low excitation levels and, at ambient conditions, vanishes under higher excitation conditions. This indicates a loss of controllability at high excitation densities in WSe_2. Figure 4.19(b) presents the achievable FWM enhancement factor in a WSe_2 monolayer as a function of laser fluence. The enhancement factor is determined from the SOD/TOD scan series as the ratio of the maximum measured FWM intensity to the signal intensity generated by the transform-limited pulse. At low excitation densities, a signal enhancement factor of up to 2.2 is observed. However, as the pump fluence increases, the effect diminishes and ultimately the controllability is lost.

The measurement uncertainty for the SOD/TOD scans were evaluated as $\Delta_{\text{SOD}} = 20\ fs^2$ and $\Delta_{\text{TOD}} = 23\ fs^3$ based on the standard deviation of the SLG measurements. For clarity, these error bars are not shown in Figure 4.19(a). The uncertainty of the enhancement factor in Figure 4.19(b) is determined to 10%, obtained from the quadratic sum of the relative uncertainties of the individual intensity measurements.

4.4.3. Fluence-dependent absorption spectra

To further investigate this loss of phase-control of the FWM intensity, generated by a WSe_2 monolayer at high excitation densities, fluence-dependent absorption spectra were recorded using differential reflection $\Delta R/R$ spectroscopy. These experiments were conducted with the same setup described in Section 4.2.2, utilizing the spectrometer while removing any detection filters. Saturation of the CCD camera was prevented by placing neutral density attenuation filters in the detection beam path. To cover the spectral range of the A-exciton transition, the reflection of the broadband laser spectrum with a flat phase profile was used, ensuring maximum peak intensity.

$$\Delta R/R[\%] = 100 \cdot \frac{R_{\mathrm{S}} - R_{\mathrm{TMD+S}}}{R_{\mathrm{S}}} = 100 \cdot \left(1 - \frac{R_{\mathrm{TMD+S}}}{R_{\mathrm{S}}}\right) \tag{4.11}$$

Equation 4.11 describes how the reflection contrast was determined from the reflected signal of the TMD monolayer on the glass substrate, $R_{\mathrm{TMD+S}}$, and the reflected signal from the bare substrate, R_{S}. Both signals were corrected for dark noise background.

For a monolayer on a glass-air interface a 2D sheet model for the thin film can be applied to relate the reflection contrast $\Delta R/R$ at normal incidence to the sample absorption A [181]. In this model, the optical response is described by a complex sheet optical conductivity σ_s. Since the reflection contrast $\Delta R/R$ is determined by the real part of the optical conductivity, which is equivalent to the imaginary part of the dielectric function, it is directly related to the sample absorption.

$$\begin{aligned} \Delta R/R &\approx \frac{4}{n_g^2 - 1}\mathrm{Re}[Z_0\sigma_s] \\ A &\approx \frac{4}{|1+n_g|^2}\mathrm{Re}[Z_0\sigma_s] \end{aligned}$$

$$\Rightarrow A \approx \frac{n_g^2 - 1}{|1+n_g|^2} \cdot \Delta R/R \approx 0.2 \cdot \Delta R/R \tag{4.12}$$

Thus, Equation 4.12 provides an estimate for the absorption of the TMD monolayer based on the reflection contrast. Here, $n_g = 1.51$ denotes the refractive index of the glass substrate and $Z_0 = 1/(\epsilon_0 c)$ is the impedance of free space.

Finally, Figure 4.20(a) clearly shows the dependence of the A-exciton absorption peak on the laser fluence F_{Laser}. The left axis represents the measured differential reflection contrast, determined using Equation 4.11, while the right axis shows the corresponding relative absorption, calculated from Equation 4.12. The extracted peak absorption of the A exciton in WSe_2, approximately 4%, derived from a measured reflection contrast of 19%, is in good agreement with previously reported values for monolayers on a glass substrate [54]. Note that the differential reflection contrast $\Delta R/R$ was repeatedly recorded at the same sample position while incrementally decreasing the excitation density from the highest (14.9 mJ/cm^2) to the lowest (60nJ/cm^2) laser fluence. This approach ensures that the observed reduction in the absorption peak is not caused by any potential sample degradation due to high laser fluences.

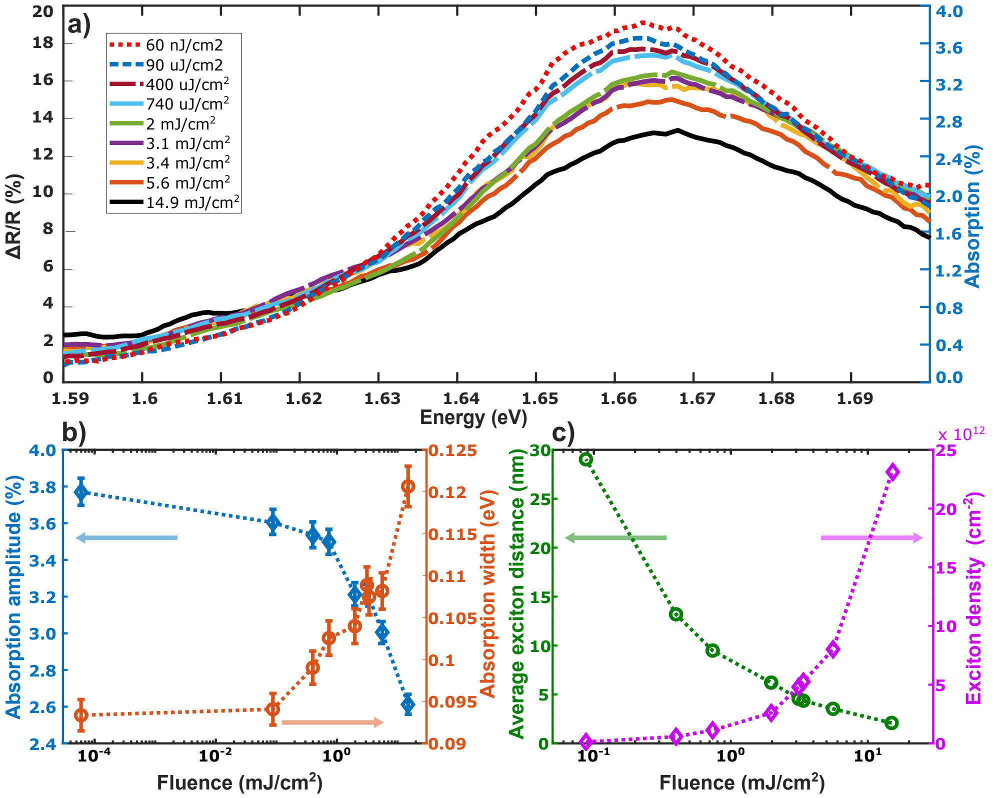

Figure 4.20.: (a) Fluence-dependent absorption spectra of a WSe$_2$ monolayer recorded with a broadband excitation spectrum, derived from differential reflection measurements $\Delta R/R$. Absorption amplitude and width were obtained by fitting an asymmetric peak function to the spectra. **(b)** As the fluence increases, the absorption amplitude (blue diamonds) decreases, while the spectral width (red circles) broadens. **(c)** Calculated average spacing between excitons generated per pulse (green circles) and the corresponding exciton density (purple diamonds), derived from the input photon density per pulse and the absorption spectra shown in (a). Dotted lines in (b) and (c) are linear interpolations and serve as guides to the eye. Reproduced with permission from [73]. Copyright 2024 American Chemical Society.

As the excitation density increases, the absorption amplitude decreases, while the width (FWHM) of the peak broadens. Both parameters were determined by fitting an asymmetric peak function to the data. Their evolution as a function of excitation fluence is shown in Figure 4.20(b), with uncertainties derived from the fit.

Ruppert et al. attribute the reduction in absorption and broadening of the excitonic peak, in their experiments observed via femtosecond broadband pump-probe spectroscopy, to Pauli blocking and excitation-induced dephasing (EID) [15]. Complementary two-dimensional Fourier Transform Spectroscopy (2DFTS) measurements by Moody et al. reveal contributions from exciton-exciton and exciton-phonon interactions to contribute to EID in monolayer WSe_2. The enhanced role of Coulomb-mediated processes is consistent with the reduced dielectric screening in these atomically thin systems [182]. Theoretical investigations by Katsch et al. identify exciton-exciton scattering as the primary mechanism behind EID in monolayer TMDs [183].

To further understand this, the fluence-dependent absorption spectrum in Figure 4.20(a) can be utilized to estimate the density of absorbed photons per pulse, which is assumed to be equivalent to the density of created excitons. The exciton density is calculated by convolution of the absorption spectrum $A(\omega)$ with the fundamental laser spectrum $I_{\text{laser}}(\omega)$ and normalizing this to the integral of the spectral laser intensity:

$$n_X = \frac{F_{\text{Laser}}}{\hbar\omega} \cdot \frac{\int A(\omega) \cdot I_{\text{Laser}}(\omega) d\omega}{\int I_{\text{Laser}}(\omega) d\omega} \tag{4.13}$$

Here, F_{Laser} denotes the corresponding laser peak fluence (energy per pulse and area) while $\hbar\omega$ is the photon energy. The calculated exciton density n_X in Equation 4.13 gives the number of excitons per unit area. The exciton spacing, i.e. the average distance between individual excitons, gives an estimate of how closely packed the excitons are and therefore is related to the area each exciton occupies. Assuming a uniform exciton distribution, their positions can be approximated as forming a square lattice.

$$d_X = \frac{1}{\sqrt{n_X}} \tag{4.14}$$

Figure 4.20(c) shows both parameters, the average spacing between excitons created per laser pulse (green cicles, left axis) together with the estimated density of excitons created per pulse (purple diamonds, right axis) as a function of the laser peak fluence. At low excitation conditions, the exciton density is on the order of 10^{12} cm^{-2}, corresponding to an exciton spacing of more than 10 nm. For comparison, the exciton Bohr radius in WSe_2 typically ranges from $1 - 2$ nm, so at $n_X = 10^{12}$ cm^{-2} excitons are still relatively well separated [12, 13, 184].

At the highest excitation densities in this experiment, however, the exciton density reaches $2 \cdot 10^{13}$ cm^{-2}, reducing the nominal average exciton spacing to the order of the exciton Bohr radius. This increased density leads to significant wavefunction overlap between neighboring excitons, enhanced Coulomb screening and effectively a reduction of the exciton binding energies. As a result, the semiconducting monolayer undergoes a Mott transition, shifting from an insulating excitonic regime to an electron-hole plasma, where excitons are no longer bound states and their characteristic resonance vanishes [4, 6–9, 185].

Additionally, the screening of Coulomb interactions between charge carriers results in a bandgap renormalization [7], which can lead to a shift of the absorption peak position, depending on the exciton density. Apparently, below a threshold of $n_X \approx 2 \cdot 10^{12}$ cm^{-2} the absorption peak experiences a red-shift, due to an increased plasma screening and bandgap renormalization. As the bandgap E_{gap} decreases faster than the binding energy E_b, the exciton resonance shifts to lower energies. This is accompanied by an exciton-exciton attraction, similar to the case of atomic van der Waals forces. Above this threshold, though, the exciton density becomes so high that excitons repel each other due to the Pauli exclusion principle of overlapping wavefunctions. Therefore, the energy cost to create an extra exciton increases. This corresponds to a blue-shift of the resonance energy [4]. Consequently, the absorption curves in Figure 4.20(a) also show a blue-shift of the peak position.

4.4.4. Classical model

The experimental results revealed that a non transform-limited pulse optimizes the FWM signal generation of TMD monolayers for the first excitonic transition overlapping with the fundamental laser spectrum and a strong fluence dependence of this effect. To further analyze this, classical simulations based on the numerical prediction of the FWM intensity in Equation 2.53 were carried out.

The measured fundamental laser spectrum, $I(\omega)$ was used as an input parameter, from which the electric field in the frequency domain could be determined. To simulate the SOD/TOD scan, the complex electric field was modified by adding a complex spectral phase profile based on the corresponding SOD and TOD parameters.

$$E(\omega) = \sqrt{I(\omega)} \cdot e^{i\varphi(\omega)} \tag{4.15}$$

with

$$\varphi(\omega) = \frac{1}{2} \cdot SOD \cdot (\omega_0 - \omega)^2 + \frac{1}{6} \cdot TOD \cdot (\omega_0 - \omega)^3 \tag{4.16}$$

As this numerical simulation aims for the comparison of the effect of different phase profiles on the generated FWM intensity, the absolute value is disregarded and any proportionality constants are neglected in the simulation.

$$I_{\text{FWM}}(\omega) \propto \left| \iint_{\omega_{\text{min}}}^{\omega_{\text{max}}} \chi^{(3)}(\omega) \cdot E(\omega_1) E(\omega_2) E^*(\omega_3) \;\; d\omega_1 d\omega_2 d\omega_3 \right|^2 \tag{4.17}$$

The nonlinear response of the material for FWM generation is specified by the third-order nonlinear susceptibility $\chi^3(\omega_{\text{FWM}}; \omega_1, \omega_2, \omega_3)$. As this parameter depends on the frequencies of all four interacting waves, the experimental determination over a broad frequency range, as used in this work, is highly challenging. No direct data was available for the relevant spectral range.

For this reason, the nonlinear susceptibility $\chi^(3)$, necessary for the determination of the FWM intensity in Equation 4.17, was modeled using a Miller's rule approach. As introduced in Section 2.1.1, Miller's rule is an empirical model to estimate the nonlinear susceptibility $\chi^{(n)}$ of a material based on its linear susceptibilities $\chi^{(1)}(\omega)$ at the corresponding frequencies. It provides a simple way to approximate higher-order nonlinearities when direct data is unavailable. Miller's rule states that the nonlinear susceptibility can be approximated as the product of the linear susceptibilities at the fundamental frequencies:

$$\chi^{(3)}(\omega_{\text{FWM}};\omega_1,\omega_2,\omega_3) \propto \chi^{(1)}(\omega_1)\cdot\chi^{(1)}(\omega_2)\cdot\chi^{(1)}(\omega_3)\cdot\chi^{(1)}(\omega_{\text{FWM}}) \tag{4.18}$$

Originally developed for SHG in transparent nonlinear materials [27], its applicability was recently demonstrated for FWM in plasmonic nanoantennas [29]. It further suggests that materials with a high linear susceptibility exhibit stronger nonlinear optical responses. This is supported by studies indicating that both the second- and third-order nonlinear susceptibilities, $\chi^{(2)}$ and $\chi^{(3)}$, become particularly large in the spectral range close to the excitonic resonances [3, 64, 65, 72, 186].

As introduced in Section 2.1.1, the linear susceptibility $\chi^{(1)}(\omega)$ can be modeled as a single Lorentzian resonance.

$$\chi^{(1)}(\omega) \propto \frac{1}{\omega_0 - \omega - i\gamma} \tag{4.19}$$

The center frequency ω_0 and linewidth γ of the A-exciton resonance were extracted from the absorption spectra, shown in Figure 4.16, by fitting a Lorentzian lineshape to the corresponding peak. The resulting overlap of the modeled Lorentzian resonance with the broadband laser spectrum is illustrated in Figure 4.21.
The function $\chi^{(1)}$ behaves like a local complex field enhancement factor, combining the resonant enhancement at the excitonic transition frequency with the associated arctan π-step phase shift.

As the calculation of the FWM intensity in the frequency space takes great numerical effort, in the model the FWM response of the material is calculated in the time domain and the FWM spectrum is obtained via Fourier transformation. To include the material response $\chi^{(1)}(\omega)$, the linear polarization was determined as:

$$P^{(1)}(\omega) = \chi^{(1)}(\omega)\cdot E(\omega) \tag{4.20}$$

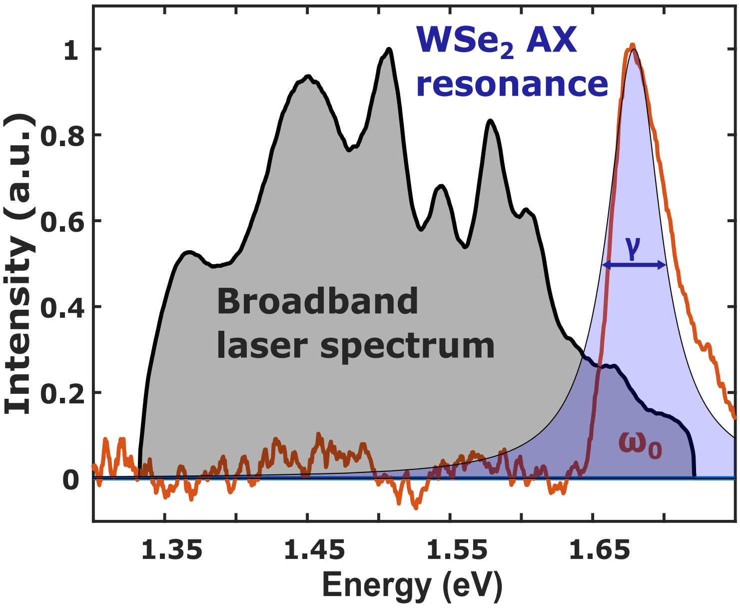

Figure 4.21.: Laserspectrum together with the A-exciton resonance of WSe_2 The broadband laser spectrum (gray shaded) overlaps with the A-exciton resonance of WSe_2. The modeled Lorentzian function (blue shaded) fits to the measured absorption curve (red). Adapted with permission from [73]. Copyright 2024 American Chemical Society.

Subsequently, the corresponding pulse shape in the time domain was obtained using the inverse Fourier transformation routine:

$$P^{(1)}(t) = \mathfrak{F}^{-1}\Big\{P^{(1)}(\omega)\Big\} \tag{4.21}$$

In the time domain the third-order nonlinear polarization, responsible for FWM generation, was computed as:

$$P^{(3)}_{FWM}(t) = \Big[P^{(1)}(t)\Big]^2 \cdot P^{(1)}(t)^* \tag{4.22}$$

Here, the * markes the complex conjugate. Finally, the nonlinear polarization for the FWM signal in the frequency domain is obtained by Fourier transformation:

$$P^{(3)}_{FWM}(\omega) = \mathfrak{F}\Big\{P^{(3)}_{FWM}(t)\Big\} \tag{4.23}$$

To summarize the procedure outlined above, Equation 4.24 consolidates all steps described in Equations 4.20-4.23, yielding a result equivalent to Equation 4.17. The integration in the frequency domain was effectively carried out as a multiplication of the electric fields in the time domain.

$$I^{(3)}_{FWM}(\omega) \propto \left|P^{(3)}_{FWM}(\omega)\right|^2 \propto \left|\mathfrak{F}\Big\{\left(\mathfrak{F}^{-1}\left\{\chi^{(1)}(\omega)\cdot E(\omega)\right\}\right)^2 \cdot \mathfrak{F}^{-1}\left\{\chi^{(1)}(\omega)\cdot E(\omega)\right\}^*\Big\}\right|^2 \tag{4.24}$$

$P^{(3)}_{FWM}(\omega)$ now provides the spectral information about the FWM signal generated by the electric field $E(\omega)$ in a material with the linear susceptibility $\chi^{(1)}$.

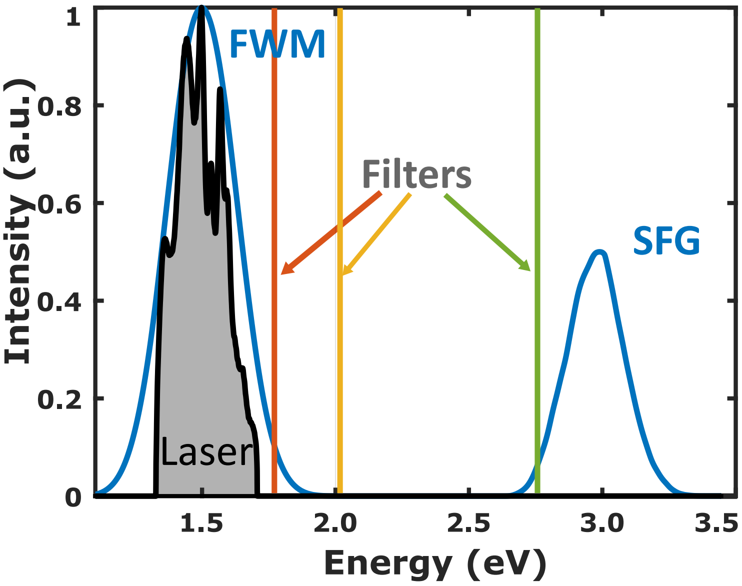

Figure 4.22.: Nonlinear spectra produced by the classical model. The fundamental laser spectrum (black shaded area) causes a nonlinear polarization resulting in a SFG and a FWM response (blue) of the material with the linear susceptibility $\chi^{(1)}$. Nonlinear spectra are not calibrated. Spectral integration over the relevant frequency range yields the signal intensity. Red, yellow and green lines mark the integration boundaries, representing optical filters in the experiment. Reproduced with permission from [73]. Copyright 2024 American Chemical Society.

The resulting FWM spectrum is presented in Figure 4.22 alongside the corresponding SFG spectrum, determined analogously using Equation 4.25. This will be discussed further in Section 4.4.7.

$$I^{(2)}_{SFG}(\omega) \propto \left|P^{(2)}_{SFG}(\omega)\right|^2 \propto \left|\mathfrak{F}\Big\{\left(\mathfrak{F}^{-1}\left\{\chi^{(1)}(\omega)\cdot E(\omega)\right\}\right)^2\Big\}\right|^2 \tag{4.25}$$

The intensity of the nonlinear optical spectra for FWM and SFG is not calibrated, neither in absolute terms nor relative to each other, since arbitrary proportionality constants were used in the calculations to enhance clarity. The FWM spectrum envelopes the fundamental laser spectrum, being slightly broader and ranging up to 1.9 eV at the high-energy edge. Spectral integration over the relevant frequency range (1.77-2.02 eV / 450-350 nm), marked by red and yellow lines in Figure 4.22, yields the signal intensity. This result can be directly compared with the experimental data presented in Section 4.4.2.

As a result, the SOD/TOD scan pattern, experimentally obtained in Section 4.4.2 and shown in Figure 4.17, can be simulated. Figure 4.23 shows a comparison of the experimental ($F_{\text{laser}} = 0.7$ mJ/cm^2) and the classical model results.

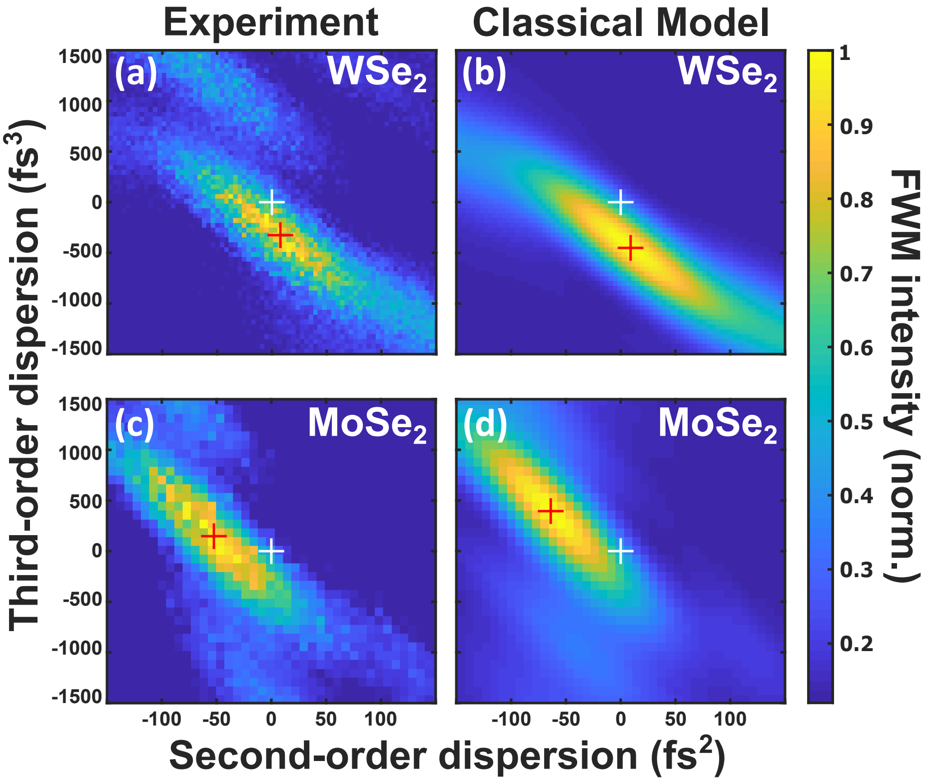

Figure 4.23.: Comparison of experimental and numerical SOD/TOD scans for optimal FWM signal intensity for WSe$_2$ (**a**, **b**) and MoSe$_2$ (**c**, **d**) monolayers. The experimental results, obtained at a fluence of 0.7 mJ/cm^2, were previously shown in Figure 4.17. The numerical results were obtained from the classical model, considering only the fundamental laser spectrum along with the peak energy and linewidth of the exciton resonance. The optimal FWM signal is indicated by the red "+", while the transform-limited shortest pulse is marked by the white "+". A slight discrepancy between the experimentally observed and theoretically predicted phase shifts for maximum FWM generation is attributed to the fluence dependence of the phase shift. Reproduced with permission from [73]. Copyright 2024 American Chemical Society.

The classical model is seen to reproduce the experimental phase dependence of the FWM intensity in WSe_2 and $MoSe_2$ notably well at low excitation densities. However, the experimentally observed optimal phase shifts are slightly smaller than those predicted by the model. This discrepancy can be attributed to the fluence dependence of the phase shift observed in the experiments. Since the model operates without any free parameters, its only inputs are the fundamental laser spectrum, along with the center energy and linewidth of the A-exciton peak, obtained from low-intensity absorption spectra (Figure 4.16). Consequently, a fluence dependence is not inherently included in the model. However, the broadening of the A-exciton linewidth with increasing excitation density, as observed in Figure 4.20(a), can be implemented to account for EID of excitons, effectively integrated in the absorption spectrum.

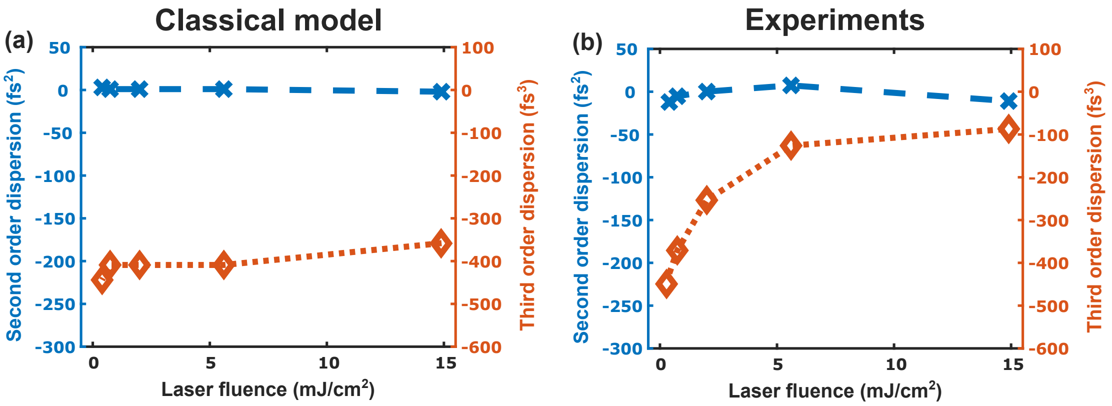

Figure 4.24.: Comparison of **(a)** classical model and **(b)** experimental SOD/TOD values for optimal FWM signal intensity in WSe_2. The fluence dependence in the classical model is incorporated by accounting for the broadening of the A-exciton absorption peak with increasing excitation density, reflecting EID of the resonance. The optimal SOD values (blue crosses) are close to zero for both, model results and experimental results. However, although the model predicts a reduction in the TOD parameter (red diamonds) with increasing fluence, it does not capture the strong experimentally observed decrease. Dotted and dashed lines are linear interpolations and serve as guides to the eye. Adapted with permission from [73]. Copyright 2024 American Chemical Society.

Figure 4.24 compares the evolution of the SOD and TOD parameters in the classical model (a) with the experimental results (b). While the model qualitatively reproduces the experimentally observed reduction of the TOD parameter, the decrease is significantly less pronounced within the investigated fluence range. This suggests that EID of the resonance, manifested as broadening of the absorption peak, is, by itself, insufficient to fully account for the diminishing influence of the excitonic resonance on the optimal spectral phase for FWM generation.

4.4.5. Quantum-mechanical model

To further explore the dependence of excitation density on the phase shift in SOD/TOD scans, exciton population effects, such as phase-space filling, needs to be incorporated. This requires a quantum-mechanical approach, going beyond the classical description. The model used in this work is based on the time-dependent solution of density-matrix dynamics, derived from the *Von Neumann master equation.* This approach utilizes a simplified state description of specific two-level-systems and was recently applied to describe Rabi flopping effects in SHG spectra, as well as the influence of delay time between two laser pulses on SHG and FWM, in WSe_2 at cryogenic temperatures [32, 148]. The simulations of SOD/TOD scans were carried out by Dr. Sebastian Bange from the research group of Prof. John M. Lupton at the Department of Physics, University of Regensburg.

The model calculates the material polarization in the time-domain $P(t) \propto \sum_{j,k} \mu_{jk}\rho_{jk}$, which is induced by the external laser field and serves as the source term for scattered radiation, based on the induced dipole moment μ and the density matrix ρ. Spectral analysis of the nonlinear signal intensity for FWM is performed in the frequency domain. The time evolution of the density matrix dynamics is solved numerically, based on the Lindblad master equation. The concept has been introduced in Section 2.1.4.

$$\frac{d\rho}{dt} = -\frac{i}{\hbar}[H,\rho] + \sum_j \left(L_j \rho L_j^\dagger - \frac{1}{2}\{L_j^\dagger L_j, \rho\} \right) \tag{4.26}$$

The simplified state space consists of a ground state $|1\rangle$ and higher energy states $|j\rangle$ with $j = 2, 3, 4$ to describe the first three excitonic excitaions.

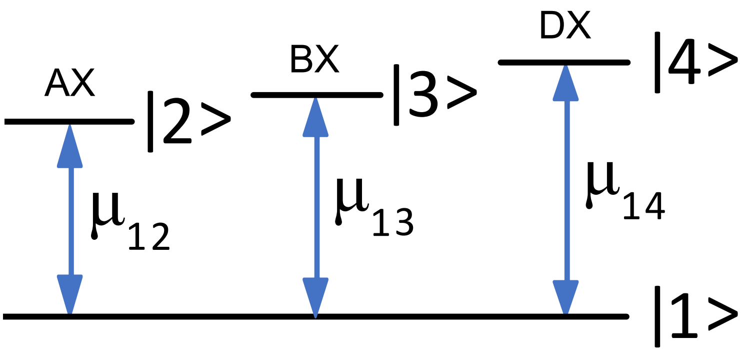

Figure 4.25.: Schematic illustration of the simplified state space for the quantum-mechanical model. The groundstate is labels as $|1\rangle$. The first three excitonic excitation states, referred to as AX, BX, DX are labeled $|2\rangle$, $|3\rangle$, $|4\rangle$. The transition dipole moments are labeled μ_{12}, μ_{13}, μ_{14}.

Quantum jump operators for spontaneous emission are given by $L_j = \sqrt{\gamma_j}\,|1\rangle\langle j|$ with the decay rate γ_j. These operators result in both off-diagonal dephasing and on-diagonal probability redistribution within the density matrix. The Hamiltonian is constructed as $H_{jj} = E_j$ and $H_{jk} = -\mu_{jk}\mathcal{E}(t)$ with $j \neq k$, where E_j is the energy of the state $|j\rangle$. The transition dipoles μ_{jk} are linked to the the off-diagonal elements ρ_{jk}. $\mathcal{E}(t)$ is the time-dependent electric field. For simplicity, vectorial properties of the electric field and resulting polarization are neglected. The experimental laser spectrum for an unchirped pulse serves as the basis for the time-domain electric field, which is modified by a spectral phase in the SOD/TOD scans according to Equation 4.5. The time evolution is calculated over an 800 fs interval with a resolution of 0.05 fs. By fitting the experimental absorption spectrum of WSe_2, shown in Figure 4.16, the exciton resonance energies and decay rates were determined, as summarized in the table below:

Exciton	Energy E (eV)	Linewidth $\hbar\gamma$ (eV)
A	1.676	0.045
B	2.102	0.160
D	2.952	0.351

Table 4.1.: Exciton energies and decay rates of WSe_2 for the quantum-mechanical model

From the same absorption spectrum, the transition dipole moments μ_{13}/μ_{12} and μ_{14}/μ_{12} were determined relative to the first excitonic transition. For absolute calibration, μ_{12} was extracted by comparing the simulated absorption spectra with the experimental fluence-dependent absorption spectrum in Figure 4.20. From this procedure, the transition dipole moments were determined.

Transition	Dipole moment (e·nm)
μ_{12}	0.046
μ_{13}	0.065
μ_{14}	0.187

Table 4.2.: Absolute values for the transition dipole moments of WSe_2 for the quantum-mechanical model

Figure 4.26 presents the simulated SOD/TOD scan patterns obtained from the quantum-mechanical two-level model for the A-exciton resonance os WSe_2 only. At low excitation fluences in panel (a), the model qualitatively reproduces the optimal dispersion terms observed in both the low-fluence experiments and the classical model. However, as the excitation density increases to values similar to the experimental maximum in panel (b), the implicit fluence dependence of the two-level system, accounting for bleaching of the excitonic transition, fails to fully capture the experimentally observed reduction of the TOD parameter at high fluences. Notably, when the excitation fluence is numerically increased to ten times the experimental maximum, in panels (c) and (d), the quantum-mechanical model does predict a pronounced reduction of the third-order dispersion parameter qualitatively, aligning with the experimental trend. However, such extreme fluence levels exceed the material's damage threshold under ambient conditions.

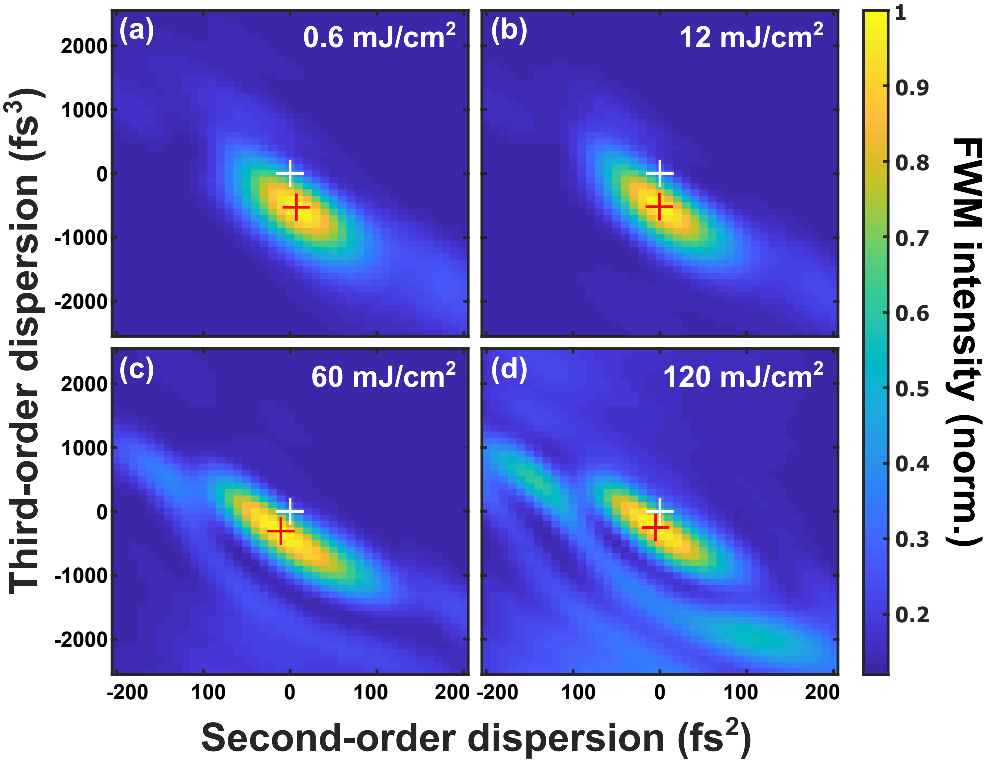

Figure 4.26.: Simulated SOD/TOD scan pattern for WSe_2 from the quantum-mechanical model for different laser fluences. The optimal SOD/TOD value case is marked by an red "+", while the white "+" markes the transform-limited case. At a low excitation density **(a)**, the model reproduces the experimentally observed optimal phase shift towards negative TOD values. However, at the highest excitation densities applied in the experiments **(b)**, the model fails to predict the reduction of the TOD value for the optimal spectral phase. This suggests that the implicit fluence dependence of the model based purely on ground state bleaching seems is insufficient to explain the effect. For excitation densities ten times higher than in the experiments, **(c)** and **(d)**, the model shows the reduction of optimal TOD, along with additional features indicating the onset of Rabi flopping. Reproduced with permission from [73]. Copyright 2024 American Chemical Society.

The issue that the quantum-mechanical model fails to predict the trend of decreasing TOD value with increasing excitation density as observed experimentally is further illustrated in

Figure 4.27. Similar to the classical model compared to the experimental results in Figure 4.24, the quantum-mechanical model shows a slight decrease of the TOD values with increasing laser fluence but does not reproduce the strong decrease experimentally observed within the investigated fluence range.

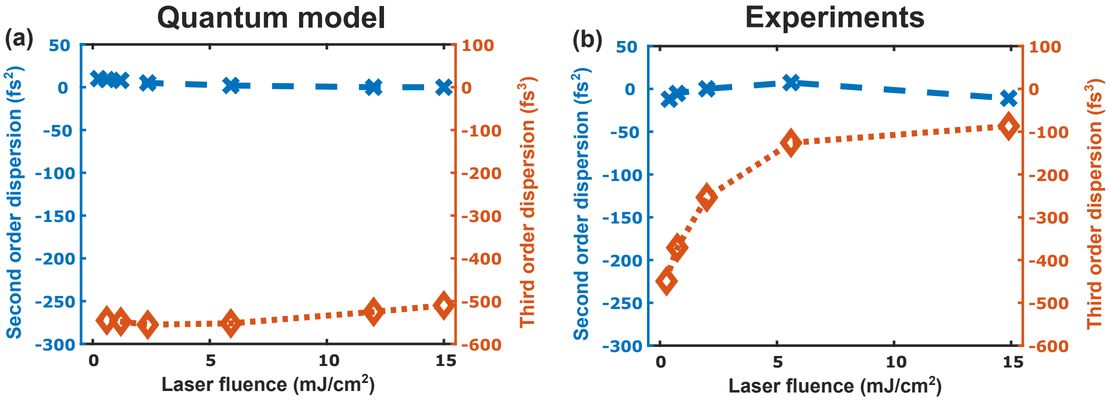

Figure 4.27.: Comparison of **(a)** quantum model and **(b)** experimental SOD/TOD values for optimal FWM signal intensity in WSe_2. While the resulting optimal SOD values (blue crosses) are close to zero for both, model and experimental results, the resulting decrease of the TOD parameter (red diamonds) does not match the experimental observation. The model fully assigns the experimentally observed reduction in absorption to ground state bleaching. Dotted and dashed lines are linear interpolations and serve as guides to the eye. Adapted with permission from [73]. Copyright 2024 American Chemical Society.

Interestingly, in an extended fluence range, up to ten times the fluence that was experimentally accessible, due to the damage threshold of the monolayer material at ambient conditions, the quantum-mechanical model predicts a stronger decrease of the optimal TOD value. This extended fluence range is presented in Figure 4.28.

Intriguingly, in this high-fluence regime, the density matrix approach predicts pronounced and structured features in the SOD/TOD scan patterns shown in panels (c) and (d). These features cannot be captured by the classical theory and are attributed to the onset of Rabi flopping. As the excitation density increases, the Rabi frequency $\Omega_R(t) = \frac{\mu \cdot E(t)}{\hbar}$, defined by the external electric field $E(t)$ and the transition dipole μ, becomes sufficiently large such that the coherence time exceeds the Rabi period, $\tau_{\text{coh}} > \frac{1}{\Omega_R}$. In this regime, Rabi oscillations become observable, as the system can undergo at least one coherent cycle within its coherence time. This suggests that, beyond a certain excitation density, exceeding the damage threshold of the material in the presented experiments at ambient conditions, coherent population oscillations might become significant, adding further complexity into the nonlinear optical response. However, as discussed in Section 4.4.3, higher excitation densities also lead to enhanced EID, which counteracts the benefits of the increased Rabi frequency by reducing the coherence time.

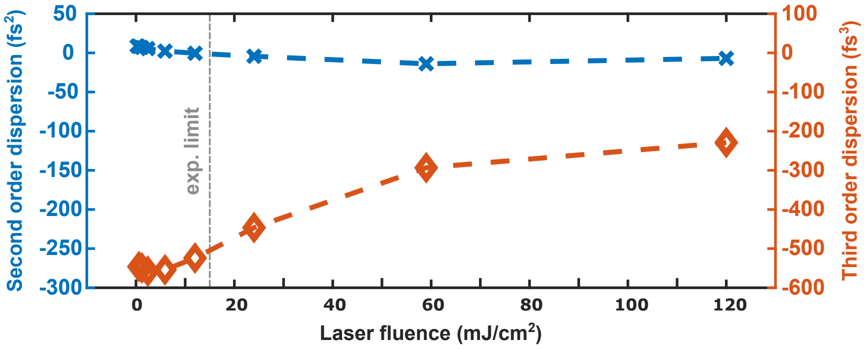

Figure 4.28.: Optimal SOD/TOD values from the quantum-mechanical model as a function of laser fluence in an extended fluence range. The results of the quantum-mechanical model are presented over an extended fluence range, approximately ten times larger than what was experimentally accessible, due to the damage threshold of the material. Within this range, the model predicts a more pronounced decrease in the optimal TOD value (red circles), comparable to the experimental observations. The optimal SOD values (blue crosses) remain close to zero. Dashed lines are linear interpolations and serve as guides to the eye. Reproduced with permission from [73]. Copyright 2024 American Chemical Society.

The results of the quantum-mechanical model show that while it can qualitatively describe the experimental findings, it fails to accurately predict the inherent power-dependence of the TOD value. This behavior is crucially depending on the input parameters, particularly the values of the transition dipole moments μ. The applied procedure likely overestimates these values, as the experimentally observed reduction in absorption with increasing fluence was entirely attributed to ground state bleaching. In fact, additional contributions from attractive and repulsive exciton-exciton, exciton-charge and exciton-phonon interactions also play a role and influence the power dependence of the absorption spectrum, as discussed in Section 4.4.3.

For the highest excitation densities realized experimentally, Figure 4.20 shows that the average exciton density reaches 10^{13} cm^{-2}, meaning the average exciton spacing is on the order of the exciton Bohr radius [12, 48, 184]. In this regime, the increased screening of the Coulomb interaction leads to a transition from bound excitons to an electron-hole plasma, known as the Mott transition [6–9, 185]. This transition likely reduces the dominance of excitonic resonances over the optical properties of the monolayer and in particular the phase shifts in the experimental SOD/TOD scans.

4.4.6. Experimental π-step phase scans

The SOD/TOD phase scans to determine the optimal pulse shape for nonlinear signal generation in 2D TMDs, as discussed experimentally in Section 4.4.2 and numerically in the Sections 4.4.4 and 4.4.5 are a general approach without any restriction or pre-definition of the spectral phase shape. The applied phase function was modeled as a Taylor series up to the third-order.
However, in Section 2.1.1 and in the classical model (Section 4.4.4) the excitonic resonance was successfully describes by a Lorentzian line shape. This lineshape of the excitonic resonance, apparently influencing the optimal pulse shape, is directly associated with an arctan-π-step phase function and indicates that, for optimal nonlinear signal generation, this phase needs to be compensated by the SLM.

To complement the SOD/TOD phase scans, dedicated arctan-π-step phase scans were carried out, using the setup described in Section 4.2.2, wherein the applied phase profile was explicitly restricted to:

$$\phi(\omega) = -\arctan\left(\frac{\omega - \omega_0}{\gamma}\right) \tag{4.27}$$

Here, ω_0 and γ represents the central frequency and the width of the resonance function, respectively. By scanning ω_0 and γ, the phase profile that compensates best for the phase shift, introduced by the excitonic resonance, was identified. When ω_0 and γ matches the excitonic resonance frequency and decay rate, respectively, the imprinted phase is supposed to cancel the phase contribution of the excitonic resonance, leading to optimal local pulse compression.
Figure 4.29 shows the experimental results of arctan π-step phase scans at a low laser fluence (0.4 mJ/cm^2), investigating the anti-Stokes ND-FWM signal of (a) WSe$_2$ and (c) MoSe$_2$. A distinct signal enhancement was observed for both materials at this low fluence when ω_0 matches the resonance frequencies at 1.67 eV and 1.59 eV, respectively, with γ remaining below 0.1 eV. As γ increases beyond 0.1 eV, the signal enhancement decays gradually. The corresponding numerical results obtained from the classical model ((b), (d)) exhibit the same behavior and are in good agreement with the experiments results.

In contrast, no such enhancement was detected for SLG (Figure 4.29 (e) and (f)), which served as reference material without excitonic resonances. The vanishing FWM intensity between $\hbar\omega_0 = 1.35$ - 1.7 eV and $\hbar\gamma = 0.0$ - 0.1 eV across all results is a direct consequence of destructive quantum interference within the structured laser spectrum, as shown by the numerical simulations for SLG.

The enhancement factors of the optimal arctan phase profile compared to the transform-limited pulse were lower than those obtained from the SOD/TOD scans. Specifically, enhancement factors of 1.50 ± 0.30 for WSe$_2$ and of 1.66 ± 0.33 for MoSe$_2$ were determined.

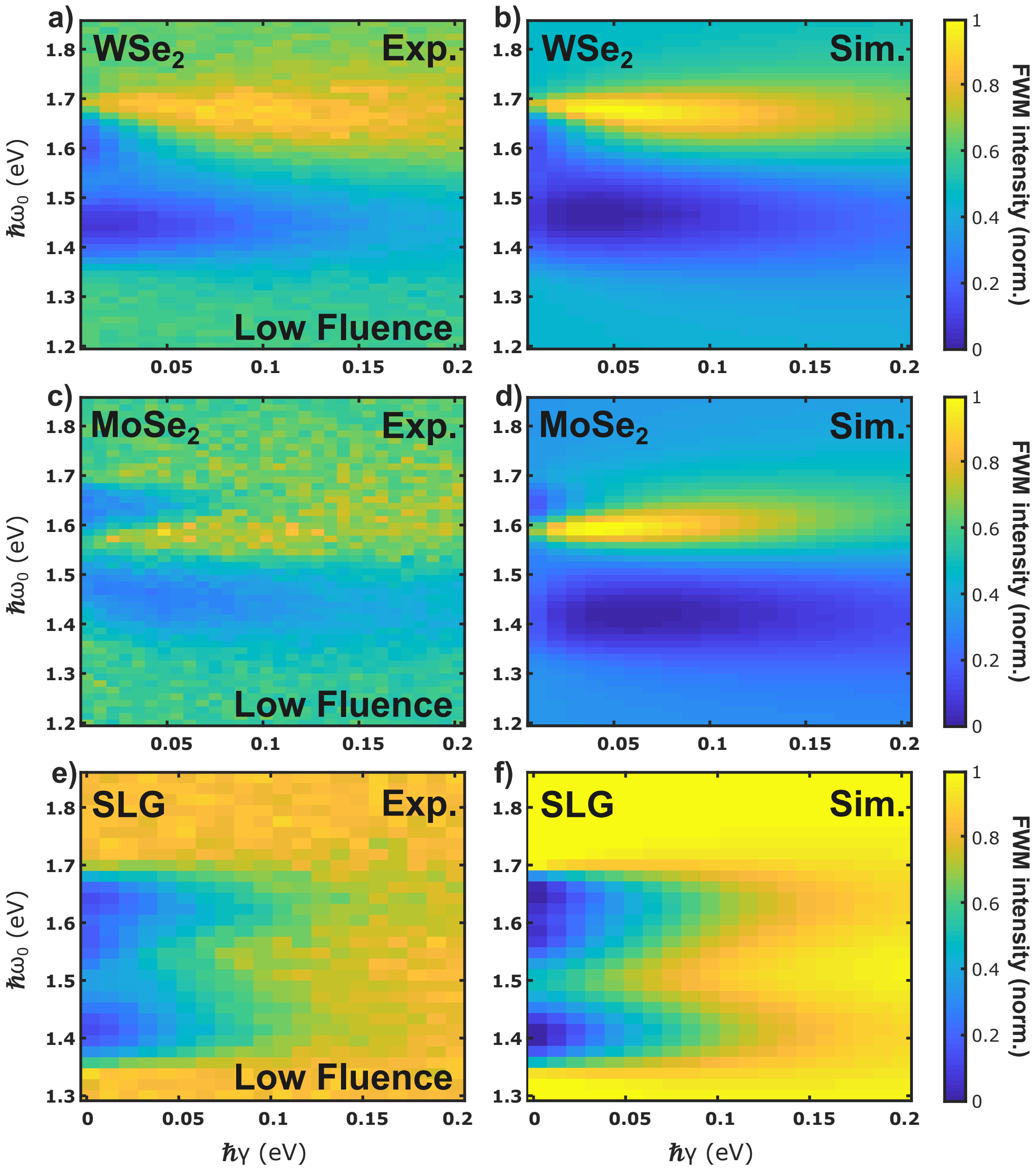

Figure 4.29.: Arctan π-step phase scans of the FWM intensity at low laser fluence on **(a)** WSe$_2$, **(c)** MoSe$_2$ and **(e)** SLG, experimentally obtained at a laser fluence of 0.4 mJ/cm^2. The corresponding numerical results of the classical model are shown in **(b)**, **(d)** and **(f)**, respectively. In WSe$_2$ and MoSe$_2$ a clear signal enhancement is observed when the center frequency of the arctan phase function aligns with the A-exciton resonance. In contrast no such enhancement is observed in SLG, serving as reference material. Reproduced with permission from [73]. Copyright 2024 American Chemical Society.

This observation aligns with the fluence-dependent measurements shown in Figure 4.19, which indicate that even at a low fluence of 0.4 mJ/cm^2, excitation-induced attenuation of the excitonic resonance alters the required phase profile for optimal FWM generation.

At high laser fluence (5.6 mJ/cm^2), this signal enhancement was no longer observed, as shown in Figure 4.30(b), and the results closely resembled those of SLG. This outcome is consistent with the suppression of excitonic effects, as discussed in the previous Sections 4.4.3, 4.4.4, and 4.4.5. The loss of enhancement can be attributed to EID, ground state bleaching, scattering interactions and screening mechanisms at high excitation densities. High-intensity measurements on MoSe$_2$ were not feasible due to rapid photo-induced damage.

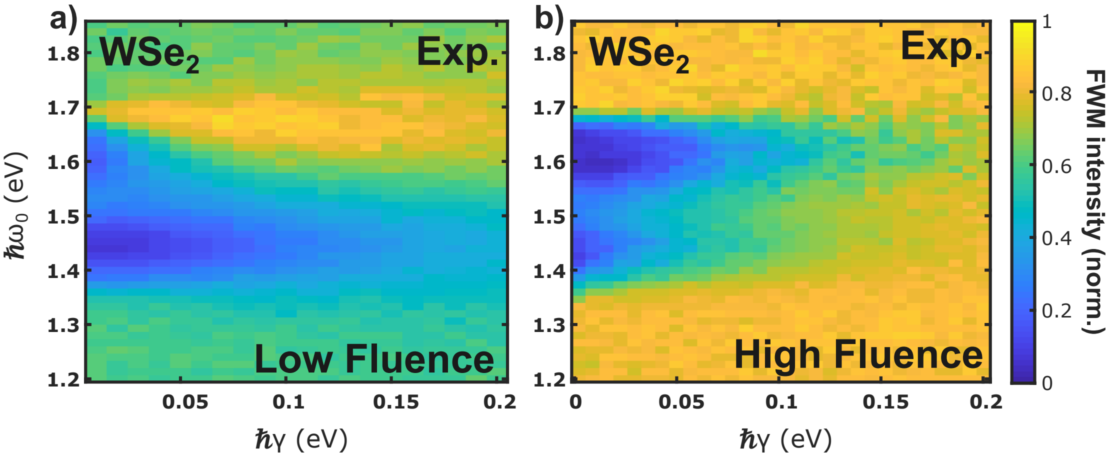

Figure 4.30.: Arctan π-step phase scans in WSe$_2$ experimentally obtained at **(a)** low fluence of 0.4 mJ/cm^2 and **(b)** high fluence of 5.6 mJ/cm^2. In the high fluence measurement the signal enhancement at 1.67 eV vanishes. Reproduced with permission from [73]. Copyright 2024 American Chemical Society.

Figure 4.31 illustrates the fluence-dependent evolution of the spectral phase profiles that maximize FWM in WSe$_2$. The laser spectrum is depicted as the gray-shaded background, while the A-exciton resonance of WSe$_2$ is indicated by the purple-shaded area. The corresponding phase profile of the resonance is represented by a purple dotted line. Experimentally obtained SOD/TOD scan phase profiles are shown for different fluences as: blue line for 0.4 mJ/cm^2, green line for 2 mJ/cm^2 and red line for 14.9 mJ/cm^2. As the fluence increases, the phase profile progressively converges toward the flat phase profile of a transform-limited pulse, indicated by the black dotted line. Conversely, at lower fluences, the optimal spectral phase profile closely resembles the arctan π-step phase profile (yellow dotted line), which effectively compensates for the Lorentzian phase response of the excitonic resonance. Due to the arbitrary choice of phase offset and slope (as constant and first-order terms do not affect the pulse shape), the SOD/TOD phase profiles were normalized such that they intersect the theoretical Lorentzian phase step at $\pi/2$.

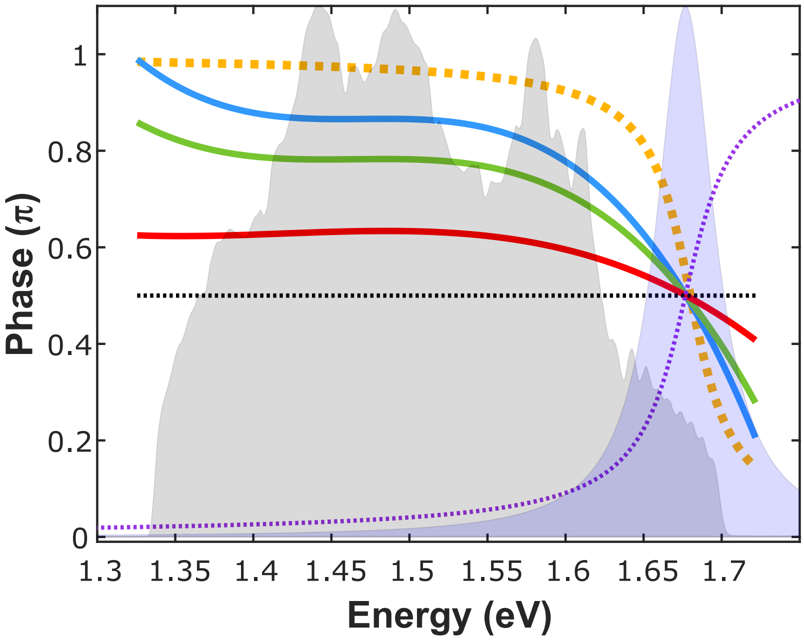

Figure 4.31.: Experimental fluence-dependent evolution of spectral phase profiles maximizing FWM in WSe$_2$. The gray-shaded background represents the laser spectrum, while the purple-shaded background highlights the A-exciton resonance in WSe$_2$. The corresponding modeled Lorentzian phase profile is shown as a purple dotted line. The experimentally determined SOD/TOD scan phase profiles are displayed in blue (0.4 mJ/cm^2), green (2 mJ/cm^2) and red (14.9 mJ/cm^2). As fluence increases, the phase profile gradually approaches that of a transform-limited pulse (black dotted line). At lower fluences, the optimal spectral phase profile approaches the arctan π-step phase profile (yellow dotted line), which compensates for the Lorentzian phase response. Reproduced with permission from [73]. Copyright 2024 American Chemical Society.

4.4.7. Phase shaping of the SFG signal

Following the analysis of the impact of excitonic resonances on the spectral phase dependence of the FWM signal generation, in this section the influence on the SFG signal is investigated. Since FWM and SFG both involve multipathway intrapulse interference and share the same spectral overlap of the laser spectrum with the A-exciton resonance, one might anticipate a similar dependence of the optimal spectral phase. However, the experimental results reveal a distinct behavior, suggesting differences between the two processes. To explore the influence of the excitonic resonance in 2D TMDs on the SFG signal, the process was examined under the same experimental conditions and with the same numerical models as employed above in the Sections 4.4.2, 4.4.4 and 4.4.5.

Analogue to the procedure in Section 4.4.2, systematic SOD/TOD phase scans were performed on WSe_2 and $MoSe_2$ at a medium fluence of 2 mJ/cm^2 using the same setup, described in Section 4.2.2. The optical filters were replaced by a 450 nm (2.76 eV) short-pass filter to isolate the SFG signal. The resulting intensity pattern, shown in Figure 4.32, reveal that, unlike FWM, the optimal spectral phase for SFG exhibits no significant shift. This behavior remains consistent across different excitation fluences and is similarly observed for both materials.

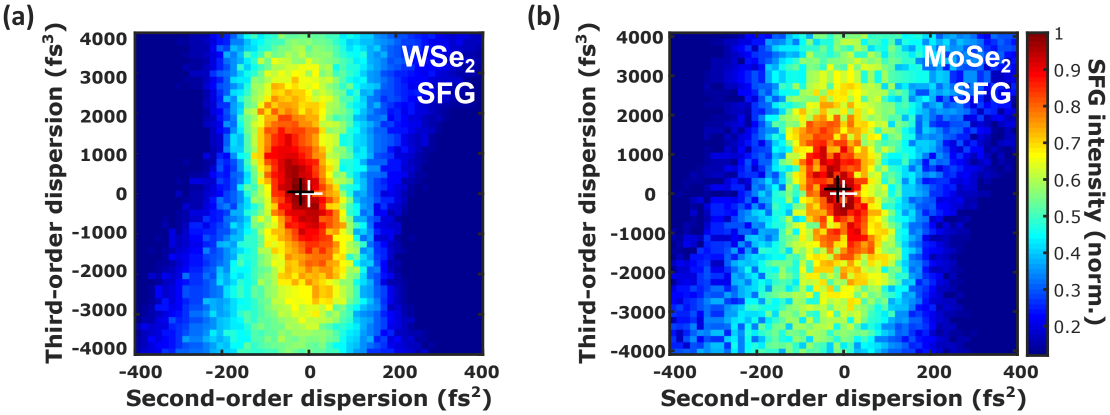

Figure 4.32.: Experimental SOD/TOD scans of the SFG signal intensity of **(a)** WSe_2 and **(b)** $MoSe_2$ monolayers at a fluence of 2 mJ/cm^2. The intensity was normalized to the maximum of each image. The strongest SFG intensity (marked by the black "+") is observed closely to the transform-limited shortest pulse (marked by the white "+") for both, WSe_2 and $MoSe_2$. Adapted with permission from [73]. Copyright 2024 American Chemical Society.

A notable difference between the SOD/TOD scans of FWM (presented in Figure 4.17) and SFG is the broader response observed for SFG, particularly when considering the significantly larger SOD and TOD range of the scans. This broader dependence arises from the lower sensitivity of the second-order nonlinear process to the pulse shape, compared to the third-order FWM process. The A-exciton resonance and the connected phase shift seem to have no significant effect on the SFG signal intensity.

To further investigate this discrepancy, numerical simulations based on the classical and the quantum-mechanical model were performed for WSe_2. The classical model was adjusted to account for SFG by considering Equation 4.25.

The quantum-mechanical model was adjusted following the approach described in [32] and [148]. An additional higher-energy state was introduced, which is essential because, in a quantum-mechanical two-level system, any interaction with the excited state can only lead to de-excitation, meaning the system undergoes a transition to the ground state. Such higher-energy states may correspond to other excitonic states, such as the 2s, 2p, ... substates associated with relative electron-hole motion, or they may be linked to other electronic bands [187]. Figure 4.33 illustrates the energy diagram of the modeled ladder-type three-level system. The excitonic state was tested to be resonant with the A exciton in panel (a) and the D exciton in panel (b) of WSe_2. The additional state was placed 1.5 eV above the excitonic state. The transition-dipole moments between the excited excitonic state $|2\rangle$ and $|3\rangle$, respectively, and the additional state, $|4\rangle$ and $|5\rangle$, are labeled μ_{24} and μ_{35} and were chosen ten times the values for the transition between the ground state $|1\rangle$ and the higher-energy state (μ_{14} and μ_{15}) to ensure an efficient population of this state.

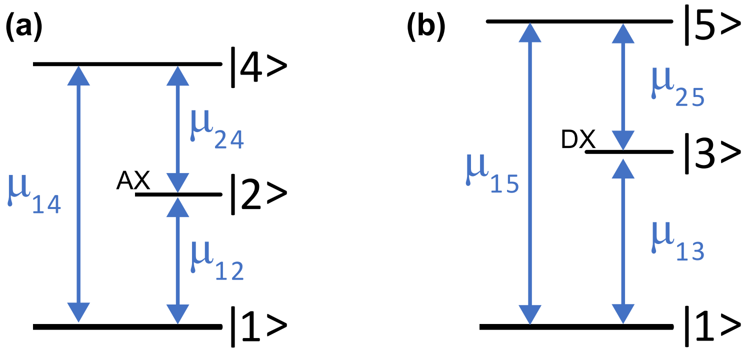

Figure 4.33.: Ladder-type three-level system for the quantum-mechanical model to describe SFG The states $|2\rangle$ and $|3\rangle$ describe (a) the A exciton and (b) the D exciton in WSe_2, respectively. The higher-energy state is necessary to model SFG and was placed 1.5 eV above the excitonic state.

The predictions from these models, shown in Figures 4.34 for the A-exciton of WSe_2, (a) and (c), fail to accurately reproduce the experimental results. Besides the overall pattern that strongly differ from the experimental scan pattern in Figure 4.32, for both the classical model and the quantum-mechanical model, the A exciton results predict a substantial shift of the SOD and TOD parameters, as seen in the FWM results. However, when considering the D-exciton, instead of the A-exciton, an agreement between theoretical predictions and experimental data is achieved by both models (Figure 4.34 (b) and (d)) for the shape of the pattern as well as the minimal phase shift. This suggests that the A-exciton resonance does not account for the observed behavior in SFG. Instead, the SFG signal seems to be affected by the higher-energy D-exciton, which is known to have a large oscillator strength and to play a dominant role in the SHG process [63–65, 188].

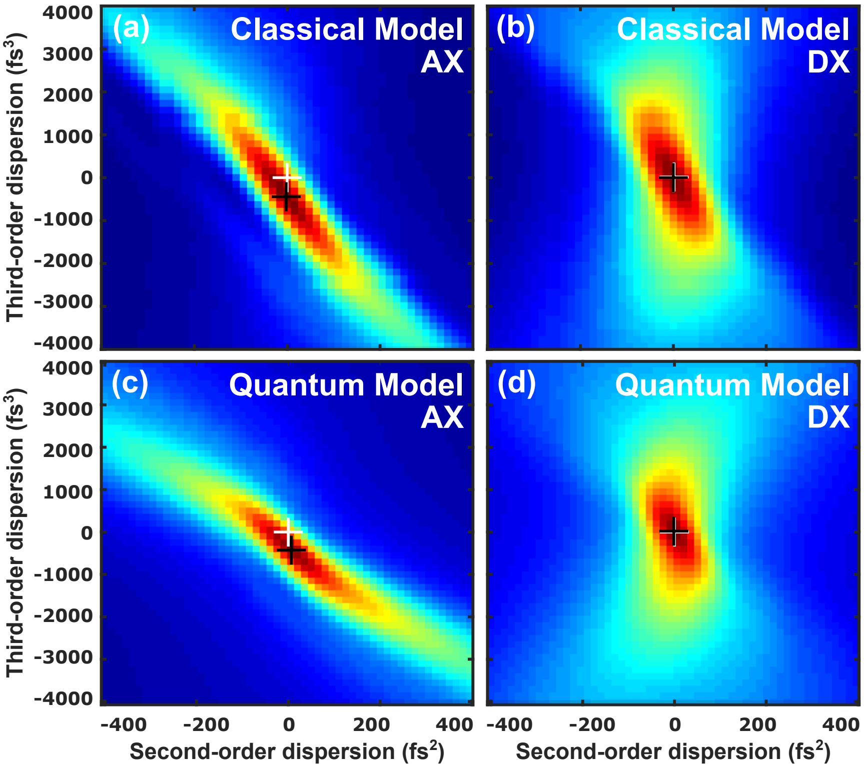

Figure 4.34.: Numerical model predictions for SOD/TOD scan of the SFG intensity in WSe$_2$. Considering the A exciton in (a) the classical model and (c) the quantum-mechanical model leads to predicted scan patterns that do not align with the experimental results in either shape or shift of the patterns. However, when only the D exciton is considered, as shown in (b) for the classical model and (d) for the quantum-mechanical model, the predictions closely match the experimental data. Adapted with permission from [73]. Copyright 2024 American Chemical Society.

To assess the impact of these two excitonic resonances on the SFG process, small bandwidth SHG measurements on WSe$_2$ and MoSe$_2$ were conducted using the setup described in Section 4.2.3. The fundamental frequencies of two separate fs laser sources, a MIRA 900 and a tunable Raman fiber laser, were tuned to overlap and cover the excitation range from 1.3 to 1.7 eV. The SHG intensity was referenced against the corresponding SHG signal intensity of a quartz crystal. As shown in Figure 4.35, the SHG efficiency reaches its peak when the generated 2ω signal resonates with the D-exciton in WSe$_2$ or the C-exciton in MoSe$_2$, respectively.

Importantly, no noticeable enhancement is detected when the fundamental frequency ω is in resonance with the A-exciton. This observation aligns with the SFG SOD/TOD scan results, reinforcing the speculation that the A-exciton resonance does not significantly influence the optimal phase profile for SFG intensity.

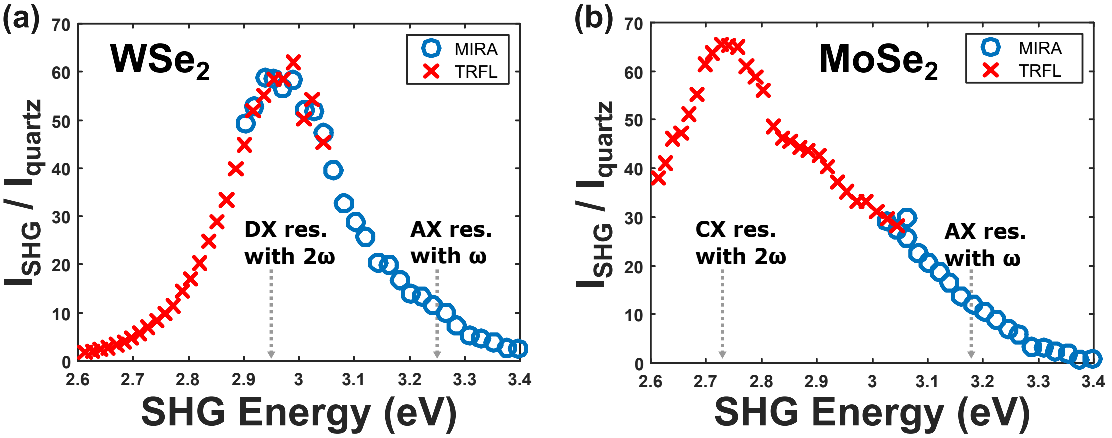

Figure 4.35.: Experimental SHG excitation intensity for (a) WSe_2 and (b) $MoSe_2$. The data was obtained by tuning the fundamental excitation frequencies of two fs laser sources, a MIRA900 (blue circles) and a TRFL (red crosses), to jointly cover the range from 1.3 to 1.7 eV. The results show a pronounced enhancement of generated SHG intensity when 2ω resonates with the D exciton. Notably, no significant enhancement is observed when the fundamental frequency ω is in resonance with the A exciton. Adapted with permission from [73]. Copyright 2024 American Chemical Society.

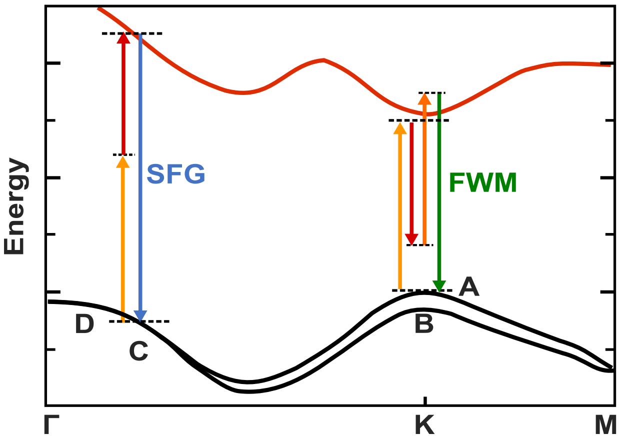

Figure 4.36.: Schematic representation of the band structure of TMDs, highlighting potential pathways for resonant SFG and FWM at distinct locations within the Brillouin zone. Adapted with permission from [73]. Copyright 2024 American Chemical Society.

It may seem counterintuitive that while the A-exciton resonance strongly influences the optimal spectral phase for FWM, no such effect is observed for SFG. However, the results presented in Figure 4.35 show that, for both investigated TMDs, the SHG/SFG signals are primarily enhanced by the C exciton in $MoSe_2$ and the D exciton in WSe_2, whereas the A-exciton plays a marginal role. Figure 4.36 provides a schematic representation of possible quantum pathways leading to resonant SFG and FWM at different k-vector positions within the band structure. The A-exciton is located at the K point of the Brillouin zone, where it dictates the resonant behavior of FWM [44]. In contrast, SHG and SFG are predominantly enhanced by the C- and D-exciton, which reside in the band nesting region near the Γ point [54, 55, 57]. This higher-lying excitonic states possess a significantly greater oscillator strength for two-photon transitions compared to the A-exciton, making it the dominant contributor to SHG and SFG [63–65, 188].

4.5. Conclusion and Outlook

In this chapter, room-temperature phase control of the nonlinear optical response of WSe_2 and $MoSe_2$ monolayers, based on the overlap of the A-exciton resonance and the broadband laser spectrum, has been demonstrated. A significant enhancement of the FWM signal intensity, reaching a factor of approximately 2 within the examined fluence range and depending on the specific TMD material, was achieved by tailoring the spectral phase of the laser pulse. The enhancement was a direct consequence of compensating for the phase shift introduced by the excitonic resonance. This leads to the counterintuitive effect of increased FWM intensity when the laser pulse is stretched compared to its transform-limited shape. Recently, Meron and co-workers observed an enhancement factor of 2.6 in similar experiments, using an arctan phase profile, at comparable, yet lower excitation intensities on WSe_2 [153]. This aligns with the enhancement factor of 2.2 ± 0.2 determined from the SOD/TOD scans presented in Section 4.4.2. Moreover, the trend shown in Figure 4.19(b) suggests that even higher enhancement factors may be achievable at further reduced excitation intensities.

In contrast, no such enhancement was found for SFG, where the signal intensity is maximized for the transform-limited pulse. The primary reason for this difference likely is the dominant role of the C- and D-exciton resonances on the resonant SFG process, whereas the A-exciton at the fundamental frequency has only a negligible influence.

Furthermore, the influence of the A-exciton resonance on the optimal FWM phase profile was found to decrease with increasing excitation density, as confirmed by differential reflection measurements on WSe_2. Numeric simulations indicate that this effect is influenced by excitation-induced processes such as ground state bleaching and dephasing of the excitonic resonance. Since the employed models suggest that these effects are insufficient to explain the strong reduction in TOD phase parameter, the onset of the Mott transition to an electron-hole plasma is proposed as the dominating effect.

A clear trend in the optimal spectral phase profile as a function of excitation fluence was identified. At low fluences, the optimal phase closely resembles an arctan π-step function, which effectively compensates for the Lorentzian phase profile of the excitonic resonance. However, as the laser fluence is increased, a gradual transition of the optimal phase toward the flat phase profile of a transform-limited pulse was observed.

Finally, the results suggest that direct spectral phase control of the excitonic state population via Rabi oscillations is hindered at room temperature due to exciton dissociation at high excitation densities. However, performing similar experiments at cryogenic temperatures, where excitonic coherence times are significantly longer, could provide a pathway to achieving coherent control of the excited state population in TMD monolayers.

Complementary, future experiments could aim to directly manipulate the coherent many-body dynamics of excitons in TMD monolayers. Recent theoretical work by Katsch and Knorr [189] has shown that ultrafast exciton-biexciton oscillations can emerge from Coulomb-mediated interactions in dense exciton gases, distinct from conventional Rabi oscillations. These oscillations are not driven by the external light field but arise from the coherent evolution of a superposition state formed after photoexcitation. In particular, linear polarization facilitates biexciton generation, while circular polarization suppresses it, enabling control over the coherent oscillation amplitude. To explore this regime experimentally, polarization-resolved and excitation-tuned measurements of the FWM response could be implemented to control biexciton formation and the coupling to the scattering continuum.

Furthermore, performing similar experiments at cryogenic temperatures, where excitonic dephasing is significantly reduced, may allow direct observation of exciton-biexciton population dynamics. In this way, the current approach based on spectral phase shaping could be extended to enable coherent population control of strongly interacting excitonic systems in the solid state.

5. Summary

In summary, this work presents two projects that investigate the potential of exploiting exciton dynamics in low-dimensional materials to control light-matter interactions and tailor the optical response, addressing key challenges in emerging photonic and quantum technologies. While differing in their methods - one employing near-field spatial control via optical antennas, and the other ultrafast spectral pulse shaping - both approaches demonstrate how exciton dynamics can be utilized for precise control over photon emission at the nanoscale.

The first project demonstrates antenna-controlled antibunching in the PL of SWCNTs, providing a proof-of-concept for local control over SPE in quasi-one-dimensional systems. By enhancing the local optical field, the optical antenna promotes efficient EEA and increases the radiative recombination rate in a spatially confined region. This mechanism leads to a measurable reduction in the second-order correlation function at zero time delay $g^{(2)}(0)$, experimentally by approximately 0.2. Numerical simulations further indicate that under realistic field enhancements, $g^{(2)}(0)$ could be reduced to around 0.3 and in optimized conditions down to 0.1. These findings not only demonstrate the potential of non-invasive and reversible spatial control over the photon emission statistics but also suggest that the concept might be applicable to other quasi-1D systems, such as inorganic semiconducting nanowires. The ability to precisely control the position of the antenna and thus the location of the SPS offers a highly tunable platform for nanophotonic device integration, avoiding the limitations associated with chemical doping or mechanical strain methods.

The second project focuses on phase shaping of ultrafast laser pulses to control the coherent nonlinear optical response of monolayer TMDs, specifically WSe_2 and $MoSe_2$, at room temperature. By tailoring the spectral phase of the excitation pulse, it is demonstrated to compensate for the phase shifts imposed by the A-exciton resonance, resulting in an enhancement of the FWM signal intensity by a factor of about 2. The optimal spectral phase profile was found to evolve with excitation fluence, transitioning from an arctan-like profile at low intensities to a flat profile at higher fluences. This behavior is partially attributed to excitation-induced effects such as ground state bleaching and dephasing, but is suggested to be dominated by the onset of the Mott transition at higher densities, where exciton populations dissociate into an electron-hole plasma. Corresponding experiments at cryogenic conditions could extend this approach toward coherent population control of excitons. Furthermore, the results provide a foundation for exploring coherent many-body dynamics.

Together, these two projects illustrate the potential of complementary spatial and temporal control schemes for manipulating excitonic processes in low-dimensional materials. While the SWCNT antenna-control project addresses localized enhancement of photon emission via near-field engineering, the TMD phase-control project demonstrates coherent phase control of exciton dynamics through spectral pulse shaping. Both approaches share the ability to utilize intrinsic excitonic interactions to obtain tunable optical responses, which is critical for applications ranging from SPS to nonlinear optical devices and quantum photonics.

Looking forward, an interesting prospect seems to be the combination of these two approaches. By integrating antenna-enhanced local fields with spectrally shaped ultrafast pulses, it may be possible to achieve simultaneous spatial and temporal control over exciton populations. Such a hybrid strategy could exploit strong light-matter coupling between resonant antennas and excitons to control the creation and time evolution of exciton states in a predictable, phase-coherent way. This could lay grounds for ultra-efficient SPS, the control of coherent nonlinear processes and steering of the population of strongly coupled exciton-polariton states in low-dimensional systems.

A. Appendix

A.1. SOD/TOD scan power series data

Here, the full data series of the fluence-dependent SOD/TOD scans, discussed in Section 4.4.2 are presented for SLG in Figure A.1 and for WSe_2 in Figure A.2. The data was normalized to the maximum of each scan pattern. The optimal SOD and TOD values were calculated by a center of mass C procedure using equation A.1.

$$C_{\mathrm{SOD}} = \frac{\sum_{i=1}^{n} \mathrm{SOD}_i \cdot I_{\mathrm{FWM},i}}{\sum_{i=1}^{n} \mathrm{SOD}_i} \qquad C_{\mathrm{TOD}} = \frac{\sum_{i=1}^{n} \mathrm{TOD}_i \cdot I_{\mathrm{FWM},i}}{\sum_{i=1}^{n} \mathrm{TOD}_i} \tag{A.1}$$

Here, n is the total number of data points in a scan pattern. The second-order and third-order values were weighted by the corresponding FWM intensity.
The obtained values are presented in Figure 4.19 and discussed in the corresponding section.

The SLG sample was photo-damaged during the measurement with the highest fluence of 14.9 mJ/cm^2.

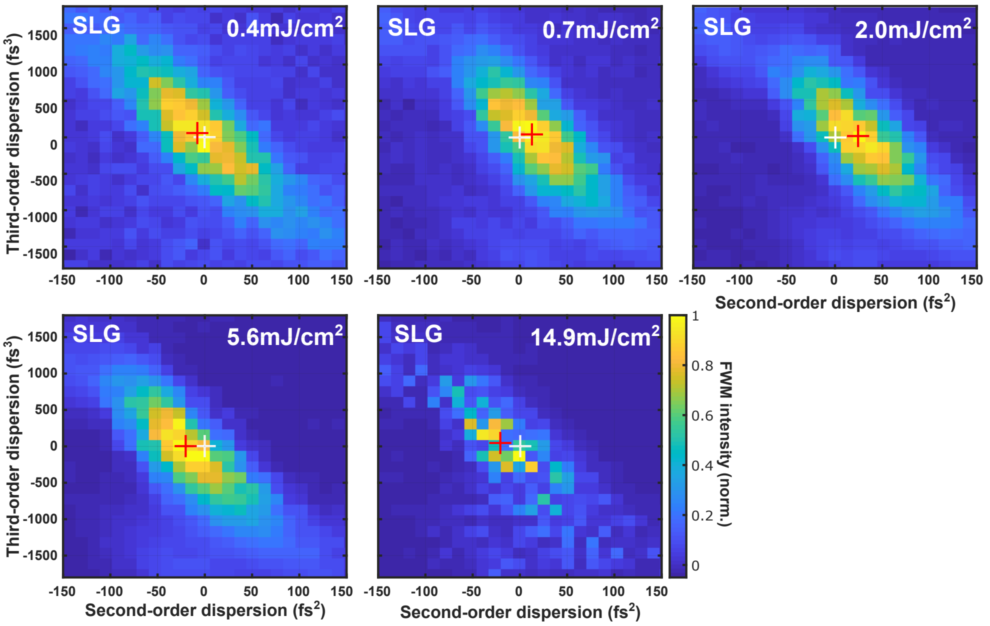

Figure A.1.: SOD/TOD scan series of SLG for varying laser fluences. The white cross markes the case of a transform-limited pulse, while the red cross markes the optimal SOD and TOD value composition derived from Equation A.1. Reproduced with permission from [73]. Copyright 2024 American Chemical Society.

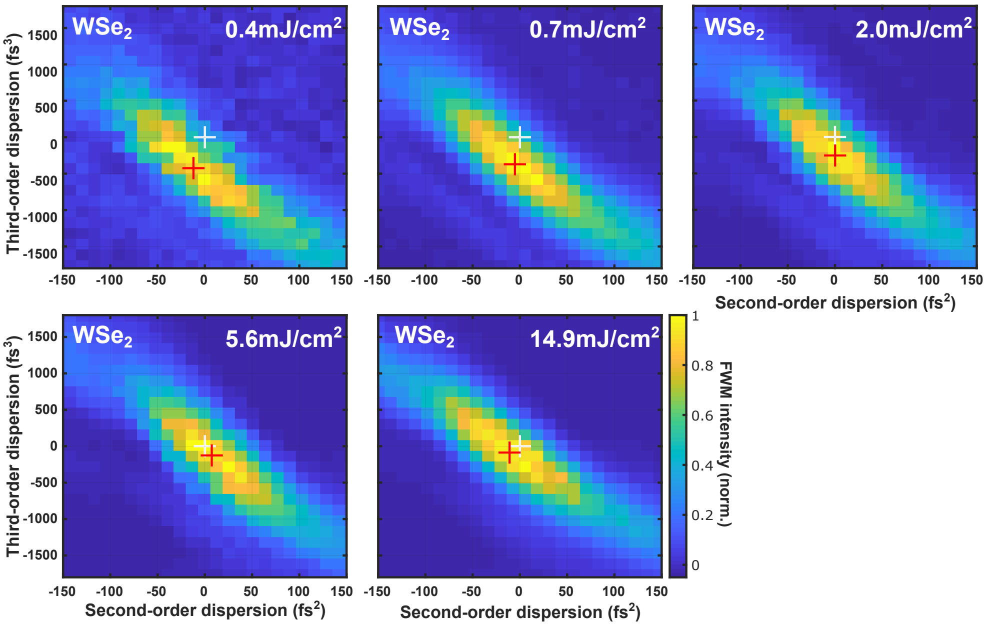

Figure A.2.: SOD/TOD scan series of SLG for varying laser fluences. The white cross markes the case of a transform-limited pulse, while the red cross markes the optimal SOD and TOD value composition derived from Equation A.1. Reproduced with permission from [73]. Copyright 2024 American Chemical Society.

A.2. Double bandpass measurements as FWM proof

To confirm that the observed third-order nonlinear signal, manifested as a spectral broadening on the anti-Stokes side of the laser spectrum, originates from FWM, double-bandpass scans were conducted on WSe_2. In this experiments, the laser spectrum was split into two spectral bands using the pulse shaper's amplitude modulation function as a double bandpass filter and block any undesired spectral components. One band was fixed within the range of 900 - 907 nm (1.378 - 1.367 eV), while the other was scanned stepwise from a center position at 765 nm to 801 nm (1.621 ev to 1.548 eV) in 4.5 nm steps and with a bandwidth of 10 nm. This is illustrated in Figure A.3 (a). For FWM, the two spectral bands generate new spectral components at higher energies, following the relationship $\omega_{\mathrm{FWM}} = 2\omega_{\mathrm{scan}} - \omega_{\mathrm{fixed}}$, and at lower energies for $\omega_{\mathrm{FWM}} = 2\omega_{\mathrm{fixed}} - \omega_{\mathrm{scan}}$. Figure A.3 (b) shows the resulting generated spectral components at the high-energy side of the laser spectrum. Shifting the ω_{scan} to lower energies results in a corresponding shift of the generated nonlinear signal to lower energies as well, which aligns with the expected FWM behavior.

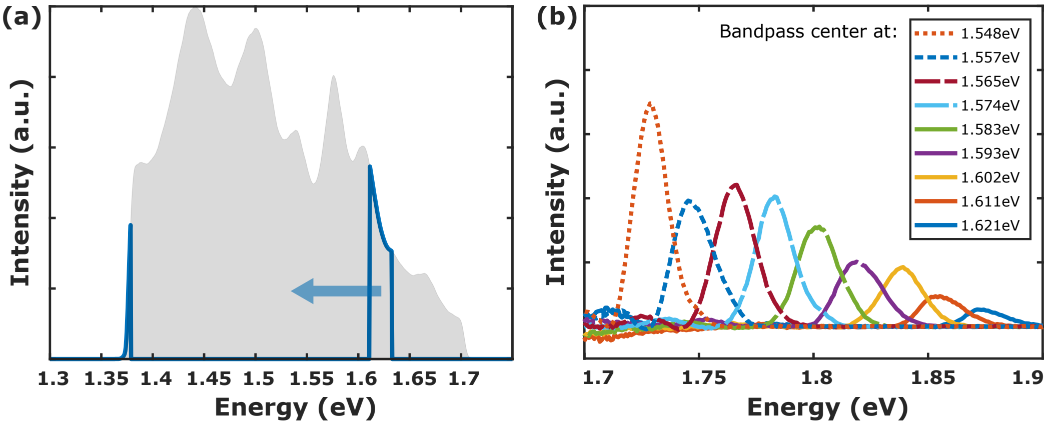

Figure A.3.: Double-bandpass experiment on WSe_2 to validate the origin of the observed signal to be FWM. (a) Displays the laser spectrum with two selectively applied spectral bandpass filters. These filters are implemented using the pulse shaper, which blocks unwanted spectral components. The high-energy bandpass is gradually shifted stepwise toward lower energies, while the low-energy bandpass remains fixed. (b) Presents the resulting FWM spectra, where the newly generated spectral components on the anti-Stokes side shift accordingly, in agreement with the expected FWM behavior. Reproduced with permission from [73]. Copyright 2024 American Chemical Society.

A.3. Origin of tilted SOD/TOD pattern

It may seem surprising that the SOD/TOD scan patterns, shown in Section 4.4.2, appear tilted rather than symmetric relative to the vertical axis. To verify that this asymmetry arises directly from the shape of the excitation spectrum, the classical model introduced in Section 4.4.4 was employed to systematically investigate the effect.
Figure A.4 presents the simulated SOD/TOD scan patterns for two different spectral shapes using the classical model. The excitation spectrum is modeled as a Gaussian, defined by:

$$E(\omega) = \exp\left(-\frac{(\omega - \omega_0)^2}{\sigma^2}\right) \tag{A.2}$$

with a central energy of $\omega_0 = 1.4759$ eV and a width of $\sigma = 0.132$ eV.

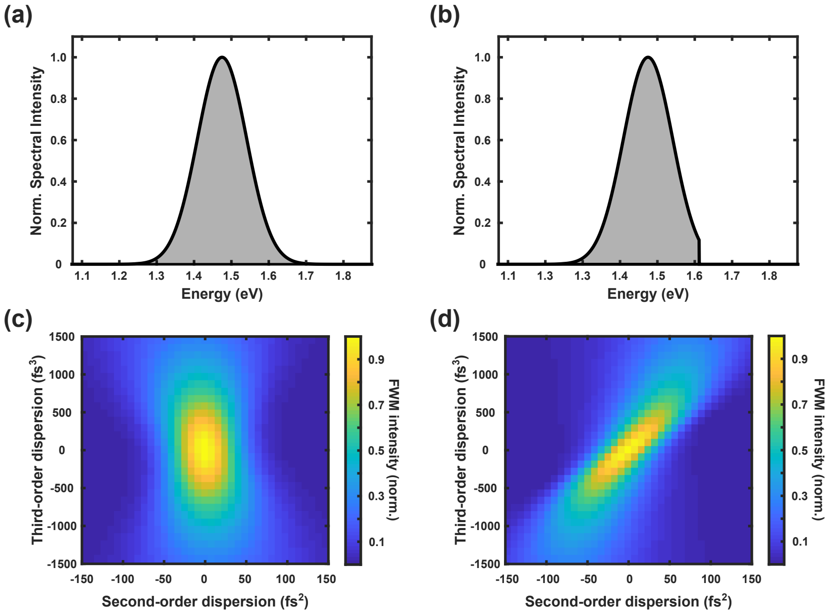

Figure A.4.: Simulated SOD/TOD scan patterns illustrating the influence of spectral asymmetry. (a) Symmetric Gaussian excitation spectrum centered at $\omega_0 = 1.4759$ eV with $\sigma = 0.132$ eV. (b) The same Gaussian spectrum truncated at 1.61 eV to introduce asymmetry. (c) SOD/TOD scan pattern resulting from the symmetric spectrum in (a), exhibiting vertical elongation. (d) SOD/TOD scan pattern for the asymmetric spectrum in (b), showing a pronounced tilt. These results confirm that asymmetry in the excitation spectrum leads to a tilted SOD/TOD scan pattern.

Panel (a) shows a symmetric Gaussian spectrum, and the corresponding scan pattern in panel (c) is elongated along the vertical (SOD) axis, as expected. In contrast, panel (b) displays the same Gaussian spectrum but cut at 1.61 eV to mimic the asymmetry. The resulting scan pattern in panel (d) is visibly tilted, confirming that the asymmetry in the scan originates from the spectral shape. This clearly demonstrates that the tilt of the SOD/TOD pattern is a direct consequence of an asymmetric excitation spectrum.

List of Abbreviations

AC	Autocorrelation
APD	Avalanche Photo Diode
CBM	Conduction Band Minimum
CC	Cross-Correlation
CCD	Charge-Coupled Device
CNT	Carbon Nanotube
CVD	Chemical Vapor Deposition
DFG	Difference Frequency Generation
EEA	Exciton-Exciton Annihilation
EID	Excitation Induced Dephasing
FWM	Four-Wave Mixing
GDD	Group Delay Dispersion
HHG	Higher Harmonic Generation
LSPR	Localized Surface Plasmon Resonance
MBE	Molecular Beam Epitaxy
ND-FWM	Near-Degenerate Four-Wave Mixing
OPA	Optical Parametric Amplification
OPO	Optical Parametric Oscillation
PMT	Photo-Multiplier Tube
SFG	Sum Frequency Generation
SHG	Second Harmonic Generation
SLM	Spatial Light Modulator
SPE	Single Photon Emission
SPDC	Spontaneous Parametric Down Conversion
SPM	Self-Phase Modulation
SPS	Single Photon Source
SWCNT	Single-Walled Carbon Nanotube
THG	Third Harmonic Generation
TMD	Transition Metal Dichalcogenide
TRFL	Tunable Raman Fiber Laser
VBM	Valence Band Maximum

List of Figures

Bibliography

[1] X. Wen, Z. Gong, and D. Li, “Nonlinear optics of two-dimensional transition metal dichalcogenides,” *InfoMat*, vol. 1, no. 3, pp. 317–337, 2019. `https://doi.org/10.1002/inf2.12024`.

[2] A. Autere, H. Jussila, Y. Dai, Y. Wang, H. Lipsanen, and Z. Sun, “Nonlinear optics with 2D layered materials,” *Adv. Mater.*, vol. 30, no. 24, p. 1705963, 2018. `https://doi.org/10.1002/adma.201705963`.

[3] L. Lafeta, A. Corradi, T. Zhang, E. Kahn, I. Bilgin, B. R. Carvalho, S. Kar, M. Terrones, and L. M. Malard, “Second-and third-order optical susceptibilities across excitons states in 2d monolayer transition metal dichalcogenides,” *2D Mater.*, vol. 8, no. 3, p. 035010, 2021. `https://doi.org/10.1088/2053-1583/abeed4`.

[4] E. J. Sie, A. Steinhoff, C. Gies, C. H. Lui, Q. Ma, M. Rosner, G. Schönhoff, F. Jahnke, T. O. Wehling, Y.-H. Lee, J. Kong, P. Jarillo-Herrero, and N. Gedik, “Observation of exciton redshift–blueshift crossover in monolayer WS_2,” *Nano Lett.*, vol. 17, no. 7, pp. 4210–4216, 2017. `https://doi.org/10.1021/acs.nanolett.7b01034`.

[5] X. Ma, O. Roslyak, J. G. Duque, X. Pang, S. K. Doorn, A. Piryatinski, D. H. Dunlap, and H. Htoon, “Influences of exciton diffusion and exciton-exciton annihilation on photon emission statistics of carbon nanotubes,” *Phys. Rev. Lett.*, vol. 115, no. 1, p. 017401, 2015. `https://doi.org/10.1103/PhysRevLett.115.017401`.

[6] F. B. Sousa, R. Perea-Causin, S. Hartmann, L. Lafetá, B. Rosa, S. Brem, C. Palekar, S. Reitzenstein, A. Hartschuh, E. Malic, and L. M. Malard, “Ultrafast hot electron–hole plasma photoluminescence in two-dimensional semiconductors,” *Nanoscale*, vol. 15, no. 15, pp. 7154–7163, 2023. `https://doi.org/10.1039/D2NR06732C`.

[7] A. Chernikov, C. Ruppert, H. M. Hill, A. F. Rigosi, and T. F. Heinz, “Population inversion and giant bandgap renormalization in atomically thin WS_2 layers,” *Nat. Photonics*, vol. 9, no. 7, pp. 466–470, 2015. `https://doi.org/10.1038/nphoton.2015.104`.

[8] L. Meckbach, T. Stroucken, and S. Koch, “Giant excitation induced bandgap renormalization in tmdc monolayers,” *Appl. Phys. Lett.*, vol. 112, no. 6, p. 061104, 2018. `https://doi.org/10.1063/1.5017069`.

[9] A. W. Bataller, R. A. Younts, A. Rustagi, Y. Yu, H. Ardekani, A. Kemper, L. Cao, and K. Gundogdu, “Dense electron–hole plasma formation and ultralong charge lifetime in monolayer MoS_2 via material tuning,” *Nano Lett.*, vol. 19, no. 2, pp. 1104–1111, 2019. `https://doi.org/10.1021/acs.nanolett.8b04408`.

[10] W. Liang, “Excitons,” *Phys. Educ.*, vol. 5, no. 4, p. 226, 1970. `https://doi.org/10.1088/0031-9120/5/4/003`.

[11] A. V. Kolobov and J. Tominaga, *Two-Dimensional Transition-Metal Dichalcogenides.* Springer, 2016. `https://doi.org/10.1007/978-3-319-31450-1`.

[12] G. Wang, A. Chernikov, M. M. Glazov, T. F. Heinz, X. Marie, T. Amand, and B. Urbaszek, “Colloquium: Excitons in atomically thin transition metal dichalcogenides,” *Rev. Mod. Phys.*, vol. 90, no. 2, p. 021001, 2018. `https://doi.org/10.1103/RevModPhys.90.021001`.

[13] K. F. Mak and J. Shan, “Photonics and optoelectronics of 2D semiconductor transition metal dichalcogenides,” *Nat. Photonics*, vol. 10, no. 4, pp. 216–226, 2016. `https://doi.org/10.1038/nphoton.2015.282`.

[14] S. Reich, C. Thomsen, and J. Maultzsch, *Carbon Nanotubes: Basic Concepts and Physical Properties.* Wiley-VCH, 2004. `https://doi.org/10.1002/9783527618040`.

[15] C. Ruppert, A. Chernikov, H. M. Hill, A. F. Rigosi, and T. F. Heinz, “The role of electronic and phononic excitation in the optical response of monolayer WS_2 after ultrafast excitation,” *Nano Lett.*, vol. 17, no. 2, pp. 644–651, 2017. `https://doi.org/10.1021/acs.nanolett.6b03513`.

[16] Y.-Z. Ma, L. Valkunas, S. L. Dexheimer, S. M. Bachilo, and G. R. Fleming, “Femtosecond spectroscopy of optical excitations in single-walled carbon nanotubes: Evidence for exciton-exciton annihilation,” *Phys. Rev. Lett.*, vol. 94, no. 15, p. 157402, 2005. `https://doi.org/10.1103/PhysRevLett.94.157402`.

[17] L. Yuan and L. Huang, “Exciton dynamics and annihilation in WS_2 2D semiconductors,” *Nanoscale*, vol. 7, no. 16, pp. 7402–7408, 2015. `https://doi.org/10.1039/c5nr00383k`.

[18] D. Sun, Y. Rao, G. A. Reider, G. Chen, Y. You, L. Brézin, A. R. Harutyunyan, and T. F. Heinz, “Observation of rapid exciton–exciton annihilation in monolayer molybdenum disulfide,” *Nano Lett.*, vol. 14, no. 10, pp. 5625–5629, 2014. `https://doi.org/10.1021/nl5021975`.

[19] X. Liu, Q. Guo, and J. Qiu, “Emerging low-dimensional materials for nonlinear optics and ultrafast photonics,” *Adv. Mater.*, vol. 29, no. 14, p. 1605886, 2017. `https://doi.org/10.1002/adma.201605886`.

[20] I. Aharonovich, D. Englund, and M. Toth, "Solid-state single-photon emitters," *Nat. Photonics*, vol. 10, no. 10, pp. 631–641, 2016. `https://doi.org/10.1038/nphoton.2016.186`.

[21] P.-Y. Wu, W.-Q. Lee, C.-H. Liu, and C.-B. Huang, "Coherent control of enhanced second-harmonic generation in a plasmonic nanocircuit using a transition metal dichalcogenide monolayer," *Nat. Commun.*, vol. 15, no. 1, p. 1855, 2024. `https://doi.org/10.1038/s41467-024-46209-8`.

[22] Paras, K. Yadav, P. Kumar, D. R. Teja, S. Chakraborty, M. Chakraborty, S. S. Mohapatra, A. Sahoo, M. M. Chou, C.-T. Liang, and D.-R. Hang, "A review on low-dimensional nanomaterials: nanofabrication, characterization and applications," *Nanomaterials*, vol. 13, no. 1, p. 160, 2022. `https://doi.org/10.3390/nano13010160`.

[23] S. Joseph, J. Mohan, S. Lakshmy, S. Thomas, B. Chakraborty, S. Thomas, and N. Kalarikkal, "A review of the synthesis, properties, and applications of 2D transition metal dichalcogenides and their heterostructures," *Mater. Chem. Phys.*, vol. 297, p. 127332, 2023. `https://doi.org/10.1016/j.matchemphys.2023.127332`.

[24] X. He, H. Htoon, S. Doorn, W. Pernice, F. Pyatkov, R. Krupke, A. Jeantet, Y. Chassagneux, and C. Voisin, "Carbon nanotubes as emerging quantum-light sources," *Nat. Mater.*, vol. 17, no. 8, pp. 663–670, 2018. `https://doi.org/10.1038/s41563-018-0109-2`.

[25] H. Haug and S. W. Koch, *Quantum Theory of the Optical and Electronic Properties of Semiconductors.* World Scientific, 2004. `https://doi.org/10.1142/7184`.

[26] M. Fox, *Optical Properties of Solids.* Oxford University Press, 2001. ISBN: 0198506139.

[27] R. W. Boyd, *Nonlinear Optics.* Academic Press, 2008. ISBN: 978-0-12-369470-6.

[28] R. C. Miller, "Optical second harmonic generation in piezoelectric crystals," *Appl. Phys. Lett.*, vol. 5, no. 1, pp. 17–19, 1964. `https://doi.org/10.1063/1.1754022`.

[29] V. Giegold, K. Kolataj, T. Liedl, and A. Hartschuh, "Phase-selective four-wave mixing of resonant plasmonic nanoantennas," *ACS Photonics*, vol. 9, no. 11, pp. 3727–3733, 2022. `https://doi.org/10.1021/acsphotonics.2c01362`.

[30] J.-C. Diels and W. Rudolph, *Ultrashort Laser Pulse Phenomena.* Elsevier, 2006. `https://doi.org/10.1016/B978-0-12-215493-5.X5000-9`.

[31] D. Goswami, "Optical pulse shaping approaches to coherent control," *Phys. Rep.*, vol. 374, no. 6, pp. 385–481, 2003. `https://doi.org/10.1016/S0370-1573(02)00480-5`.

[32] K.-Q. Lin, S. Bange, and J. M. Lupton, “Quantum interference in second-harmonic generation from monolayer WSe_2,” *Nat. Phys.*, vol. 15, no. 3, pp. 242–246, 2019. `https://doi.org/10.1038/s41567-018-0384-5`.

[33] J. J. Sakurai, *Modern Quantum Mechanics*. Addison-Wesley Publishing Company, 1994. ISBN: 978-0201539295.

[34] J. Frenkel, “On the transformation of light into heat in solids. i,” *Phys. Rev.*, vol. 37, no. 1, pp. 17–44, 1931. `https://doi.org/10.1103/PhysRev.37.17`.

[35] X.-F. He, “Excitons in anisotropic solids: The model of fractional-dimensional space,” *Phys. Rev. B*, vol. 43, no. 3, p. 2063, 1991. `https://doi.org/10.1103/PhysRevB.43.2063`.

[36] F. Wang, Y. Wu, M. S. Hybertsen, and T. F. Heinz, “Auger recombination of excitons in one-dimensional systems,” *Phys. Rev. B*, vol. 73, no. 24, p. 245424, 2006. `https://doi.org/10.1103/PhysRevB.73.245424`.

[37] T. Ogawa and T. Takagahara, “Optical absorption and sommerfeld factors of one-dimensional semiconductors: An exact treatment of excitonic effects,” *Phys. Rev. B*, vol. 44, no. 15, p. 8138, 1991. `https://doi.org/10.1103/PhysRevB.44.8138`.

[38] H. W. Kroto, J. R. Heath, S. C. O’Brien, R. F. Curl, and R. E. Smalley, “C60: Buckminsterfullerene,” *Nature*, vol. 318, no. 6042, pp. 162–163, 1985. `https://doi.org/10.1038/318162a0`.

[39] S. Iijima, “Helical microtubules of graphitic carbon,” *Nature*, vol. 354, no. 6348, pp. 56–58, 1991. `https://doi.org/10.1038/354056a0`.

[40] K. S. Novoselov, A. K. Geim, S. V. Morozov, D.-e. Jiang, Y. Zhang, S. V. Dubonos, I. V. Grigorieva, and A. A. Firsov, “Electric field effect in atomically thin carbon films,” *Science*, vol. 306, no. 5696, pp. 666–669, 2004. `https://doi.org/10.1126/science.1102896`.

[41] H. Liu, A. T. Neal, Z. Zhu, Z. Luo, X. Xu, D. Tománek, and P. D. Ye, “Phosphorene: an unexplored 2D semiconductor with a high hole mobility,” *ACS Nano*, vol. 8, no. 4, pp. 4033–4041, 2014. `https://doi.org/10.1021/nn501226z`.

[42] C. R. Dean, A. F. Young, I. Meric, C. Lee, L. Wang, S. Sorgenfrei, K. Watanabe, T. Taniguchi, P. Kim, K. L. Shepard, and J. Hone, “Boron nitride substrates for high-quality graphene electronics,” *Nat. Nanotechnol.*, vol. 5, no. 10, pp. 722–726, 2010. `https://doi.org/10.1038/nnano.2010.172`.

[43] K. F. Mak, C. Lee, J. Hone, J. Shan, and T. F. Heinz, “Atomically thin MoS_2: a new direct-gap semiconductor,” *Phys. Rev. Lett.*, vol. 105, no. 13, p. 136805, 2010. `https://doi.org/10.1103/PhysRevLett.105.136805`.

[44] A. Splendiani, L. Sun, Y. Zhang, T. Li, J. Kim, C.-Y. Chim, G. Galli, and F. Wang, "Emerging photoluminescence in monolayer MoS_2," *Nano Lett.*, vol. 10, no. 4, pp. 1271–1275, 2010. `https://doi.org/10.1021/nl903868w`.

[45] A. Castellanos-Gomez, M. Buscema, R. Molenaar, V. Singh, L. Janssen, H. S. Van Der Zant, and G. A. Steele, "Deterministic transfer of two-dimensional materials by all-dry viscoelastic stamping," *2D Mater.*, vol. 1, no. 1, p. 011002, 2014. `https://doi.org/10.1088/2053-1583/1/1/011002`.

[46] C. Zhang, "Recent progress on chemical vapor deposition growth of 2D materials," *J. Comput. Methods Sci. Eng.*, vol. 23, no. 5, pp. 2595–2608, 2023. `https://doi.org/10.3233/JCM-226864`.

[47] E. Xenogiannopoulou, P. Tsipas, K. Aretouli, D. Tsoutsou, S. Giamini, C. Bazioti, G. Dimitrakopulos, P. Komninou, S. Brems, C. Huyghebaert, I. P. Radu, and A. Dimoulas, "High-quality, large-area $MoSe_2$ and $MoSe_2/Bi_2Se_3$ heterostructures on aln (0001)/si (111) substrates by molecular beam epitaxy," *Nanoscale*, vol. 7, no. 17, pp. 7896–7905, 2015. `https://doi.org/10.1039/C4NR06874B`.

[48] K. He, N. Kumar, L. Zhao, Z. Wang, K. F. Mak, H. Zhao, and J. Shan, "Tightly bound excitons in monolayer WSe_2," *Phys. Rev. Lett.*, vol. 113, no. 2, p. 026803, 2014. `https://doi.org/10.1103/PhysRevLett.113.026803`.

[49] A. Arora, M. Koperski, K. Nogajewski, J. Marcus, C. Faugeras, and M. Potemski, "Excitonic resonances in thin films of WSe_2: from monolayer to bulk material," *Nanoscale*, vol. 7, no. 23, pp. 10421–10429, 2015. `https://doi.org/10.1039/C5NR01536G`.

[50] D. Xiao, G.-B. Liu, W. Feng, X. Xu, and W. Yao, "Coupled spin and valley physics in monolayers of MoS_2 and other group-vi dichalcogenides," *Phys. Rev. Lett.*, vol. 108, no. 19, p. 196802, 2012. `https://doi.org/10.1103/PhysRevLett.108.196802`.

[51] K. F. Mak, K. He, J. Shan, and T. F. Heinz, "Control of valley polarization in monolayer MoS2 by optical helicity," *Nat. Nanotechnol.*, vol. 7, no. 8, pp. 494–498, 2012. `https://doi.org/10.1038/nnano.2012.96`.

[52] W. Yao, D. Xiao, and Q. Niu, "Valley-dependent optoelectronics from inversion symmetry breaking," *Phys. Rev. B*, vol. 77, no. 23, p. 235406, 2008. `https://doi.org/10.1103/PhysRevB.77.235406`.

[53] X. Xu, W. Yao, D. Xiao, and T. F. Heinz, "Spin and pseudospins in layered transition metal dichalcogenides," *Nat. Phys.*, vol. 10, no. 5, pp. 343–350, 2014. `https://doi.org/10.1038/nphys2942`.

[54] Y. Li, A. Chernikov, X. Zhang, A. Rigosi, H. M. Hill, A. M. Van Der Zande, D. A. Chenet, E.-M. Shih, J. Hone, and T. F. Heinz, "Measurement of the optical dielectric

function of monolayer transition-metal dichalcogenides: MoS_2, $MoSe_2$, WS_2, and WSe_2," *Phys. Rev. B*, vol. 90, no. 20, p. 205422, 2014. `https://doi.org/10.1103/PhysRevB.90.205422`.

[55] T. Goswami, H. Bhatt, K. J. Babu, G. Kaur, N. Ghorai, and H. N. Ghosh, "Ultrafast insights into high energy (c and d) excitons in few layer WS2," *J. Phys. Chem. Lett.*, vol. 12, no. 28, pp. 6526–6534, 2021. `https://doi.org/10.1021/acs.jpclett.1c01627`.

[56] W. Zhao, Z. Ghorannevis, L. Chu, M. Toh, C. Kloc, P.-H. Tan, and G. Eda, "Evolution of electronic structure in atomically thin sheets of WS2 and WSe2," *ACS Nano*, vol. 7, no. 1, pp. 791–797, 2013. `https://doi.org/10.1021/nn305275h`.

[57] S. H. Aleithan, M. Y. Livshits, S. Khadka, J. J. Rack, M. E. Kordesch, and E. Stinaff, "Broadband femtosecond transient absorption spectroscopy for a cvd mo s 2 monolayer," *Phys. Rev. B*, vol. 94, no. 3, p. 035445, 2016. `https://doi.org/10.1103/PhysRevB.94.035445`.

[58] R. Perea-Causin, D. Erkensten, J. M. Fitzgerald, J. J. Thompson, R. Rosati, S. Brem, and E. Malic, "Exciton optics, dynamics, and transport in atomically thin semiconductors," *APL Mater.*, vol. 10, no. 10, 2022. `https://doi.org/10.1063/5.0107665`.

[59] P. Rivera, H. Yu, K. L. Seyler, N. P. Wilson, W. Yao, and X. Xu, "Interlayer valley excitons in heterobilayers of transition metal dichalcogenides," *Nat. Nanotechnol.*, vol. 13, no. 11, pp. 1004–1015, 2018. `https://doi.org/10.1038/s41565-018-0193-0`.

[60] K. F. Mak, K. He, C. Lee, G. H. Lee, J. Hone, T. F. Heinz, and J. Shan, "Tightly bound trions in monolayer MoS_2," *Nat. Mater.*, vol. 12, no. 3, pp. 207–211, 2013. `https://doi.org/10.1038/nmat3505`.

[61] E. Malic, R. Perea-Causin, R. Rosati, D. Erkensten, and S. Brem, "Exciton transport in atomically thin semiconductors," *Nat. Commun.*, vol. 14, no. 1, p. 3430, 2023. `https://doi.org/10.1038/s41467-023-38556-9`.

[62] Y. You, X.-X. Zhang, T. C. Berkelbach, M. S. Hybertsen, D. R. Reichman, and T. F. Heinz, "Observation of biexcitons in monolayer WSe_2," *Nat. Phys.*, vol. 11, no. 6, pp. 477–481, 2015. `https://doi.org/10.1038/nphys3324`.

[63] L. M. Malard, T. V. Alencar, A. P. M. Barboza, K. F. Mak, and A. M. De Paula, "Observation of intense second harmonic generation from MoS_2 atomic crystals," *Phys. Rev. B*, vol. 87, no. 20, p. 201401, 2013. `https://doi.org/10.1103/PhysRevB.87.201401`.

[64] G. Wang, X. Marie, I. Gerber, T. Amand, D. Lagarde, L. Bouet, M. Vidal, A. Balocchi, and B. Urbaszek, "Giant enhancement of the optical second-harmonic emission

of WSe_2 monolayers by laser excitation at exciton resonances," *Phys. Rev. Lett.*, vol. 114, no. 9, p. 097403, 2015. `https://doi.org/10.1103/PhysRevLett.114.097403`.

[65] M. L. Trolle, Y.-C. Tsao, K. Pedersen, and T. G. Pedersen, "Observation of excitonic resonances in the second harmonic spectrum of MoS_2," *Phys. Rev. B*, vol. 92, no. 16, p. 161409, 2015. `https://doi.org/10.1103/PhysRevB.92.161409`.

[66] Y. Li, Y. Rao, K. F. Mak, Y. You, S. Wang, C. R. Dean, and T. F. Heinz, "Probing symmetry properties of few-layer MoS_2 and h-BN by optical second-harmonic generation," *Nano Lett.*, vol. 13, no. 7, pp. 3329–3333, 2013. `https://doi.org/10.1021/nl401561r`.

[67] J. Ribeiro-Soares, C. Janisch, Z. Liu, A. Elías, M. Dresselhaus, M. Terrones, L. Cançado, and A. Jorio, "Second harmonic generation in WSe_2," *2D Mater.*, vol. 2, no. 4, p. 045015, 2015. `https://doi.org/10.1088/2053-1583/2/4/045015`.

[68] F. B. Sousa, L. Lafeta, G. R. Fonseca, and A. M. de Paula, "Nonlinear optical imaging of two-dimensional nanomaterials," *Front. Nanotechnol.*, vol. 7, p. 1537299, 2025. `https://doi.org/10.3389/fnano.2025.1537299`.

[69] L. Lafeta, S. Hartmann, B. Rosa, S. Reitzenstein, L. M. Malard, and A. Hartschuh, "Probing noncentrosymmetric 2D materials by fourier space second harmonic imaging," *ACS Photonics*, 2025. `https://doi.org/10.1021/acsphotonics.4c01724`.

[70] A. Säynätjoki, L. Karvonen, H. Rostami, A. Autere, S. Mehravar, A. Lombardo, R. A. Norwood, T. Hasan, N. Peyghambarian, H. Lipsanen, K. Kieu, A. C. Ferrari, M. Polini, and Z. Sun, "Ultra-strong nonlinear optical processes and trigonal warping in MoS_2 layers," *Nat. Commun.*, vol. 8, no. 1, p. 893, 2017. `https://doi.org/10.1038/s41467-017-00749-4`.

[71] D. Li, W. Xiong, L. Jiang, Z. Xiao, H. Rabiee Golgir, M. Wang, X. Huang, Y. Zhou, Z. Lin, J. Song, S. Ducharme, L. Jiang, J.-F. Silvain, and Y. Lu, "Multimodal nonlinear optical imaging of MoS_2 and MoS_2-based van der waals heterostructures," *ACS Nano*, vol. 10, no. 3, pp. 3766–3775, 2016. `https://doi.org/10.1021/acsnano.6b00371`.

[72] B. A. Ko, A. V. Sokolov, M. O. Scully, Z. Zhang, and H. W. H. Lee, "Enhanced four-wave mixing process near the excitonic resonances of bulk MoS_2," *Photonics Res.*, vol. 7, no. 3, pp. 251–259, 2019. `https://doi.org/10.1364/PRJ.7.000251`.

[73] L. Lange, K. Wang, S. Bange, L. Lafeta, B. Rosa, S. Reitzenstein, J. M. Lupton, and A. Hartschuh, "Ultrafast phase-control of the nonlinear optical response of 2D semiconductors," *ACS Photonics*, vol. 11, no. 8, pp. 3112–3122, 2024. `https://doi.org/10.1021/acsphotonics.4c00388`.

[74] Y. Dai, Y. Wang, S. Das, S. Li, H. Xue, A. Mohsen, and Z. Sun, "Broadband plasmon-enhanced four-wave mixing in monolayer MoS_2," *Nano Lett.*, vol. 21, no. 14, pp. 6321–6327, 2021. `https://doi.org/10.1021/acs.nanolett.1c02381`.

[75] S. Iijima and T. Ichihashi, "Single-shell carbon nanotubes of 1-nm diameter," *Nature*, vol. 363, no. 6430, pp. 603–605, 1993. `https://doi.org/10.1038/363603a0`.

[76] S. Rathinavel, K. Priyadharshini, and D. Panda, "A review on carbon nanotube: An overview of synthesis, properties, functionalization, characterization, and the application," *Mater. Sci. Eng. B*, vol. 268, p. 115095, 2021. `https://doi.org/10.1016/j.mseb.2021.115095`.

[77] A. Jorio, R. Saito, T. Hertel, R. B. Weisman, G. Dresselhaus, and M. S. Dresselhaus, "Carbon nanotube photophysics," *MRS Bull.*, vol. 29, no. 4, pp. 276–280, 2004. `https://doi.org/10.1557/mrs2004.80`.

[78] W. A. Harrison, *Electronic Structure and the Properties of Solids: The Physics of the Chemical Bond.* Dover Publications, 1989. ISBN: 9780486660219.

[79] A. H. Castro Neto, F. Guinea, N. M. Peres, K. S. Novoselov, and A. K. Geim, "The electronic properties of graphene," *Rev. Mod. Phys.*, vol. 81, no. 1, pp. 109–162, 2009. `https://doi.org/10.1103/RevModPhys.81.109`.

[80] R. Saito, G. , Dresselhaus, and M. S. Dresselhaus, *Physical Properties of Carbon Nanotubes.* World scientific, 1998. `https://doi.org/10.1142/p080`.

[81] M. Böhmler, *Tip-enhanced near-field optical microscopy on the quasi 1D semiconductors carbon nanotubes and CdSe nanowires.* PhD thesis, LMU Munich University, 2012. `https://doi.org/10.5282/edoc.14652`.

[82] N. Hartmann, *Coupling of Emitters to Surface Plasmons investigated by Back Focal Plane Microscopy.* PhD thesis, LMU Munich University, 2013. `https://doi.org/10.5282/edoc.16423`.

[83] A. Jorio, G. Dresselhaus, and M. S. Dresselhaus, *Carbon Nanotubes: Advanced Topics in the Synthesis, Structure, Properties and Applications.* Topics in Applied Physics, 111, Springer, 2008. `https://doi.org/10.1007/978-3-540-72865-8`.

[84] T. D. Gokus, *Time-Resolved Photoluminescence and Elastic White Light Scattering Studies of Individual Carbon Nanotubes and Optical Characterization of Oxygen Plasma Treated Graphene.* PhD thesis, LMU Munich University, 2011. `https://doi.org/10.5282/edoc.13731`.

[85] J. Mintmire and C. White, "Universal density of states for carbon nanotubes," *Phys. Rev. Lett.*, vol. 81, no. 12, p. 2506, 1998. `https://doi.org/10.1103/PhysRevLett.81.2506`.

[86] K. J. Birkmeier, *Time resolved microscopy of exciton dynamics in nanoscopic objects.* PhD thesis, LMU Munich University, 2024. `https://doi.org/10.5282/edoc.33467`.

[87] Y. Miyauchi, M. Oba, and S. Maruyama, "Cross-polarized optical absorption of single-walled nanotubes by polarized photoluminescence excitation spectroscopy," *Phys. Rev. B*, vol. 74, no. 20, p. 205440, 2006. `https://doi.org/10.1103/PhysRevB.74.205440`.

[88] Y.-Z. Ma, J. Stenger, J. Zimmermann, S. M. Bachilo, R. E. Smalley, R. B. Weisman, and G. R. Fleming, "Ultrafast carrier dynamics in single-walled carbon nanotubes probed by femtosecond spectroscopy," *J. Chem. Phys.*, vol. 120, no. 7, pp. 3368–3373, 2004. `https://doi.org/10.1063/1.1640339`.

[89] F. Wang, G. Dukovic, L. E. Brus, and T. F. Heinz, "The optical resonances in carbon nanotubes arise from excitons," *Science*, vol. 308, no. 5723, pp. 838–841, 2005. `https://doi.org/10.1126/science.1110265`.

[90] T. Hertel, V. Perebeinos, J. Crochet, K. Arnold, M. Kappes, and P. Avouris, "Intersubband decay of 1-d exciton resonances in carbon nanotubes," *Nano Lett.*, vol. 8, no. 1, pp. 87–91, 2008. `https://doi.org/10.1021/nl0720915`.

[91] J. Maultzsch, R. Pomraenke, S. Reich, E. Chang, D. Prezzi, A. Ruini, E. Molinari, M. Strano, C. Thomsen, and C. Lienau, "Exciton binding energies in carbon nanotubes from two-photon photoluminescence," *Phys. Rev. B*, vol. 72, no. 24, p. 241402, 2005. `https://doi.org/10.1103/PhysRevB.72.241402`.

[92] G. Soavi, F. Scotognella, G. Lanzani, and G. Cerullo, "Ultrafast photophysics of single-walled carbon nanotubes," *Adv. Opt. Mater.*, vol. 4, no. 11, pp. 1670–1688, 2016. `https://doi.org/10.1002/adom.201600361`.

[93] C. Mann and T. Hertel, "13 nm exciton size in (6, 5) single-wall carbon nanotubes," *J. Phys. Chem. Lett.*, vol. 7, no. 12, pp. 2276–2280, 2016. `https://doi.org/10.1021/acs.jpclett.6b00797`.

[94] C. Georgi, M. Böhmler, H. Qian, L. Novotny, and A. Hartschuh, "Probing exciton propagation and quenching in carbon nanotubes with near-field optical microscopy," *Phys. Status Solidi B*, vol. 246, no. 11-12, pp. 2683–2688, 2009. `https://doi.org/10.1002/pssb.200982306`.

[95] F. Jakubka, S. B. Grimm, Y. Zakharko, F. Gannott, and J. Zaumseil, "Trion electroluminescence from semiconducting carbon nanotubes," *ACS Nano*, vol. 8, no. 8, pp. 8477–8486, 2014. `https://doi.org/10.1021/nn503046y`.

[96] B. Yuma, S. Berciaud, J. Besbas, J. Shaver, S. Santos, S. Ghosh, R. B. Weisman, L. Cognet, M. Gallart, M. Ziegler, B. Hönerlage, B. Lounis, and P. Gilliot, "Biexciton,

single carrier, and trion generation dynamics in single-walled carbon nanotubes," *Phys. Rev. B*, vol. 87, no. 20, p. 205412, 2013. `https://doi.org/10.1002/pssb.200982306`.

[97] K. J. Hughes, K. A. Iyer, R. E. Bird, J. Ivanov, S. Banerjee, G. Georges, and Q. A. Zhou, "Review of carbon nanotube research and development: materials and emerging applications," *ACS Appl. Nano Mater.*, vol. 7, no. 16, pp. 18695–18713, 2024. `https://doi.org/10.1021/acsanm.4c02721`.

[98] A. Thess, R. Lee, P. Nikolaev, H. Dai, P. Petit, J. Robert, C. Xu, Y. H. Lee, S. G. Kim, A. G. Rinzler, D. T. Colbert, G. E. Scuseria, D. Tománek, J. E. Fischer, and R. E. Smalley, "Crystalline ropes of metallic carbon nanotubes," *Science*, vol. 273, no. 5274, pp. 483–487, 1996. `https://doi.org/0.1126/science.273.5274.483`.

[99] L. Lange, F. Schäfer, A. Biewald, R. Ciesielski, and A. Hartschuh, "Controlling photon antibunching from 1d emitters using optical antennas," *Nanoscale*, vol. 11, no. 31, pp. 14907–14911, 2019. `https://doi.org/10.1039/C9NR03688A`.

[100] M. Esmann, S. C. Wein, and C. Antón-Solanas, "Solid-state single-photon sources: Recent advances for novel quantum materials," *Adv. Funct. Mater.*, vol. 34, no. 30, p. 2315936, 2024. `https://doi.org/10.1002/adfm.202315936`.

[101] W. Luo, L. Cao, Y. Shi, L. Wan, H. Zhang, S. Li, G. Chen, Y. Li, S. Li, Y. Wang, S. Sun, M. F. Karim, H. Cai, K. Chuan, and A. Q. Liu, "Recent progress in quantum photonic chips for quantum communication and internet," *Light Sci. Appl.*, vol. 12, no. 1, p. 175, 2023. `https://doi.org/10.1038/s41377-023-01173-8`.

[102] E. Meyer-Scott, C. Silberhorn, and A. Migdall, "Single-photon sources: Approaching the ideal through multiplexing," *Rev. Sci. Instrum.*, vol. 91, no. 4, 2020. `https://doi.org/10.1063/5.0003320`.

[103] M. Koperski, K. Nogajewski, A. Arora, V. Cherkez, P. Mallet, J.-Y. Veuillen, J. Marcus, P. Kossacki, and M. Potemski, "Single photon emitters in exfoliated WSe2 structures," *Nat. Nanotechnol.*, vol. 10, no. 6, pp. 503–506, 2015. `https://doi.org/10.1038/nnano.2015.67`.

[104] J. Kern, I. Niehues, P. Tonndorf, R. Schmidt, D. Wigger, R. Schneider, T. Stiehm, S. Michaelis de Vasconcellos, D. E. Reiter, T. Kuhn, and B. Rudolf, "Nanoscale positioning of single-photon emitters in atomically thin WSe2.," *Adv. Mater.*, vol. 28, no. 33, pp. 7101–7105, 2016. `https://doi.org/10.1002/adma.201600560`.

[105] R. Bourrellier, S. Meuret, A. Tararan, O. Stéphan, M. Kociak, L. H. Tizei, and A. Zobelli, "Bright uv single photon emission at point defects in h-BN," *Nano Lett.*, vol. 16, no. 7, pp. 4317–4321, 2016. `https://doi.org/10.1021/acs.nanolett.6b01368`.

[106] T. T. Tran, C. Elbadawi, D. Totonjian, C. J. Lobo, G. Grosso, H. Moon, D. R. Englund, M. J. Ford, I. Aharonovich, and M. Toth, “Robust multicolor single photon emission from point defects in hexagonal boron nitride,” *ACS Nano*, vol. 10, no. 8, pp. 7331–7338, 2016. `https://doi.org/10.1021/acsnano.6b03602`.

[107] M. J. Holmes, K. Choi, S. Kako, M. Arita, and Y. Arakawa, “Room-temperature triggered single photon emission from a iii-nitride site-controlled nanowire quantum dot,” *Nano Lett.*, vol. 14, no. 2, pp. 982–986, 2014. `https://doi.org/10.1021/nl404400d`.

[108] A. Högele, C. Galland, M. Winger, and A. Imamoğlu, “Photon antibunching in the photoluminescence spectra of a single carbon nanotube,” *Phys. Rev. Lett.*, vol. 100, no. 21, p. 217401, 2008. `https://doi.org/10.1103/PhysRevLett.100.217401`.

[109] M. S. Hofmann, J. T. Glückert, J. Noé, C. Bourjau, R. Dehmel, and A. Högele, “Bright, long-lived and coherent excitons in carbon nanotube quantum dots,” *Nat. Nanotechnol.*, vol. 8, no. 7, pp. 502–505, 2013. `https://doi.org/10.1038/nnano.2013.119`.

[110] A. Jeantet, Y. Chassagneux, T. Claude, P. Roussignol, J.-S. Lauret, J. Reichel, and C. Voisin, “Exploiting one-dimensional exciton–phonon coupling for tunable and efficient single-photon generation with a carbon nanotube,” *Nano Lett.*, vol. 17, no. 7, pp. 4184–4188, 2017. `https://doi.org/10.1021/acs.nanolett.7b00973`.

[111] A. Ishii, T. Uda, and Y. K. Kato, “Room-temperature single-photon emission from micrometer-long air-suspended carbon nanotubes,” *Phys. Rev. Appl.*, vol. 8, no. 5, p. 054039, 2017. `https://doi.org/10.1103/PhysRevApplied.8.054039`.

[112] R. Kawabe, H. Takaki, T. Ibi, Y. Maeda, K. Nakagawa, and H. Maki, “Pure and efficient single-photon sources by shortening and functionalizing air-suspended carbon nanotubes,” *ACS Appl. Nano Mater.*, vol. 3, no. 1, pp. 682–690, 2019. `https://doi.org/10.1021/acsanm.9b02209`.

[113] X. Ma, N. F. Hartmann, J. K. Baldwin, S. K. Doorn, and H. Htoon, “Room-temperature single-photon generation from solitary dopants of carbon nanotubes,” *Nat. Nanotechnol.*, vol. 10, no. 8, pp. 671–675, 2015. `https://doi.org/10.1038/nnano.2015.136`.

[114] X. He, N. F. Hartmann, X. Ma, Y. Kim, R. Ihly, J. L. Blackburn, W. Gao, J. Kono, Y. Yomogida, A. Hirano, T. Tanaka, H. Kataura, H. Htoon, and S. K. Doorn, “Tunable room-temperature single-photon emission at telecom wavelengths from sp 3 defects in carbon nanotubes,” *Nat. Photonics*, vol. 11, no. 9, pp. 577–582, 2017. `https://doi.org/10.1038/nphoton.2017.119`.

[115] A. Ishii, X. He, N. F. Hartmann, H. Machiya, H. Htoon, S. K. Doorn, and Y. K. Kato, “Enhanced single-photon emission from carbon-nanotube dopant states coupled to

silicon microcavities," *Nano Lett.*, vol. 18, no. 6, pp. 3873–3878, 2018. `https://doi.org/10.1021/acs.nanolett.8b01170`.

[116] Z. Li, K. Otsuka, D. Yamashita, D. Kozawa, and Y. K. Kato, "Quantum emission assisted by energy landscape modification in pentacene-decorated carbon nanotubes," *ACS Photonics*, vol. 8, no. 8, pp. 2367–2374, 2021. `https://doi.org/10.1021/acsphotonics.1c00539`.

[117] T. Endo, J. Ishi-Hayase, and H. Maki, "Photon antibunching in single-walled carbon nanotubes at telecommunication wavelengths and room temperature," *Appl. Phys. Lett.*, vol. 106, no. 11, 2015. `https://doi.org/10.1063/1.4915618`.

[118] A. G. Curto, G. Volpe, T. H. Taminiau, M. P. Kreuzer, R. Quidant, and N. F. Van Hulst, "Unidirectional emission of a quantum dot coupled to a nanoantenna," *Science*, vol. 329, no. 5994, pp. 930–933, 2010. `https://doi.org/10.1126/science.1191922`.

[119] A. F. Koenderink, "Single-photon nanoantennas," *ACS Photonics*, vol. 4, no. 4, pp. 710–722, 2017. `https://doi.org/10.1021/acsphotonics.7b00061`.

[120] K. G. Lee, X. W. Chen, H. Eghlidi, P. Kukura, R. Lettow, A. Renn, V. Sandoghdar, and S. Götzinger, "A planar dielectric antenna for directional single-photon emission and near-unity collection efficiency," *Nat. Photonics*, vol. 5, no. 3, pp. 166–169, 2011. `https://doi.org/10.1038/nphoton.2010.312`.

[121] A. Singh, P. M. de Roque, G. Calbris, J. T. Hugall, and N. F. van Hulst, "Nanoscale mapping and control of antenna-coupling strength for bright single photon sources," *Nano Lett.*, vol. 18, no. 4, pp. 2538–2544, 2018. `https://doi.org/10.1021/acs.nanolett.8b00239`.

[122] A. Einstein, "Über einen die erzeugung und verwandlung des lichtes betreffenden heuristischen gesichtspunkt [adp 17, 132 (1905)]," *Ann. Phys.*, vol. 517, pp. 164–181, 1905. `https://doi.org/10.1002/andp.2005517S111`.

[123] G. Breit, "Are quanta unidirectional?," *Phys. Rev.*, vol. 22, no. 4, p. 313, 1923. `https://doi.org/10.1103/PhysRev.22.313`.

[124] D. Ferreira, R. Bachelard, W. Guerin, R. Kaiser, and M. Fouché, "Connecting field and intensity correlations: The siegert relation and how to test it," *Am. J. Phys.*, vol. 88, no. 10, pp. 831–837, 2020. `https://doi.org/10.1119/10.0001630`.

[125] R. H. Brown and R. Q. Twiss, "Correlation between photons in two coherent beams of light," *Nature*, vol. 177, no. 4497, pp. 27–29, 1956. `https://doi.org/10.1038/177027a0`.

[126] H. Paul, *Photonen: eine Einführung in die Quantenoptik.* Springer-Verlag, 1995. `https://doi.org/10.1007/978-3-322-90681-6`.

[127] A. M. Fox, *Quantum Optics: An Introduction*, vol. 15. Oxford University Press, 2006. `https://global.oup.com/academic/product/quantum-optics-9780198566731?cc=de&lang=en&#`.

[128] M. Quine and E. Seneta, "Bortkiewicz's data and the law of small numbers," *Int. Stat. Rev.*, pp. 173–181, 1987. `https://doi.org/10.2307/1403193`.

[129] L. Novotny and N. Van Hulst, "Antennas for light," *Nat. Photonics*, vol. 5, no. 2, pp. 83–90, 2011. `https://doi.org/10.1038/nphoton.2010.237`.

[130] L. Novotny and B. Hecht, *Principles of Nano-Optics.* Cambridge University Press, 2012. `https://doi.org/10.1017/CBO9780511794193`.

[131] N. Mauser, *Antenna-enhanced optoelectronic probing of carbon nanotube devices.* PhD thesis, LMU Munich University, 2014. `https://doi.org/10.5282/edoc.17623`.

[132] N. Mauser and A. Hartschuh, "Tip-enhanced near-field optical microscopy," *Chem. Soc. Rev.*, vol. 43, no. 4, pp. 1248–1262, 2014. `https://doi.org/10.1039/C3CS60258C`.

[133] P. Bharadwaj, B. Deutsch, and L. Novotny, "Optical antennas," *Adv. Opt. Photonics*, vol. 1, no. 3, pp. 438–483, 2009. `https://doi.org/10.1364/AOP.1.000438`.

[134] X. Shi, N. Coca-Lopez, J. Janik, and A. Hartschuh, "Advances in tip-enhanced near-field raman microscopy using nanoantennas," *Chem. Rev.*, vol. 117, no. 7, pp. 4945–4960, 2017. `https://doi.org/10.1021/acs.chemrev.6b00640`.

[135] N. K. Subbaiyan, S. Cambré, A. N. G. Parra-Vasquez, E. H. Hároz, S. K. Doorn, and J. G. Duque, "Role of surfactants and salt in aqueous two-phase separation of carbon nanotubes toward simple chirality isolation," *ACS Nano*, vol. 8, no. 2, pp. 1619–1628, 2014. `https://doi.org/10.1021/nn405934y`.

[136] G. Ao, C. Y. Khripin, and M. Zheng, "Dna-controlled partition of carbon nanotubes in polymer aqueous two-phase systems," *J. Am. Chem. Soc.*, vol. 136, no. 29, pp. 10383–10392, 2014. `https://doi.org/10.1021/ja504078b`.

[137] C. Georgi, *Exciton Mobility and Localized Defects in Single Carbon Nanotubes Studied with Tip-Enhanced Near-Field Optical Microscopy.* PhD thesis, LMU Munich University, 2011. `https://doi.org/10.5282/edoc.12668`.

[138] T. Gokus, L. Cognet, J. G. Duque, M. Pasquali, A. Hartschuh, and B. Lounis, "Mono-and biexponential luminescence decays of individual single-walled carbon nanotubes," *J. Phys. Chem. C*, vol. 114, no. 33, pp. 14025–14028, 2010. `https://doi.org/10.1021/jp1049217`.

[139] M. Stalder and M. Schadt, “Linearly polarized light with axial symmetry generated by liquid-crystal polarization converters,” *Opt. Lett.*, vol. 21, no. 23, pp. 1948–1950, 1996. `https://doi.org/10.1364/OL.21.001948`.

[140] Y. Lai, Z. Shen, Y. Chen, J. Wang, J. Guo, and Z. Wei, “The impact of afterpulsing effects in single-photon detectors on the performance metrics of single-photon detection systems,” *Photonics*, vol. 11, no. 11, 2024. `https://doi.org/10.3390/photonics11111074`.

[141] R. B. Capaz, C. D. Spataru, S. Ismail-Beigi, and S. G. Louie, “Diameter and chirality dependence of exciton properties in carbon nanotubes,” *Phys. Rev. B*, vol. 74, no. 12, p. 121401, 2006. `https://doi.org/10.1103/PhysRevB.74.121401`.

[142] F. Wang, G. Dukovic, L. E. Brus, and T. F. Heinz, “Time-resolved fluorescence of carbon nanotubes and its implication for radiative lifetimes,” *Phys. Rev. Lett.*, vol. 92, no. 17, p. 177401, 2004. `https://doi.org/10.1103/PhysRevLett.92.177401`.

[143] P. Anger, P. Bharadwaj, and L. Novotny, “Enhancement and quenching of single-molecule fluorescence,” *Phys. Rev. Lett.*, vol. 96, no. 11, p. 113002, 2006. `https://doi.org/10.1103/PhysRevLett.96.113002`.

[144] H. Htoon, J. A. Hollingsworth, R. Dickerson, and V. I. Klimov, “Effect of zero- to one-dimensional transformation on multiparticle auger recombination in semiconductor quantum rods,” *Phys. Rev. Lett.*, vol. 91, no. 22, p. 227401, 2003. `https://doi.org/10.1103/PhysRevLett.91.227401`.

[145] I. Robel, B. A. Bunker, P. V. Kamat, and M. Kuno, “Exciton recombination dynamics in cdse nanowires: bimolecular to three-carrier auger kinetics,” *Nano Lett.*, vol. 6, no. 7, pp. 1344–1349, 2006. `https://doi.org/10.1021/nl060199z`.

[146] M. Böhmler, Z. Wang, A. Myalitsin, A. Mews, and A. Hartschuh, “Optical imaging of cdse nanowires with nanoscale resolution,” *Angew. Chem. Int. Ed.*, vol. 50, no. 48, pp. 11536–11538, 2011. `https://doi.org/10.1002/anie.201105217`.

[147] Y. Luo, E. D. Ahmadi, K. Shayan, Y. Ma, K. S. Mistry, C. Zhang, J. Hone, J. L. Blackburn, and S. Strauf, “Purcell-enhanced quantum yield from carbon nanotube excitons coupled to plasmonic nanocavities,” *Nat. Commun.*, vol. 8, no. 1, p. 1413, 2017. `https://doi.org/10.1038/s41467-017-01777-w`.

[148] J. M. Bauer, L. Chen, P. Wilhelm, K. Watanabe, T. Taniguchi, S. Bange, J. M. Lupton, and K.-Q. Lin, “Excitonic resonances control the temporal dynamics of nonlinear optical wave mixing in monolayer semiconductors,” *Nat. Photonics*, vol. 16, no. 11, pp. 777–783, 2022. `https://doi.org/10.1038/s41566-022-01080-1`.

[149] E. Brühl, T. Buckup, and M. Motzkus, “Experimental and numerical investigation of a phase-only control mechanism in the linear intensity regime,” *J. Chem. Phys.*, vol. 148, no. 21, p. 214310, 2018. `https://doi.org/10.1063/1.5029805`.

[150] D. Meshulach and Y. Silberberg, "Coherent quantum control of two-photon transitions by a femtosecond laser pulse," *Nature*, vol. 396, no. 6708, pp. 239–242, 1998. `https://doi.org/10.1038/24329`.

[151] J. Lahiri, S. H. Yuwono, I. Magoulas, M. Moemeni, B. Borhan, G. Blanchard, P. Piecuch, and M. Dantus, "Controlling quantum interference between virtual and dipole two-photon optical excitation pathways using phase-shaped laser pulses," *J. Phys. Chem. A*, vol. 125, no. 34, pp. 7534–7544, 2021. `https://doi.org/10.1021/acs.jpca.1c03069`.

[152] D. Meshulach and Y. Silberberg, "Coherent quantum control of multiphoton transitions by shaped ultrashort optical pulses," *Phys. Rev. A*, vol. 60, no. 2, p. 1287, 1999. `https://doi.org/10.1103/PhysRevA.60.1287`.

[153] O. Meron, U. Arieli, E. Bahar, S. Deb, M. Ben Shalom, and H. Suchowski, "Shaping exciton polarization dynamics in 2D semiconductors by tailored ultrafast pulses," *Light Sci. Appl.*, vol. 14, no. 1, p. 80, 2025. `https://doi.org/10.1038/s41377-025-01748-7`.

[154] R. Fork, B. Greene, and C. V. Shank, "Generation of optical pulses shorter than 0.1 psec by colliding pulse mode locking," *Appl. Phys. Lett.*, vol. 38, no. 9, pp. 671–672, 1981. `https://doi.org/10.1063/1.92500`.

[155] C. W. Hillegas, J. X. Tull, D. Goswami, D. Strickland, and W. S. Warren, "Femtosecond laser pulse shaping by use of microsecond radio-frequency pulses," *Opt. Lett.*, vol. 19, no. 10, pp. 737–739, 1994. `https://doi.org/10.1364/OL.19.000737`.

[156] A. M. Weiner, "Femtosecond optical pulse shaping and processing," *Prog. Quantum. Electron.*, vol. 19, no. 3, pp. 161–237, 1995. `https://doi.org/10.1016/0079-6727(94)00013-O`.

[157] A. M. Weiner, "Femtosecond pulse shaping using spatial light modulators," *Rev. Sci. Instrum.*, vol. 71, no. 5, pp. 1929–1960, 2000. `https://doi.org/10.1063/1.1150614`.

[158] A. M. Weiner, "Ultrafast optical pulse shaping: A tutorial review," *Opt. Commun.*, vol. 284, no. 15, pp. 3669–3692, 2011. `https://doi.org/10.1016/j.optcom.2011.03.084`.

[159] P. Nuernberger, S. Ruetzel, and T. Brixner, "Multidimensionale elektronische spektroskopie photochemischer reaktionen," *Angew. Chem.*, vol. 127, no. 39, pp. 11526–11546, 2015. `https://doi.org/10.1002/ange.201502974`.

[160] A. M. Weiner, *Ultrafast Optics.* John Wiley & Sons, 2011. `https://www.wiley.com/Ultrafast+Optics-p-9781118211472`.

[161] R. Trebino, K. W. DeLong, D. N. Fittinghoff, J. N. Sweetser, M. A. Krumbügel, B. A. Richman, and D. J. Kane, "Measuring ultrashort laser pulses in the time-frequency domain using frequency-resolved optical gating," *Rev. Sci. Instrum.*, vol. 68, no. 9, pp. 3277–3295, 1997. `https://doi.org/doi.org/10.1063/1.1148286`.

[162] C. Iaconis and I. A. Walmsley, "Spectral phase interferometry for direct electric-field reconstruction of ultrashort optical pulses," *Opt. Lett.*, vol. 23, pp. 792–794, May 1998. `https://doi.org/10.1364/OL.23.000792`.

[163] F. Duarte, "Prismatic pulse compression: beam deviations and geometrical perturbations," *Opt. Quantum Electron.*, vol. 22, pp. 467–471, 1990. `https://doi.org/10.1007/BF02113970`.

[164] E. Treacy, "Optical pulse compression with diffraction gratings," *IEEE J. Quantum Electron.*, vol. 5, no. 9, pp. 454–458, 1969. `https://doi.org/10.1109/JQE.1969.1076303`.

[165] G. Steinmeyer, "A review of ultrafast optics and optoelectronics," *J. Opt. A: Pure Appl. Opt.*, vol. 5, no. 1, p. R1, 2002. `https://doi.org/10.1088/1464-4258/5/1/201`.

[166] V. V. Lozovoy, I. Pastirk, and M. Dantus, "Multiphoton intrapulse interference. iv. ultrashort laser pulse spectral phase characterization and compensation," *Opt. Lett.*, vol. 29, no. 7, pp. 775–777, 2004. `https://doi.org/10.1364/OL.29.000775`.

[167] A. Comin, R. Ciesielski, G. Piredda, K. Donkers, and A. Hartschuh, "Compression of ultrashort laser pulses via gated multiphoton intrapulse interference phase scans," *J. Opt. Soc. Am. B*, vol. 31, no. 5, pp. 1118–1125, 2014. `https://doi.org/10.1364/JOSAB.31.001118`.

[168] A. Comin, R. Ciesielski, N. Coca-López, and A. Hartschuh, "Phase retrieval of ultrashort laser pulses using a miips algorithm," *Opt. Express*, vol. 24, no. 3, pp. 2505–2512, 2016. `https://doi.org/10.1364/OE.24.002505`.

[169] A. Fraser and D. Burnell, *Computer Models in Genetics.* McGraw-Hill, 1970. `https://doi.org/10.1126/science.172.3979.147.a`.

[170] J. L. Crosby, *Computer Simulation in Genetics.* John Wiley & Sons, 1973. ISBN: 9780471188803.

[171] J. H. Holland, *Adaptation in Natural and Artificial Systems: An Introductory Analysis with Applications to Biology, Control, and Artificial Intelligence.* MIT Press, 2nd ed., 1992. `https://doi.org/10.7551/mitpress/1090.001.0001`.

[172] T. Baumert, T. Brixner, V. Seyfried, M. Strehle, and G. Gerber, "Femtosecond pulse shaping by an evolutionary algorithm with feedback," *Appl. Phys. B*, vol. 65, no. 6, 1997. `https://doi.org/10.1007/S003400050346`.

[173] R. Ciesielski, *Ultrafast dynamics in single nanostructures investigated by pulse shaping microscopy.* PhD thesis, LMU Munich University, 2016. `https://doi.org/10.5282/edoc.19742`.

[174] R. Ciesielski, A. Comin, M. Handloser, K. Donkers, G. Piredda, A. Lombardo, A. C. Ferrari, and A. Hartschuh, “Graphene near-degenerate four-wave mixing for phase characterization of broadband pulses in ultrafast microscopy,” *Nano Lett.*, vol. 15, no. 8, pp. 4968–4972, 2015. `https://doi.org/10.1021/acs.nanolett.5b00893`.

[175] L. Bonacina, Y. Mugnier, F. Courvoisier, R. Le Dantec, J. Extermann, Y. Lambert, V. Boutou, C. Galez, and J.-P. Wolf, “Polar $Fe(IO_3)_3$ nanocrystals as local probes for nonlinear microscopy,” *Appl. Phys. B*, vol. 87, pp. 399–403, 2007. `https://doi.org/10.1007/s00340-007-2612-z`.

[176] E. Hendry, P. J. Hale, J. Moger, A. K. Savchenko, and S. A. Mikhailov, “Coherent nonlinear optical response of graphene,” *Phys. Rev. Lett.*, vol. 105, p. 097401, Aug 2010. `https://doi.org/10.1103/PhysRevLett.105.097401`.

[177] K. S. Novoselov, A. K. Geim, S. V. Morozov, D. Jiang, Y. Zhang, S. V. Dubonos, I. V. Grigorieva, and A. A. Firsov, “Electric field effect in atomically thin carbon films,” *Science*, vol. 306, no. 5696, pp. 666–669, 2004. `https://doi.org/10.1126/science.1102896`.

[178] R. Schmidt, G. Berghauser, R. Schneider, M. Selig, P. Tonndorf, E. Malic, A. Knorr, S. Michaelis de Vasconcellos, and R. Bratschitsch, “Ultrafast coulomb-induced intervalley coupling in atomically thin WS_2,” *Nano Lett.*, vol. 16, no. 5, pp. 2945–2950, 2016. `https://doi.org/10.1021/acs.nanolett.5b04733`.

[179] N. Dudovich, B. Dayan, S. M. G. Faeder, and Y. Silberberg, “Transform-limited pulses are not optimal for resonant multiphoton transitions,” *Phys. Rev. Lett.*, vol. 86, pp. 47–50, Jan 2001. `https://doi.org/10.1103/PhysRevLett.86.47`.

[180] H. G. Rosa, Y. W. Ho, I. Verzhbitskiy, M. J. Rodrigues, T. Taniguchi, K. Watanabe, G. Eda, V. M. Pereira, and J. C. Gomes, “Characterization of the second-and third-harmonic optical susceptibilities of atomically thin tungsten diselenide,” *Sci. Rep.*, vol. 8, no. 1, p. 10035, 2018. `https://doi.org/10.1038/s41598-018-28374-1`.

[181] Y. Li and T. F. Heinz, “Two-dimensional models for the optical response of thin films,” *2D Mater.*, vol. 5, no. 2, p. 025021, 2018. `https://doi.org/10.1088/2053-1583/aab0cf`.

[182] G. Moody, C. Kavir Dass, K. Hao, C.-H. Chen, L.-J. Li, A. Singh, K. Tran, G. Clark, X. Xu, G. Berghäuser, E. Malic, A. Knorr, and X. Li, “Intrinsic homogeneous linewidth and broadening mechanisms of excitons in monolayer transition metal dichalcogenides,” *Nat. Commun.*, vol. 6, no. 1, p. 8315, 2015. `https://doi.org/10.1038/ncomms9315`.

[183] F. Katsch, M. Selig, and A. Knorr, “Exciton-scattering-induced dephasing in two-dimensional semiconductors,” *Phys. Rev. Lett.*, vol. 124, no. 25, p. 257402, 2020. `https://doi.org/10.1103/PhysRevLett.124.257402`.

[184] A. Chernikov, T. C. Berkelbach, H. M. Hill, A. Rigosi, Y. Li, B. Aslan, D. R. Reichman, M. S. Hybertsen, and T. F. Heinz, “Exciton binding energy and nonhydrogenic rydberg series in monolayer WS_2,” *Phys. Rev. Lett.*, vol. 113, no. 7, p. 076802, 2014. `https://doi.org/10.1103/PhysRevLett.113.076802`.

[185] A. Steinhoff, M. Florian, M. Rösner, G. Schönhoff, T. O. Wehling, and F. Jahnke, “Exciton fission in monolayer transition metal dichalcogenide semiconductors,” *Nat. Commun.*, vol. 8, no. 1, p. 1166, 2017. `https://doi.org/10.1038/s41467-017-01298-6`.

[186] D. B. Soh, C. Rogers, D. J. Gray, E. Chatterjee, and H. Mabuchi, “Optical nonlinearities of excitons in monolayer MoS_2,” *Phys. Rev. B*, vol. 97, no. 16, p. 165111, 2018. `https://doi.org/10.1103/PhysRevB.97.165111`.

[187] Y. V. Zhumagulov, V. D. Neverov, A. E. Lukyanov, D. R. Gulevich, A. V. Krasavin, A. Vagov, and V. Perebeinos, “Nonlinear spectroscopy of excitonic states in transition metal dichalcogenides,” *Phys. Rev. B*, vol. 105, no. 11, p. 115436, 2022. `https://doi.org/10.1103/PhysRevB.105.115436`.

[188] M. L. Trolle, G. Seifert, and T. G. Pedersen, “Theory of excitonic second-harmonic generation in monolayer MoS_2,” *Phys. Rev. B*, vol. 89, no. 23, p. 235410, 2014. `https://doi.org/10.1103/PhysRevB.89.235410`.

[189] F. Katsch and A. Knorr, “Optical preparation and coherent control of ultrafast nonlinear quantum superpositions in exciton gases: A case study for atomically thin semiconductors,” *Phys. Rev. X*, vol. 10, no. 4, p. 041039, 2020. `https://doi.org/10.1103/PhysRevX.10.041039`.

Acknowledgement

Over the past years, I have had the great pleasure of engaging daily with fascinating scientific questions, carrying out exciting experiments and working together with wonderful people. I would like to express my special gratitude to everyone who has accompanied and supported me and with whom I have had the pleasure of working and learning throughout this time.

First and foremost, I would like to express my deepest gratitude to my supervisor, **Prof. Achim Hartschuh**, for his guidance, continuous support and patience throughout my PhD. He gave me the freedom to try everything in the lab and was always there to help whenever needed. His valuable insights and constant encouragement have been of invaluable importance for my personal and scientific development.

I am also grateful to **Prof. Alexander Högele** for acting as the second referee of this thesis. Furthermore, I would like to sincerely thank **Prof. Lamb, Prof. Laquai, Prof. Tinnefeld** and **Prof. Wintterlin** for their willingness to constitute my thesis committee.

Special thanks go to my colleagues and friends in the **Hartschuh group — Alex, Lucas, Hari, Veit, Richard, Konrad, Kunliang, Zehua, Amir, Rico, Frank, Oliver, Sean, Rachid, Meriem, Alberto, Nico, Meltem, David and Irene**. I truly appreciated the scientific discussions, the collaborative work, and the time we spent together outside the lab. **Alex**, thank you for your outstanding scientific support, your friendship and the good coffee. **Lucas**, thank you for your openness, the good times and your scientific expertise. **Veit**, thank you for introducing me to the pulse-shaping setup and for your support. **Hari**, thank you for all the laughter we shared in the office.

A particularly silent and sorrowful thanks goes to **Uta**.

Thank you to all members of the Department of Physical Chemistry – in particular **Lennart, Vicky, Michi and Evelyn** – for the great atmosphere and conversations.

I am grateful to **Dr. Sebastian Bange** for the productive scientific collaboration and insightful discussions. I would also like to thank all my collaboration partners, especially **Dr. Bárbara Rosa** and **Dr. Chentao Li** for providing high quality sample materials.

Special appreciation goes to **Dr. Matthias Handloser** for his guidance and encouragement in making the decision to return to university.

Einen besonderen Dank möchte ich meiner Familie für ihre unermüdliche und großartige Unterstützung aussprechen. Meinen Eltern **Otto, Susanne und Martin** danke ich herzlich für die Möglichkeiten, die Rückendeckung und Ermutigungen während meiner gesamten Ausbildung. **Cornelia** und **Jan Dirk** danke ich für eure tatkräftige Hilfe, die mir Freiraum für meine Arbeit geschaffen hat. **Vivien, Emilia** und **Bennet**, danke, dass ihr da seid und für eure ständige Unterstützung auf dem gesamten Weg!